REPORT DOCUMENTATION PAGE

Form Approved OMB No. 0704-0188

1. AGENCY USE ONLY (*Leave Blank*)	2. REPORT DATE	3. REPORT TYPE AND DATES COVERED
		Technical 10/1/96-9/15/98

4. TITLE AND SUBTITLE

Experimental Study of High Reynolds Number (Re =23000) Two and Three-Dimensional Turbulent Boundary Layers

5. FUNDING NUMBERS

N00014-94-1-0092

6. AUTHOR(S)

M. Semih Olcmen, Roger L. Simpson, Jacob George, and Cindy Whitfield

7. PERFORMING ORGANIZATION NAME(S) AND ADDRESS(ES)

Dept. of Aerospace and Ocean Engineering
Virginia Polytechnic Institute and State University
Blacksburg, VA 24061-0203

8. PERFORMING ORGANIZATION REPORT NUMBER

VPI-AOE-260

9. SPONSORING/MONITORING AGENCY NAME(S) AND ADDRESS(ES)

Office of Naval Research
800 N. Quincy Street
Arlington, VA 22217

10. SPONSORING/MONITORING AGENCY REPORT NUMBER

11. SUPPLEMENTARY NOTES

12a. DISTRIBUTION/AVAILABILITY STATEMENT

UNLIMITED

12b. DISTRIBUTION CODE

13. ABSTRACT (*Maximum 200 words*)

Experimental data obtained in a two-dimensional turbulent boundary layer (TBL) flow and a three-dimensional (3D) pressure-driven TBL flow around a wing/body junction are presented. Reynolds number effects are investigated. Fine spatial resolution laser-Doppler velocimeter measurements of mean velocity and higher order statistics including the third order products measured for 9 stations are reported. Reynolds number based on momentum thickness (Re_θ) of the developing 2-D boundary layer on the wall was Re_θ=23200, and the approach nominal reference velocity of the undisturbed air flow was 32 m/sec. The wing shape used had a 3:2 elliptical nose, NACA 0020 profiled tail and it was mounted on a flat wall. Distribution of measured static pressure variation on the wall, turbulent kinetic energy and some derived quantities such as the flow angle, flow gradient angle, shear stress angle, and modeling parameters such as $\tau/\overline{v^2}$, $B=\overline{v^3}/(\overline{u^2v}+\overline{v^3}+\overline{vw^2})$, $B_2=\overline{v^3}/[(\overline{uv^2})^2+(\overline{v^2w})^2]$ are also discussed.

14. SUBJECT TERMS

Three-Dimensional FLow, Turbulence Structure, High Reynolds Number Turbulence

15. NUMBER OF PAGES

168

16. PRICE CODE

17. SECURITY CLASSIFICATION OF REPORT	18. SECURITY CLASSIFICATION OF THIS PAGE	19. SECURITY CLASSIFICATION OF ABSTRACT	20. LIMITATION OF ABSTRACT
UNCLASSIFIED	UNCLASSIFIED	UNCLASSIFIED	UNLIMITED

NSN 7540-01-280-5500

Standard Form 298 (Rev. 2-89)
Prescribed by ANSI Std. Z39-18
298-102

TABLE OF CONTENTS

LIST OF TABLES

LIST OF FIGURES

ABSTRACT

Experimental data obtained in a two-dimensional turbulent boundary layer (TBL) flow and a three-dimensional (3D) pressure-driven TBL flow around a wing/body junction are presented. Reynolds number effects are investigated. Fine spatial resolution laser-Doppler velocimeter measurements of mean velocity and higher order statistics including the third order products measured for 9 stations are reported. Reynolds number based on momentum thickness (Re_θ) of the developing 2-D boundary layer on the wall was Re_θ=23200, and the approach nominal reference velocity of the undisturbed air flow was 32 m/sec. The wing shape used had a 3:2 elliptical nose, NACA 0020 profiled tail and it was mounted on a flat wall. Distribution of measured static pressure variation on the wall, turbulent kinetic energy and some derived quantities such as the flow angle, flow gradient angle, shear stress angle, and modeling parameters such as $\tau/\overline{v^2}$, $B=\overline{v^3}/(\overline{u^2v}+\overline{v^3}+\overline{vw^2})$, $B_2=\overline{v^3}/[(\overline{uv^2})^2+(\overline{v^2w})^2]$ are also discussed.

NOMENCLATURE

$\overline{u_i u_j}$	Reynolds' stress tensor
$\overline{u_i u_j u_l}$	Triple product tensor
U,V,W	mean velocity components (m/sec)
U_e	mean velocity magnitude above the layer edge at each station
δ	Boundary layer thickness. Distance where the velocity magnitude in the layer reaches to 0.995 of the U_e.
C_p	pressure coefficient=$(p-p_{ref})/(p_{stag}-p_{ref})$
p	mean static pressure measured on the wall-surface
p'	pressure fluctuating component
p_{stag}	stagnation pressure
p_{ref}	reference static pressure of the undisturbed freestream measured at the tunnel entrance.
y	distance from wall (microns)
y^+	nondimensional distance to the wall, $y^+=yu_\tau/\nu$
ρ	flow density (kg/m^3)
ν	kinematic viscosity (m^2/sec)
$\overline{u^2}, \overline{v^2}, \overline{w^2}$	Reynolds' normal stresses (m^2/sec^2)
$\overline{uv}, \overline{uw}, \overline{vw}$	Reynolds' shear stresses (m^2/sec^2)
u_τ	Skin-friction velocity=$\sqrt{\tau_w/\rho}$
τ_w	Wall shear stress (Newton/m^2)
τ	shear stress magnitude=$\sqrt{(\overline{uv})^2+(\overline{vw})^2}$
A_1	Townsend's structural parameter, $A_1=\frac{\sqrt{(\overline{uv})^2+(\overline{vw})^2}}{\overline{u^2}+\overline{v^2}+\overline{w^2}}$
TKE	Turbulent kinetic energy=$\frac{1}{2}(\overline{u^2}+\overline{v^2}+\overline{w^2})$
B	$B=\overline{v^3}/(\overline{u^2 v}+\overline{v^3}+\overline{vw^2})$, triple product ratio
B_2	$B_2=\overline{v^3}/[(\overline{uv^2})^2+(\overline{v^2 w})^2]$, triple product ratio
β_w	wall-stress angle with respect to the tunnel coordinates
β_{FS}	free-stream angle with respect to the tunnel coordinates

CHAPTER I. INTRODUCTION

Wing-body junction flows have been the subject of many studies in the past. The flow at the nose of the wing has aperiodic (bimodal) double-peaked fluctuating velocity histograms with very large Reynolds stress values compared to the approaching boundary layer values (Devenport and Simpson, 1990a). Shinpaugh and Simpson (1995) used a scanning LDV and a pressure transducer to further investigate this velocity and the pressure field simultaneously.

The approach boundary layer separates due to the adverse pressure gradient in this region and rolls in towards the floor, generating backflow. The flow visualization water tunnel studies of Khan et al. (1995) and Kim et al., (1991) also show these characteristics and describe the time development of the motion. The vortical flow is stretched around the wing and is reoriented by the wing, which results in vortical flow along the sides of the wing-body junction.

The 3-D TBL of the pressure-driven type has been the subject of many papers. Reviews of recent experimental data were done by Anderson and Eaton (1989), Johnston and Flack (1996), Schwarz and Bradshaw (1994), and Ölçmen and Simpson (1992, 1993). DNS studies of Spalart (1989) and Moin et al. (1990) also show the capability of CFD in explaining the flow physics at low Reynolds numbers. Three-dimensional boundary layer/vortex interaction, which is relevant to the work undertaken here, was studied by Eaton's group (Eaton, 1995).

In the present study the detailed mean flow, Reynolds stress and triple product characteristics of 3-D turbulent boundary layers forming on the wall around a wing/body junction flow at 9 stations are presented. The wing shape used had a NACA 0020 tail; 3:2 elliptical nose wing (maximum thickness t= 7.17 cm). Figure 1 shows the measurement locations. All the data, unless otherwise specified, are presented in tunnel coordinates where x is along the tunnel centerline and y axis is perpendicular to the wall. Table 1 gives some of the flow parameters at the measurement locations.

Flow around this wing at a lower approach Reynolds number of Re_θ=5940 is extremely well documented and detailed references can be found in the work by Simpson (1995, 1996) and Ölçmen and Simpson (1995a, 1996e). Mc Mahon, Merati and Yoo (1987), Mc Mahon, Hubbart and Kubendran (1982), and Dickinson (1986) made measurements with a similar model at other Reynolds numbers to report the flow field around and in the wake of the wing using hot-wire probes.

The present study differs from these previous studies with more detailed and more accurate near wall information of not only of the mean flow and Reynolds stresses but also of the triple products. Present detailed data are the highest Re_θ wing/body junction flow studied. In high Re_θ flows there is a dire need for data sets which include triple products for better understanding of the diffusion processes, and data sets should also include near wall sublayer data since the most interesting flow physics occur in that region.

The five-component laser-Doppler velocimeter that was used for the near-wall measurements and the data reduction techniques were previously discussed (Ölçmen and Simpson, 1995a, b). The effective probe volume had a diameter of 30 microns. The probe volume could traverse as close as 50 microns to the wall and the wall could be

found with an uncertainty of ±10 microns. In this study the five component LDV system was modified to reach higher distances away from the wall. The probe volume could be traversed to 6 inches away from the wall with reduced spatial resolution. The near wall measurements were made using the original design, and measurements above 40mm were made using the modified LDV system. Two overlapping measurements made at each station were used to form composite profiles.

In Chapter II, design modifications of the 5 component LDV system are described. The high Re_θ flow generation procedure is described in Chapter III. The present 2D zero-pressure gradient high Re_θ data are compared to previous high Re_θ 2DTBL data. In Chapter IV selected 3-D data are presented and the differences in flow characteristics at selected locations due to different flow conditions are explained. Unless otherwise specified the data are presented in tunnel coordinates. The report includes the mean velocity, Reynolds' stress, all triple products. The derived quantities such as: skewnesses for different velocity components, turbulent kinetic energy, $\overline{uv}/\overline{u^2}$, shear stress magnitude, Townsend's structural parameter A_1, $(\overline{u^2}+\overline{w^2})/\overline{v^2}$, and velocity magnitude are presented in Chapter V. In Chapter VI the high Reynolds number data are compared to previously obtained low Re_θ=5940 data in the same tunnel using the same wing geometry and with a reference nominal velocity of U_{ref}=27.5 m/sec.

CHAPTER II.DESIGN MODIFICATIONS FOR THE 5 COMPONENT LDV SYSTEM

In the first part of this Chapter the design modifications applied to the 5 component LDV system are described, and in the last part the data reduction program is summarized. The design modifications were required to traverse the measurement probe volume in a range 0 to 6.35" away from the wind tunnel floor. Expected boundary layer thicknesses were less than 6.35". The design changes included changing the transmitting/receiving optical lenses, and changing the orientation of the transmitting/receiving optical heads (see figure 2). The focal lengths of the transmitting/receiving optics were changed since the probe volumes were required to form further away from the optics heads. The orientation of the transmitting optics heads were changed to allow the traversing without major changes to the system.

The modified system has 56 degrees between the bisectors of the beams emerging from the two transmitting probe heads, as opposed to 90 degrees obtained with the original LDV system (figure 2). This was accomplished by inserting 17° apex angled aluminum wedges between the transmitting optics heads and the translators that hold the heads in their place. In the modified system the velocities are thus not measured in an orthogonal frame, however the three components measured could easily be transformed into an orthogonal frame.

The transmitting lenses used in the modified system had 200mm (JML Direct Inc., part no: DBL14130) focal lengths. The separation of the beams emerging from the transmitting head was kept as 9.1mm, which resulted in an included angle of 2.606° between the beams passing through the focusing lenses. With a nominal effective focal length of 200 mm, a 1 mm diameter laser beam focuses down to 174.7μm in diameter. The length of the crossing along the optical axis is calculated as 7.681 mm, and the fringe spacing for the 514.5nm laser beams is calculated as 11.3 μm. The light collection probe volume for the system is defined by the overlapping portions of the individual probe volumes. Thus the long interference region of individual probe volumes do not reduce the spatial resolution. However the probe volume of the system in the modified system is larger than the original 5CLDV due to the larger size of the focused beam diameters. On the other hand the modified system is intended to be used only in regions of the flow away from the wall where the velocity gradients are not large, therefore the reduced spatial resolution does not effect the overall quality of the measured velocities.

The receiving lens unit uses two achromatic lenses with 175 mm (JML Direct Inc., part no: DBL14110) and 60 mm (JML Direct Inc., part no: DBL13985) focal lengths, instead of two 120mm focal length achromats used in the original system. The 1:1 magnification ratio of the previous system is thus reduced to 2.92:1 magnification ratio. The receiving fiber core diameter was kept as 50 microns. Previous LDV measurements with the original 5CLDV system showed that the light was collected only through the 30 μm portion of the fiber core. Based on this fact with a 2.92:1 magnification ratio the light is collected from 88 μm portion of the overlapping measurement probe volumes. The receiving fiber thus collects the light from 7-8 fringes.

Besides the mechanical differences between the original and the modified systems, specific electronic data acquisition parameters needed to be adjusted for the modified

system. In the modified design Macrodyne 3100 frequency domain processors used needed 64 record length setting/frequency analysis. The record length is the number of samples used by the processors to calculate the Doppler frequency using fast-Fourier transform process. The setting proved to be important, since the data obtained with 32 record length with a larger than 95% validation rate was observed to result in very high, unusual normal stress values. The record length setting did not effect the shear stress information obtained form the data. The noise content in separate processor do not correlate with each other thus the shear stresses are not affected. For the original system the record length was kept as 32.

The measurements with the near wall LDV probe were repeated up to 6 times at different stations. The outer layer profiles were also acquired many times. The main reason was to explain the differences observed between the measurements obtained with the near wall and outer layer LDV probes. The discrepancy in the measured velocity values with original and the modified systems were minimized by using the correct record length setting for the Macrodyne frequency domain processors. The uncertainties presented are calculated using differences in the measured quantities from different data sets obtained at the same station (Table 2.).

II A. Summary of data reduction program

In this section the data reduction program is summarized. The detailed data reduction program description can be found in the paper by Ölçmen and Simpson, (1995b). At every measurement point total number of 30000 samples with more than 95% validation ratio of the Macrodyne units were acquired. Each of the three simultaneous components measured were used to form three histograms in the optics coordinate system. The histograms were first cleaned in that coordinate system by fitting parabolas to the logarithm of the histogram values one on each side of the peak and then discarding the points which laid outside the parabolas crossing with the ln(1) line. Once a component of the velocity was discarded the accompanying two velocity measurements were also discarded. Next the measured simultaneous velocity components were used to calculate the simultaneous velocity components in tunnel coordinates by a transformation. The cleaning process was repeated one more time in the tunnel coordinates to eliminate the noise at the skirts of the histograms. The noise-free data were used to calculate new histograms using the inverse-velocity-magnitude as the weighting function. The bias-corrected histograms were next used to calculate the mean velocity and higher order terms. Table 2 gives 21:1 uncertainties calculated using the Kline and Mc Clintock method. The uncertainties in individual terms were estimated using 2 to 6 separate data sets measured at each measurement location.

CHAPTER III.GENERATION OF THE Re_θ=23200 APPROACH FLOW AND COMPARISON WITH DATA FROM LITERATURE

III A. Roughness plate and tunnel flow characteristics comparison

Two-dimensional roughness elements were used to artificially thicken the boundary layer. The configuration of these elements (0.125" square ribs) is shown in the figure 3a. The leading edge of this configuration is placed at a distance of 53" from the entrance to the test section. The test section is over 29 ft long (about 353 inches) with a width of 3 feet and a variable height. The test section is divided into three sections numbered from the contraction as sections one, two, and three. The first section has an accelerating flow up to five feet from the contraction and approximately a constant inviscid core velocity downstream. The second section has a constant height, but the third section has a varying height that has been suitably adjusted to get a zero pressure gradient 2-D boundary layer. The third section begins at a distance of about 200.375 inches from the entrance to the test section. Plexiglass inserts of 0.25" thick were placed along the side walls beginning at the streamwise distance of 200.37" to a distance of 260.31". The heights (H) of this section at various streamwise distances (X) are shown in the following table. The dimensions are in inches

X(in)	200.38	206	212	218	224	230	236	242	248
H(in)	10.875	10.85	10.875	10.906	10.938	10.938	10.938	10.938	10.969
X(in)	254	260	266	272	278	284	290	296	308
H(in)	11.031	11.031	10.938	10.844	10.812	10.75	10.688	10.75	10.75

The rest of the test section downstream is at a constant height of 10.75 inches. The height adjustment in this third section was done to obtain a nominally zero pressure boundary layer. The free stream velocity in the test section as a function of the streamwise distance (X) is shown in figure 3b. The high Reynolds number measurements were made at the streamwise location of 276 inches, approximately. Appendix I describes in detail the additional pitot-static tube spanwise measurements made in boundary layers to document the symmetry of the flow. Measurements were also used to validate the boundary layer flow quality.

III B. DNW data (Nockemann, et. al, 1994) and the present 2D data comparison

DNW (Re_θ=22140, and Re_θ=20920) and the present 2D data (Re_θ=23200) mean velocity and the normal stresses are plotted in figures 4 and 5, respectively. The mean U/u_τ values differ ≈2.5 from each other throughout the measurement range. The differences between the nondimensional normal stresses are approximately 0.5. The differences are not easily attributable to the size of the hot-wire probe or the technique itself. The single normal-wire probe used at DNW had length/diameter=220 with a corresponding l^+=22.5 (for Re_θ=20920 case, l^+=47 for the Re_θ=41260 case). These

values are close to the values suggested by Ligrani and Bradshaw (1987) l/d>200 and l^+=<20 for turbulence statistics to be free of wire length effects. The DNW skin-friction values were measured using a Preston tube, and a semi-empirical relationship by Fernholz (with a ±8% variation in the calculated skin-friction coefficient values due to different methods used (Fernholz et al., 1995). For the present data, using the semi-log law-of-the-wall concept with Coles' constants (0.41, and 5) resulted in u_τ=1.08 while with Fernholz's constants (0.4, and 5.1) the u_τ=1.057. For sublayer data using a function fit in the form of $U=a(y+c)-b(y+c)^4$, where $a=u_\tau^2/\nu$, u_τ=0.98 was calculated. The skin friction velocity was chosen as the average of these numbers as u_τ=1.03. The u_τ=1.03 used in the present study is lower than the 1.057 calculated using Fernholz's constants. Thus U^+ values are higher than the law-of-the-wall variation. The small size of the probe volume used in these studies eliminates the probe volume size effects in the turbulence measurements. The 30μm near wall probe diameter, and 88μm outer layer probe diameter correspond to l^+=1.85 and l^+=5.43, respectively, well below the requirements defined by Ligrani and Bradshaw (1987).

Ligrani and Bradshaw (1987) show that with a probe size $1 \le l^+ \le 10$ the $\frac{(\sqrt{u^2})_{max}}{u_\tau}$ changes semi-logarithmically from a value 2.72 at Re_θ=1000 to 3.03 at Re_θ=10000. For higher Re_θ flows hot wire probes can not be made small enough for conventional size tunnels, which restricts the use of the technique at high Re_θ flows. The maximum value of the ratio drops at higher Re_θ flows with the increased value of l^+. However, the present $\frac{(\sqrt{u^2})_{max}}{u_\tau}$=3.13 calculated at Re_θ=23200 is along the semi-logarithmic variation observed by Ligrani and Bradshaw (1987.

The mean velocity and the $\frac{\overline{u^2}}{u_\tau^2}$ normal stress profiles for DNW, Re_θ=20920 case and the present 2D data follow each other closely (figures 12 and 13). The agreement between the $\frac{\overline{u^2}}{u_\tau^2}$ normal stresses is better above y^+=200 as compared to Re_θ=22140 case. The DNW, Re_θ=20920 and the present flow U mean velocity values are also in better agreement than the Re_θ=22140 case. The reason for this is probably a combined effect of the hot-wire probe size and the skin-friction velocity estimation methods used both for the DNW and the present study.

The DNW data obtained at Re_θ=20920 (Fernholz and Finley, 1996, their figure 47) match well above y^+=2000 for the $\frac{\overline{v^2}}{u_\tau^2}$ (figure 5). Their data vary semi-logarithmically from ≈1.2 at y^+=30 to ≈1.45 at y^+=1500, while the present data quickly rise to ≈1.6 at y^+=100 and increases slightly till y^+=1250. The peak value location at y^+=1250 is closely predicted by the relation defined by Fernholz and Finley (1996) for the maximum location as

$y^+=0.071 * Re_\theta$.

The $\frac{\overline{w^2}}{u_\tau^2}$ peak values presented by Fernholz and Finley are ≈2.5 (their fig. 51) while the peak value for the present data is ≈2.9 (figure 5). For the present case $\frac{\overline{w^2}}{u_\tau^2}$ varies semi-logarithmically from y^+=100 to 1500, similar to the variation observed by Fernholz and Finley for Re_θ=21390 case.

The DNW $\overline{uv}$ data show a peak around ≈-1.0 at y^+=400 (figure 6). The variation above y^+=1000 is about the same as the present data.

The DNW triple product data and the present triple product data are plotted in figures 7 and 8. The low $\frac{\overline{u^2v}}{u_\tau^3}$ observed at y^+=250 for the present data is not observed by Fernholz and Finley. Bruns Re_θ=2573 data presented by Fernholz and Finley show a dip at this y^+, however the values are not less than zero. Similarly large values of $\frac{\overline{uv^2}}{u_\tau^3}$ observed for the present data at y^+=300 is not observed for data presented by Fernholz and Finley.

The "u skewness" near wall variation presented by Fernholz and Finley for Re_θ=20920 case is very similar to the variation of the present data till y^+=30 (their fig. 66), however the positive values of "u skewness" and following semi-logarithmic variation are not observed (figure 9). Data presented by Fernholz and Finley (1996) show that the "u skewness" near the wall in the sublayer is independent of Re_θ. Above y^+=1000 the present data and the DNW data for Re_θ=22140 follow each other closely. The large variation at the layer edge is due to the presence of turbulent-nonturbulent interface.

The "v skewness" values presented here are similar to the data presented by Fernholz and Finley (their fig. 72), however the near wall negative values observed for the present data are not observed for the other data sets (figure 10). The "sweep" and "ejection" type of motions observed near the wall requires that the "v skewness" to be less than zero around the y^+≈15 where the turbulent kinetic energy production is maximum. Thus it is believed that the present data is more correct indicator of the "v skewness" variation near the wall.

The "w skewness" values for both flows are close to zero (figure 11).

Figures presented in this section clearly show that the DNW turbulence data are much more scattered than the present data. The DNW data uncertainties are also not given in the papers documenting the data. In conclusion the present data set is a data set with low uncertainties (Table 2) and much less scattered than the DNW data set.

CHAPTER IV.EXPERIMENTAL RESULTS FOR THE HIGH REYNOLDS NUMBER WING/BODY JUNCTION FLOW

IV A. Oil flow visualization pictures

Oil flow visualization pictures obtained in two different Re_θ number flows are presented in figure 12a and 12b. The figures show that the incoming flow separates from the wall, rolls inward towards the wing/wall junction at the nose region and follows the contour of the wing to form a horse-shoe shape. Near the leading edge between the separation line and the leading edge there is another line where the limiting streamlines pass through. This line is formed due to the chaotic nature of the flow field and it is named as line-of-low-shear, since the shear stresses following this line is smaller than the surrounding regions. The flow separates near the trailing edge to form the fish-tail separation region. The figure 13 shows the schematic of the oil flow visualization and some important distances which were measured from the oil-flow pictures. These lengths are given in the following table.

Reynolds number	X_{sep}	X_{lols}	D	L	W	W_{max}
5940	-0.45	-0.27	1.38	3.76	1.72	2.02
23200	-0.475	0.201		3.77	1.84	1.994

The abbreviations "sep" stands for separation, "lols" stands for line of low shear.

IV B. Mean static surface-pressure distribution

The wall static pressure on the tunnel floor was measured using a plexiglass plate with 230 pressure taps around the contour of the wing and a small metal plate with 139 pressure taps at the nose region. A Scanivalve system (CTLR2P/S2-S6) was connected to all taps. Two Setra 239 pressure transducers were used to measure the port static pressure and reference dynamic pressure. A data acquisition board (DT2801) in conjunction with a PC-A7286 was used to acquire the data from the pressure transducers. Once a port was connected to the Scanivalve, pressure measurement was taken after a settling period of 15 seconds.

The figure 14 is a contour plot of the Cp values. The wing's presence generates longitudinal adverse pressure gradient region around the nose region of the wing. The pressure gradients become favorable following the contour of the wing towards the maximum thickness location. Near the trailing edge the adverse pressure gradients are generated. Details of surface mean-static pressure measurements are given in Appendix II.

IV C. Mean Flowfield

The mean velocity profiles are presented in figures 15 and 16. The U mean velocity show logarithmic variation regions similar to 2-D flow U mean velocity variations. In 2-D flow the logarithmic regions for different Reynolds number flows overlap up to $y^+ \approx 400$ to form a "law-of-the-wall" region. However in a 3-D flow the profiles at different stations do not overlap. There does not exist a similarity law-of-the-wall for 3-D TBL flows (Ölçmen and Simpson, 1992). The U mean velocity first decelerates until station 4 and then accelerates.

The W mean velocity profiles show that the peak values in the profiles are located further away from the wall proceeding downstream. The pressure gradients are most effective on the low momentum lateral flow nearer the wall and the turning of the flow is propagated throughout the layer. In the present flow the lateral pressure gradient is positive at upstream stations, negative at stations 4-7, and then positive again. Since $(\partial^2 W/\partial y^2)$ is proportional to this spanwise pressure gradient, the changes in $(\partial W/\partial y)$ propagate away from the wall. Thus, the maximum magnitude of the profiles increase until station 5 and than decrease to form the wave-like velocity profiles at station 9. The outer layer W velocity gradient is practically zero indicating a zero flow gradient angle, and reduced productions for the $\overline{w^2}$, $\overline{uw}$ and $\overline{vw}$ stresses. This also implies that the presence of the wall is propagated out into the layer at a much further downstream distance than a lower Reynolds number flow.

IV D. Stress variation

The Reynolds-stress transport equation with summation-subscript notation can be written as (Daly, and Harlow, 1970):

$$\frac{\partial \overline{u_i u_j}}{\partial t} + U_l \frac{\partial \overline{u_i u_j}}{\partial x_l} = -\left(\overline{u_i u_l}\frac{\partial U_j}{\partial x_l} + \overline{u_j u_l}\frac{\partial U_i}{\partial x_l}\right)$$

convection *production*

$$+\overline{\frac{p}{\rho}\left(\frac{\partial u_i}{\partial x_j} + \frac{\partial u_j}{\partial x_i}\right)} - \frac{\partial \left(\overline{u_i u_j u_l}\right)}{\partial x_l} - \frac{1}{\rho}\left(\frac{\partial (\overline{p u_j})}{\partial x_i} + \frac{\partial (\overline{p u_i})}{\partial x_j}\right) + \nu \frac{\partial^2 \overline{u_i u_j}}{\partial x_l^2} - 2\nu \overline{\frac{\partial u_i}{\partial x_l}\frac{\partial u_j}{\partial x_l}}$$

pressure strain *turbulent diffusion* *pressure diffusion* *viscous diffusion* *viscous dissipation*

The $\frac{\overline{u^2}}{u_\tau^2}$ profiles at the first two stations show that the fluctuations of the flow are highly increased throughout the layer, especially in the logarithmic variation region of the U mean velocity (figures 17a and 17b). This is however followed by a very high reduction in the fluctuations in the outer layers at the stations where the longitudinal pressure gradient is favorable (starting with station 4). The dimensional data show that adverse longitudinal pressure gradient reduces the $\overline{u^2}$ value below $y^+=100$, and increases the values above this y^+ location. The pressure gradient affects the flow near the wall and above $y^+=100$ in the opposite sense. The near wall values below $y^+=100$ are increased

at stations 4 through 7 where the longitudinal pressure gradients are negative, the flow is accelerating, and production of $\overline{u^2}$ increases. However, above y^+=100 the values are reduced at the same stations, suggesting that there are 2 distinct regions within the layers. In this region the production of the $\overline{u^2}$ is much lower than nearest the wall and the rapid distortion takes place.

The $\frac{\overline{v^2}}{u_\tau^2}$ values are also increased compared to the 2-D values at the first 2 stations where the longitudinal pressure gradient is an adverse pressure gradient (figures 18a and 18b). However the values are smaller than the 2-D values proceeding downstream until station 8. On the contrary the dimensional data show that the $\overline{v^2}$ normal stress values are overall increased throughout the layers with the three dimensionality of the flow as compared to the 2D flow data.

The $\frac{\overline{w^2}}{u_\tau^2}$ stresses are also increased at the first 2 stations and they gradually relax until station 8, which may be due to the redistribution of elevated $\overline{u^2}$ values (figures 19a and 19b). In a 2-D flow the production term for the $\overline{w^2}$ is practically zero, and the main source for the $\overline{w^2}$ is due to the redistribution of $\overline{u^2}$. The values increase at stations 8 and 9. Similar to the $\overline{v^2}$ normal stress, the $\overline{w^2}$ normal stress values increase proceeding downstream, once the data are plotted in dimensional units. All the three-dimensional values presented in dimensional units are larger than the 2D data values.

The $\overline{uv}$ shear stress values are increased in the outer layers of the first 2 stations compared to 2-D values and the maximum stress locations are further away from the wall. This is similar to the observations made by other researchers in 2-D flows under adverse pressure gradients (figures 20a and 20b). However the $\overline{uv}$ values reduce quickly below 2-D values with the accelerating flow in the outer regions. Below y^+=100 the values increase proceeding downstream. The dimensional $\overline{uv}$ magnitude values are increased with the three dimensionality of the flow in the outer layers above y^+=300. Near wall dimensional values however show a dependence on the longitudinal pressure gradient sign. With favorable/adverse pressure gradients the magnitude increases/decreases.

The production term for the $\overline{uw}$ stress is $-(\overline{uv}\,\partial W/\partial y+\overline{vw}\,\partial U/\partial y)$ and the production term for the $\overline{vw}$ stress is $-(\overline{v^2}\,\partial W/\partial y+\overline{vw}\,\partial V/\partial y)$. The production of these stresses, especially that of $\overline{vw}$, are close to zero where the $\partial W/\partial y$=0 (figures 21a to 22b). The peak value locations and the sign of the profiles follow the variation of the $\partial W/\partial y$. Both stresses show wave type nature throughout the layers. Even though the value of the $\overline{uw}$ is the largest it drops out of the equations used for computations once the boundary layer approximations are applied.

In an attempt to relate the variation of the U mean velocity and the $\overline{u^2}$ normal stress the following relation was observed. Dimensional data showed that the $\overline{u^2}$ normal stress and the mean velocity are inversely proportional to each other. In order to describe

this co-dependent variation the product ($\overline{u^2}$XU) was calculated using the tunnel coordinates data. The ($\overline{u^2}$XU) product nondimensionalized with the U_{ref}^3 are shown in figures (figures 23a and 23b). The product profiles overlap with each other above 5mm, which roughly corresponds to the region above 0.04 * δ (boundary layer thickness). The product can be interpreted as the faster mean flow results in smaller velocity fluctuations, or faster flow reduces the longitudinal normal stress values.

In another attempt to describe the co-dependent variation of the U mean velocity and the $\overline{u^2}$ normal stress in tunnel coordinates, Batchelor's (1953) "Sudden distortion of a turbulent stream" concept was used. The method assumes that the distortion of the stream takes place so rapidly that the inertia and the viscous forces arising from the turbulent motion have no effect. With these assumptions, the problem becomes linear. It is also assumed that in the regions upstream and the downstream of the distorting section of the stream tube, the mean flow is uniform and the turbulence is homogenous. The equations describing the co-dependent variation of the $\overline{u^2}$ normal stress is than given as:

$$\frac{(\overline{u^2})_{downstream}}{(\overline{u^2})_{upstream}} = \mu = \frac{3}{4c^2}\left(\frac{1+\alpha^2}{2\alpha^3}\ln\left(\frac{1+\alpha}{1-\alpha}\right)-\alpha^{-2}\right)$$

where $c=\frac{U_{downstream}}{U_{upstream}}$ and $\alpha^2=1-c^{-3}$.

For the lateral components the following equation holds:

$$\nu = \frac{(\overline{v^2}+\overline{w^2})_{downstream}}{(\overline{v^2}+\overline{w^2})_{upstream}} = \frac{3c}{4}+\frac{3}{4}c^{-2}\left(\frac{1}{2\alpha^2}-\frac{1-\alpha^2}{4\alpha^3}\ln\left(\frac{1+\alpha}{1-\alpha}\right)\right)$$

and, the equation for the TKE ratio reads as:

$$tkemult=\frac{(\overline{u^2}+\overline{v^2}+\overline{w^2})_{downstream}}{(\overline{u^2}+\overline{v^2}+\overline{w^2})_{upstream}} = \frac{c}{2}+\frac{1}{2c^2\alpha}\ln(c^{3/2}(1+\alpha))$$

At all stations $\overline{u^2}$ decreases in the outer layer approximately as given by "μ". The use of "μ" computed using the ratio of the local mean velocity magnitudes at 2 streamwise locations for "c" also collapsed the $\overline{u^2}$ data within 10% for $y > 10^4$ microns (figures 24a and 24b). The use of Batchelor's "ν" for the distortion of the lateral $\overline{v^2}$ and $\overline{w^2}$ stresses and the TKE ratio did not collapse those data (figures 25 and 26).

IV E. Triple Products

Triple products are presented in dimensional $(m/s)^3$ and nondimensional correlation coefficient form in tunnel coordinates in figures 27a to 36b. Presentation in correlation coefficient form shows the combined effect of the mean velocity variations due to the pressure gradients both on the normal stresses and triple products.

The $\overline{u^2v}/u^2v'$ (Fig. 27b) shows the transfer of the $\overline{u^2}$ normal stress with the "v" fluctuations. The $\overline{u^2}$ on the average diffused towards the wall below y^+=20 and away from the wall above this height. Maximum TKE production occurs at $y^+\approx$15 to 20, and most of

the TKE is stored in $\overline{u^2}$. The dimensional plot of the quantity (Fig. 27a) shows that all the station profiles collapse on top of another above 1.5 cm away from the wall and the variation is a semi-logarithmic variation. This indicates that the turbulent diffusion process is not affected by the three dimensionality of the flow in the outer region of the flow in this high Reynolds number flow. The effect of three dimensionality is felt further from the wall in this high Re flow than the previous study of the same configuration in a lower Re_θ (=5940) flow because the current boundary layer is much thicker.

The $\overline{u^2w}$ variations (Fig. 28a) are large only near the wall below y^+=100. This shows that the turbulent structures are almost aligned in the same direction of the mean flow at the first station, a similar conclusion observed from the $\overline{u^2v}$ profiles. This is also clearly observed in the $\overline{w^3}$ variation (Fig. 36a). The triple products involving "w" fluctuations above y=1.5 cm are not affected by the three dimensionality of the flow; the turbulent diffusion process is similar to 2D flow diffusion. Three-dimensional effects have not propagated into the outermost part of this thick boundary layer.

The variations of the $\overline{uw^2}$ (Fig. 31a), $\overline{u^3}$ (Fig. 34a), and the $\overline{uv^2}$ (Fig. 30a) triple products are similar to each other. The $\overline{u^2}$, $\overline{w^2}$, and the $\overline{v^2}$ normal stresses are transferred on the average in the same fashion by the "u" fluctuating velocity component. Below y^+=100 the transfer is associated with the higher-than-the-mean velocity fluctuations and above that height the transfer is with lower speed fluctuations. Positive $\overline{u^3}$ and negative $\overline{u^2v}$ nearer the wall indicates "sweep" type of motion (+u,-v) is the dominant motion in this region. Above y^+=100, the ejection type of motion (-u,+v) is dominant. Semi-logarithmic variations of the $\overline{u^3}/u'^3$ (Fig. 34b) and the $\overline{uw^2}/u'w^2$ (Fig. 31b) show that between y^+=100-4000 these triple products are scaled with the normal stresses. The dimensional profiles of the $\overline{u^3}$ and of the $\overline{uw^2}$ triple products overlap on top of another for each station, respectively. The nondimensional $\overline{v^3}$ (Fig. 35b), $\overline{vw^2}$ (Fig. 32b) plots show that the transfer of the $\overline{v^2}$ and the $\overline{w^2}$ normal stresses are away from the wall approximately above y^+=25.

CHAPTER V DERIVED QUANTITIES

V A. Flow, Flow Gradient, and Shear Stress Angles

The flow angle, flow gradient angle and shear stress angles in tunnel coordinates are shown in figures 37 to 45. The near wall flow angle first decreases until station 3 and then increases at the downstream stations to become positive at station 8. Previous three-dimensional experimental data show that the shear stress angle lags behind the flow gradient angle. However at stations 1 and 2 in the high Reynolds number case the shear stress angle near the wall seems to lead the flow gradient angle; the shear stress angle has a larger magnitude than the flow gradient angle at these stations. At downstream stations the flow gradient angle leads the shear stress angle. The changes in the flow gradient angle results in gradual change of the shear stress angle in the region above y^+=100. Above y^+=1000 the shear stress angle seems to change very slightly away from the station 1 mean free-stream flow direction. The changes in the mean flow direction due to pressure gradients and the subsequent changes in the shear stress values does not seem to affect the shear stress angle. The turbulent structure direction above y^+=1000 does not seem to change with the three-dimensionality of the flow in this high Re_θ flow.

V B. Townsend's Structural Parameter, A_1

The $A_1=\sqrt{(\overline{uv})^2+(\overline{vw})^2}\ /(\overline{u^2}+\overline{v^2}+\overline{w^2})$, Townsend's structural parameter is shown in figure 46. The maximum value at the first three stations is 0.1 which is lower than 0.14 observed for the 2-D station. The peak value obtained in the outer regions increase to 0.14 proceeding downstream. The data show that the shear stress magnitude and the turbulent kinetic energy of the flow at the first 4 stations in the 3-D flow are not as well correlated as in the 2-D flow.

V C. Turbulent Kinetic Energy

The Turbulent Kinetic Energy ($TKE=(\overline{u^2}+\overline{v^2}+\overline{w^2})/2$) profiles are shown in figure 47. This figure shows that the TKE of the flow stays constant above y^+=1000. Large changes occur nearer the wall where the production of the TKE is maximum.

V D. Stress, Normal Stress Ratio, $\tau/\overline{v^2}$

The $\tau/\overline{v^2}$ profiles show that the shear stress magnitude and the $\overline{v^2}$ normal stress are highly correlated with each other (figure 48). The ratio is practically a constant around 0.6 within the y^+=100 to 1000 range. This fact was previously shown using 9 different data sets (Ölçmen and Simpson, 1995).

V E. Triple Product Ratio, B

The parameter $B=\overline{v^3}/(\overline{u^2v}+\overline{v^3}+\overline{vw^2})$ is the ratio of the perpendicular-to-the-wall velocity fluctuation triple product to the triple product terms which appear in the TKE transport equation (figures 49a and 49b). The parameter is defined to reduce the number of independent terms that need to be modeled in governing equations. "B" varies as a constant with a value between 0.2 and 0.4 between y^+=300 to 3000. The "B" parameter was also observed to be within 0.2 to 0.4 using other available 3-D data sets (Ölçmen et al. 1995).

V F. Triple Product Ratio, B_2

The parameter $B_2=\overline{v^3}/[(\overline{uv^2})^2+(\overline{v^2w})^2]$ is the ratio formed among the triple products which appear in the transport equations for the $\overline{v^2}$ normal stress (figures 50a and 50b). The ratio is approximately a constant (ratio≈1) between y^+=500 to 6000, similar to the variations observed for other 3-D flow data (Ölçmen, et al., 1998).

V G. $\overline{uv}$ / $\overline{u^2}$, Shear Stress to Normal Stress Ratio

The $\overline{uv}/\overline{u^2}$, shear stress to normal stress ratio which shows the correlation between these stresses is plotted in Figure 51. The "v" fluctuating velocity is usually assumed to be unaffected by the large longitudinal inactive motions as described by Bradshaw. Thus the $\overline{uv}$ should not be affected by these inactive motions, since the Fourier frequency of the large scale motions generating the inactive motion and the Fourier frequency of the small scale structures generating the "v" fluctuating velocity are largely separated from one another. The quantity therefore indicates two possible flow phenomena: 1) Either "u" and "v" fluctuating velocities are less correlated at stations where the pressure gradient is adverse or 2) the inactive motion is more pronounced at adverse pressure gradient stations.

V H. $(\overline{u^2}+\overline{w^2})$ / $\overline{v^2}$, Ratio of Normal Stresses

The ratio of the stresses, $(\overline{u^2}+\overline{w^2})$ / $\overline{v^2}$ is shown in figures 52a and 52b. For an isotropic turbulent flow the ratio is equal to 2. However the ratio varies semi-logarithmically above y^+=65 in the present flow (figure 52a). The ratio near the layer is less than 2, indicating the anisotropic distribution of the turbulent kinetic energy (figure 52b). Figure 52b also shows that the semi-logarithmic variation is a first order approximation to the variation above y^+=65. The values show a sharper decay in the high Reynolds number case compared to the Re_θ=5940 case. The Re_θ=5940 case decays from a value of ≈4.5 at y^+=100 to ≈3.5 at y^+=1000, compared to the variation from ≈6 to ≈3.5 in the same range for the Re_θ=23200 case.

V I. $\sqrt{\overline{v^2}}$ / $\sqrt{\overline{u^2}}$, Ratio of Square Root of Normal Stresses

The ratio $\sqrt{\overline{v^2}}$ / $\sqrt{\overline{u^2}}$ is shown in Figure 53. The ratio shows the anisotropy of the TKE distribution between the longitudinal and perpendicular normal stresses. At adverse pressure gradient stations the ratio is lower than the 2D values indicating the increased anisotropy of the flow. However, the distributions follow a similar shape at all stations. In comparison to DNW (German-Dutch windtunnel) data (Fig. 63 of Fernholz and Finley, 1996), the 2D station variation of the parameter is very much similar to their data obtained for the Re_θ=20920 case. The values change semi-logarithmically from 0.5 to 0.58 in the y^+=100 to 1000 range. The value is increased to 0.85 by y^+=6000.

V J. $\sqrt{\overline{w^2}}$ / $\sqrt{\overline{u^2}}$, Ratio of Square Root of Normal Stresses

The profiles of the ratio $\sqrt{\overline{w^2}}$ / $\sqrt{\overline{u^2}}$ are shown in Figure 54. Similar to the $\sqrt{\overline{v^2}}$ / $\sqrt{\overline{u^2}}$ ratio, the $\sqrt{\overline{w^2}}$ / $\sqrt{\overline{u^2}}$ also show the anisotropy of the normal stresses. The variation of the 2D station data of the present study is very similar to the DNW data measured at Re_θ=20920 (Fernholz, Finley, 1996, Fig. 65). In the y^+=100 to 1000 range the ratio is approximately a constant around 0.65. The values are increased to 0.85 at y^+=6000.

CHAPTER VI STUDY OF REYNOLDS NUMBER EFFECTS

In this Chapter three-dimensional data sets obtained in high (Re_θ=23200) and low (Re_θ=5940) Reynolds number flows are compared. Both data sets were obtained in the same tunnel using the same wing geometry. The low Re_θ flow data have been presented previously by Ölçmen, and Simpson (1995a).

VI A. Mean Flowfield

The mean velocity profiles are presented in figures 55. Due to the similar distributions of the wall static pressure the mean flow field near the wall vary similarly in both Reynolds number cases. The U mean velocity has a larger logarithmic region extending further away from the wall similar to variations observed in 2-D high Reynolds number flows. The flow decelerates until station 4 and then accelerates.

The W mean velocity in the first four stations are skewed in one direction only. At stations 5 and downstream, the pressure gradient sign changes and the profiles show minima. The near wall low momentum fluid region is the region of the layers first affected by the pressure gradients. This results in negative velocity components away from the wall in the wall-coordinates system.

VI B. Stress variation

Except at stations 3 and 4 the $\frac{\overline{v^2}}{u_\tau^2}$ profiles for the high and the low Reynolds number flows follow each other very closely below y^+=1000, indicating that the wall skin-friction is closely related to the $\overline{v^2}$ normal stress (figure 56 and 57). At stations 3 and 4 the high Reynolds number values are lower than the low Reynolds number profile values.

The $\frac{\overline{u^2}}{u_\tau^2}$ values at every station for the high Reynolds number case is higher than the low Reynolds number profiles. Near the wall this might be an indicator of higher inactive motion for the higher Reynolds number case. The maxima location in the layers both for the high and the low Reynolds numbers cases are at the same y^+ value away from the wall. The production term for the $\overline{u^2}$ normal stress is $-(2\,\overline{uv}\frac{\partial U}{\partial y})$. The $\overline{uv}$ profiles nondimensionalized using the skin-friction velocity differ from each other away from the wall while the nondimensional U mean velocity have the same slope for both the Reynolds number cases. The higher level of production may be a reason for the elevated $\overline{u^2}$ values in the outer region of the profiles. Another reason maybe due to the larger boundary layer thickness. The diffusion process would take a longer distance farther downstream for its effects to be felt in the outer layer. The viscous diffusion and the viscous dissipation terms are large only near the wall.

The values of $\frac{\overline{w^2}}{u_\tau^2}$ are also larger throughout the layers including station 7, which may be due to the redistribution of elevated $\overline{u^2}$ values. In a 2-D flow the production term for the $\overline{w^2}$ is practically zero, and the main source for the $\overline{w^2}$ is due to the redistribution of $\overline{u^2}$. For the high Reynolds number case even in the 2-D flow the $\overline{w^2}/u_\tau^2$ is larger, which supports this view.

The variations of the shear stress profiles are similar to each other in both Reynolds number cases, especially below y^+=100. The nondimensional stress values are larger for higher Reynolds number case above y^+=100 as expected, since the boundary layers extend to higher y^+ units. The nondimensional $\overline{uw}$ and $\overline{vw}$ profiles follow each other more closely until y^+=1000 than the $\overline{uv}$ stress. At station 6 the maximum value of the $\overline{uw}/u_\tau^2$ is larger in magnitude than the maximum value of the $\overline{uv}/u_\tau^2$. However, the importance of the $\overline{uw}$ is diminished once the boundary layer approximations are applied to the transport equations for the Reynolds' stresses, since this stress drops out of the equations to be modeled.

VI C. Triple products

Triple products at selected stations are presented in the correlation form (figures 58 through 67). The triple product correlation in wall variables at both Reynolds numbers follow each other within the uncertainty bands nearer the wall, $y^+ < 1000$. Obviously the triple product values change with different three-dimensional flow conditions, and the values depend on the coordinate system studied. However, for these two flows the Reynolds number does not seem to play a role in the development of the triple products for $30 < y^+ < 1000$. The triple product values for the higher Re case extend to large y^+ further out in the layers since the layers are much thicker.

CHAPTER VII. CONCLUSIONS

A three-dimensional high Reynolds number flow around a wing/body junction has been experimentally investigated using laser-Doppler velocimetry. The mean velocities, shear stresses, and 10 triple products as well as the pressure distribution on the wall are presented. Some important conclusions are as follows: The triple products nondimensionalized using the normal stresses follow each other at all stations above y^+=100. The shear-stress angle lags behind the flow-gradient angle at station 3 and downstream stations. Parameters B and B_2 are constants in the outer layer also for this high Reynolds number flow. Townsend's structural parameter A_1 is not constant throughout the layers.

Two separate high Reynolds number data sets (Re_θ=5940 and Re_θ=23200) around a wing/body junction are compared with each other. For the U mean velocity u_τ is shown to be the scaling velocity. The W/u_τ mean velocity variations although close to each other show that the magnitude of the velocity for the Re_θ=23200 case is smaller. The $\overline{u^2}/u_\tau^2$, and $\overline{w^2}/u_\tau^2$ normal stresses are higher for the Re_θ=23200 case especially in the outer regions of the layers. The $\overline{v^2}/u_\tau^2$ normal stress does not seem to depend on Reynolds number. The shear stresses normalized with the skin-friction velocity show that there are two different regions forming in this type of flow: A) below y^+=100 the stresses tend to overlap with each other, B) the magnitude of the normalized shear stresses are higher for the high Re_θ case, in the outer layers. Triple product profiles for $30 < y^+ < 1000$ seem to be independent of the Re_θ. Future publications will discuss the physical meaning of these data in more detail.

Acknowledgement

The authors are grateful for the support of the Office of Naval Research Grant N00014-94-1-0092, Dr. L.P. Purtell, Program Manager.

References

AGARDOGRAPH 335, 1996, "Turbulent boundary layers in subsonic and supersonic flow", AGARD, 7 Rue Ancelle, 92200 Neuilly-sur-Seine, France. Edited by Prof. William Saric, Arizona State University, Tempe, AZ 85287-610, USA.

Anderson, S.C., and Eaton, J.K., 1989, "Reynolds stress development in a pressure-driven three-dimensional turbulent boundary layer", *J. of Fluid Mech.*, vol. 202, pp. 263-294.

Batchelor, G.K., 1953, *The Theory of Homogenous Turbulence*, Cambridge University Press.

Devenport, W.J., Simpson, R.L., 1990a, "A time-dependent and time-averaged turbulence structure near the nose of a wing-body junction", *J. of Fluid Mech.*, vol. 210, pp. 23-55.

Devenport, W.J., Simpson, R.L., 1990b, "An experimental investigation of the flow

past an idealized wing-body junction:final report", VPI&SU report, VPI-AOE-172.

Dickinson, S.C., "An Experimental Investigation of Appandage-FlatPlate Junction Flow Volume I: Description", DTNSRDC-86/051, December1986, David W. Taylor Naval Ship Research and Development Center,Bethesda, MD 20084-5000.

Eaton, J.K., 1995, "Effects of mean flow three dimensionality on turbulent boundary-layer structure", *AIAA J.*, vol. 33, number 11, November, pp. 2020-2025.

Fernholz, H.H., and Finley, P.J., 1996, "The incompressible zero-pressure-gradient turbulent boundary layer: An assessment of the data", *Prog. Aerospace Sci*, vol. 32, pp. 245-311. Elsevier Science Ltd.

Fernholz, H.H., Krause, E., Nockemann, M., Schober, M., 1995, "Comparative measurement in the canonical boundary layer at $Re_\theta \leq 6 \times 10^4$ on the wall of the German-Dutch windtunnel", *Physics of Fluids*, 7, (6), pp. 1275-1281.

Fleming, J., Simpson, R.L., Devenport, W.J., 1993, "An experimental study of a turbulent wing-body junction and wake flow", *Exp. in Fluids*, vol. 14, pp. 366-378.

Ha, S.M., and Simpson, R.L., 1993, "*An experimental study of coherent structures in a three dimensional turbulent boundary layer*", Report VPI-AOE-205, submitted to DTIC.

Johnston, J.P., and Flack, K.A., 1996, "Review-Advances in Three-Dimensional Turbulent Boundary Layers with Emphasis on the Wall-Layer Regions", *Journal of Fluid Engineering*, Vol. 118, no. 2, pp. 219-232.

Khan, M.J., Ahmed, A., Trosper, J.R., 1995, "Dynamics of the juncture vortex", *AIAA J.*, vol. 33, number 7, July, pp. 1273-1279.

Kim, S., Walker, D.A., and Simpson, R.L., 1991, "*Observation and measurement of flow structures in the stagnation region of a wing-body junction*", Report VPI-E-91-20; submitted to DTIC.

Ligrani, P.M., and Bradshaw, P., 1987, "Spatial resolution and measurement of turbulence in the viscous sublayer using subminiature hot-wire probes.", Experiments in Fluids, 5, 407-417.

Mansour, N.N., Kim, J., and Moin, P., 1988, "Reynolds-stress and dissipation-rate budgets in a turbulent channel flow", *J. of Fluid Mech.*, vol. 194, pp. 15-44.

Mansour, N.N., Kim. J., Moin., P., 1989, "Near-wall k-epsilon turbulence modelling", *AIAA J.*, vol. 27, no. 8, pp. 1068-1073.

McMahon, H.M., Hubbart, J., Kubendran, L., 1982, "Mean velocities and Reynolds stresses in a juncture flow", NASA Contractor report 3605.

McMahon, H.M., Merati, P., Yoo, K.M., 1987, "Mean velocities and Reynolds stresses in the juncture flow and in the shear layer downstream of an appendage", Georgia Tech Report, GITAER 87-4, Atlanta, Georgia, 30332.

Moin, P., Shih, T.H., Driver, D., Mansour, N.N, 1990, "Direct numerical simulation of a three-dimensional turbulent boundary layer", *Phys. of Fluids A*, vol. 2, no. 10, pp. 1846-1853.

Nockemann, M., Abstiens, R., Schober, M., Bruns, J., Eckert, D., 1994, "Messungen in einer turbulenten Wandgrenzschicht bei groβen Reynolds-Zahlen im Deutsch_Niederlandischen Windkanal Meβbericht", Aerodynamischen Institut report, der Rhein.-Wetf. Technischen Hochschule Aachen, Germany, Professor: E. Krause, Ph. D.

Ölçmen, M.S., and Simpson, R.L., 1992, "Perspective: On the Near wall similarity of three-dimensional turbulent boundary layers", Transactions of ASME, *J. of Fluids Engineering.*, vol. 114, pp. 487-495.

Ölçmen, M.S., and Simpson, R.L., 1993, Review Paper, "Evaluation of Algebraic Eddy-Viscosity Models in 3D Turbulent Boundary Layer Flows", *AIAA Journal*, vol. 31, no.1, pp. 6-15.

Ölçmen, M.S., and Simpson, R.L., 1995a, "An experimental study of a three-dimensional pressure-driven turbulent boundary layer", *J. of Fluid Mech.*, vol. 290, pp. 225-262.

Ölçmen, M.S., and Simpson, R.L., 1995b, "A five-velocity-component laser-Doppler velocimeter for measurements of a three-dimensional turbulent boundary layer", *Meas. Sci. and Tech.*, vol. 6, pp. 702-716.

Ölçmen, M.S., and Simpson, R.L., 1996a, "Experimental evaluation of pressure-strain models in complex 3-D turbulent flow near a wing/body junction", VPI&SU Report, VPI-AOE-228; submitted to DTIC.

Ölçmen, M.S., and Simpson, R.L., 1996b, "Experimental transport-rate budgets in complex 3-D turbulent flow near a wing/body junction", 27th AIAA Fluid Dynamics Conference, June 17-20, New Orleans, LA; submitted to J. of Fluid Mech..

Ölçmen, M.S., and Simpson, R.L., 1996c, "Theoretical and experimental pressure-strain comparison in a pressure-driven three-dimensional turbulent boundary layer", 1st AIAA Theoretical Fluid Mechanics Meeting, June 17-20, New Orleans, LA; submitted to J. of Fluid Mech.

Ölçmen, M.S., and Simpson, R.L., 1996d, "Some structural features of a turbulent wing-body junction vortical flow", VPI&SU Report, VPI-AOE-238; submitted to DTIC.

Ölçmen, M.S., and Simpson, R.L., 1996e, "Higher order turbulence results for a three-dimensional pressure-driven turbulent boundary layer", VPI&SU Report, VPI-AOE-237; submitted to DTIC.

Ölçmen, M.S., and Simpson, R.L., 1997, "Experimental evaluation of turbulent diffusion models in complex 3-D flow near a wing/body junction", 35th Aerospace Sciences Meeting & Exhibit, Jan 6-10, Reno, NV, paper 97-0650.

Ölçmen, M.S., Fleming, J.L., Ciochetto, D.S., and Simpson, R.L., 1998, "Some structural features of pressure-driven three-dimensional turbulent boundary layers from experiments", ICASE report accepted to be published by Elsevier Book Company.

Schwarz, W.R., and Bradshaw, P., 1994, "Term-by-term tests of stress-transport turbulence models in a three-dimensional boundary layer", *Phys. of Fluids* 6 (2), pp. 986-999.

Schwarz, W.R., and Bradshaw, P., 1994, "Turbulence structural changes for a three-dimensional turbulent boundary layer in a 30° bend", *J. of Fluid Mech.*, vol. 272, pp. 183-209.

Shinpaugh, K.A., and Simpson, R.L., 1995, "A rapidly scanning two-velocity-component laser-Doppler velocimeter", *Meas. Sci. and Tech.*, vol 6., pp. 690-701.

Simpson, R.L., 1995, "Three-dimensional turbulent boundary layers and separation", AIAA paper 95-0226.

Simpson, R.L., 1996, "Aspects of Turbulent Boundary Layer Separation", *Progress in Aerospace Sciences*, Nov.

Spalart, P.R., 1989, "Theoretical and numerical study of a three-dimensional turbulent boundary layer", *J. of Fluid Mech.*, vol. 205, pp. 319-340.

Sung, Chao-Ho, and Yang, Cheng-I, 1988, "Validation of turbulent horseshoe vortex flows", 17th symposium on Naval Hydrodynamics, 29 August-2 September, The Haguě, Netherlands.

TABLE 1. LASER-DOPPLER VELOCIMETER LOCATIONS AND FLOW PARAMETERS.									
Stations	X (in)	Z (in)	U_e (m/sec)	u_τ (m/sec)	β_w (degree)	β_{FS} (degree)	δ (cm)	$\partial C_p/\partial(x/t)$	$\partial C_p/\partial(z/t)$
2D			31.31	1.03	0	0	13.42		
1	-3.5	-6.94	29.31	0.91	-10.79	-2.19	13.64	0.0667	0.0890
2	-2.29	-6.64	28.71	0.916	-23.13	-4.7	13.51	0.0211	0.1734
3	-1.33	-6.35	29.03	1.094	-31.17	-7.74	13.68	-0.2060	0.2771
4	-0.47	-6.06	31.14	1.24	-25.66	-8.77	13.19	-0.3438	0.1875
5	0.26	-5.77	33.02	1.208	-16.31	-8.01	12.33	-0.3670	-0.0587
6	1.19	-5.47	34.66	1.208	-10.3	-5.7	12.86	-0.3208	-0.2643
7	2.17	-5.26	35.48	1.304	-3.78	-2.71	12.90	-0.0103	-0.2544
8	3.66	-4.97	35.17	1.128	4.16	0.59	13.35	0.0395	-0.1599
9	5.16	-4.67	34.3	1.104	6.62	2.31	13.46	0.0740	-0.1094

Maximum thickness of the wing (t) = 7.17 cm, Nominal reference velocity (U_{ref}) = 32m/sec,
Reynolds number based on momentum thickness in 2D flow without the wing's presence (Re_θ) = 23200.
Wing chord length = 30.48 cm.

TABLE 2. 21:1 ODDS $\pm 2\sigma$ UNCERTAINTIES OF MEAN VELOCITIES, REYNOLDS' STRESSES AND TRIPLE PRODUCTS.			
Term	Uncertainty	Term	Uncertainty
U/u_τ	0.63	$\overline{u^2v}/\overline{u^2}v'$	0.092
V/u_τ	-	$\overline{u^2w}/\overline{u^2}w'$	0.054
W/u_τ	0.29	$\overline{v^2w}/\overline{v^2}w'$	0.023
$\overline{u^2}/u_\tau^2$	0.32	$\overline{uv^2}/u'\overline{v^2}$	0.068
$\overline{v^2}/u_\tau^2$	0.11	$\overline{uw^2}/u'\overline{w^2}$	0.049
$\overline{w^2}/u_\tau^2$	0.23	$\overline{vw^2}/v'\overline{w^2}$	0.03
$\overline{uv}/u_\tau^2$	0.1	$\overline{uvw}/u'v'w'$	0.022
$\overline{uw}/u_\tau^2$	0.13	$\overline{u^3}/u'^3$	0.39
$\overline{vw}/u_\tau^2$	0.04	$\overline{v^3}/v'^3$	0.084
		$\overline{w^3}/w'^3$	0.11

TABLE 3. SOME LENGTH SCALES OBTAINED FROM LDV DATA IN TUNNEL COORDINATES.

Station	δ (cm)	δ_1 (mm)	δ_2 (mm)	δ_3 (mm)	δ_4 (mm)	δ_5 (mm)	δ_6 (mm)	δ_7 (mm)
2D	13.42	+15.80	+15.80	+12.41	-0.13	+0.01	-0.12	-0.00
1	13.64	+23.06	+22.78	+12.83	+5.96	-0.74	+5.22	-0.25
2	13.51	+19.03	+18.37	+13.90	+13.51	-1.28	+12.23	-1.15
3	13.68	+18.50	+16.84	+14.13	+19.90	-2.48	+17.42	-2.81
4	13.19	+19.34	+17.28	+12.56	+22.23	-2.42	+19.81	-3.59
5	12.33	+15.54	+13.72	+12.51	+22.17	-2.33	+19.84	-3.18
6	12.86	+18.40	+17.17	+10.53	+15.72	-1.76	+13.96	-1.78
7	12.90	+13.15	+12.87	+10.75	+7.84	-0.87	+6.97	-0.47
8	13.35	+13.01	+12.99	+10.67	-0.35	-0.09	-0.44	-0.02
9	13.46	+13.59	+13.51	+11.03	-4.50	+0.28	-4.22	-0.16

U_e=Velocity magnitude at the layer edge.

δ= *y where* $\sqrt{U^2+W^2}/U_e$=0.995= *Boundary Layer Thickness*

$$\delta_1=\int_0^\infty(1-\frac{U}{U_e})dy$$ *Streamwise Displacement Thickness*

$$\delta_2=\int_0^\infty(1-\frac{\sqrt{U^2+W^2}}{U_e})dy$$ *Magnitude Displacement Thickness*

$$\delta_3=\int_0^\infty(1-\frac{U}{U_e})\frac{U}{U_e}dy$$ *Streamwise Momentum Thickness*

$$\delta_4=\int_0^\infty(-\frac{W}{U_e})dy$$ *Lateral Displacement Thickness*

$$\delta_5=\int_0^\infty\frac{W}{U_e}(1-\frac{U}{U_e})dy$$ *Lateral Momentum Thickness*

$$\delta_6=\int_0^\infty-\frac{WU}{U_e^2}dy$$ *Cross Product Momentum Thickness*

$$\delta_7=\int_0^\infty-\frac{W^2}{U_e^2}dy$$ *Crossflow Momentum Thickness*

TABLE 4. HIGH AND LOW Re_θ LASER-DOPPLER VELOCIMETER MEASUREMENT LOCATIONS AND FLOW PARAMETERS.

Stations	X (in)	Z (in)	U_e (m/sec) Re= 6000	U_e (m/sec) Re= 23000	u_τ (m/sec) Re= 6000	u_τ (m/sec) Re= 23000	β_w (deg.) Re= 6000	β_w (deg.) Re= 23000	β_{FS} (deg.) Re= 6000	β_{FS} (deg.) Re= 23000	$\partial C_p / \partial(x/t)$ Re= 6000 WC	$\partial C_p / \partial(x/t)$ Re= 23000 WC	$\partial C_p / \partial(z/t)$ Re= 6000 WC	$\partial C_p / \partial(z/t)$ Re= 23000 WC
2D			27.1	31.31	0.98	1.03	-	0	0	0	-	-	-	-
1	-3.5	-6.94	24.9	29.31	0.864	0.91	-11.5	-10.79	-2.64	-2.19	0.069	0.0489	0.1120	0.0999
2	-2.29	-6.64	24.8	28.71	0.865	0.916	-24	-23.13	-4.81	-4.7	-0.0538	-0.0487	0.2079	0.1678
3	-1.33	-6.35	25.3	29.03	0.957	1.094	-33.7	-31.17	-8.63	-7.74	-0.3775	-0.3197	0.1464	0.1305
4	-0.47	-6.06	27.3	31.14	1.11	1.24	-30.6	-25.66	-9.45	-8.77	-0.4493	-0.3911	-0.0968	0.0201
5	0.26	-5.77	29.5	33.02	1.15	1.208	-19.7	-16.31	-7.71	-8.01	-0.4158	-0.3358	-0.2178	-0.1594
6	1.19	-5.47	30.5	34.66	1.16	1.208	-7.17	-10.3	-5.09	-5.7	-0.2869	-0.2684	-0.3998	-0.3174
7	2.17	-5.26	31	35.48	1.2	1.304	-3.5	-3.78	-2.71	-2.71	0.0416	0.0065	-0.4802	-0.2545
8	3.66	-4.97	30.9	35.17	1.024	1.128	2.63	4.16	0.96	0.59	0.0845	0.0278	-0.3203	-0.1623
9	5.16	-4.67	30.5	34.3	1.011	1.104	4.71	6.62	2.78	2.31	0.0798	0.0609	-0.1587	-0.1172

Maximum thickness of the wing (t) = 7.17 cm. Wing chord length = 30.48 cm. Nominal reference velocity for the low Re number case is (U_{ref}) = 27.5m/sec, and for the high Re numbers case is (U_{ref}) = 32m/sec. For the low Re number data Reynolds number based on momentum thickness at 0.75 chord upstream of the wing on the tunnel centerline is (Re_θ) = 5936, and for the high Re number data in a 2-D flow without the wing's presence is (Re_θ) = 23200.

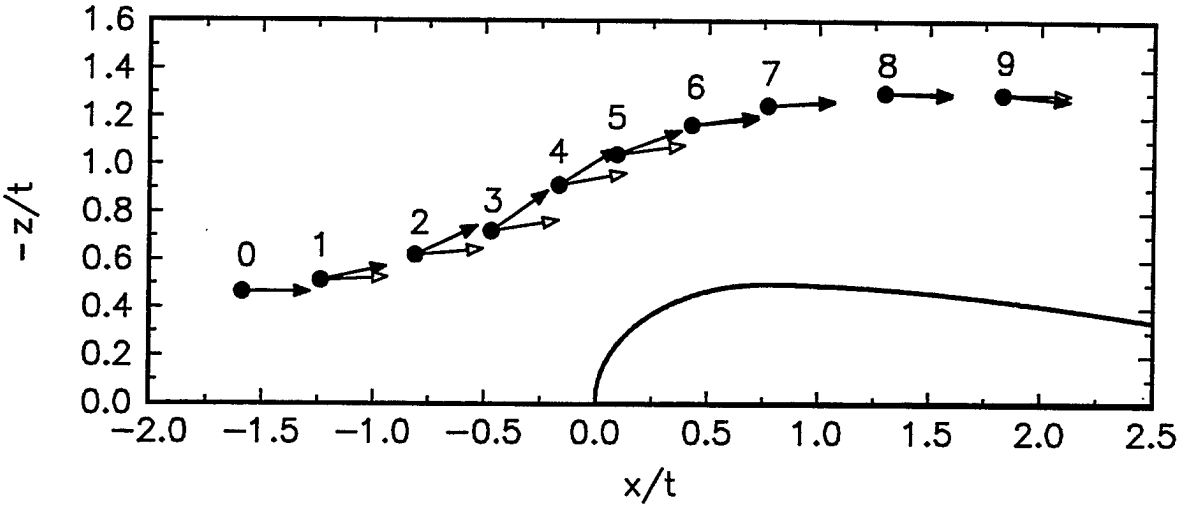

Figure 1a. Wing shape and measurement locations. Full arrows wall-stress direction. Empty arrows free-stream direction.

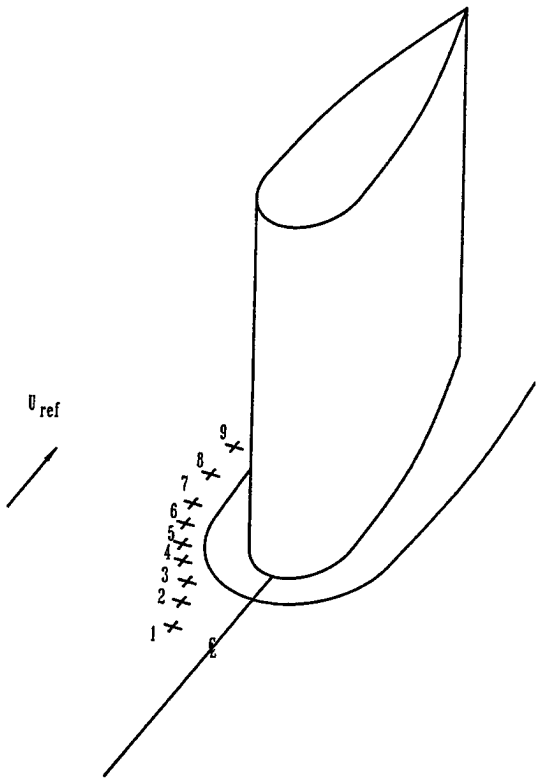

Figure 1b. Schematic of wing and measurement locations.

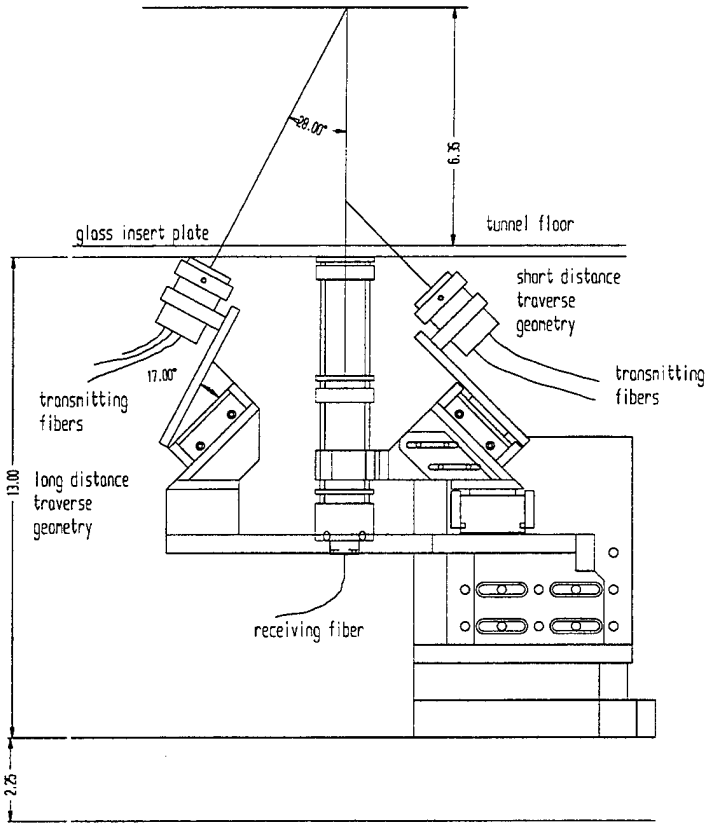

Figure 2. Short and long range transmitting lens configuration for the 5CLDV. The receiving lens configuration is for the long range design.

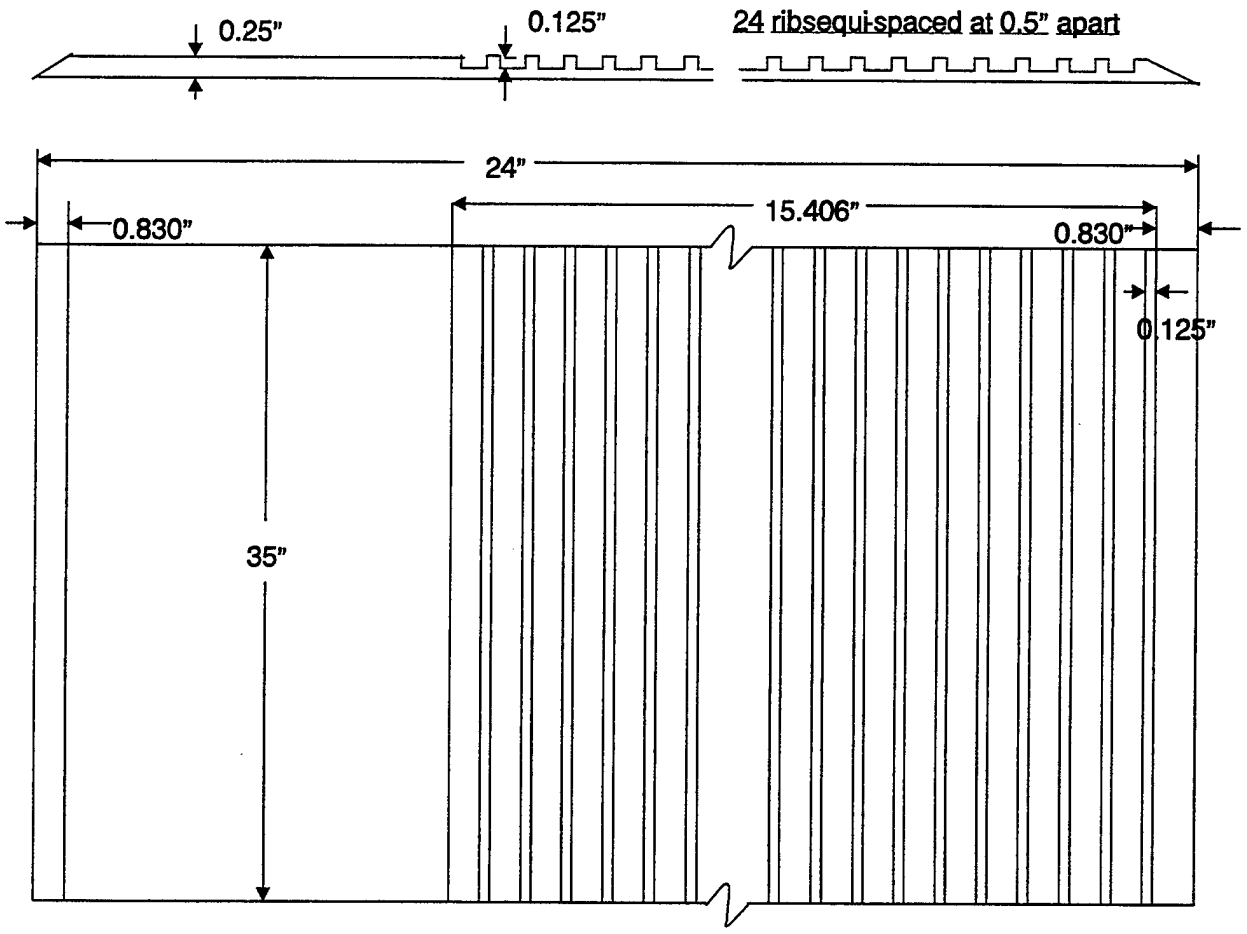

Figure 3a. The roughness plate.

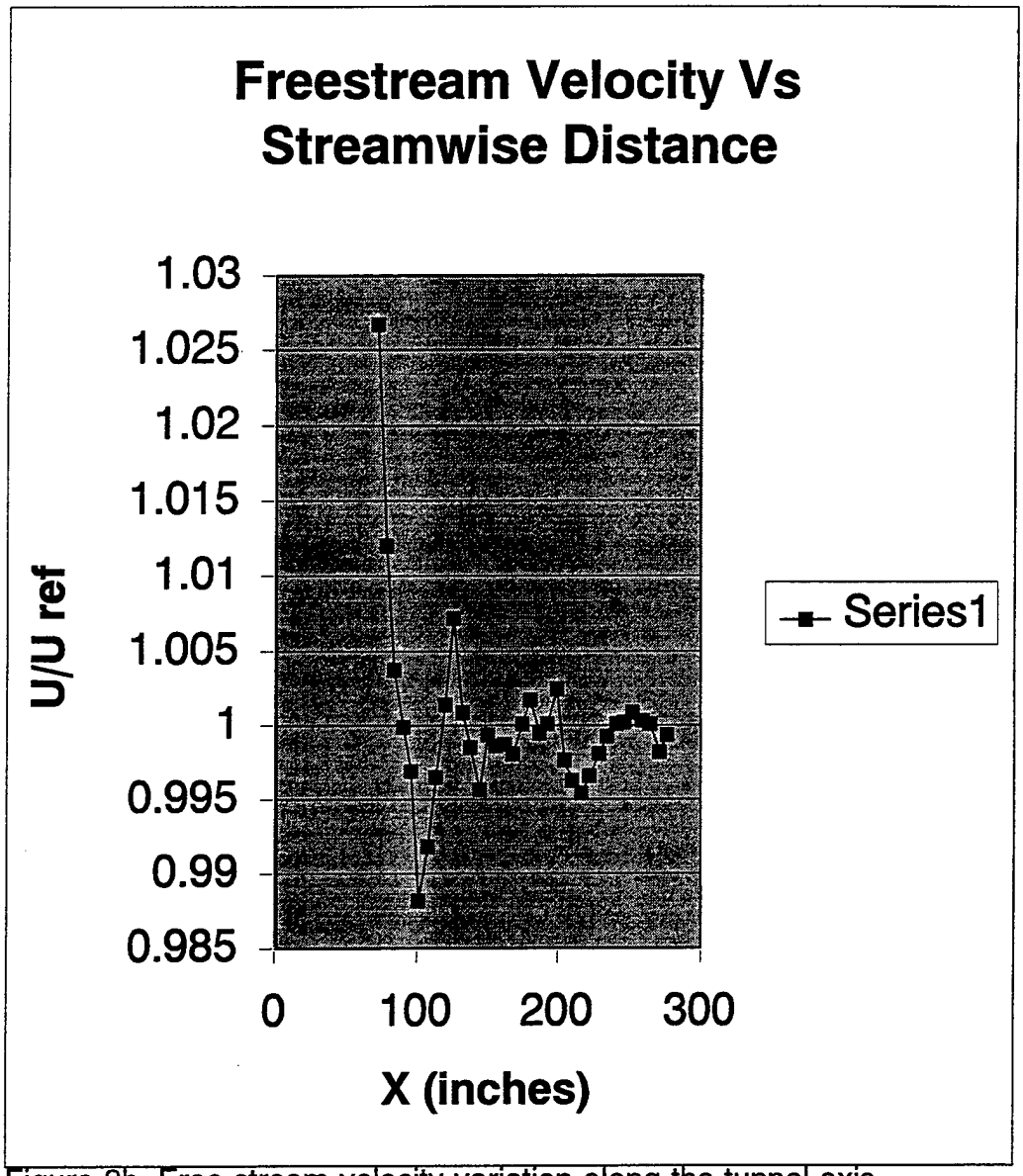

Figure 3b. Free-stream velocity variation along the tunnel axis.

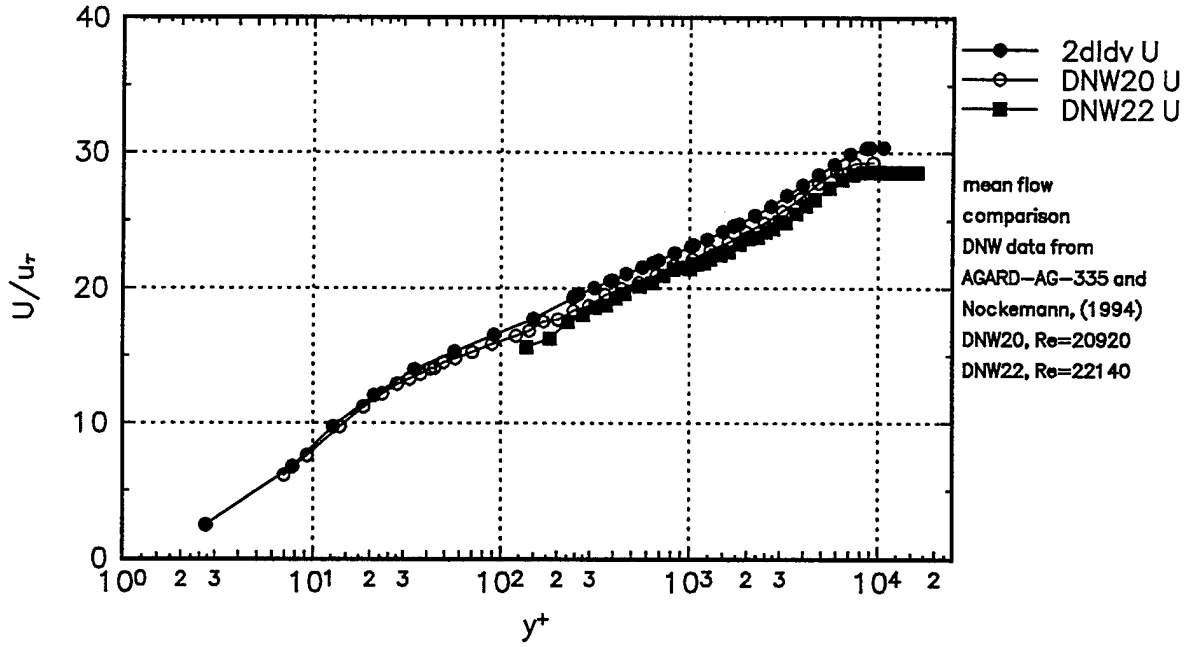

Figure 4. DNW (Re_θ=22140, Re_θ=20920) data and present 2D (Re_θ=23200) data mean velocity comparison.

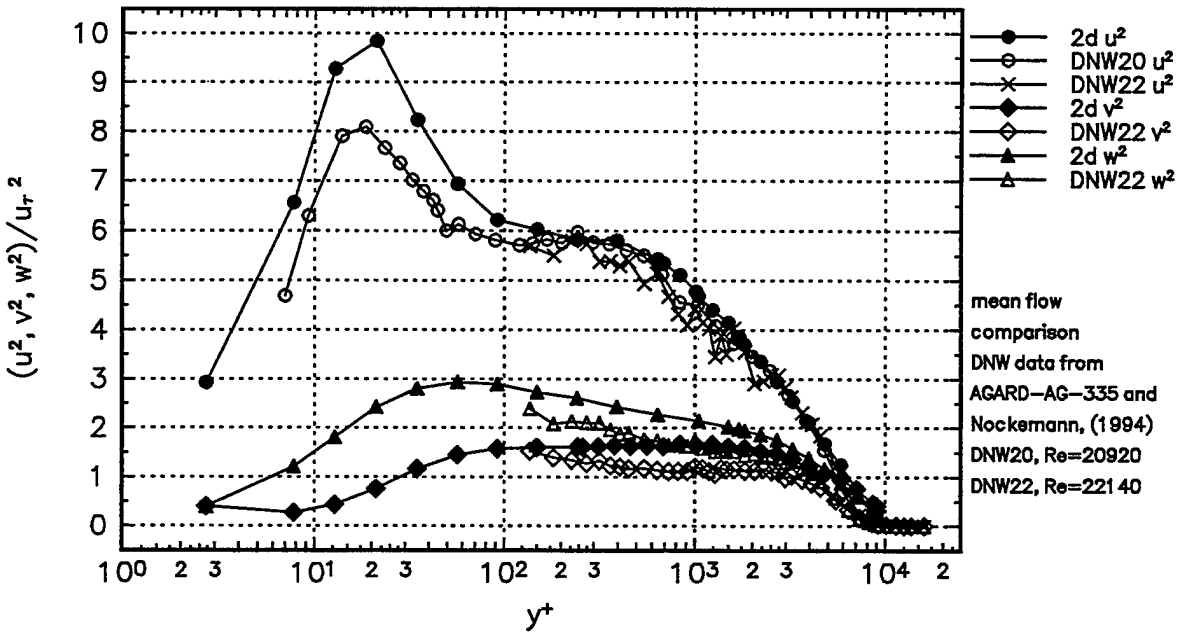

Figure 5. DNW (Re_θ=22140, Re_θ=20920) data and present 2D (Re_θ=23200) data normal stress comparison.

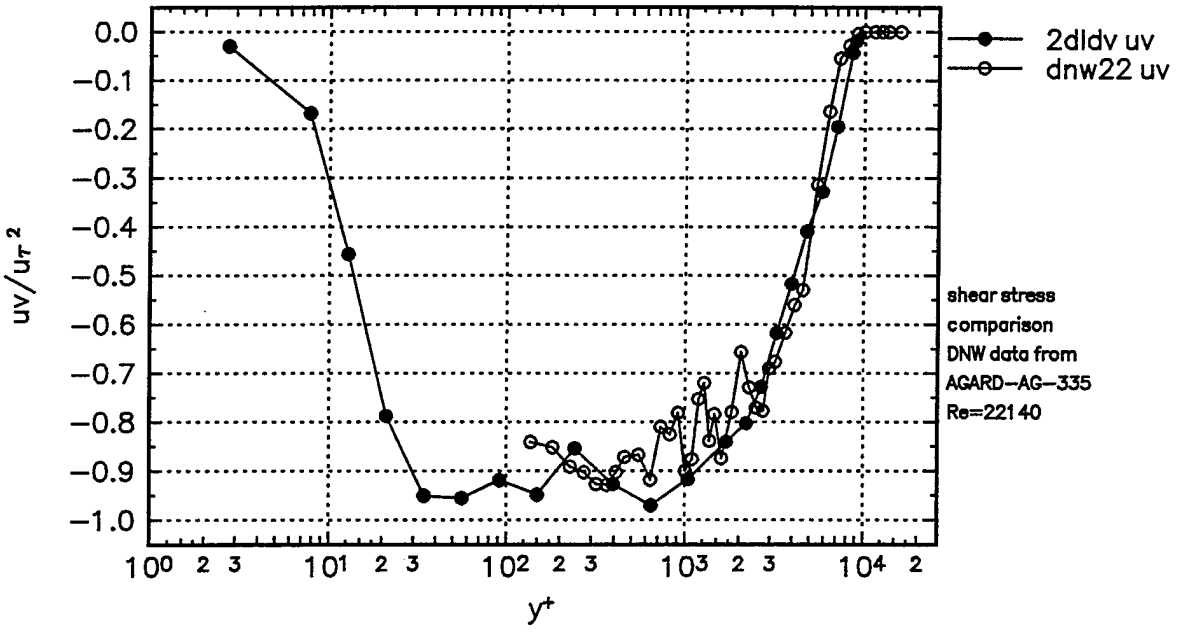

Figure 6. DNW (Re_θ=22140) data and present 2D (Re_θ=23200) data shear stress comparison.

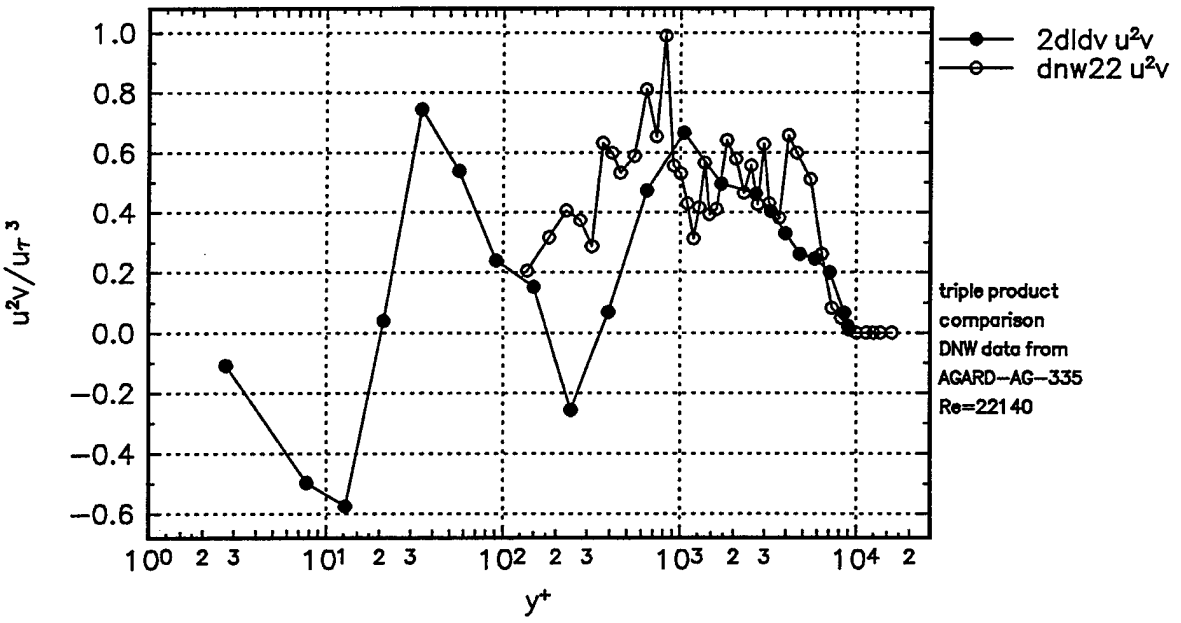

Figure 7. DNW (Re_θ=22140) data and present 2D (Re_θ=23200) data triple product comparison.

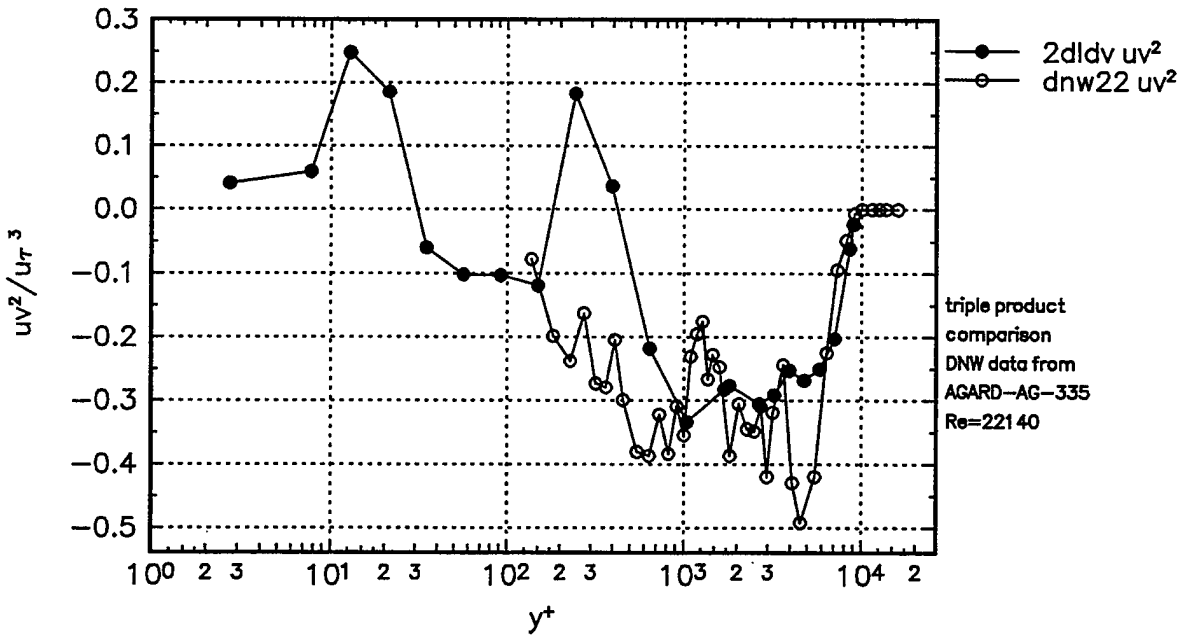

Figure 8. DNW (Re_θ=22140) data and present 2D (Re_θ=23200) data triple product comparison.

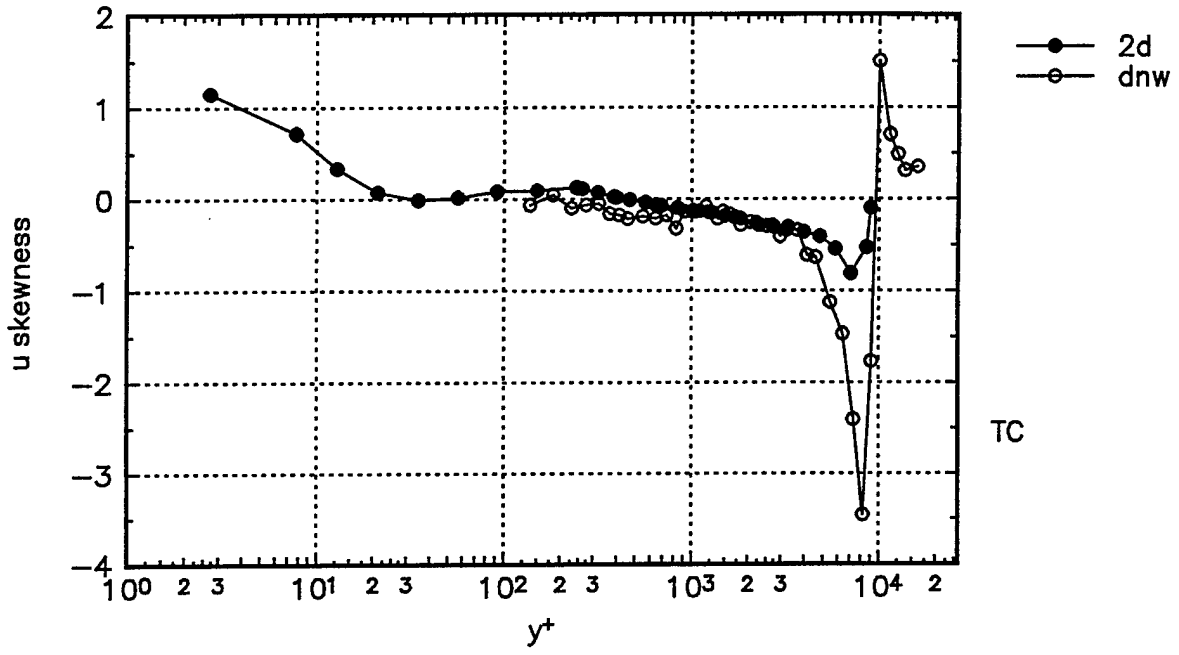

Figure 9. DNW (Re_θ=22140) data and present 2D (Re_θ=23200) data "u skewness" comparison.

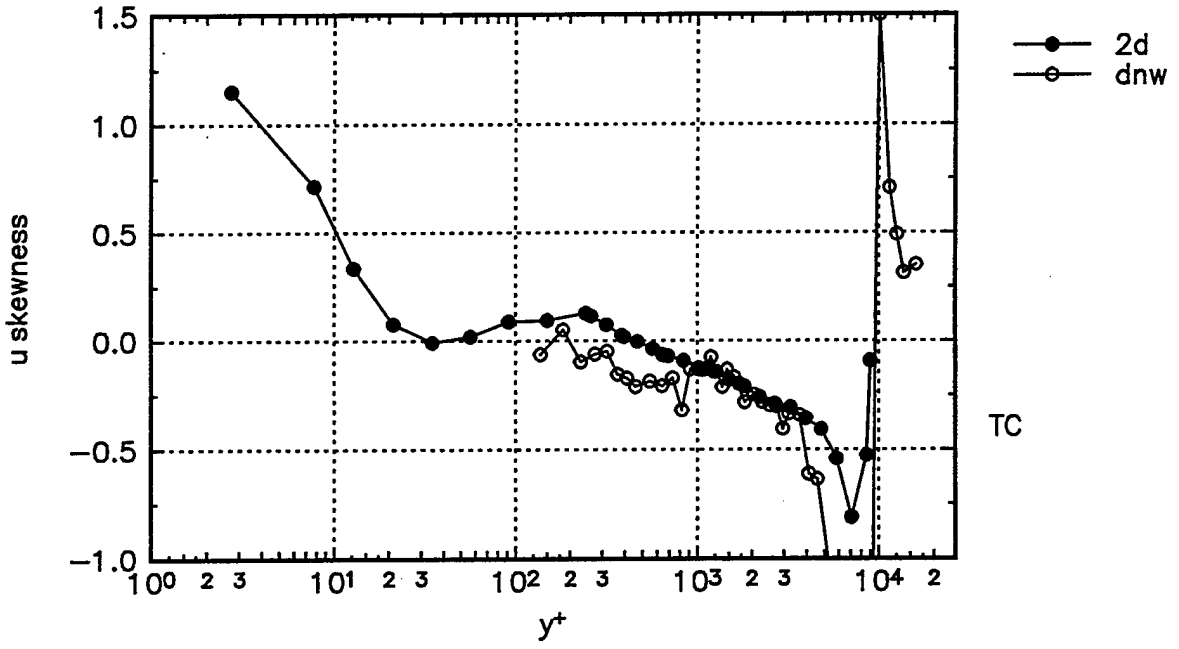

Figure 9a. DNW (Re_θ=22140) data and present 2D (Re_θ=23200) data "u skewness" comparison.

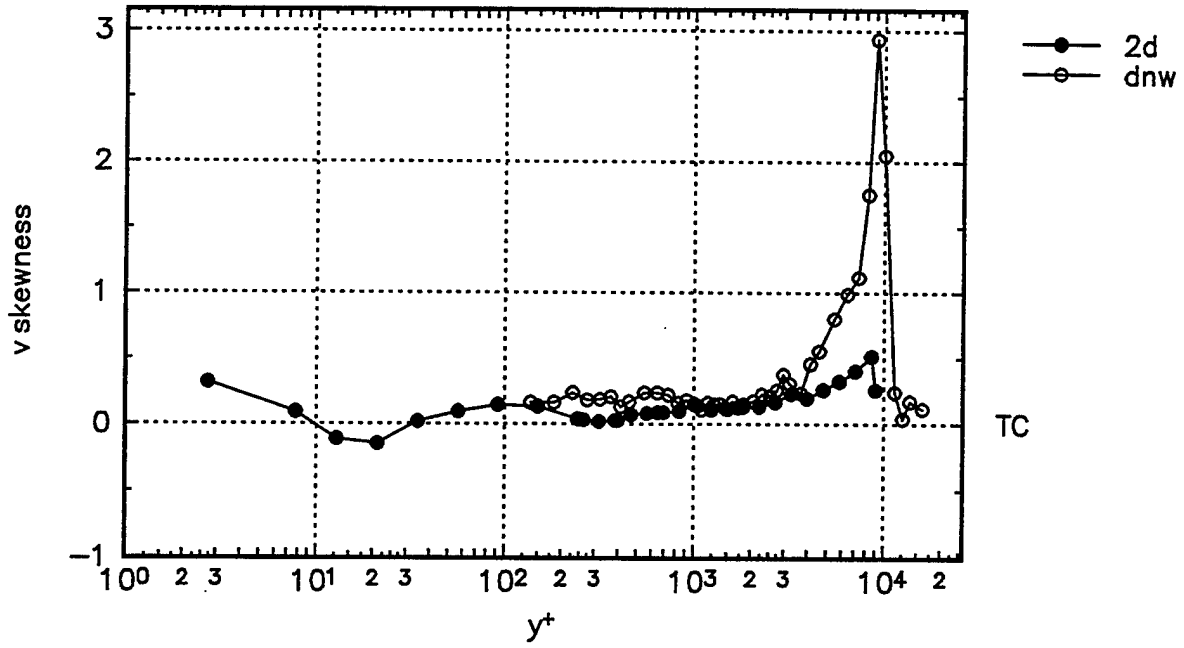

Figure 10. DNW (Re_θ=22140) data and present 2D (Re_θ=23200) data "v skewness" comparison.

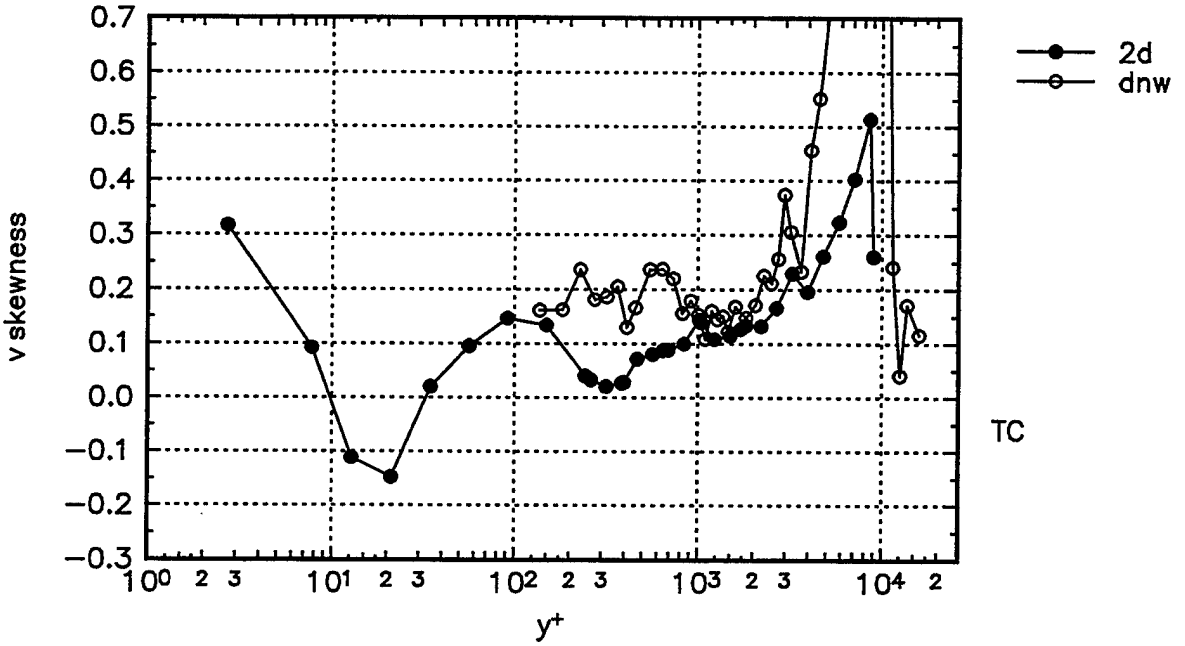

Figure 10a. DNW (Re_θ=22140) data and present 2D (Re_θ=23200) data "v skewness" comparison.

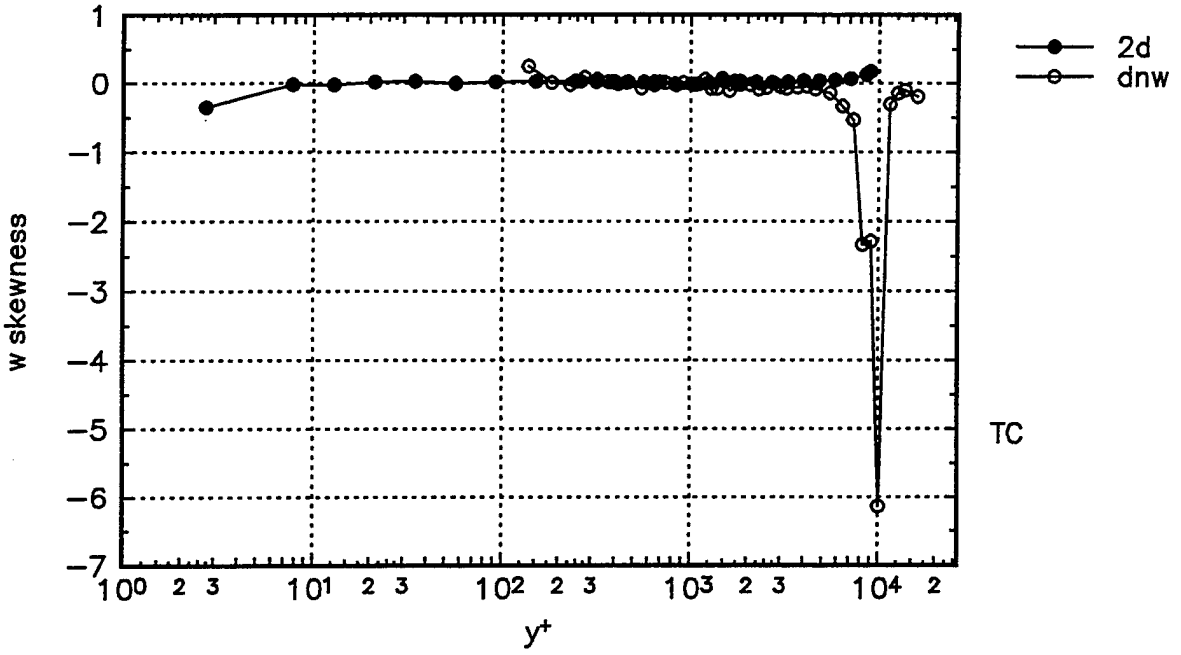

Figure 11. DNW (Re_θ=22140) data and present 2D (Re_θ=23200) data "w skewness" comparison.

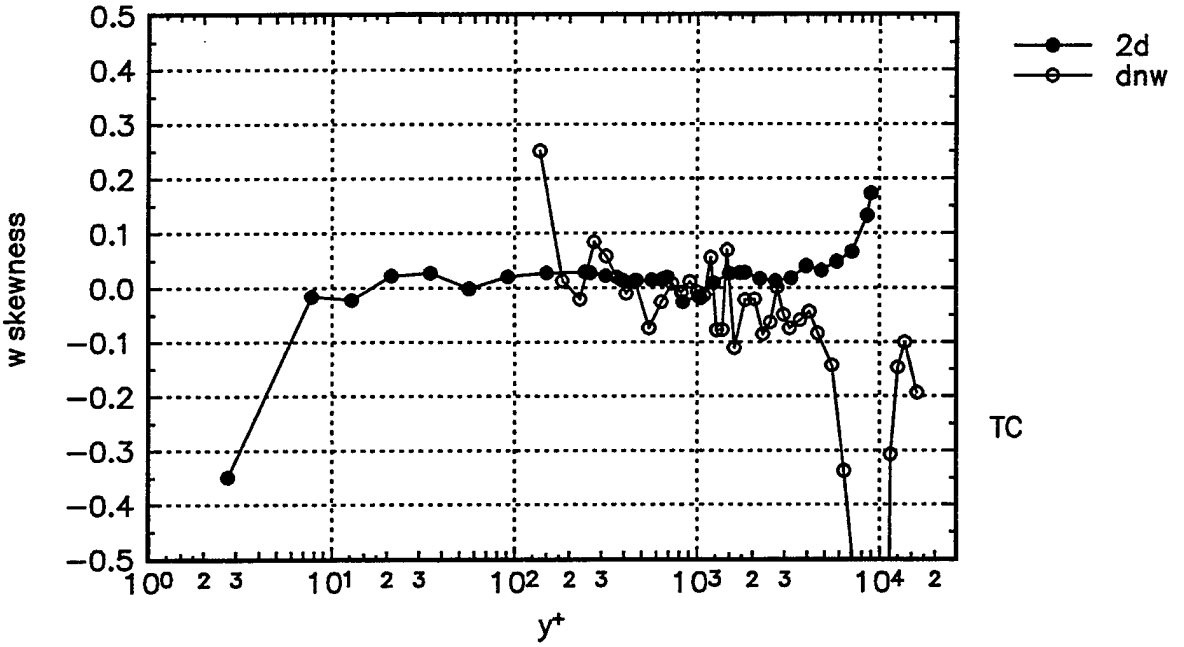

Figure 11a. DNW (Re_θ=22140) data and present 2D (Re_θ=23200) data "w skewness" comparison.

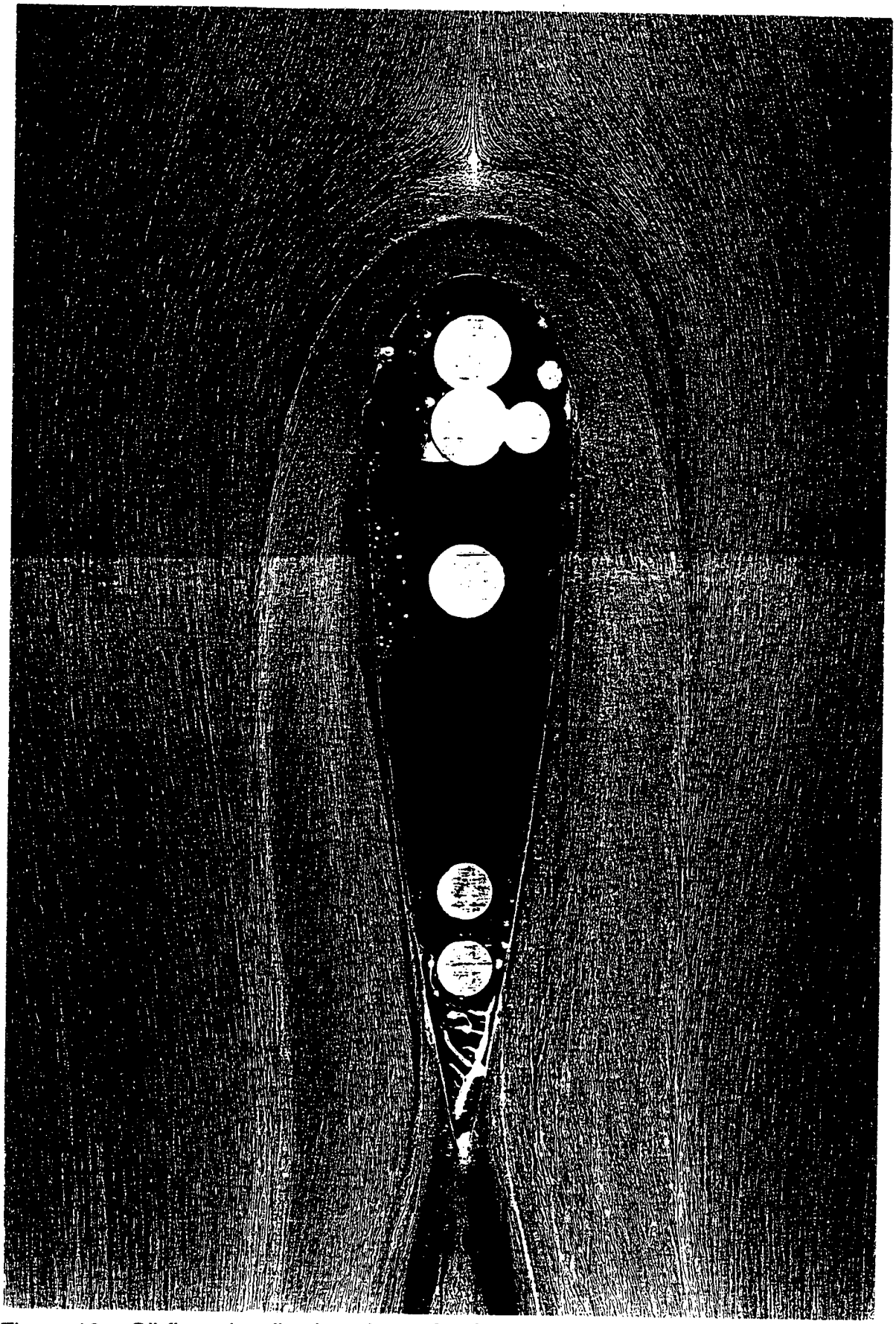

Figure 12a. Oil flow visualization picture for Re_θ=5940 case

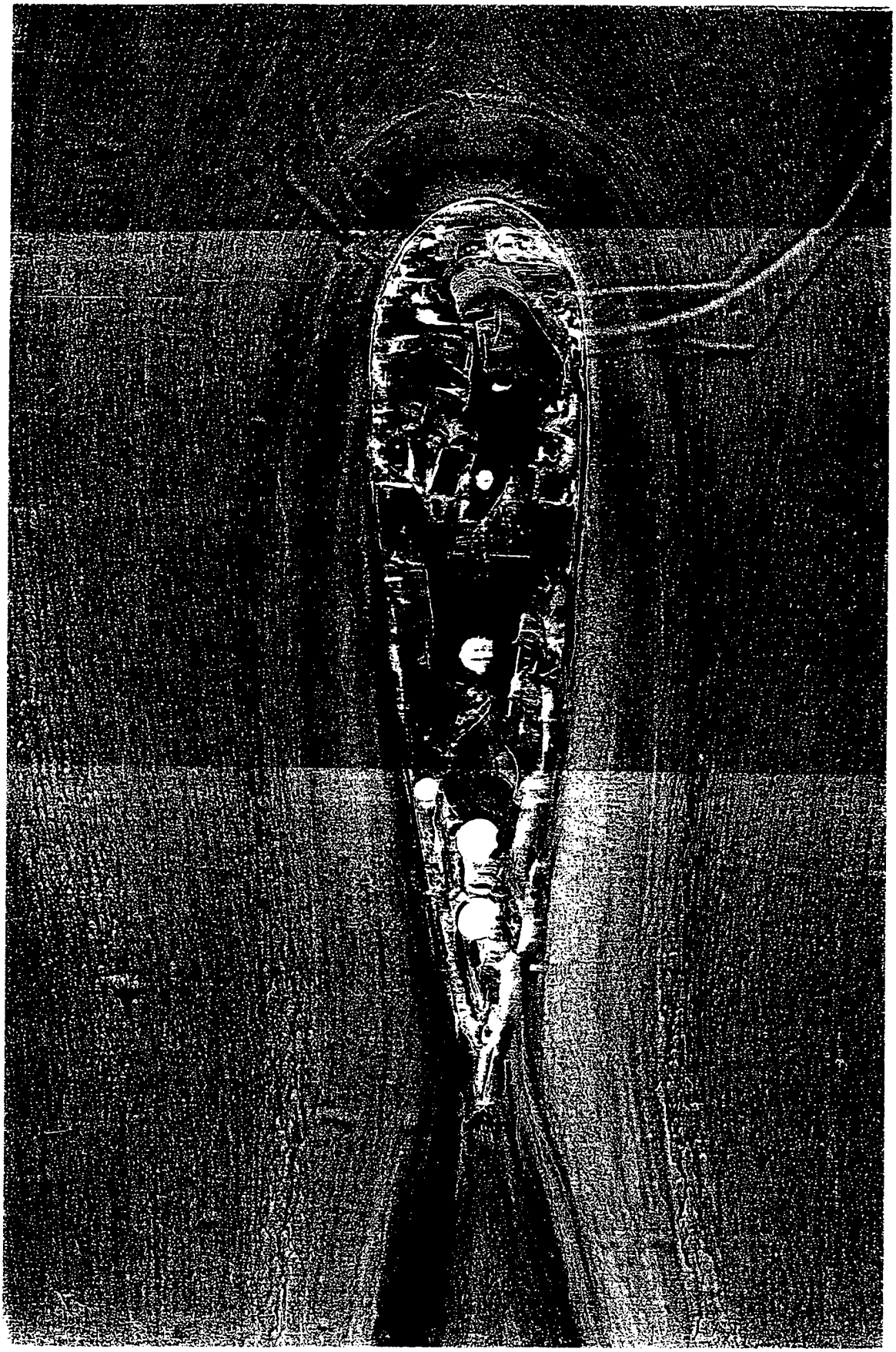

Figure 12b. Oil flow visualization picture for Re_θ=23200 case.

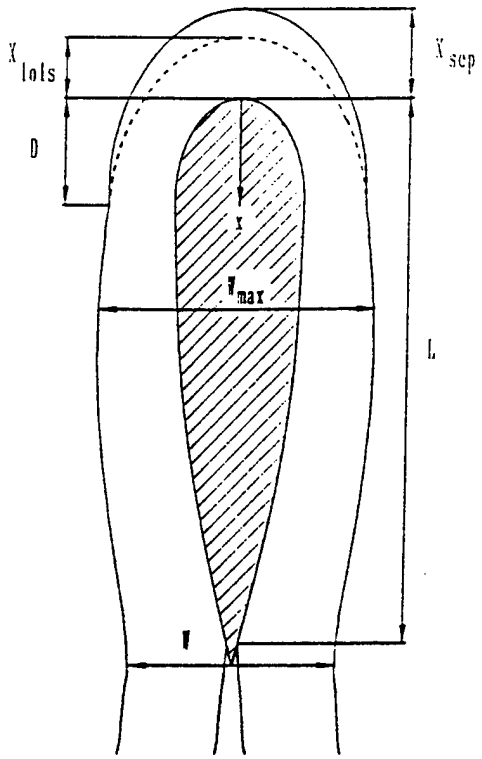

Figure 13. Definition of the characteristic lengths measured from oil flow visualization pictures.

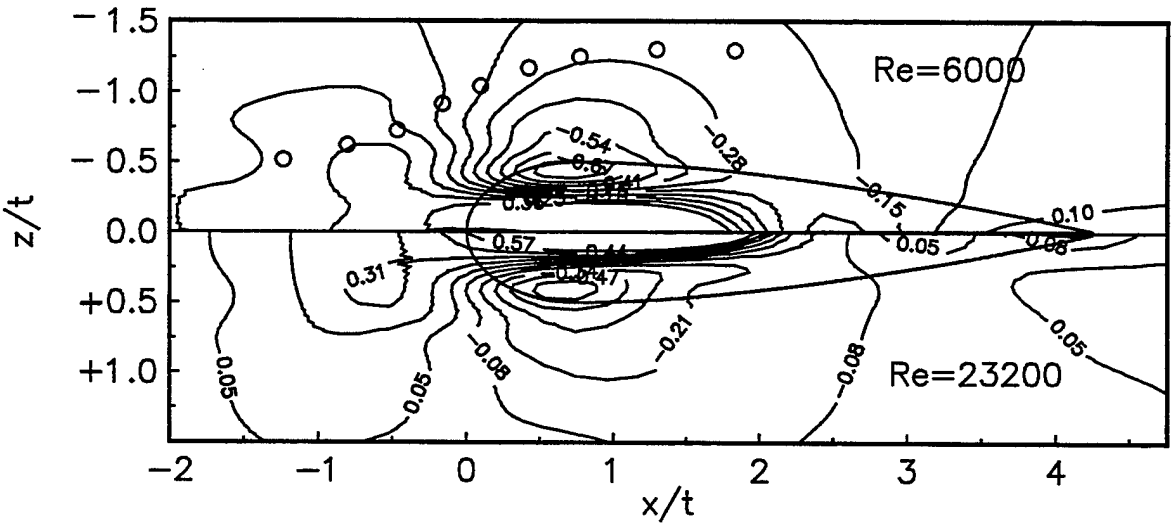

Figure 14. Wall static pressure coefficient distribution.

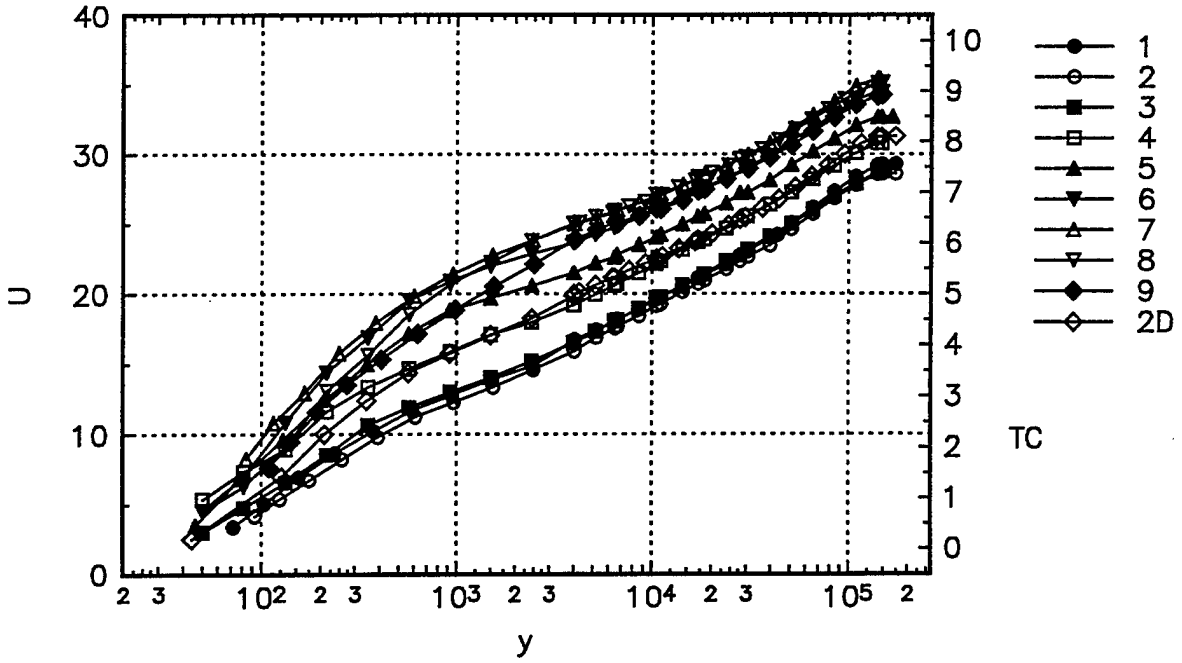

Figure 15a. U, dimensional mean velocity profiles in tunnel coordinates.

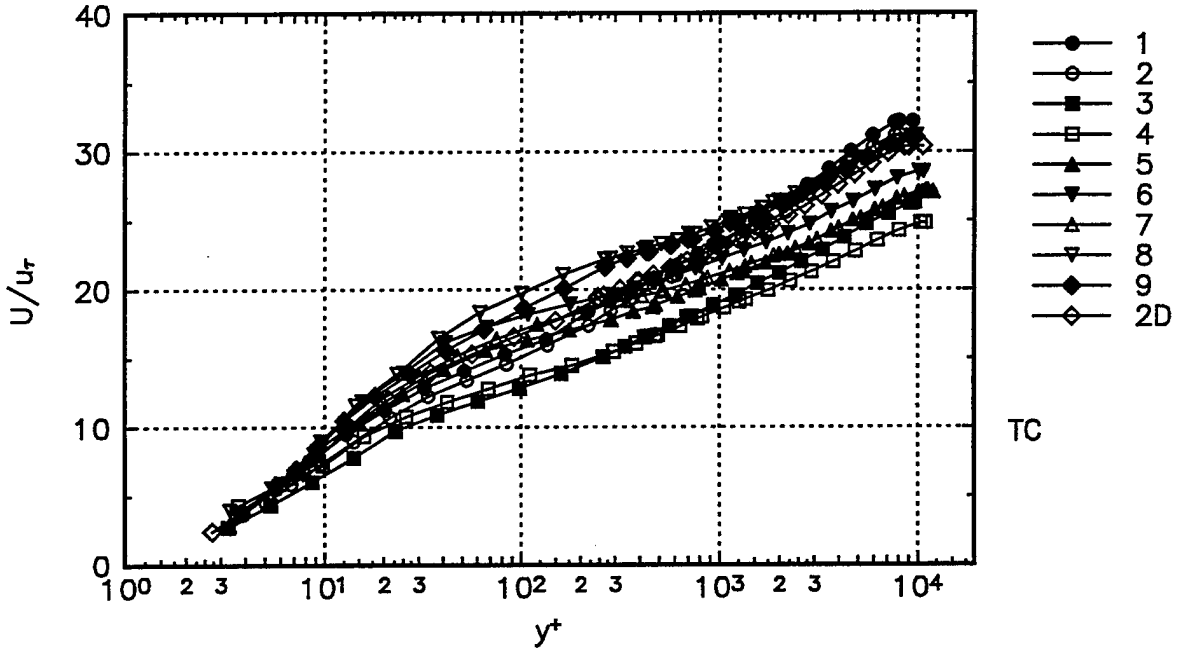

Figure 15b. U/u_τ mean velocity profiles in tunnel coordinates.

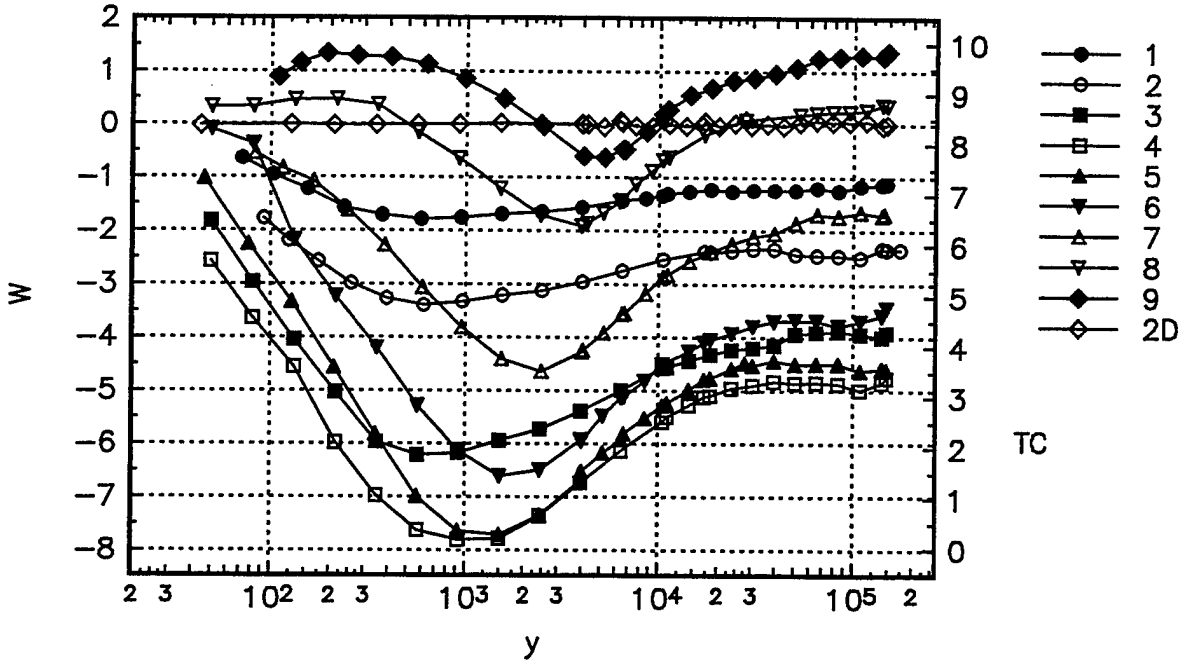

Figure 16a. W, dimensional mean velocity profiles in tunnel coordinates.

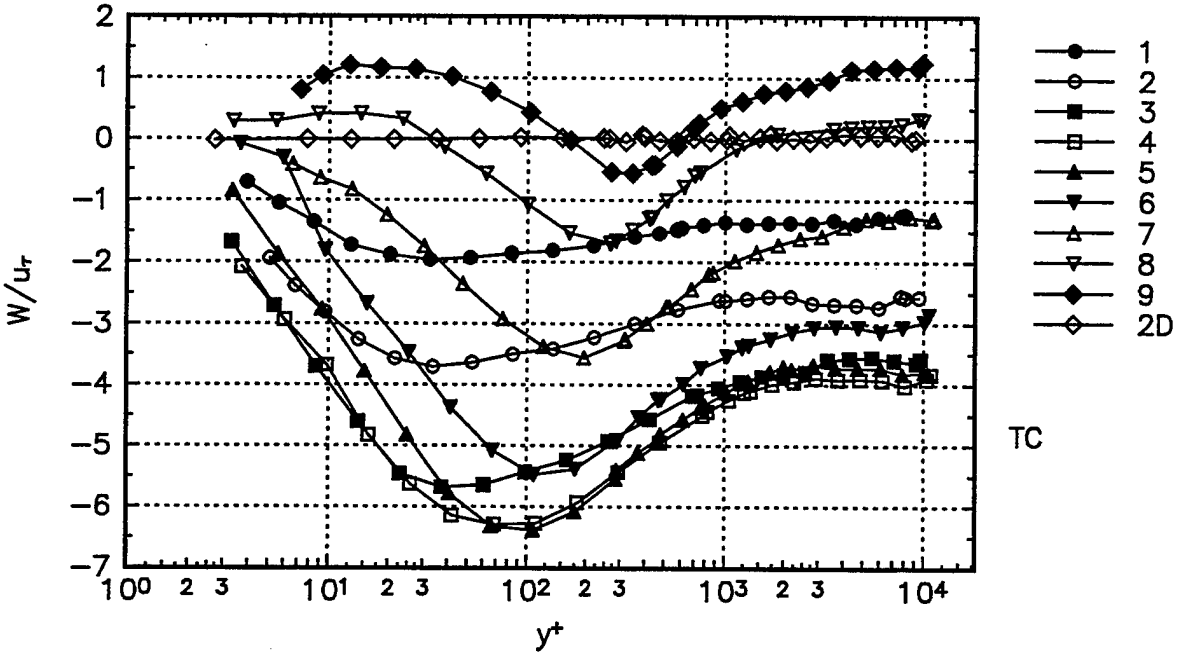

Figure 16b. W/u_τ mean velocity profiles in tunnel coordinates.

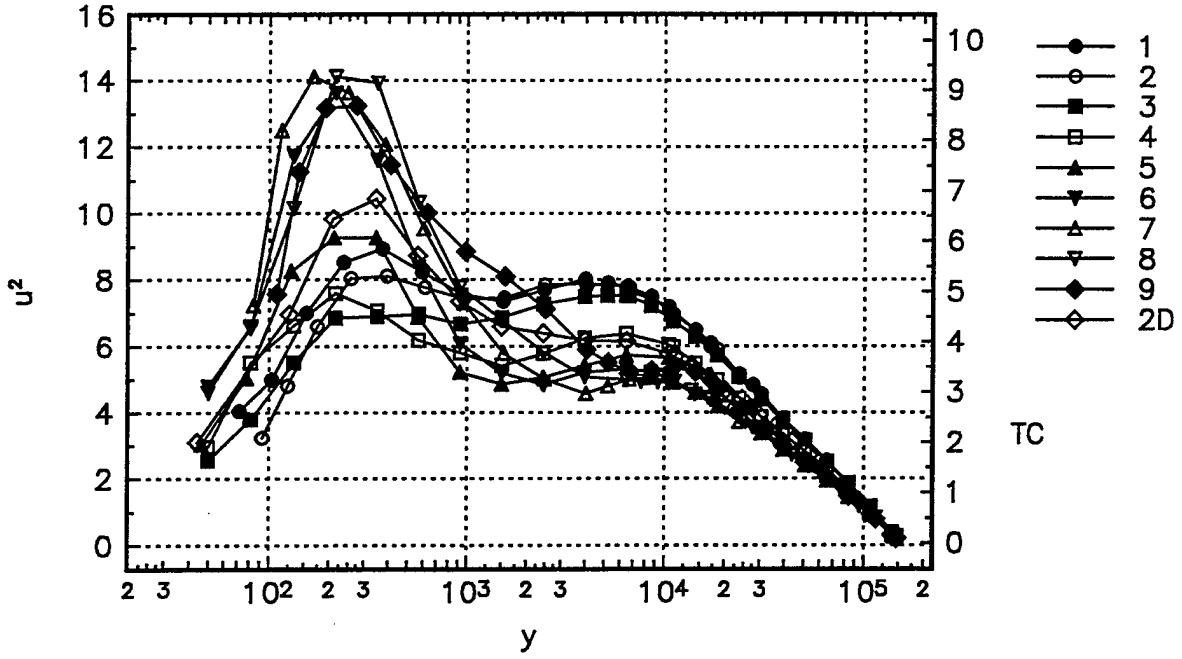

Figure 17a. $\overline{u^2}$, dimensional normal stress profiles in tunnel coordinates.

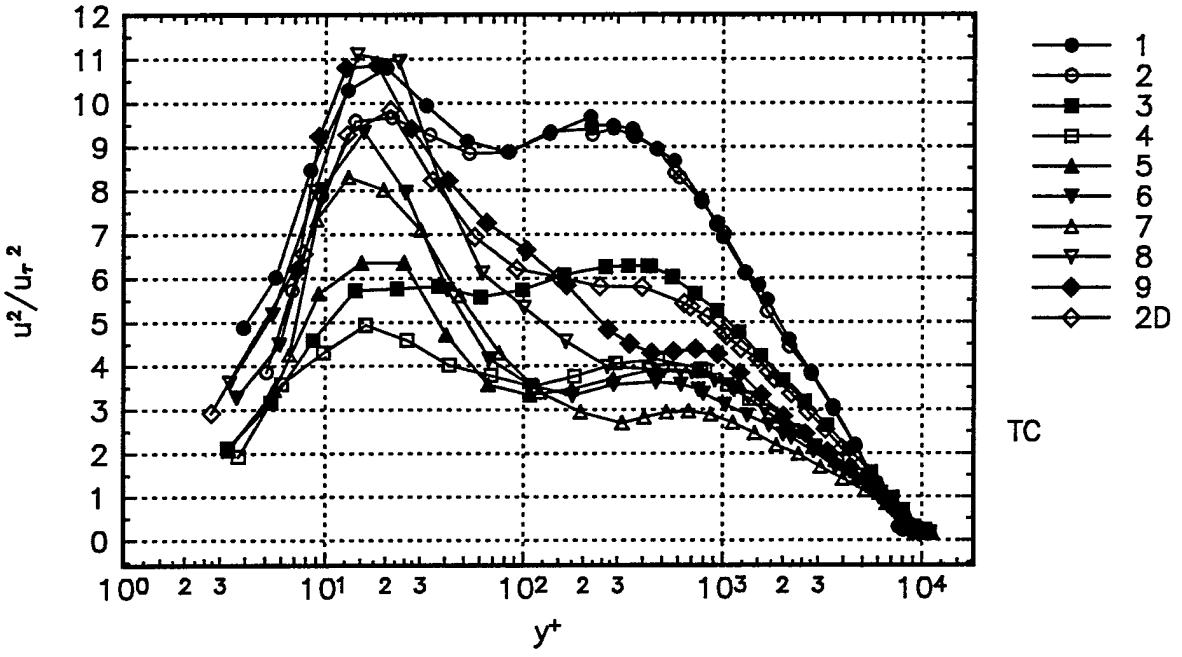

Figure 17b. $\overline{u^2}/u_\tau^2$ normal stress profiles in tunnel coordinates.

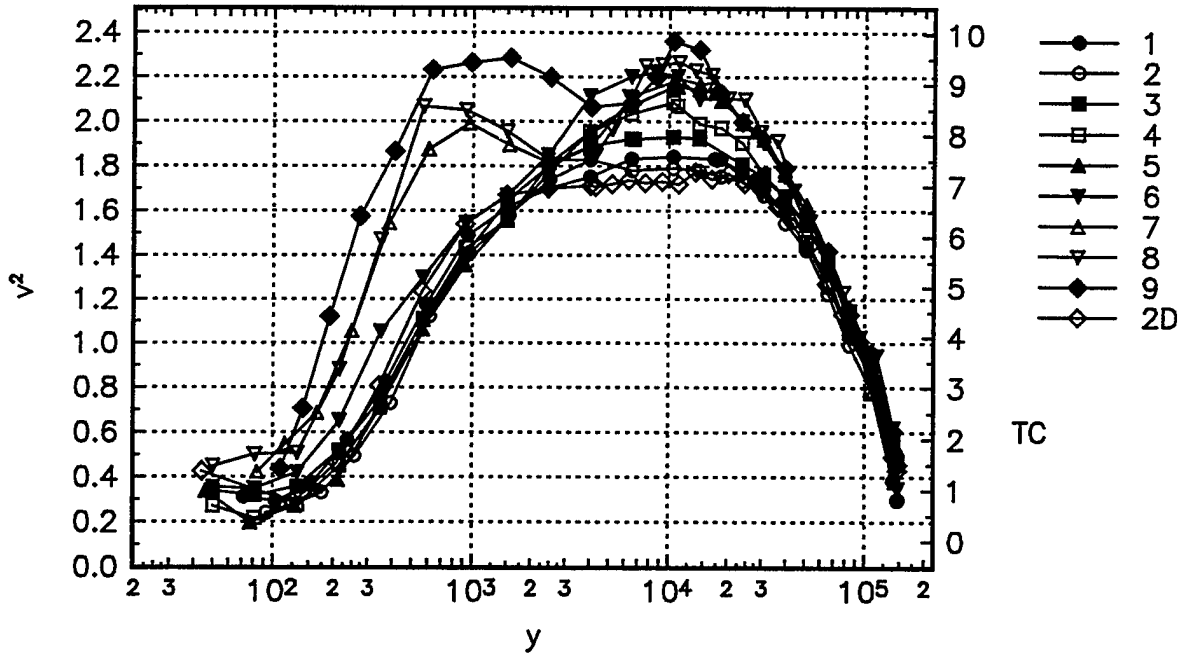

Figure 18a. $\overline{v^2}$, dimensional normal stress profiles in tunnel coordinates.

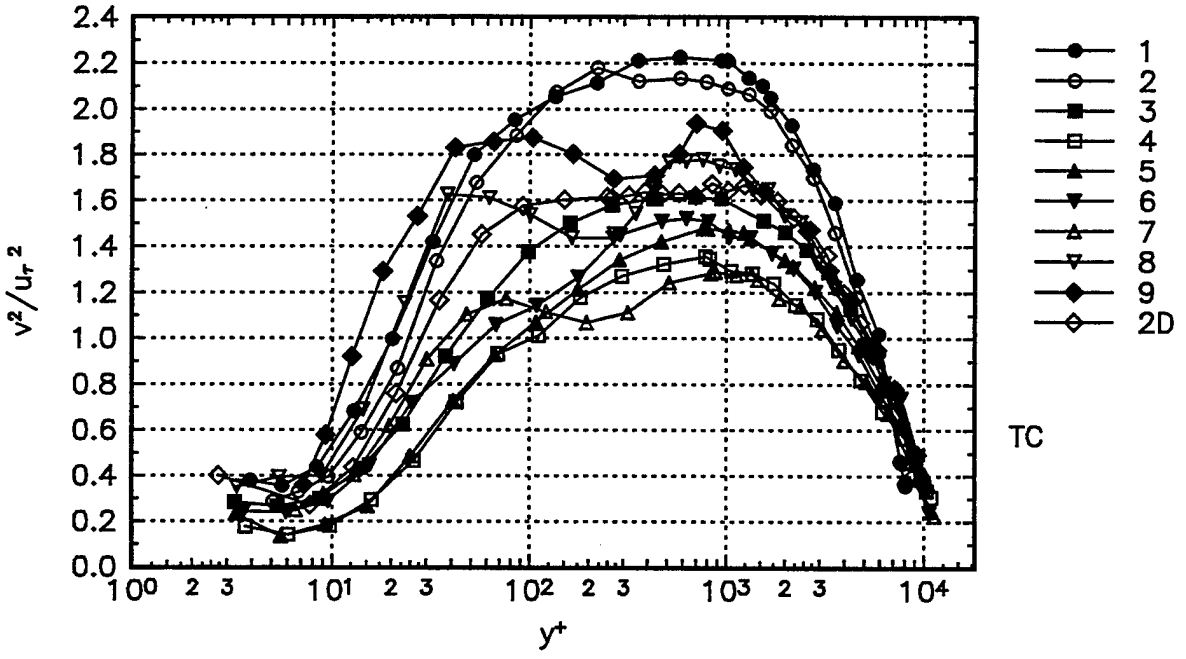

Figure 18b. $\overline{v^2}/u_\tau^2$ normal stress profiles in tunnel coordinates.

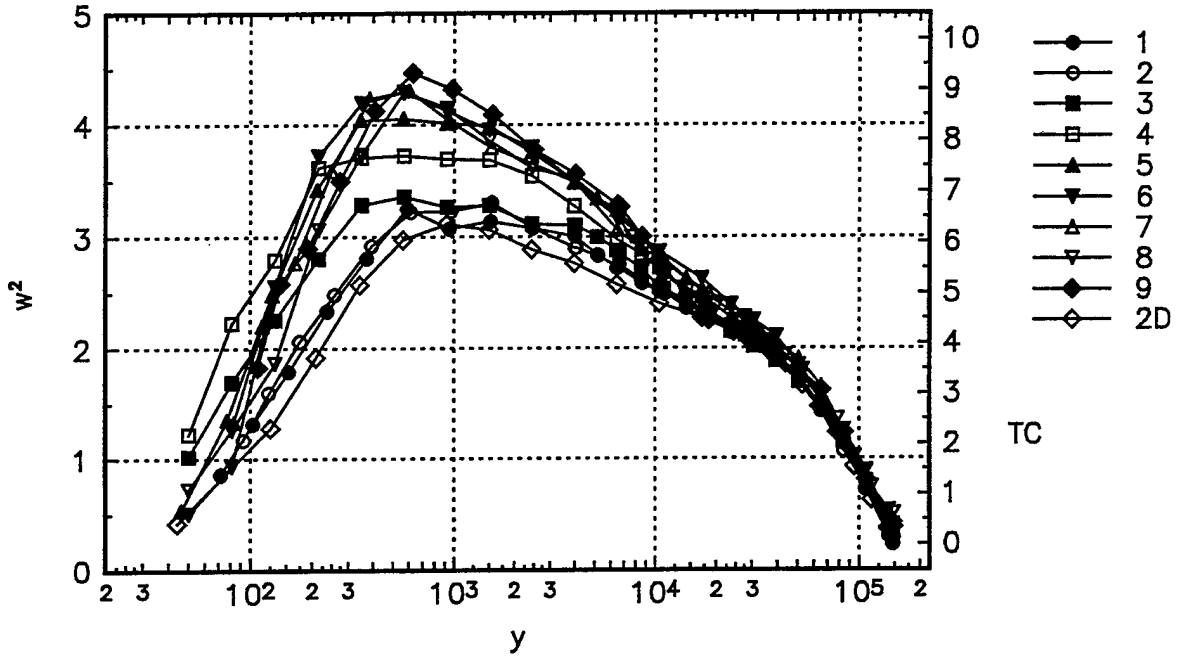

Figure 19a. $\overline{w^2}$, dimensional normal stress profiles in tunnel coordinates.

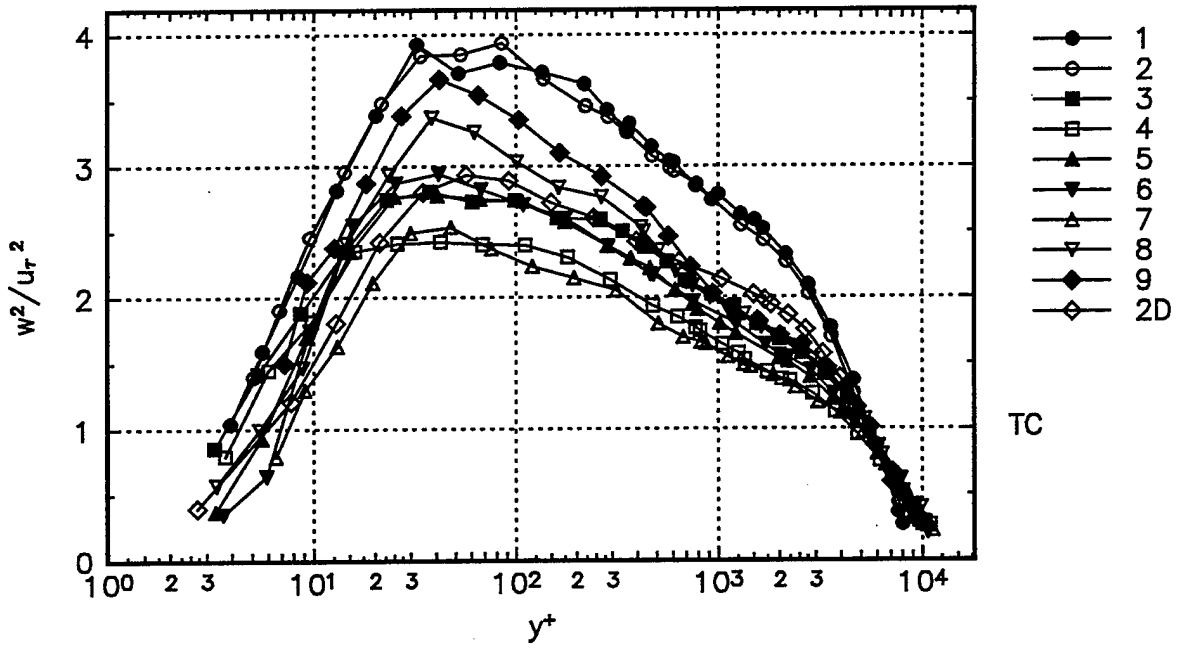

Figure 19b. $\overline{w^2}/u_\tau^2$ normal stress profiles in tunnel coordinates.

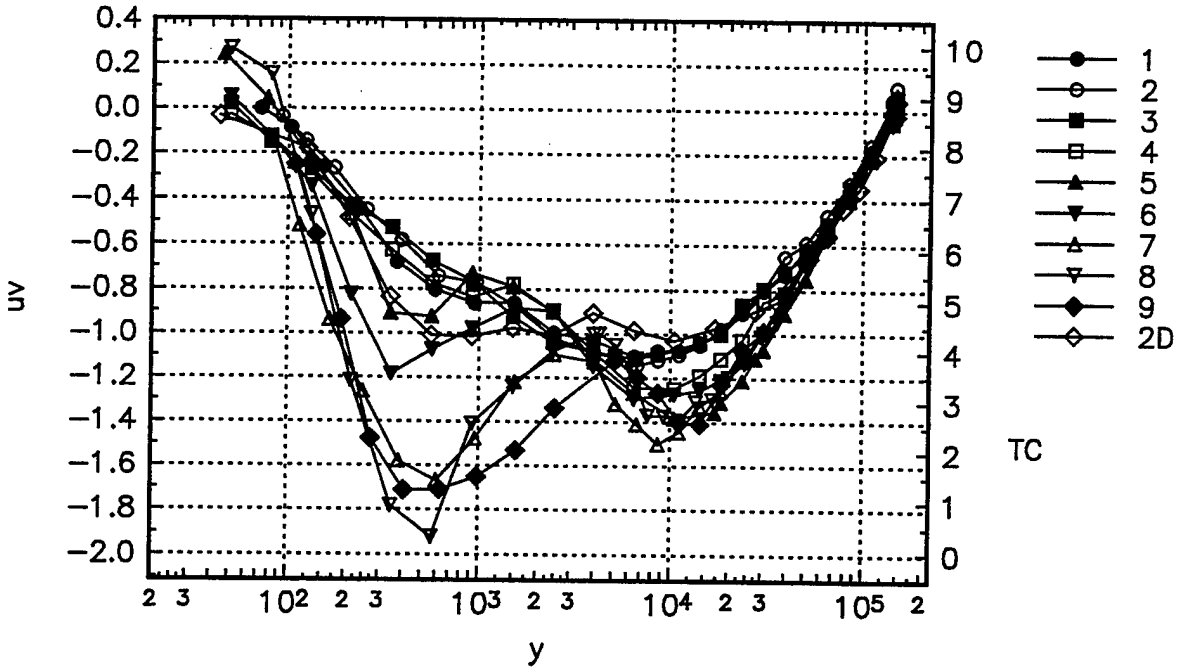

Figure 20a. $\overline{uv}$, dimensional shear stress profiles in tunnel coordinates.

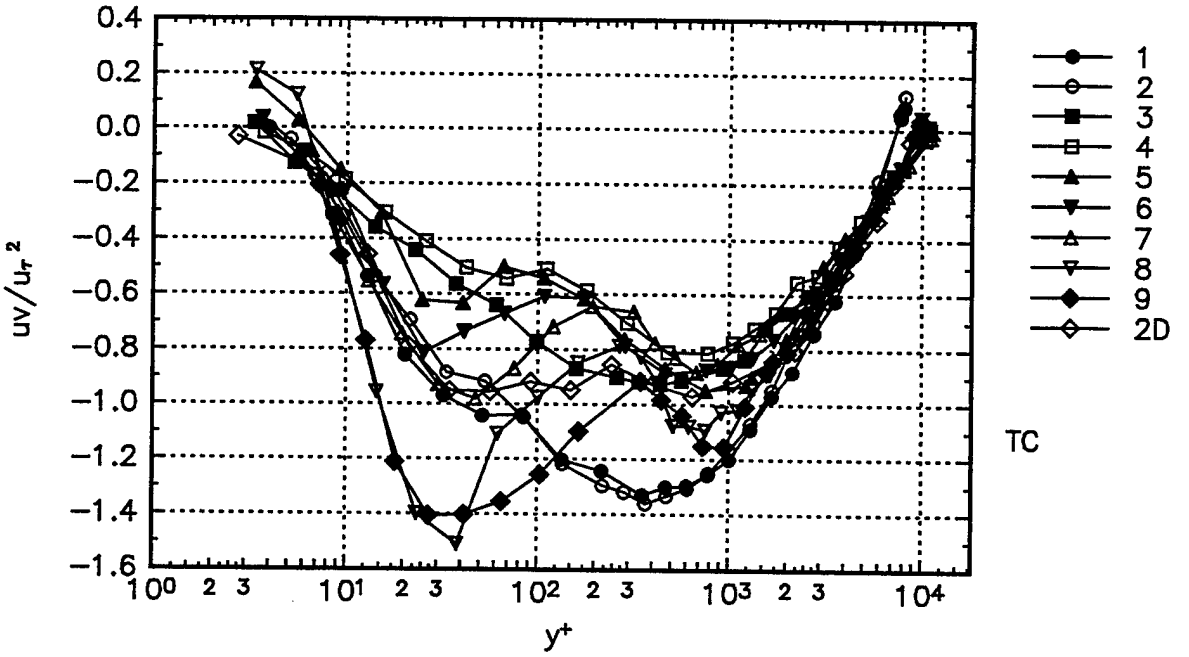

Figure 20b. $\overline{uv}/u_\tau^2$ shear stress profiles in tunnel coordinates.

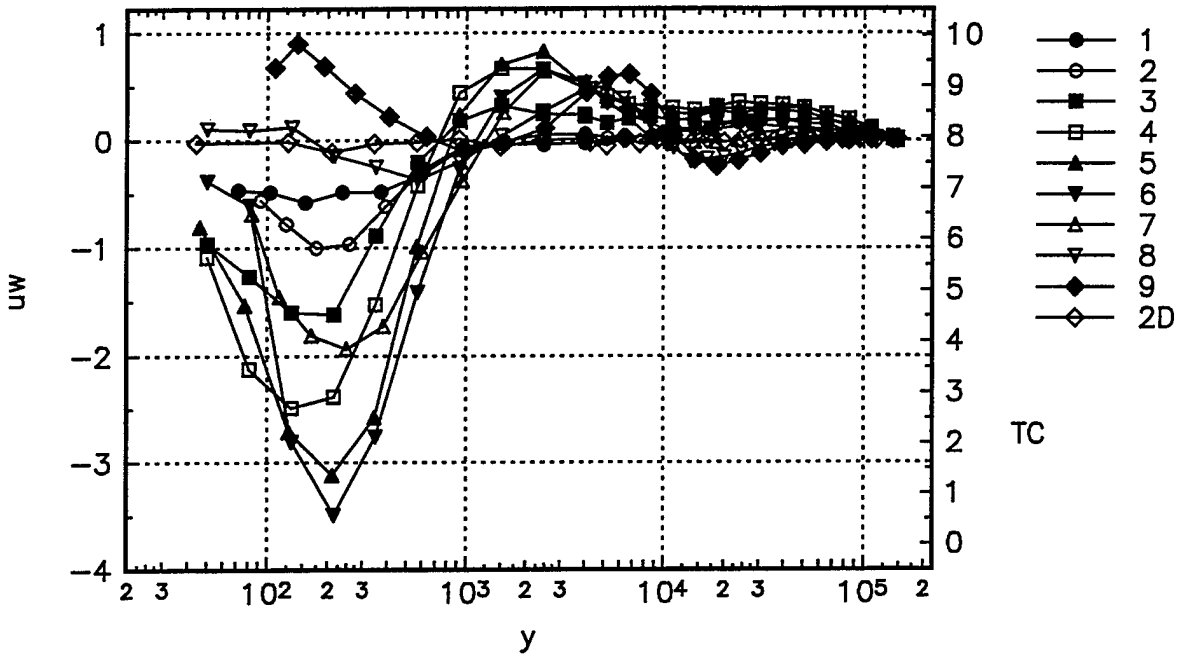

Figure 21a. $\overline{uw}$, dimensional shear stress profiles in tunnel coordinates.

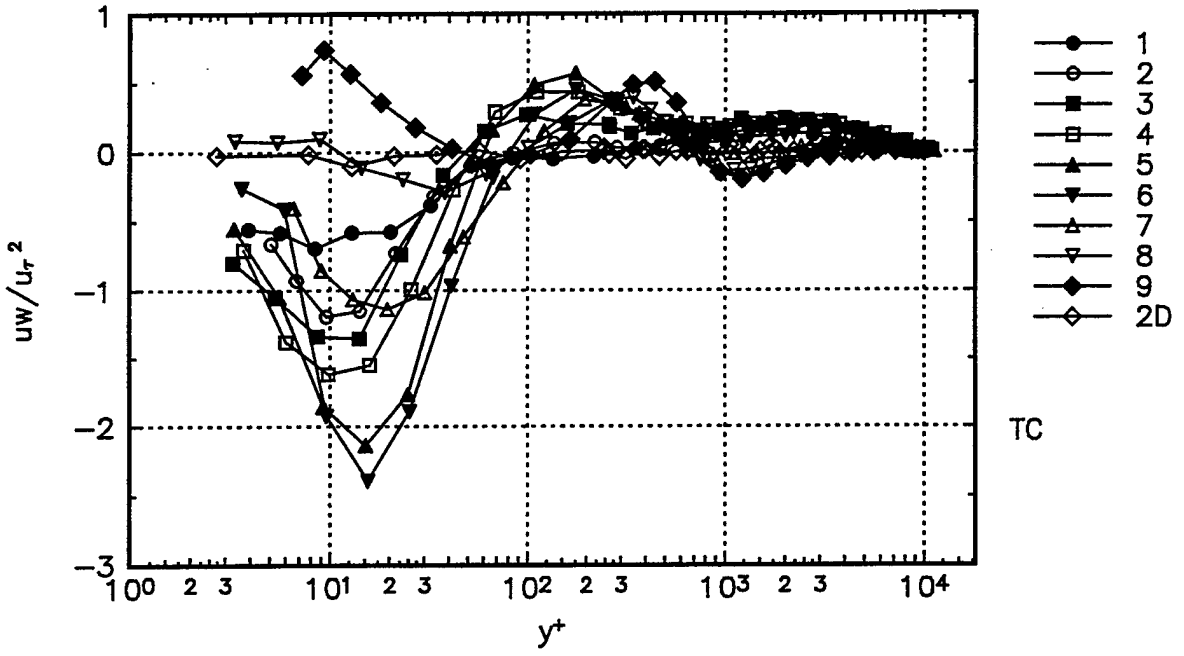

Figure 21b. $\overline{uw}/u_\tau^2$ shear stress profiles in tunnel coordinates.

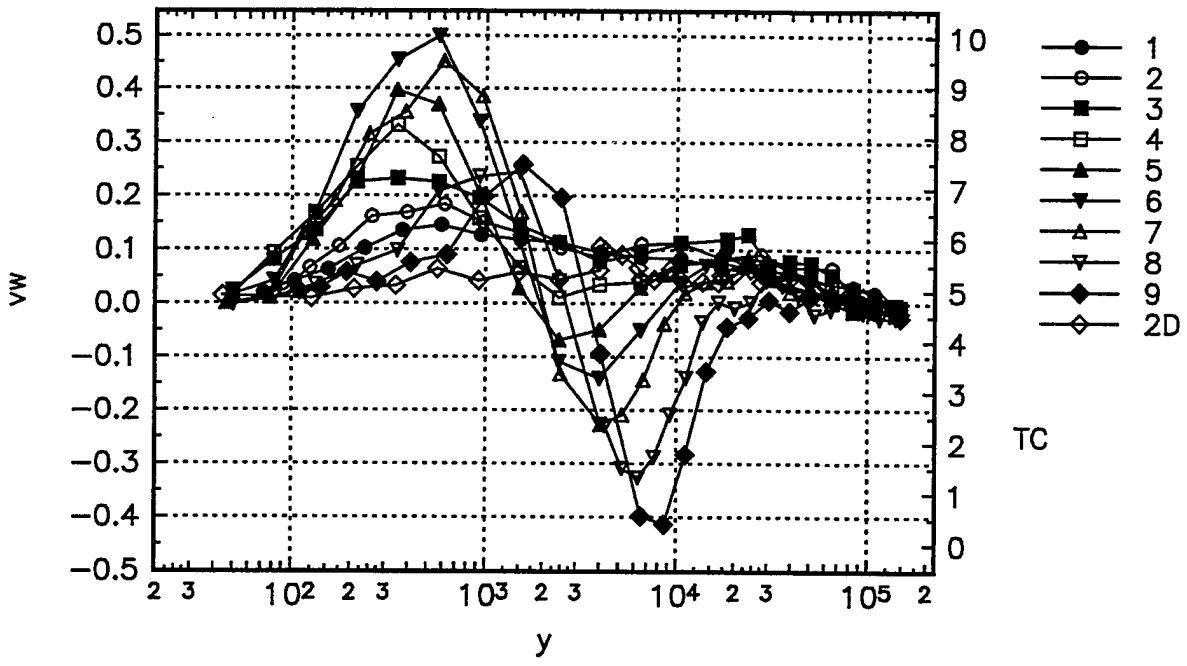

Figure 22a. $\overline{vw}$, dimensional shear stress profiles in tunnel coordinates.

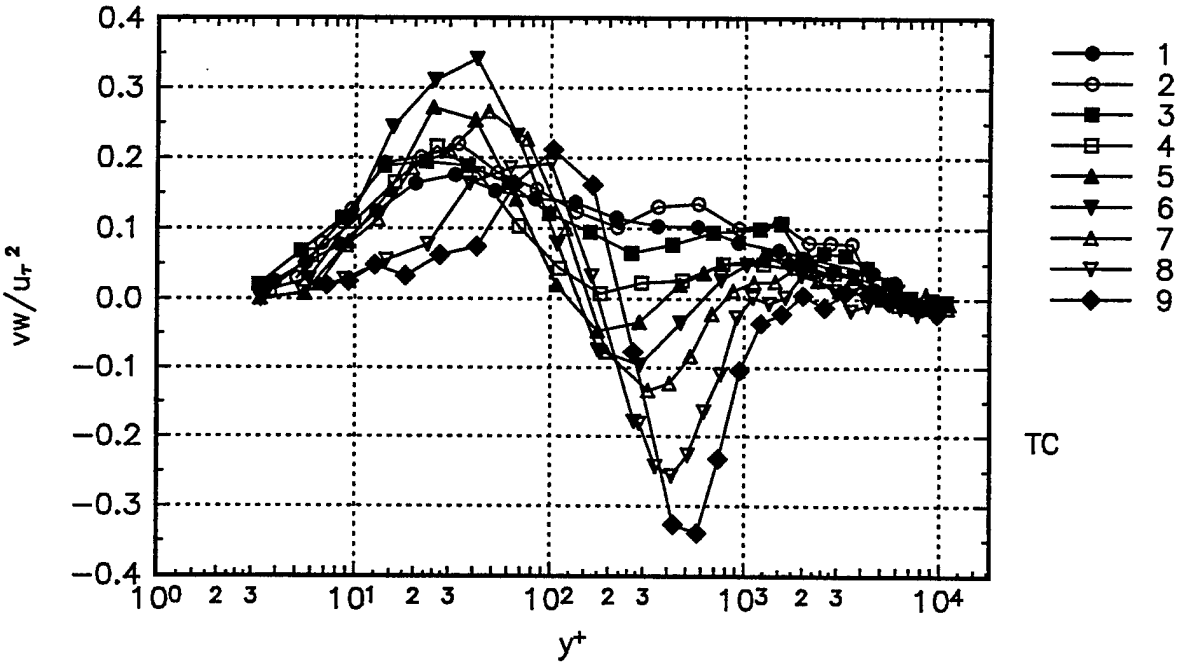

Figure 22b. $\overline{vw}/u_\tau^2$ shear stress profiles in tunnel coordinates.

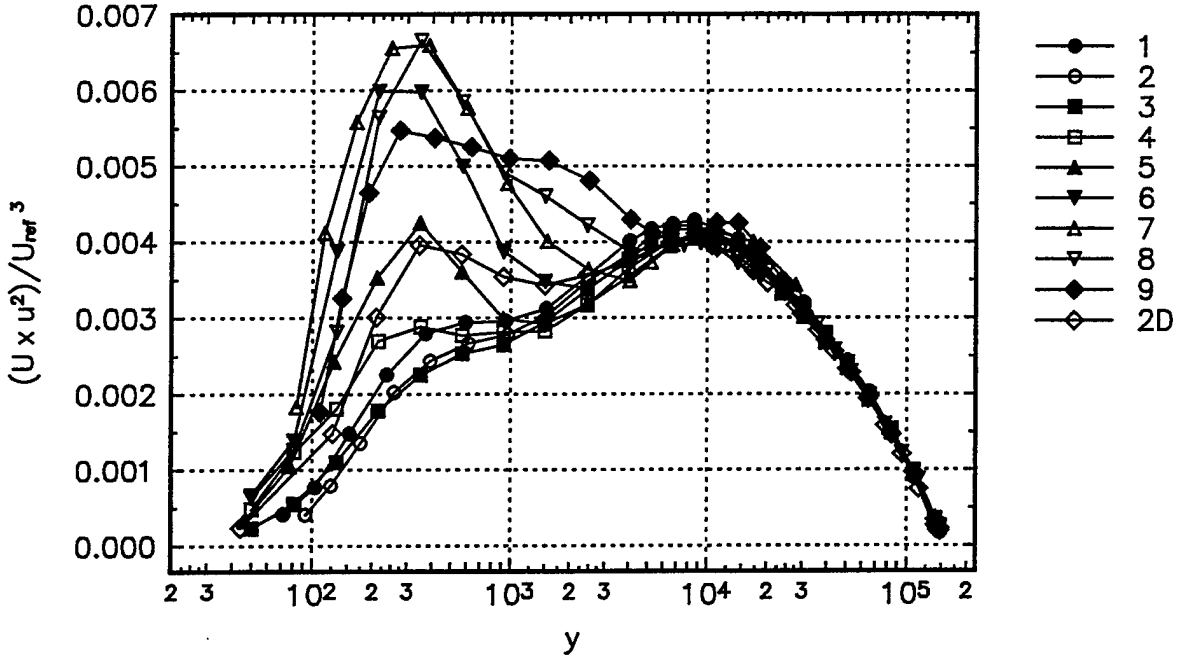

Figure 23a. Nondimensional U X $\overline{u^2}$ (mean velocity X normal stress) vs. "y" distance away from the wall for the high Reynolds number (Re_θ=23200) case.

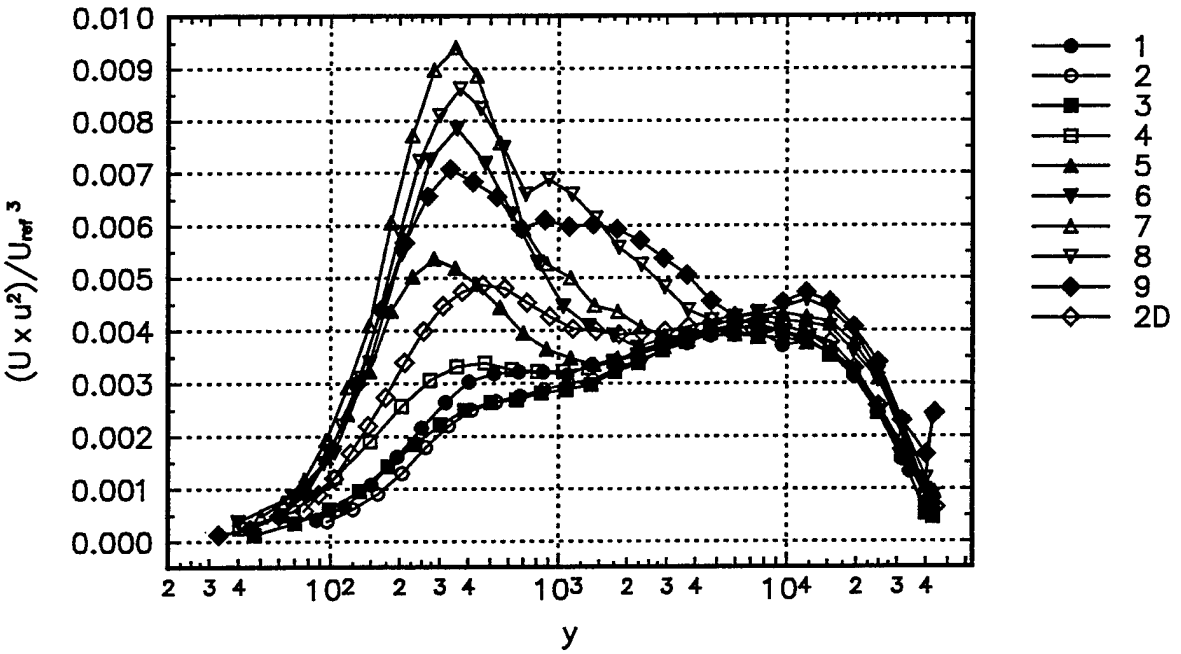

Figure 23b. Nondimensional U X $\overline{u^2}$ (mean velocity X normal stress) vs. "y" distance away from the wall for the low Reynolds number (Re_θ=5940) case.

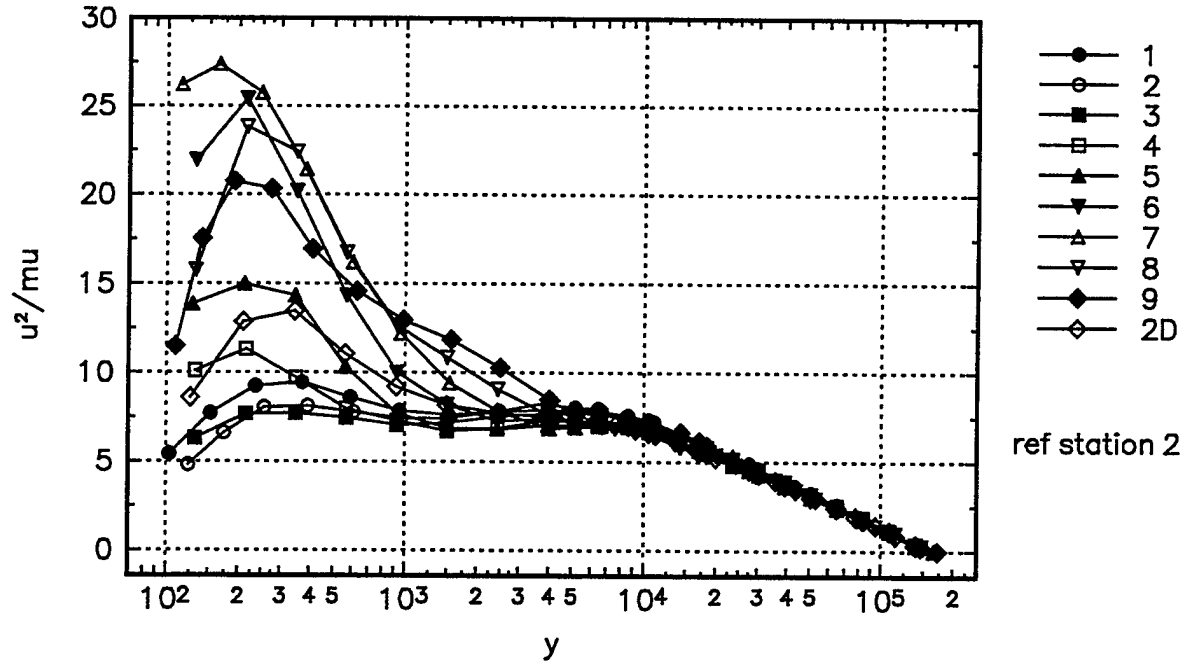

Figure 24a. $\overline{u^2}$ normal stress nondimensionalized by Batchelor's "μ" parameter.

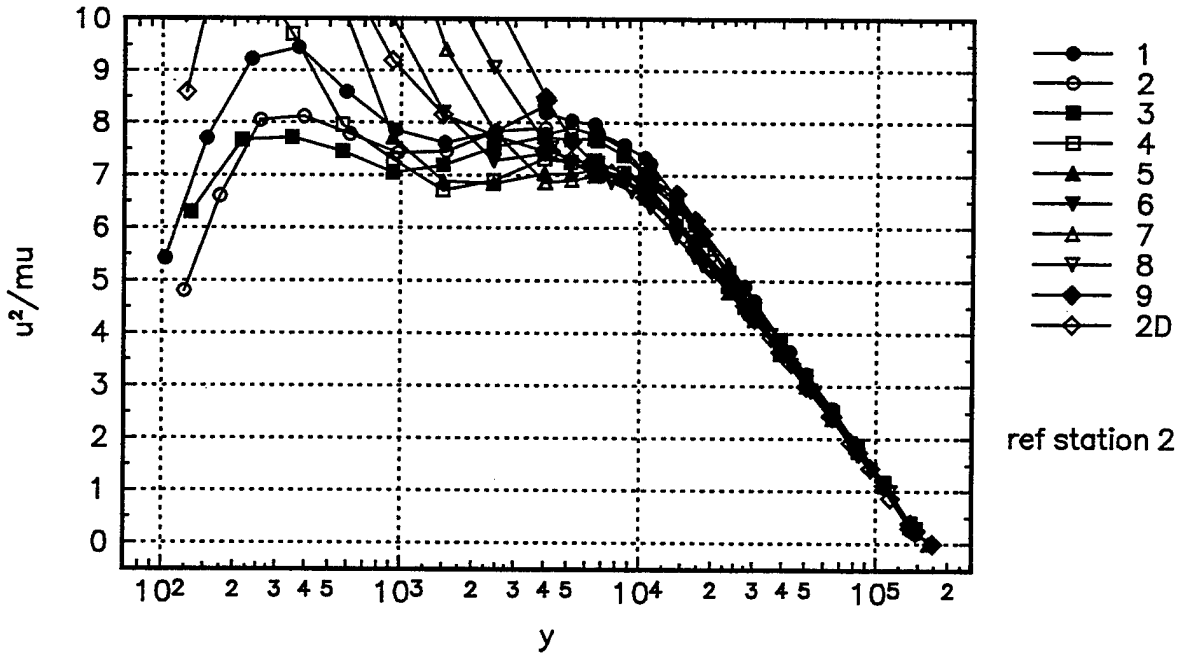

Figure 24b. The $\overline{u^2}$ normal stress nondimensionalized by Batchelor's "μ" parameter.

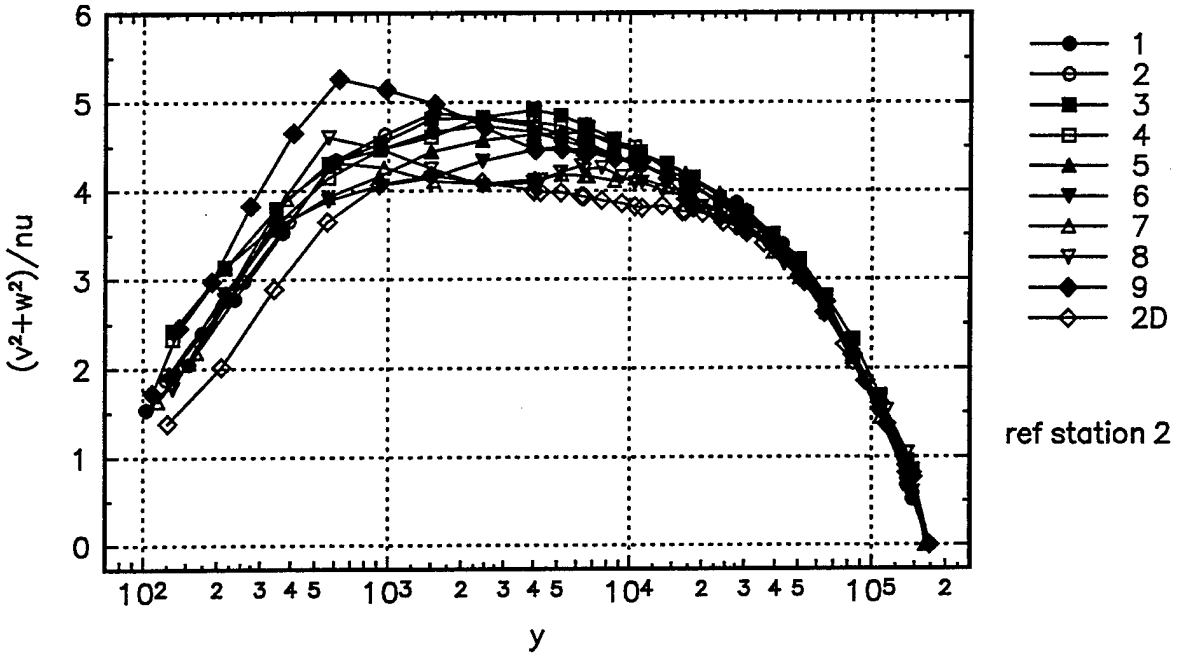

Figure 25. The $\overline{v^2}+\overline{w^2}$, sum of normal stresses nondimensionalized by Batchelor's "v" parameter.

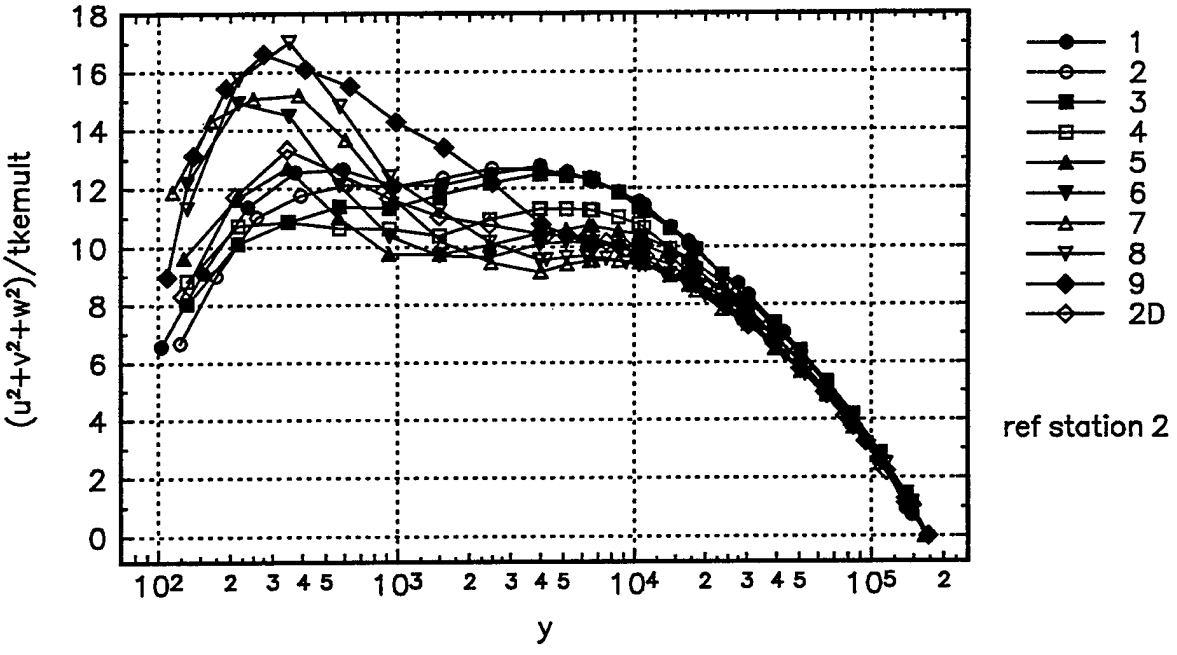

Figure 26. The $\overline{u^2}+\overline{v^2}+\overline{w^2}$, sum of normal stresses nondimensionalized by Batchelor's "tke multiplier" parameter.

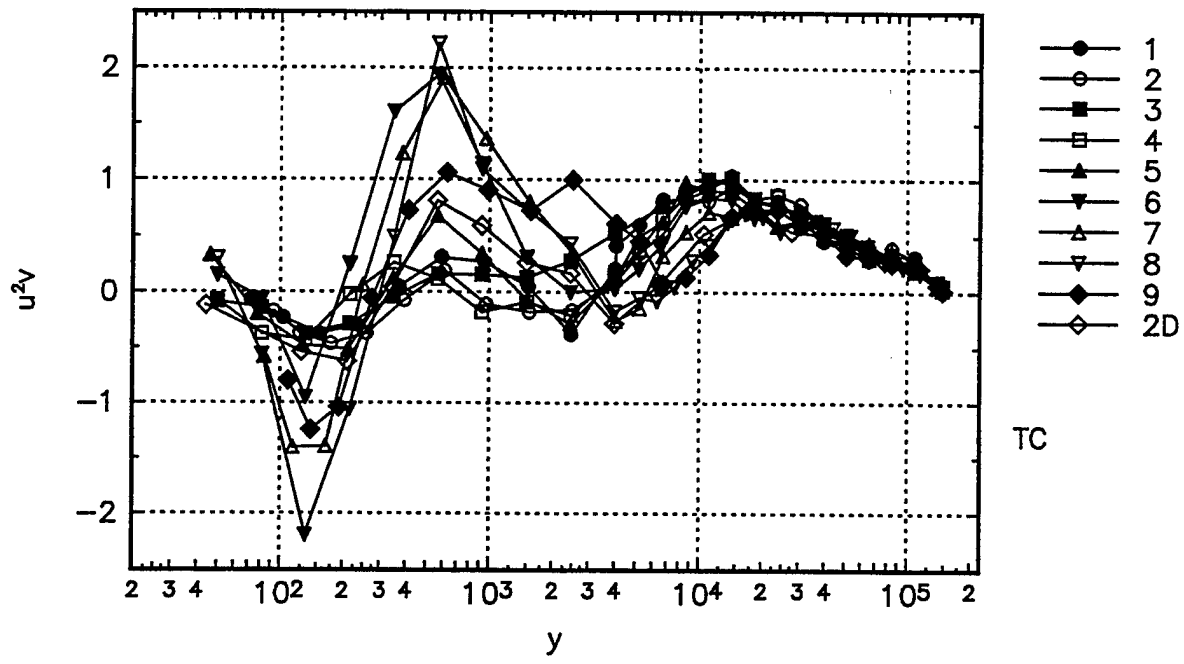

Figure 27a. Dimensional triple product in tunnel coordinates. Symbols denote the measurement stations.

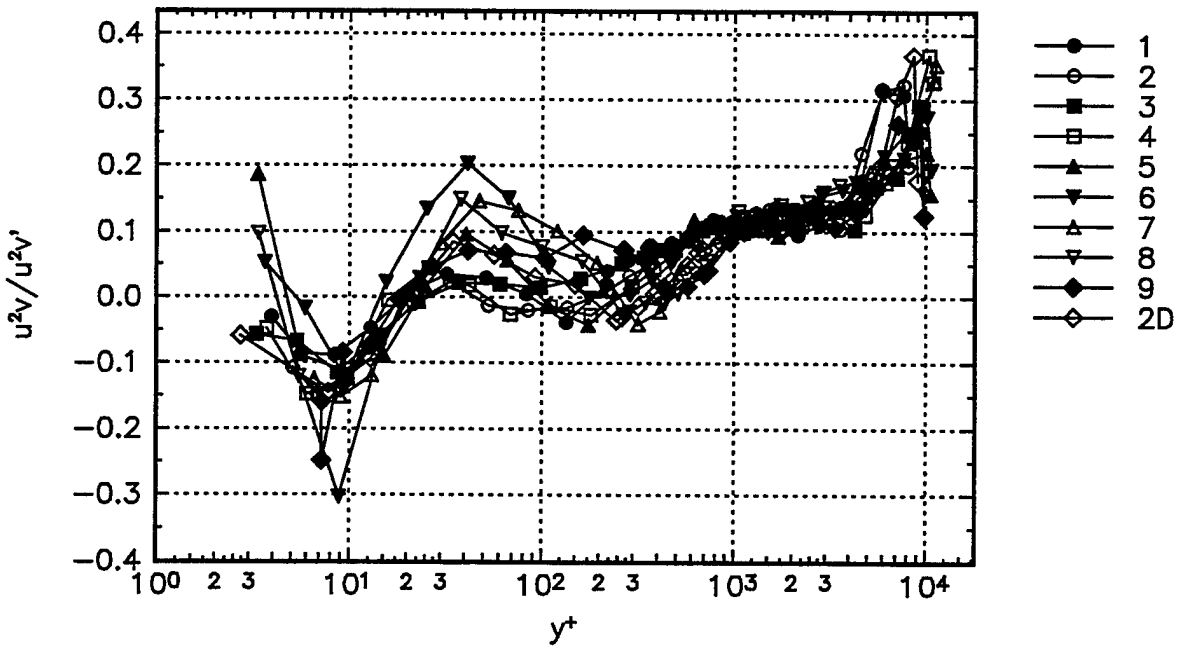

Figure 27b. Triple product in tunnel coordinates. Symbols denote the measurement stations.

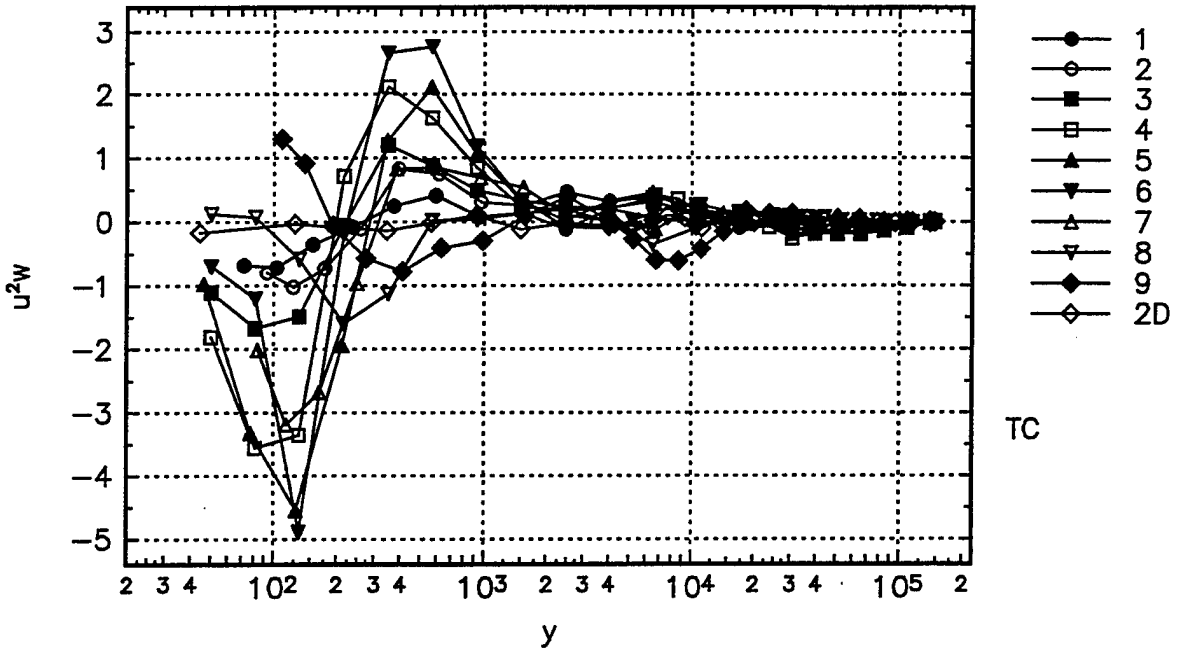

Figure 28a. Dimensional triple product in tunnel coordinates. Symbols denote the measurement stations.

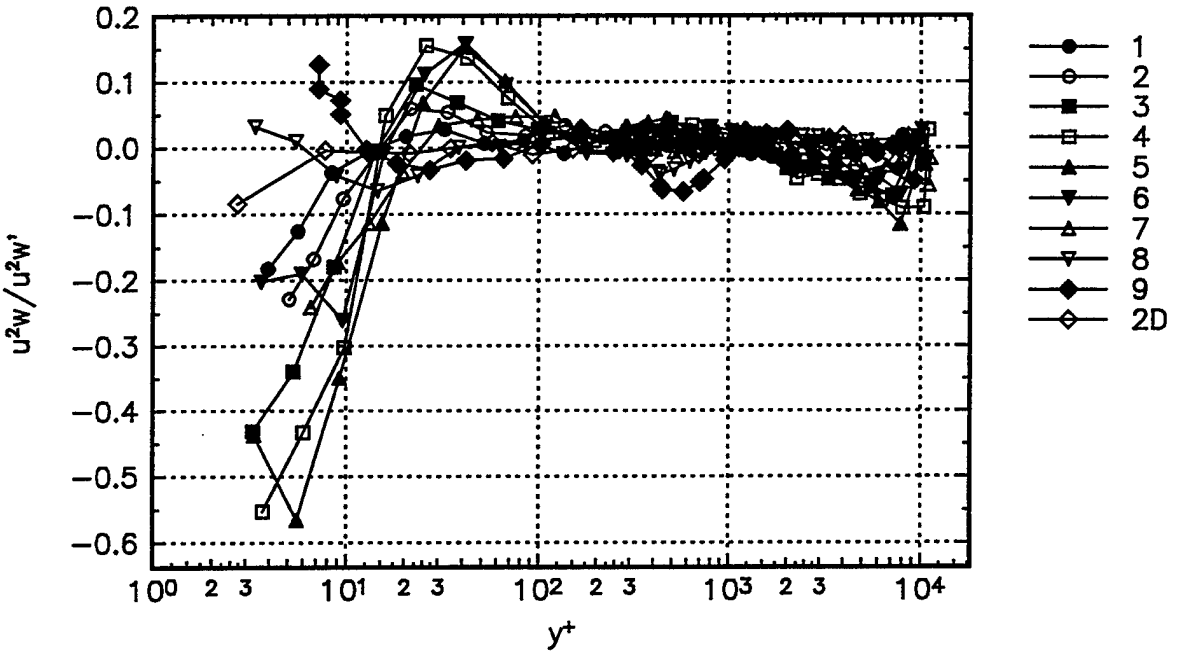

Figure 28b. Triple product in tunnel coordinates. Symbols denote the measurement stations.

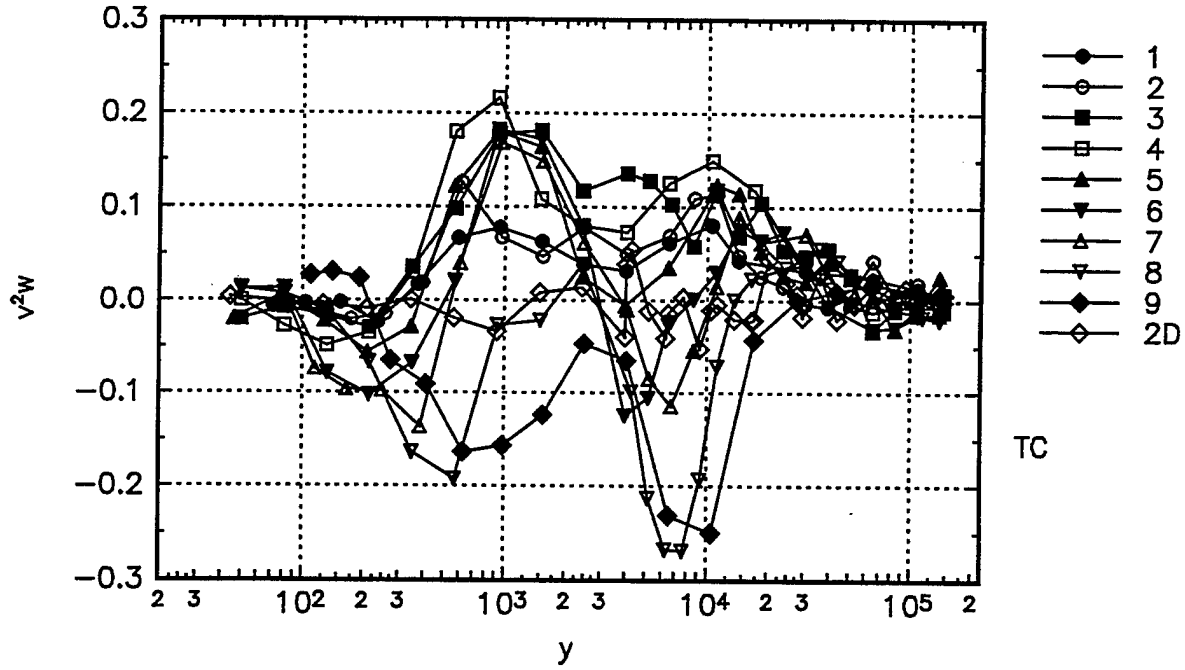

Figure 29a. Dimensional triple product in tunnel coordinates. Symbols denote the measurement stations.

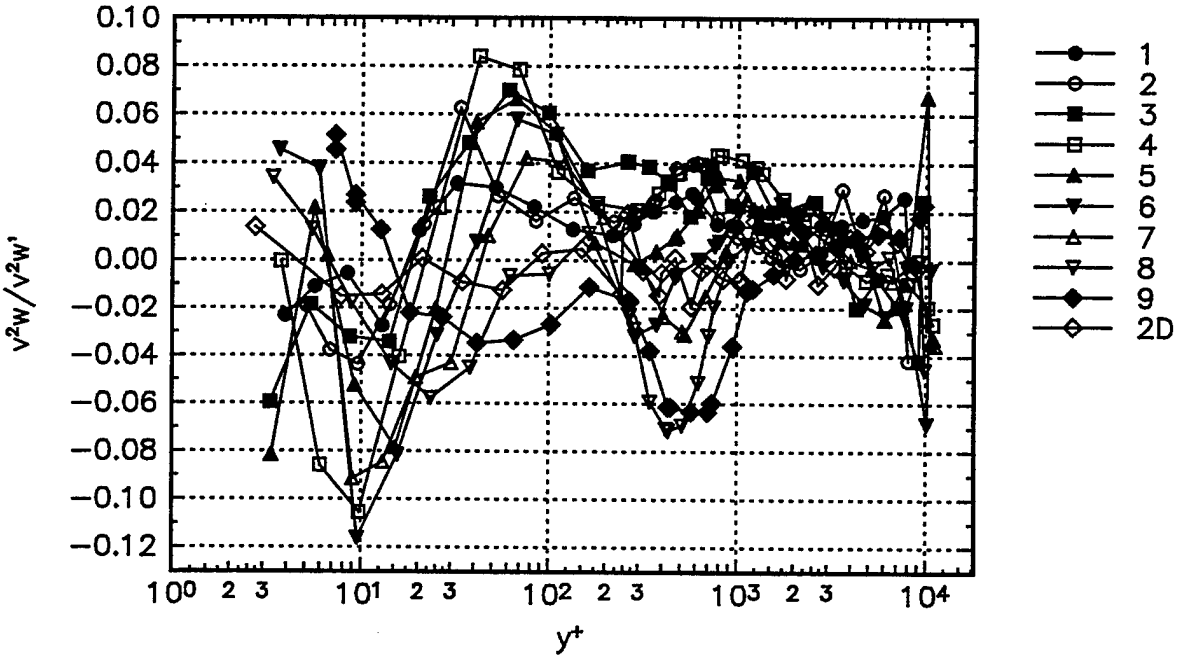

Figure 29b. Triple product in tunnel coordinates. Symbols denote the measurement stations.

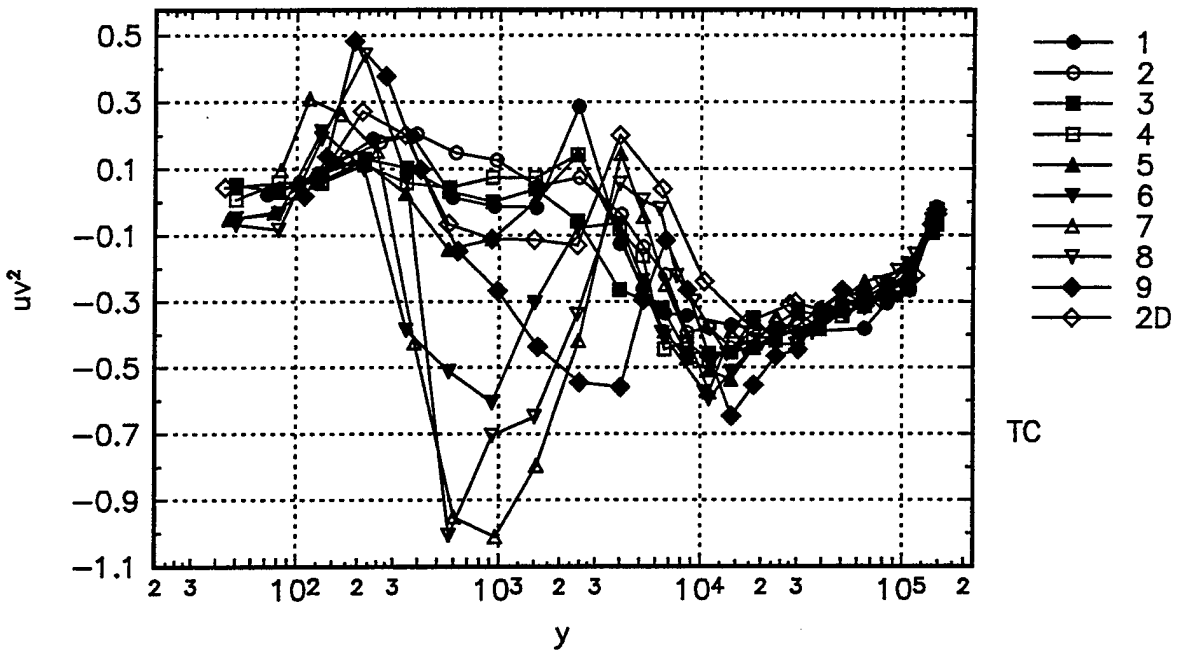

Figure 30a. Dimensional triple product in tunnel coordinates. Symbols denote the measurement stations.

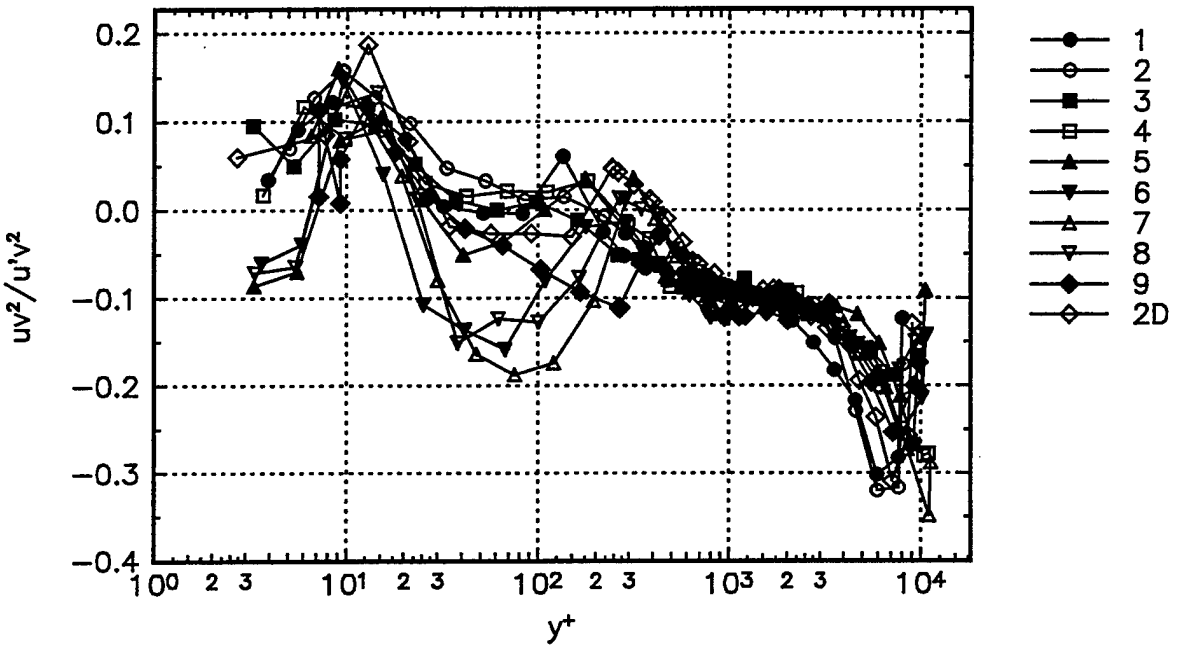

Figure 30b. Triple product in tunnel coordinates. Symbols denote the measurement stations.

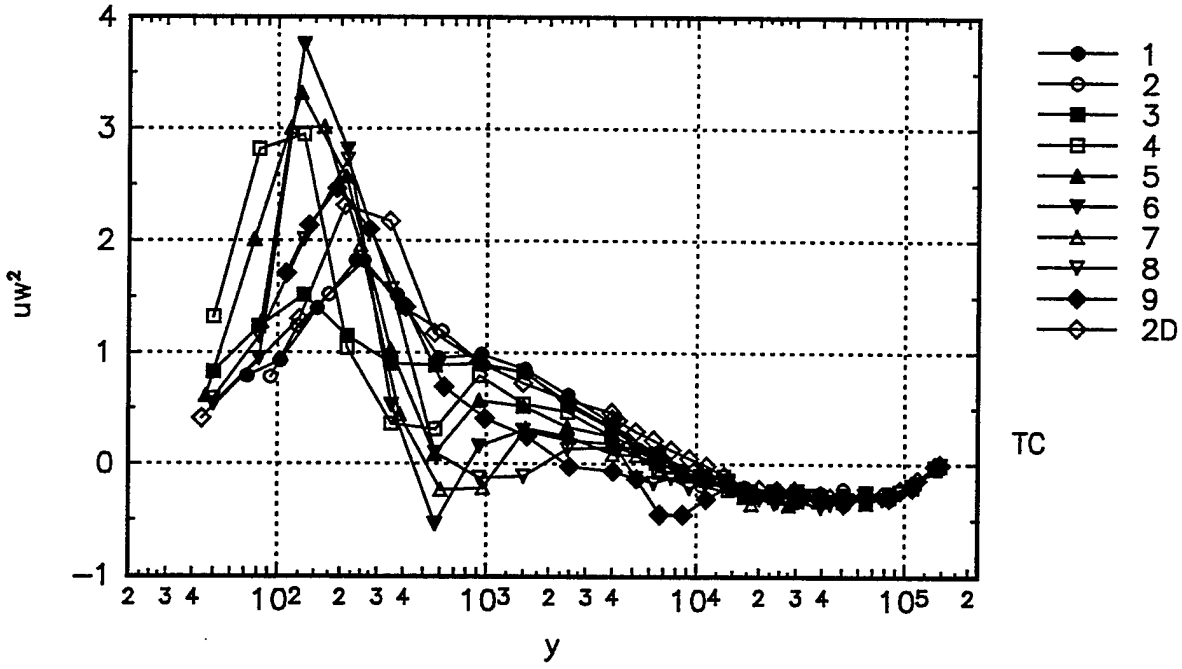

Figure 31a. Dimensional triple product in tunnel coordinates. Symbols denote the measurement stations.

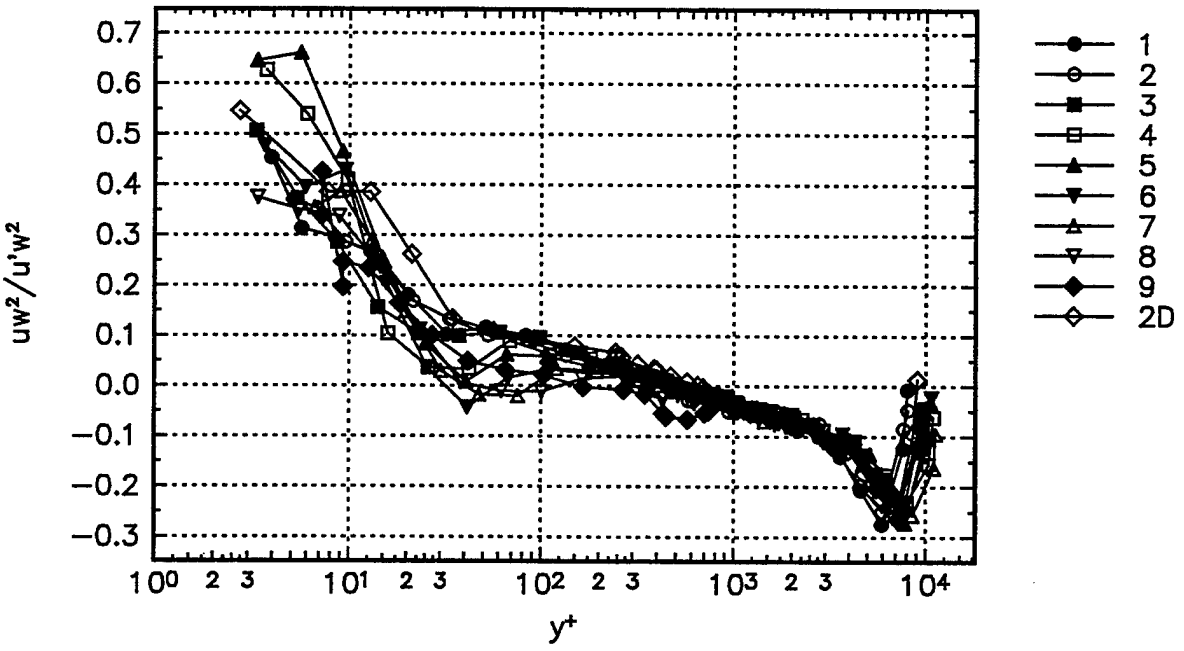

Figure 31b. Triple product in tunnel coordinates. Symbols denote the measurement stations.

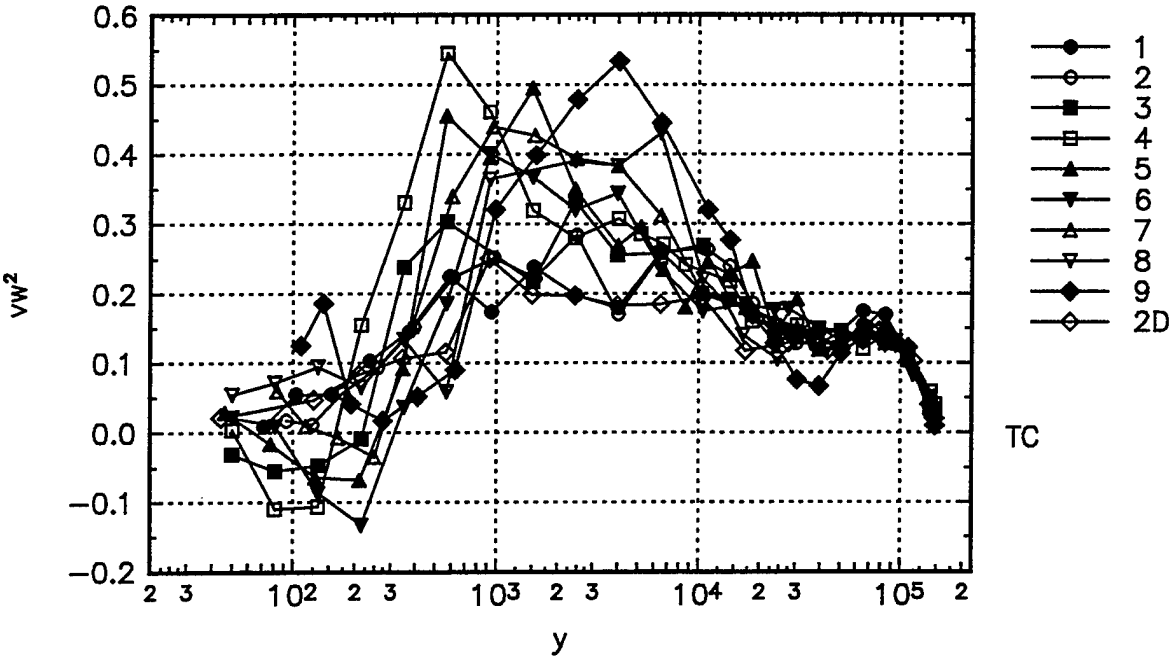

Figure 32a. Dimensional triple product in tunnel coordinates. Symbols denote the measurement stations.

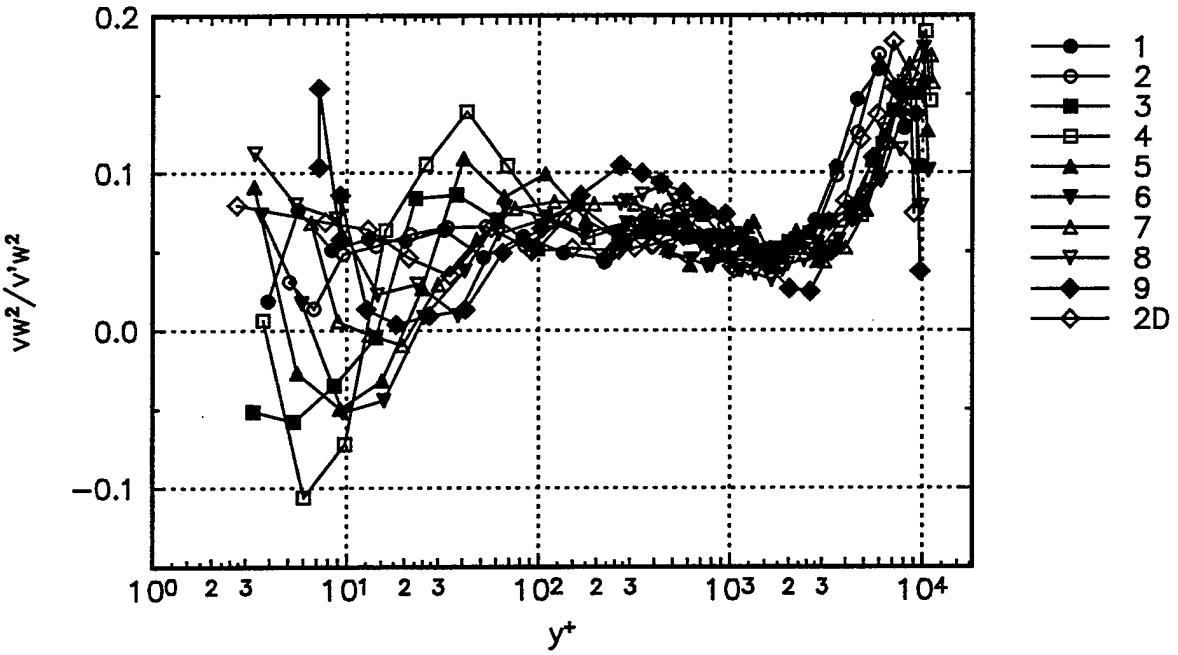

Figure 32b. Triple product in tunnel coordinates. Symbols denote the measurement stations.

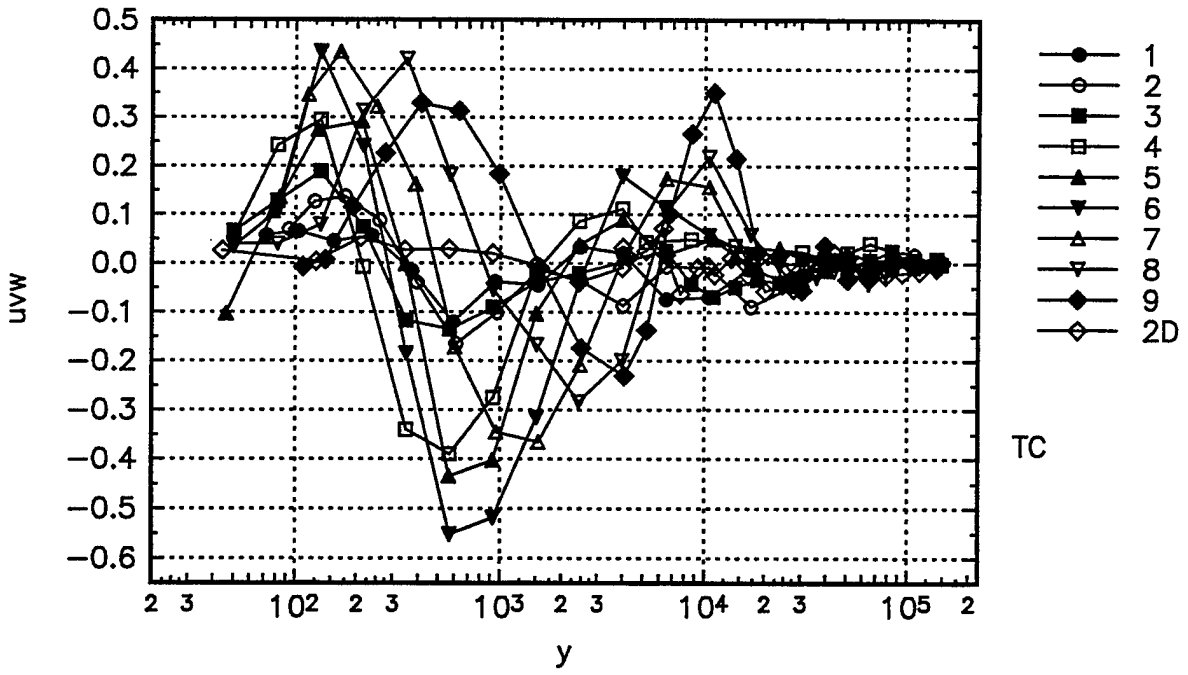

Figure 33a. Dimensional triple product in tunnel coordinates. Symbols denote the measurement stations.

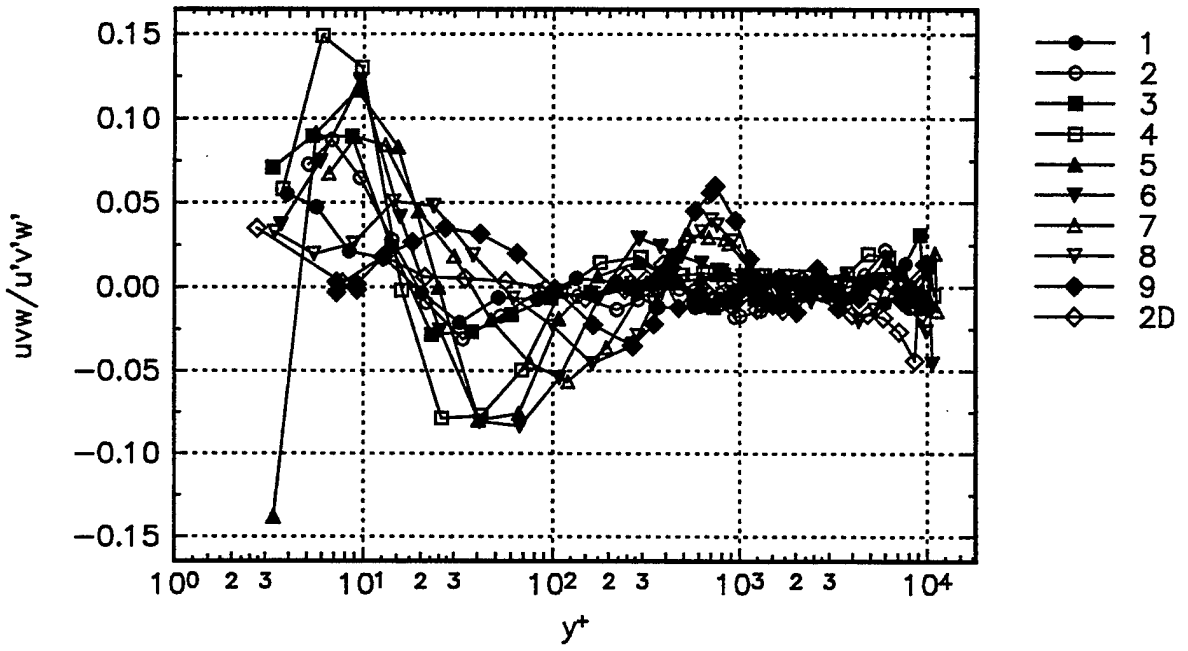

Figure 33b. Triple product in tunnel coordinates. Symbols denote the measurement stations.

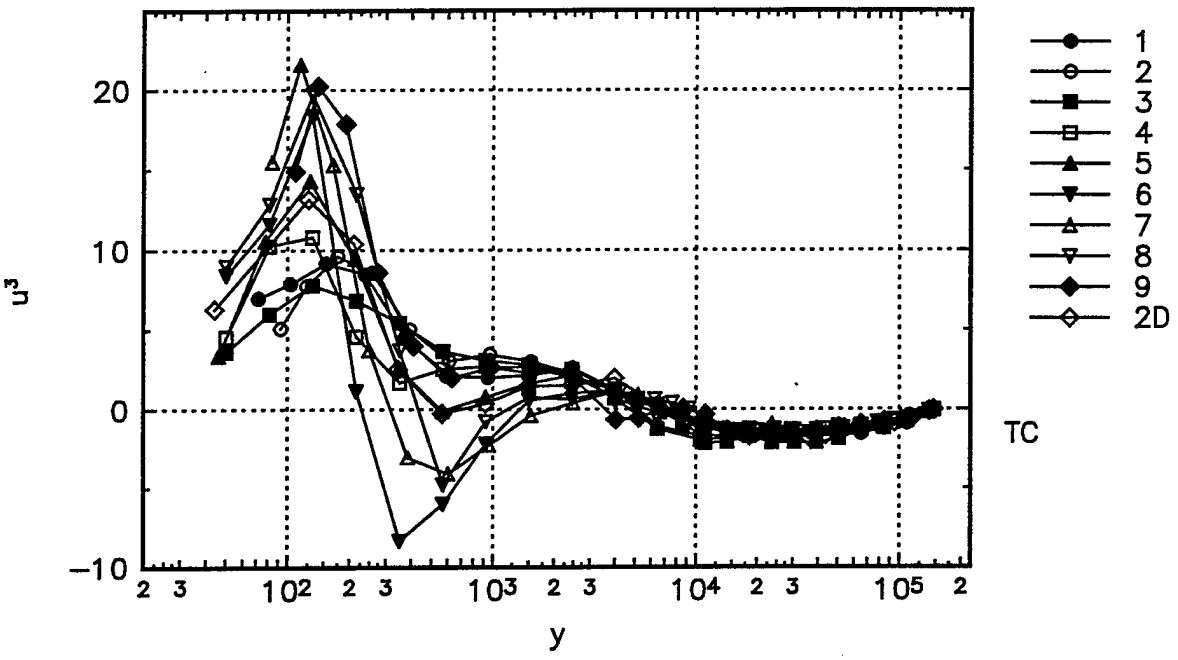

Figure 34a. Dimensional triple product in tunnel coordinates. Symbols denote the measurement stations.

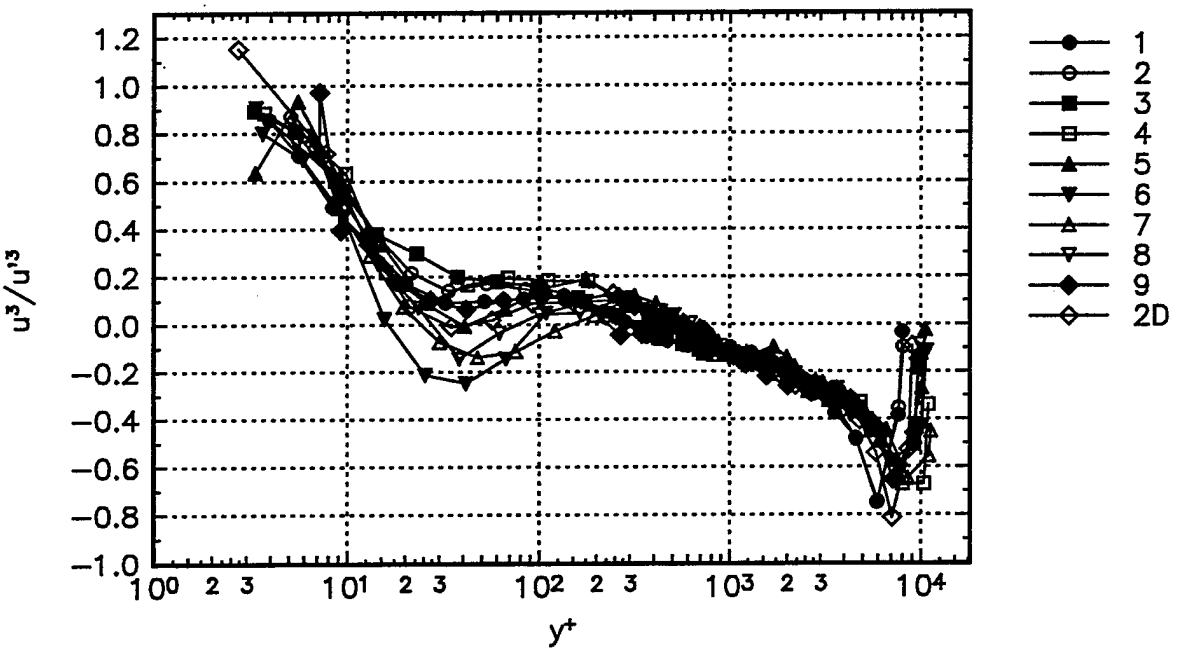

Figure 34b. Triple product in tunnel coordinates. Symbols denote the measurement stations.

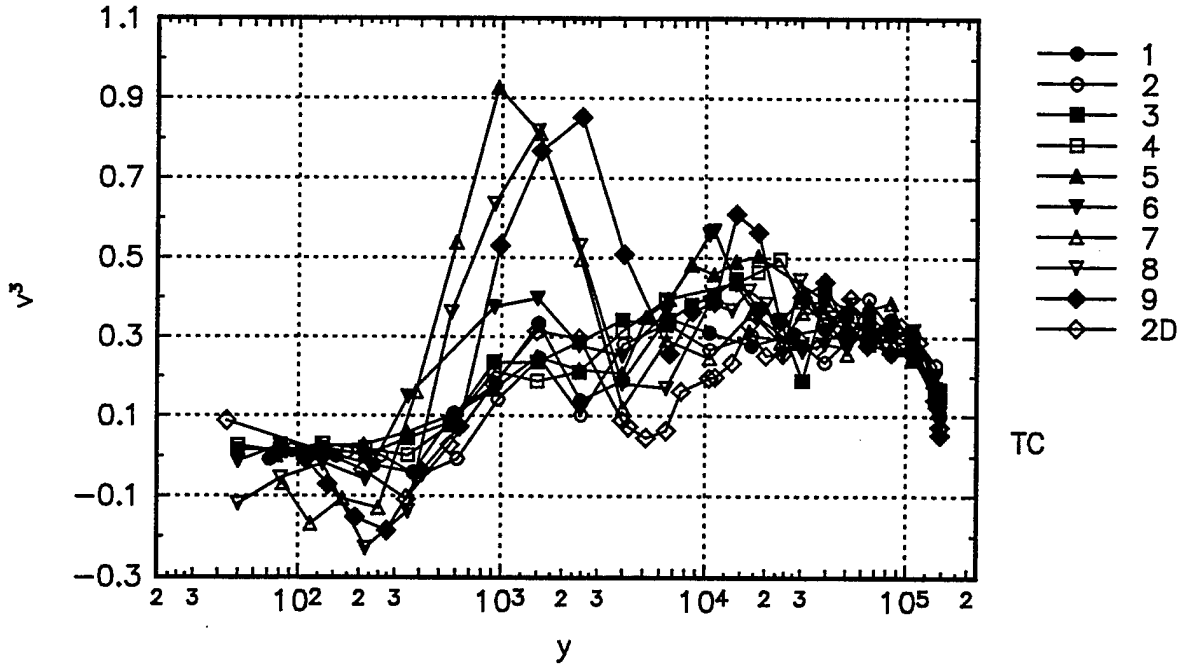

Figure 35a. Dimensional triple product in tunnel coordinates. Symbols denote the measurement stations.

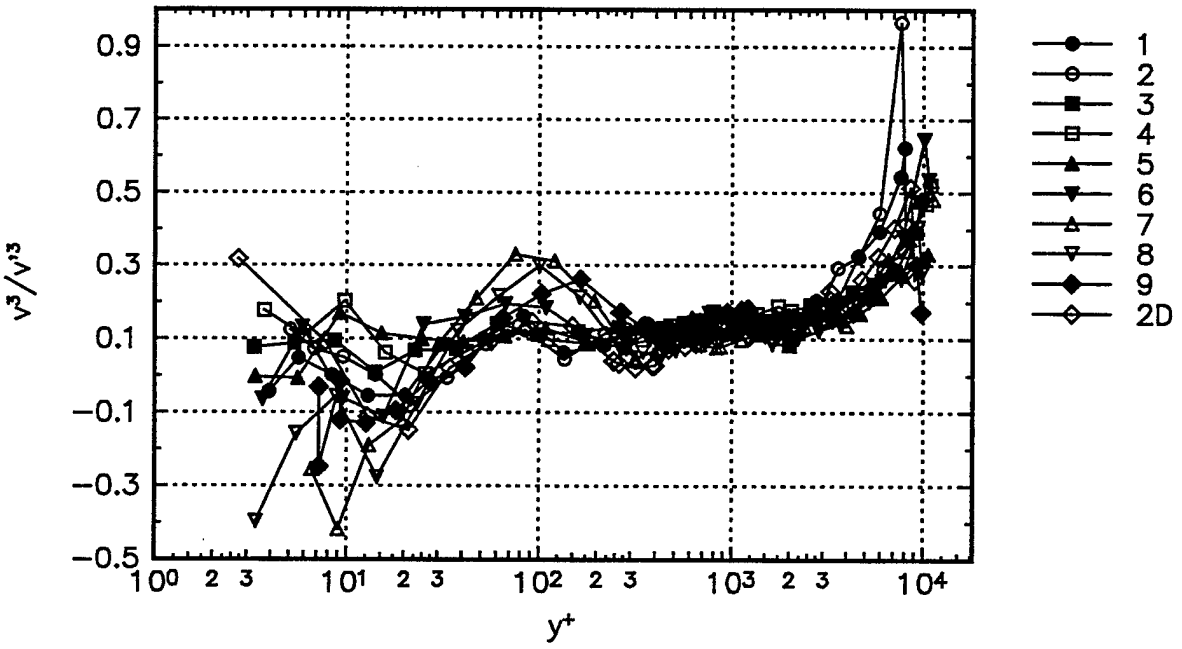

Figure 35b. Triple product in tunnel coordinates. Symbols denote the measurement stations.

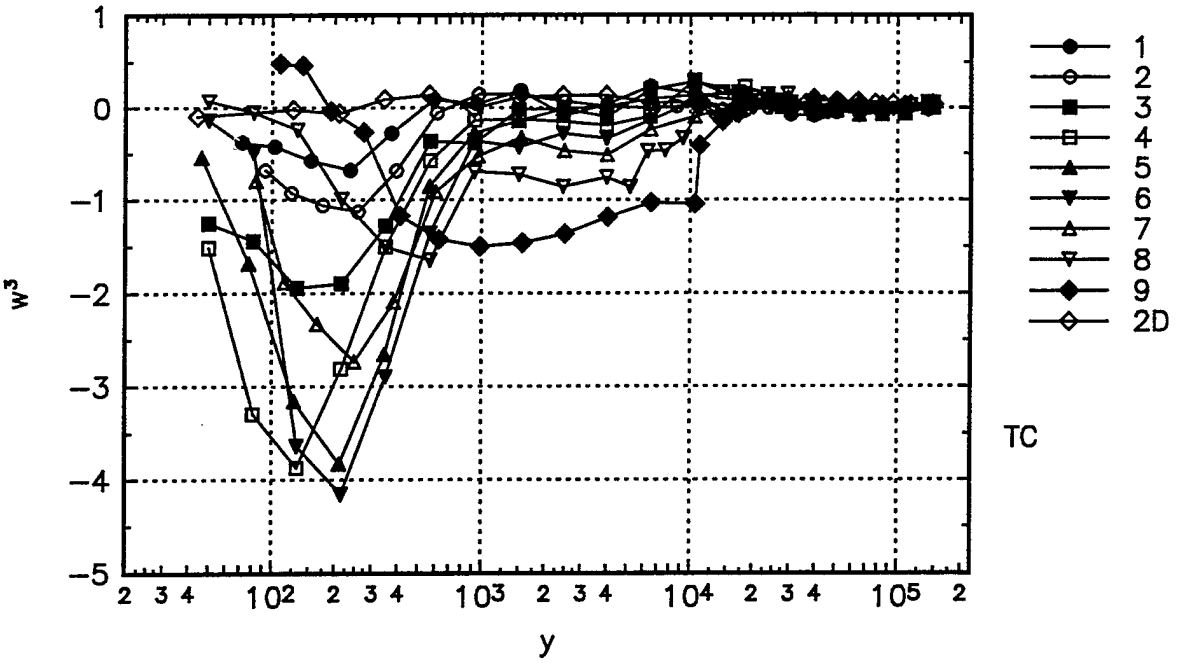

Figure 36a. Dimensional triple product in tunnel coordinates. Symbols denote the measurement stations.

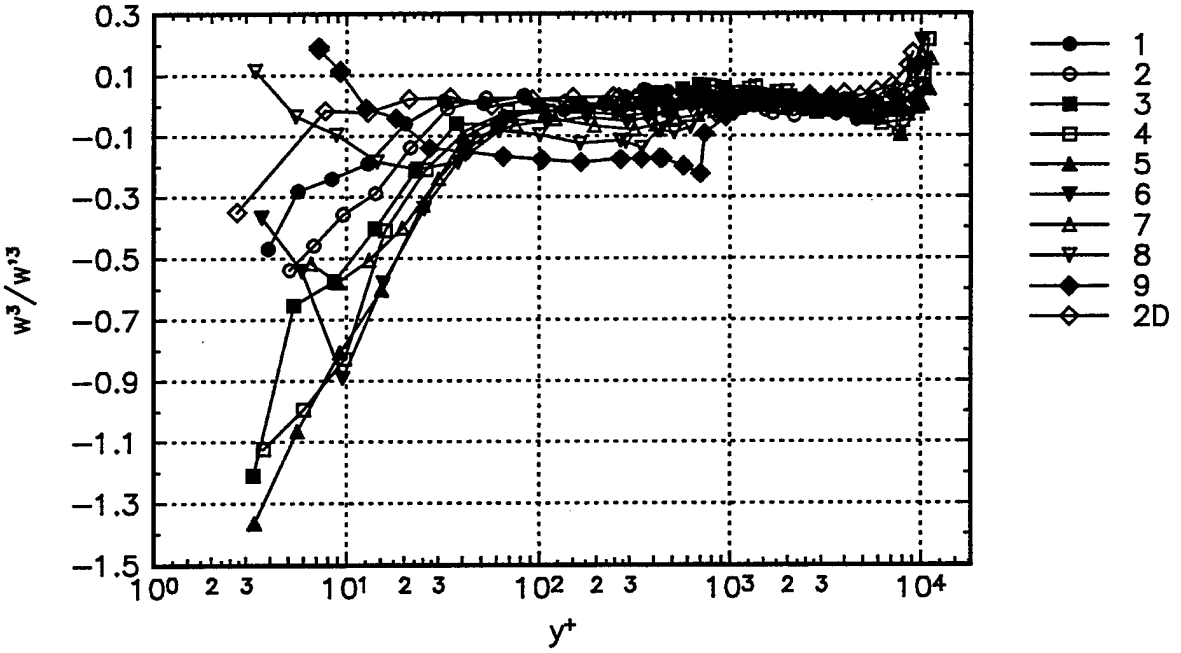

Figure 36b. Triple product in tunnel coordinates. Symbols denote the measurement stations.

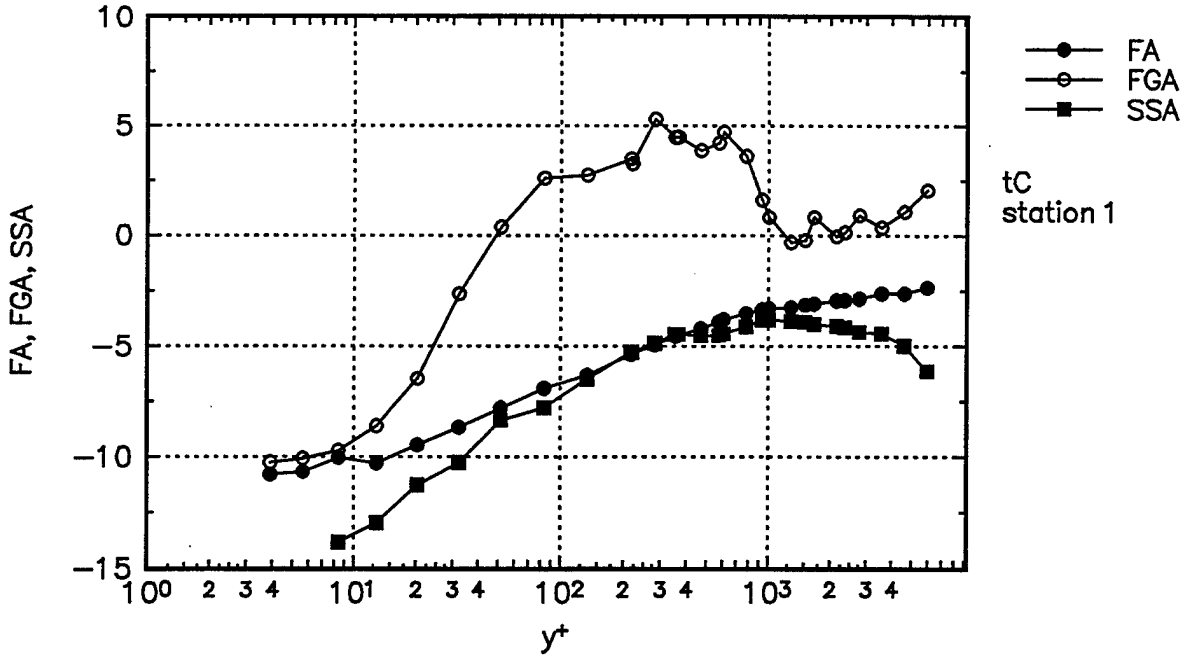

Figure 37. Flow angle, flow-gradient angle, and shear-stress angle calculated at Station 1.

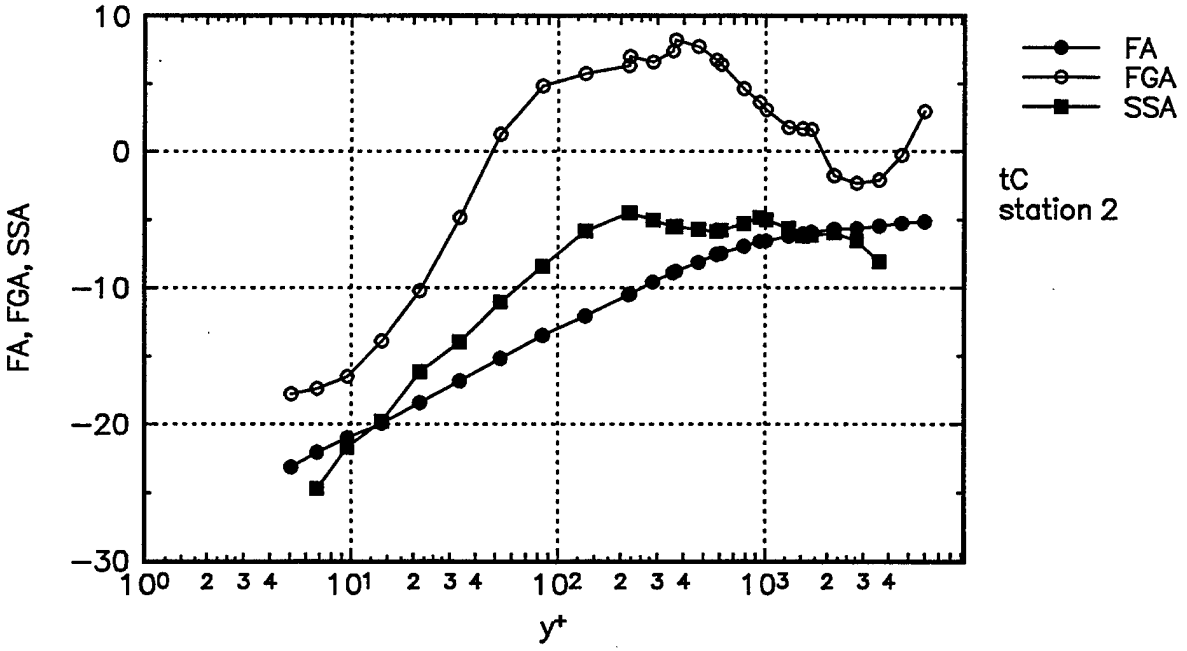

Figure 38. Flow angle, flow-gradient angle, and shear-stress angle calculated at Station 2.

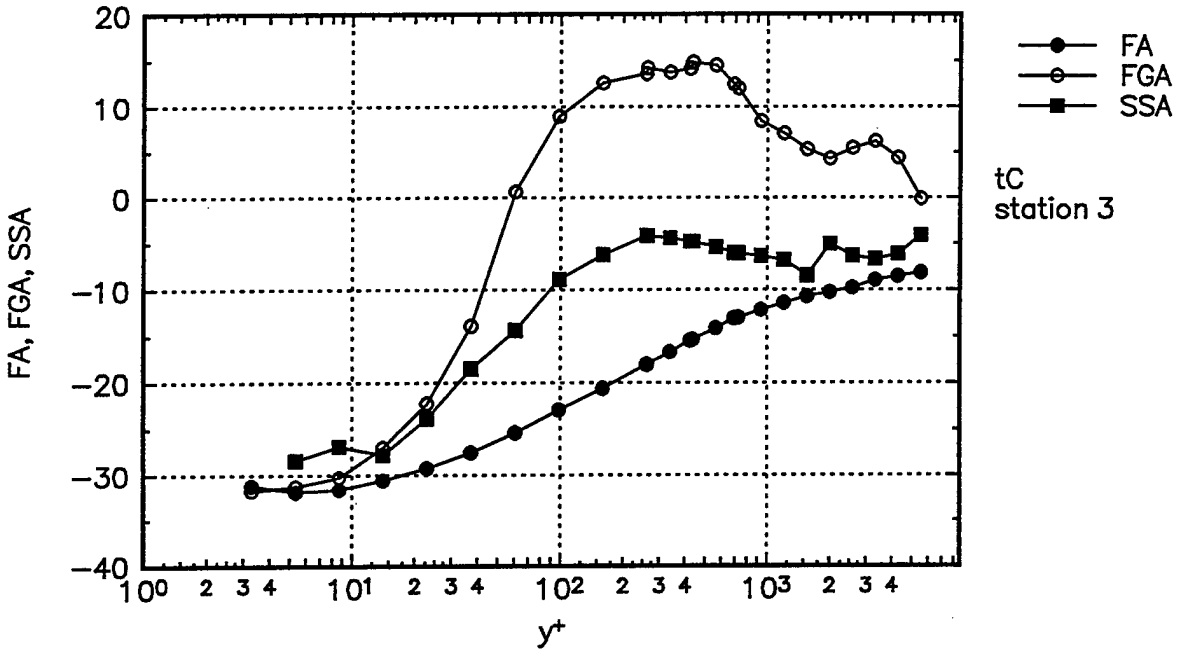

Figure 39. Flow angle, flow-gradient angle, and shear-stress angle calculated at Station 3.

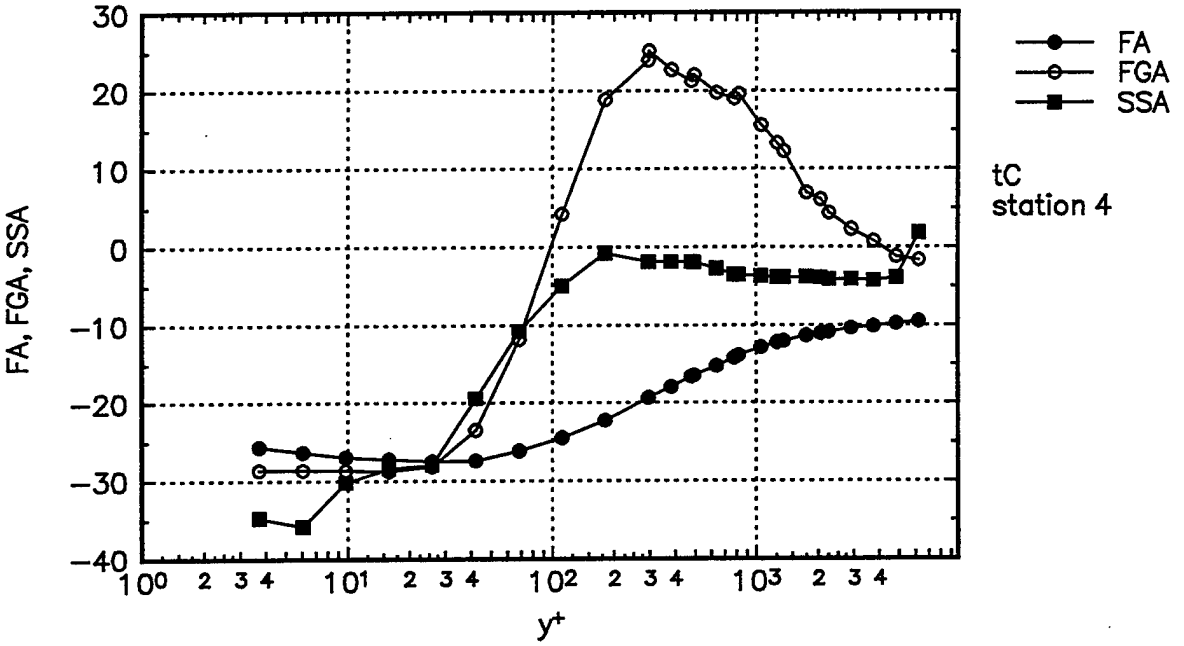

Figure 40. Flow angle, flow-gradient angle, and shear-stress angle calculated at Station 4.

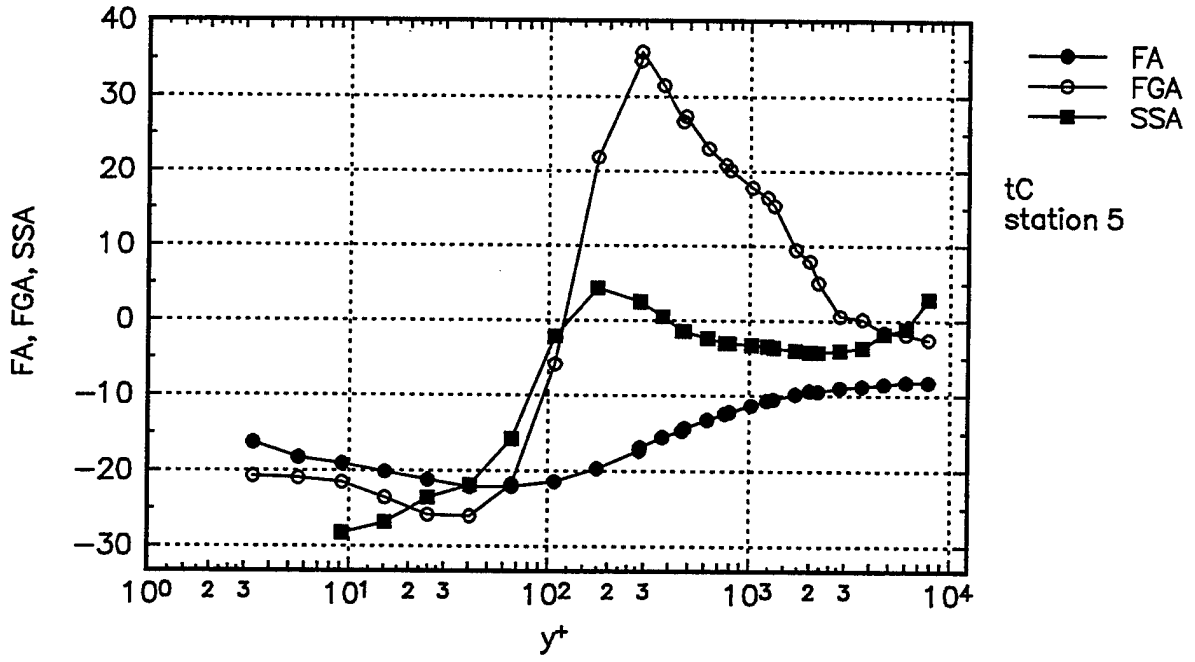

Figure 41. Flow angle, flow-gradient angle, and shear-stress angle calculated at Station 5.

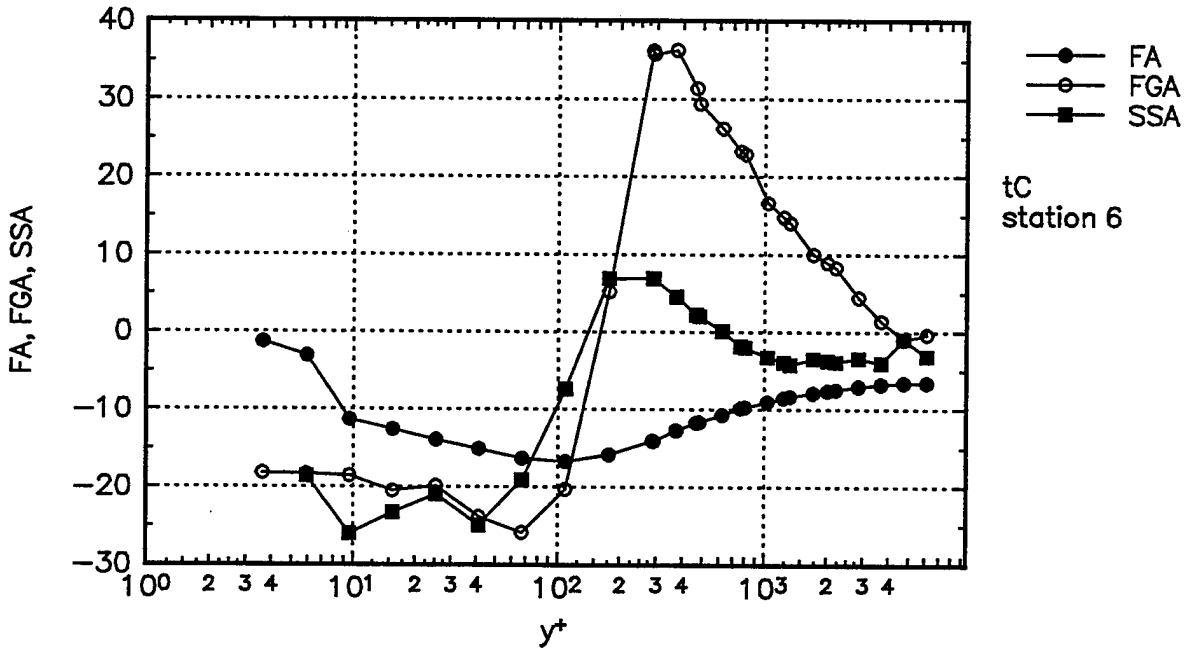

Figure 42. Flow angle, flow-gradient angle, and shear-stress angle calculated at Station 6.

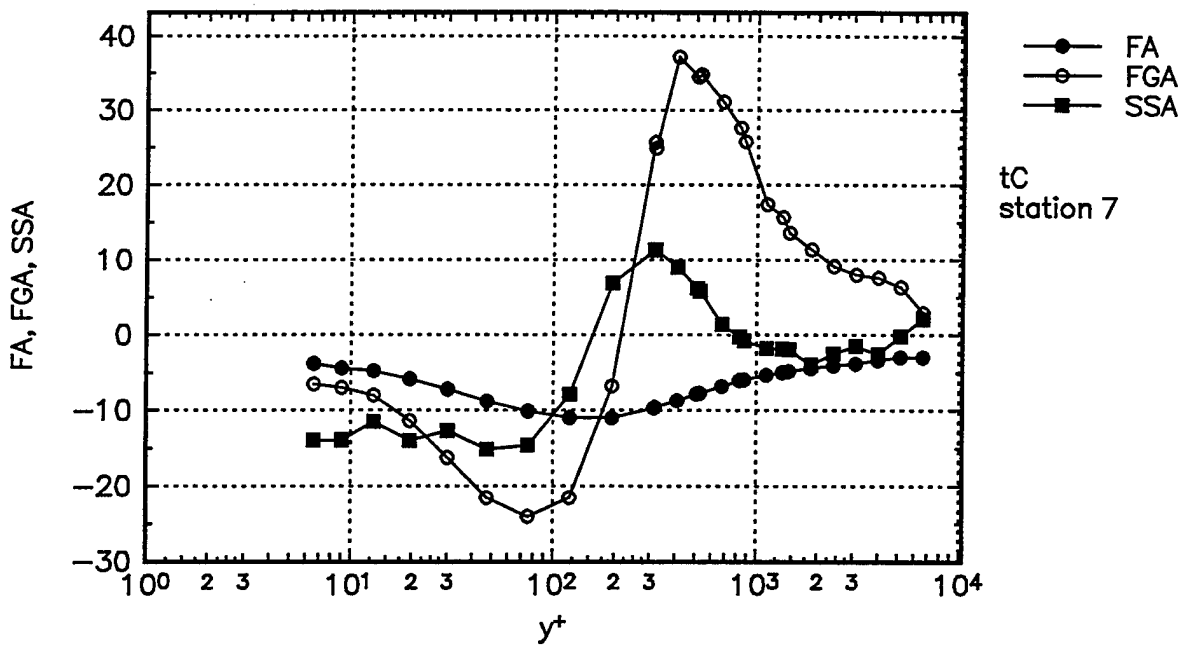

Figure 43. Flow angle, flow-gradient angle, and shear-stress angle calculated at Station 7.

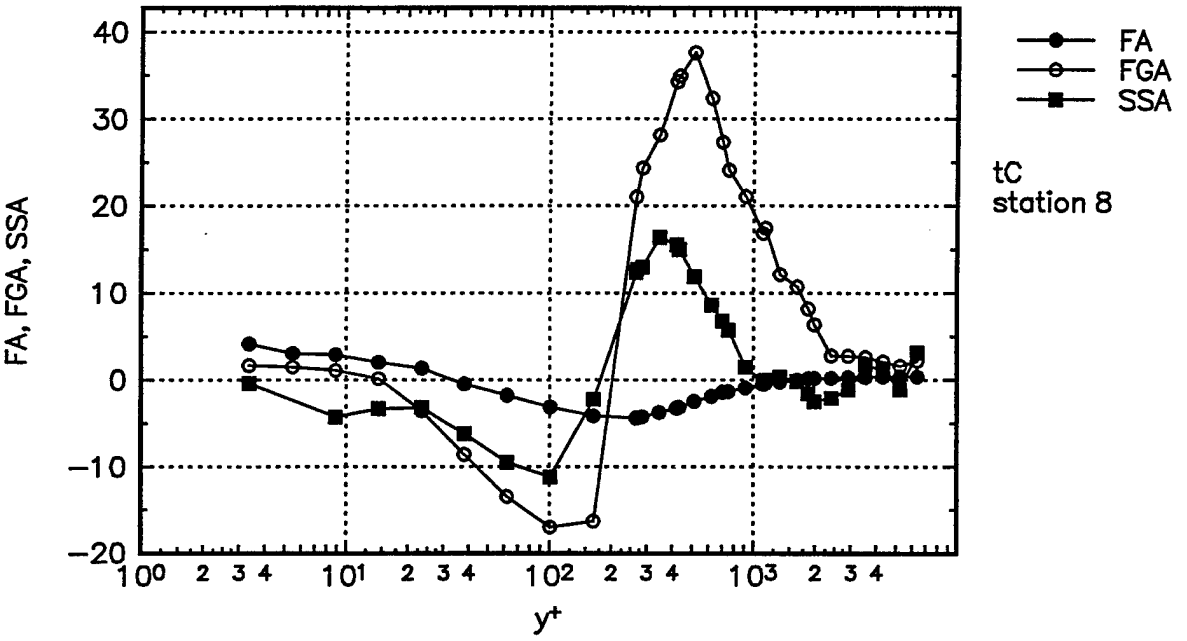

Figure 44. Flow angle, flow-gradient angle, and shear-stress angle calculated at Station 8.

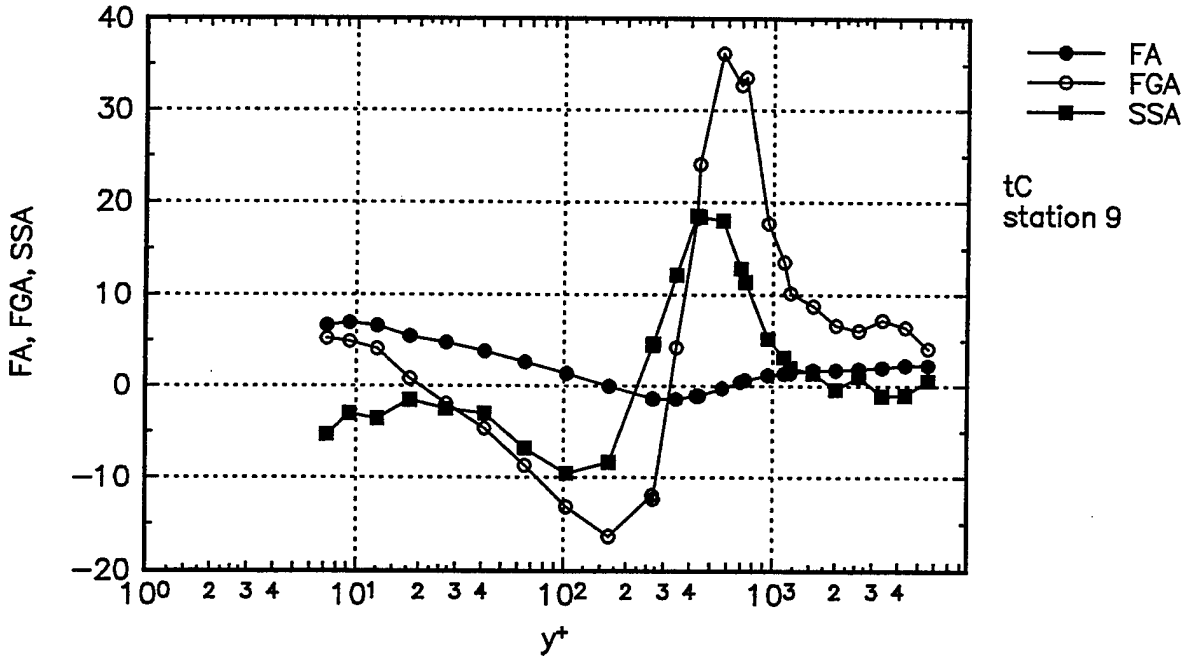

Figure 45. Flow angle, flow-gradient angle, and shear-stress angle calculated at Station 9.

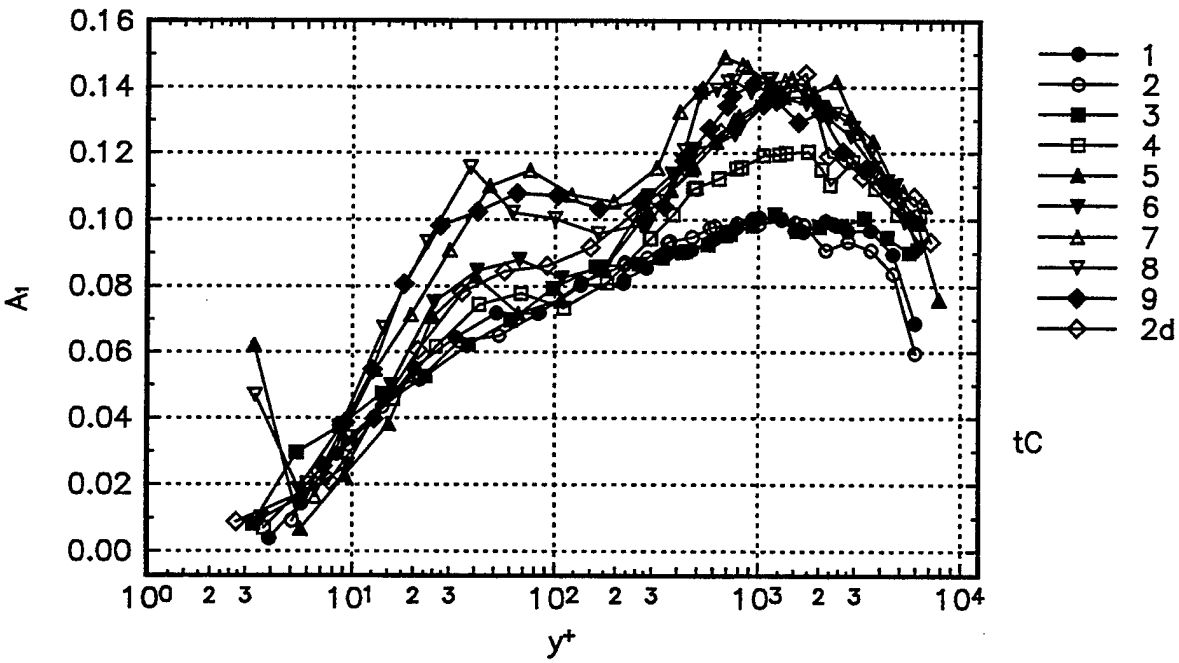

Figure 46. Townsend's A1 parameter for high Re flow.

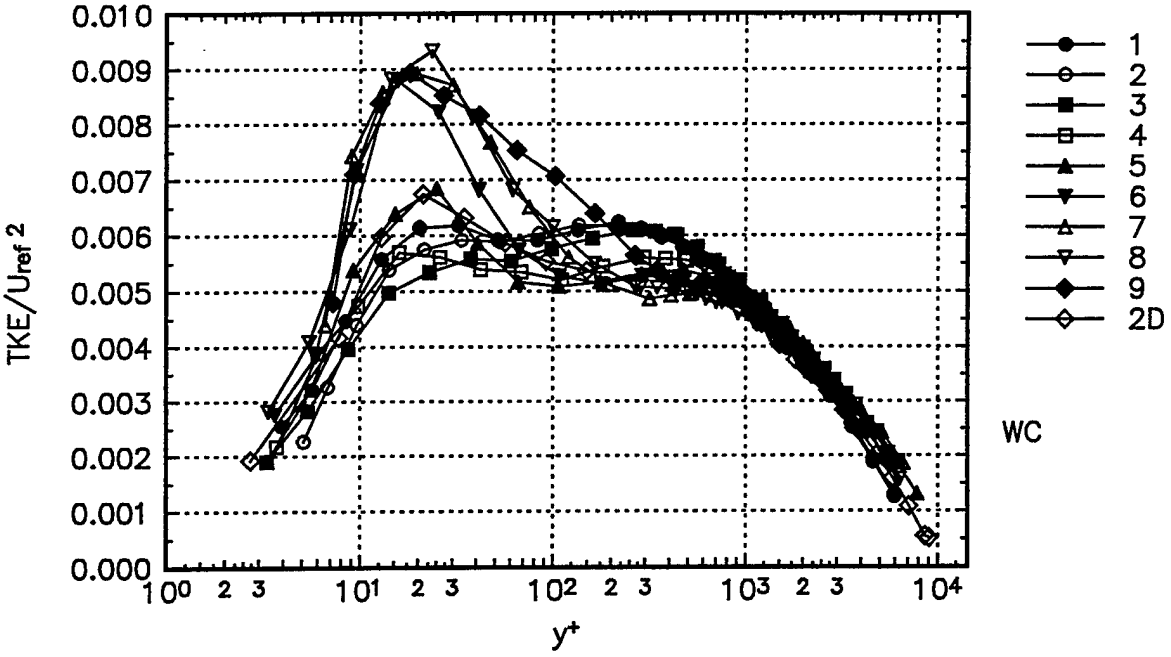

Figure 47. TKE distribution at different stations.

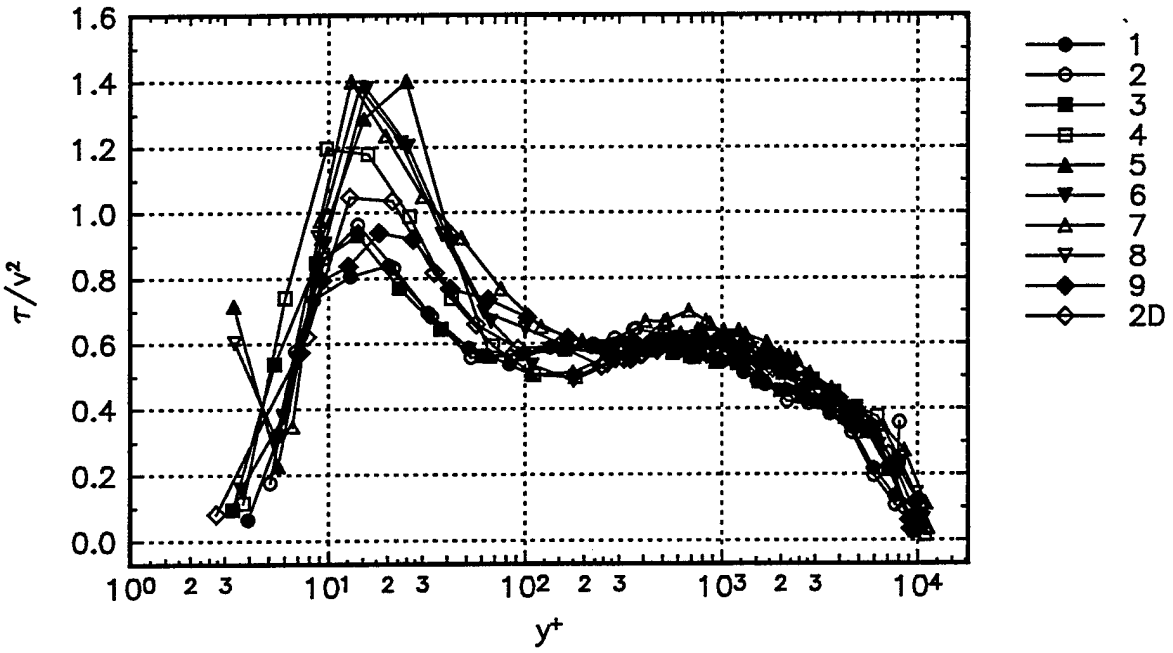

Figure 48a. $1/S=\tau/\overline{v^2}$ flow parameter.

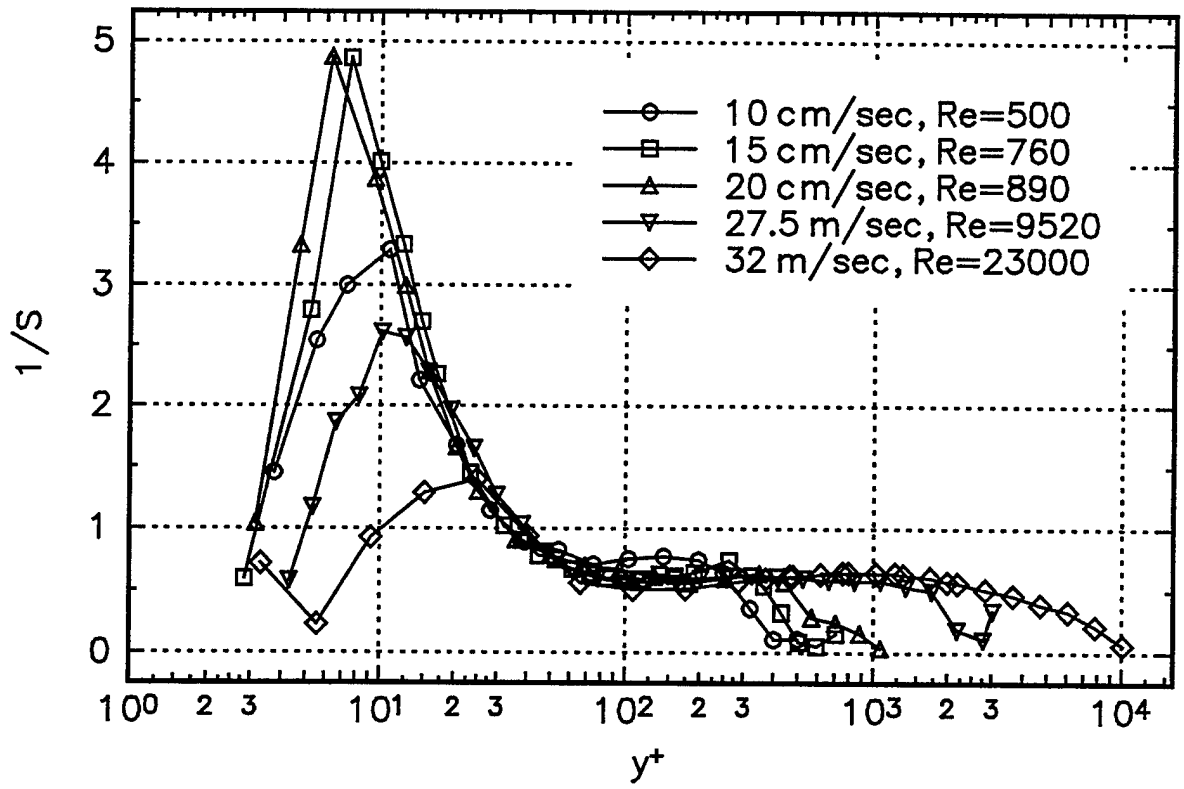

Figure 48b. $1/S=\tau/\overline{v^2}$ flow parameter calculated for different Reynolds number data obtained at Station 5.

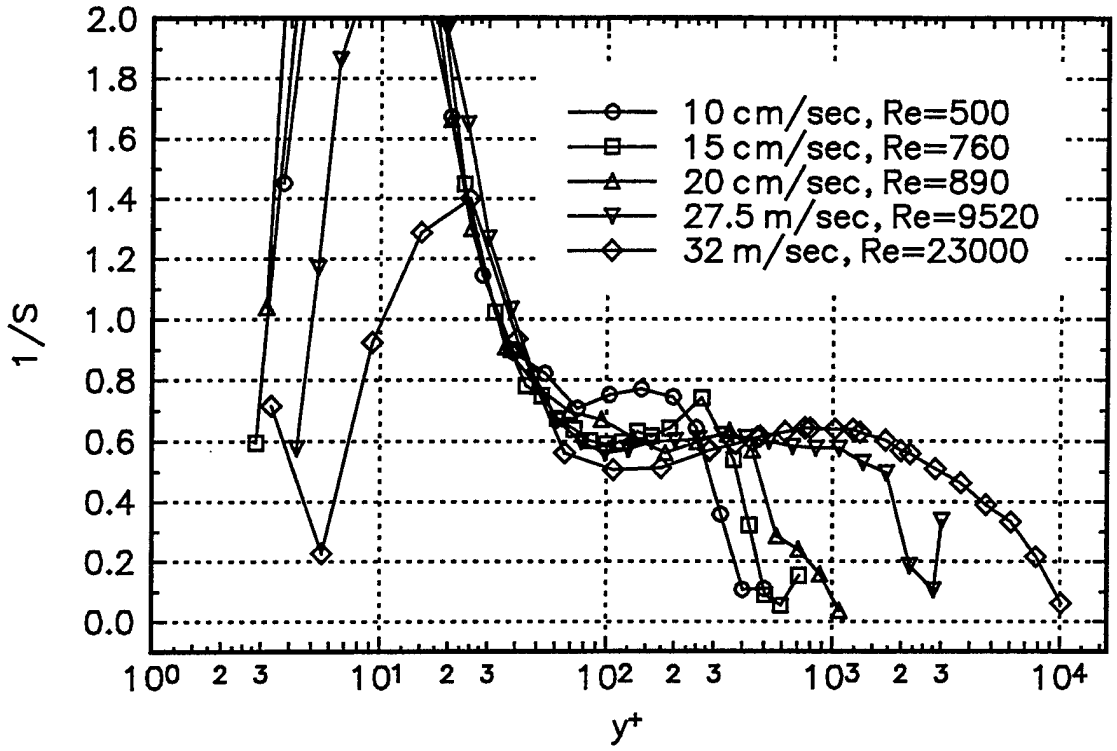

Figure 48c. $1/S=\tau/\overline{v^2}$ flow parameter calculated for different Reynolds number data obtained at Station 5.

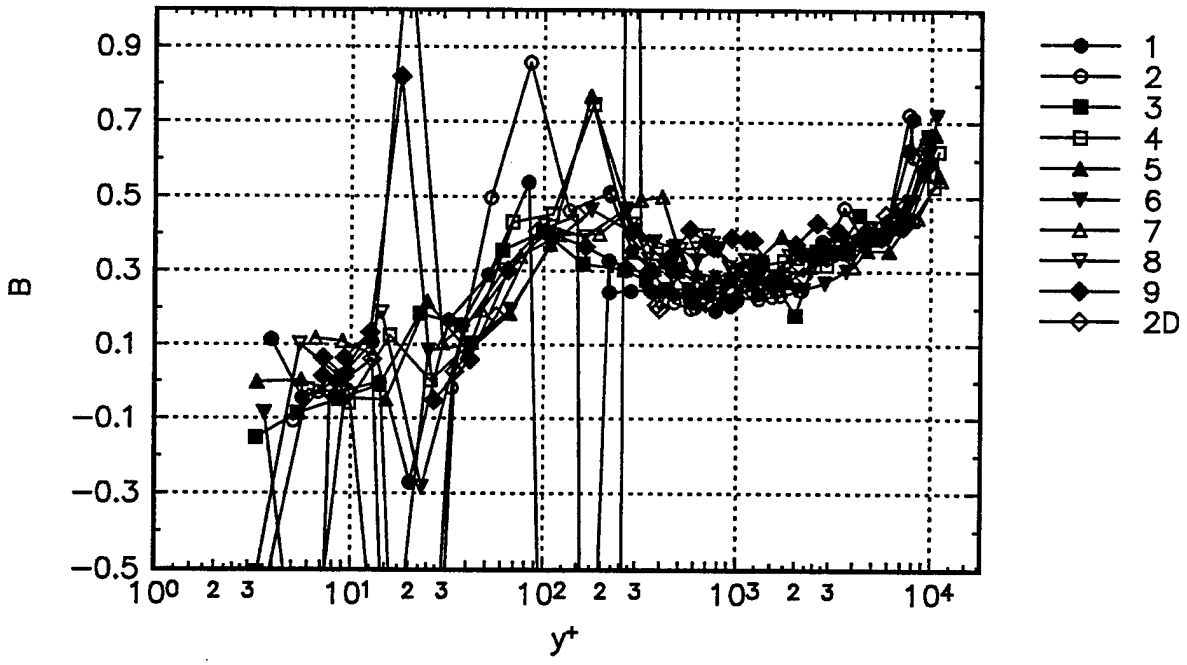

Figure 49a. $B=\overline{v^3}/(\overline{u^2v}+\overline{v^3}+\overline{vw^2})$ flow parameter.

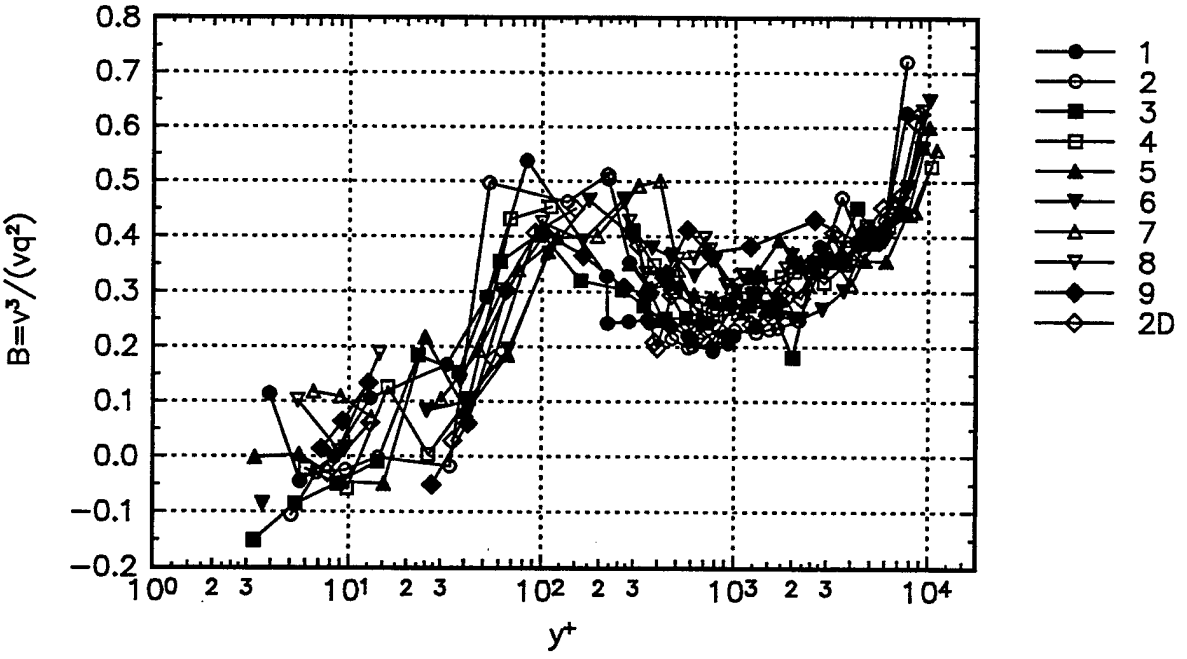

Figure 49b. $B=\overline{v^3}/(\overline{u^2v}+\overline{v^3}+\overline{vw^2})$ flow parameter.

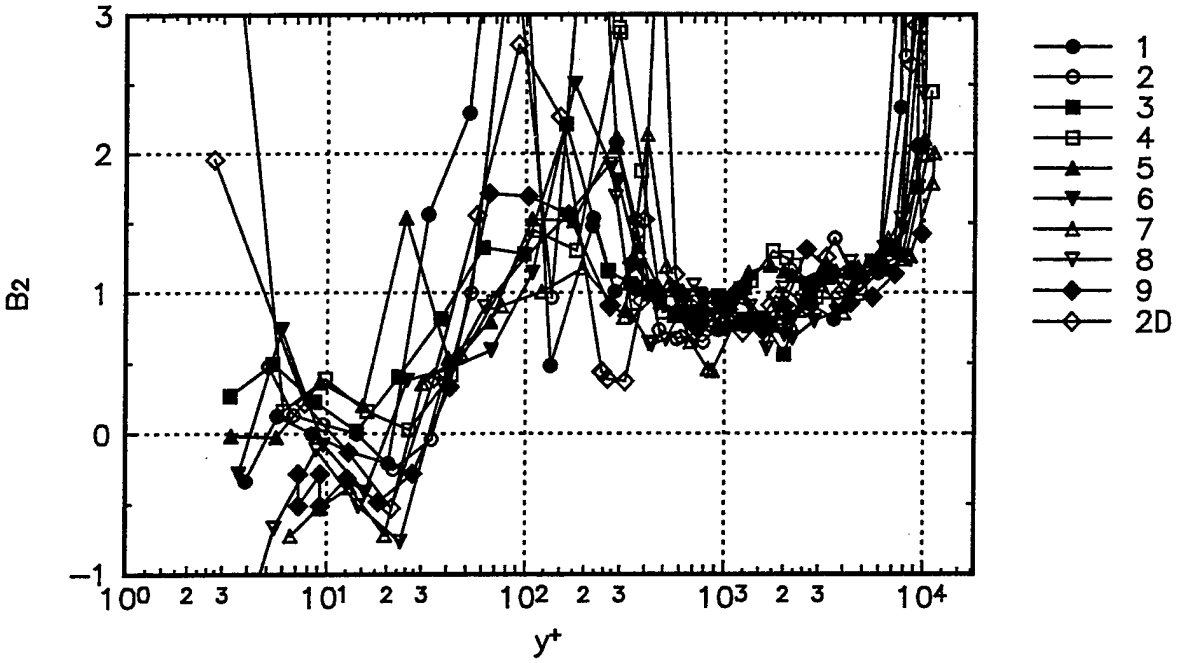

Figure 50a. $B_2 = \overline{v^3}/[(\overline{uv^2})^2 + (\overline{v^2 w})^2]$ flow parameter.

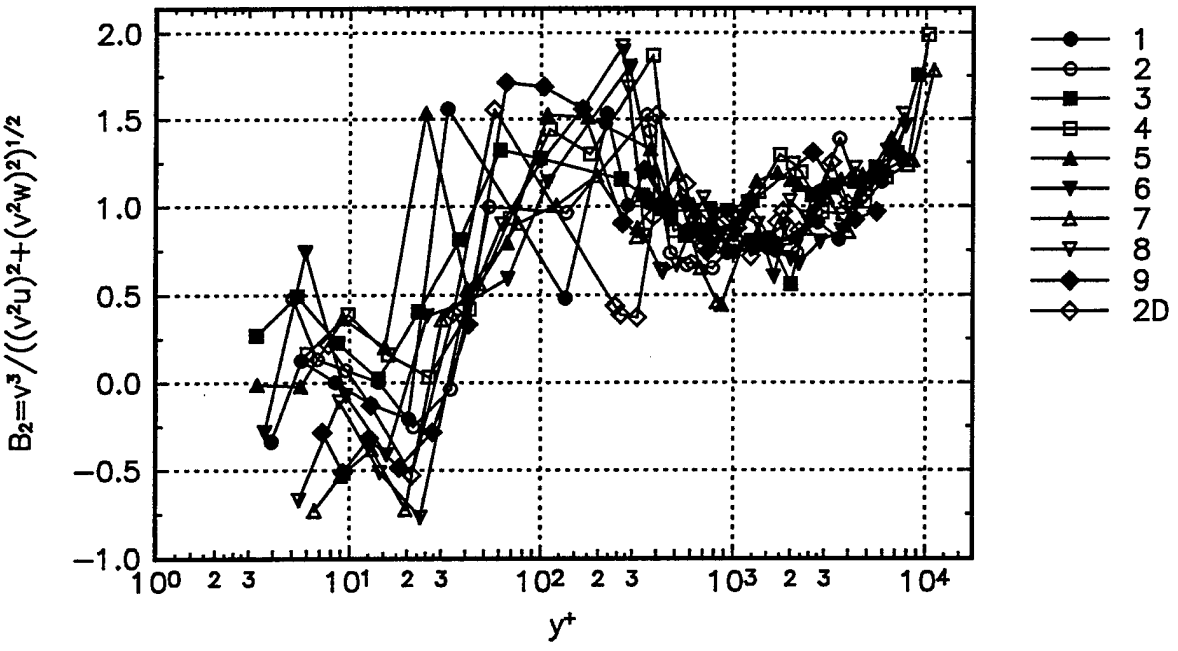

Figure 50b. $B_2 = \overline{v^3}/[(\overline{uv^2})^2 + (\overline{v^2 w})^2]$ flow parameter.

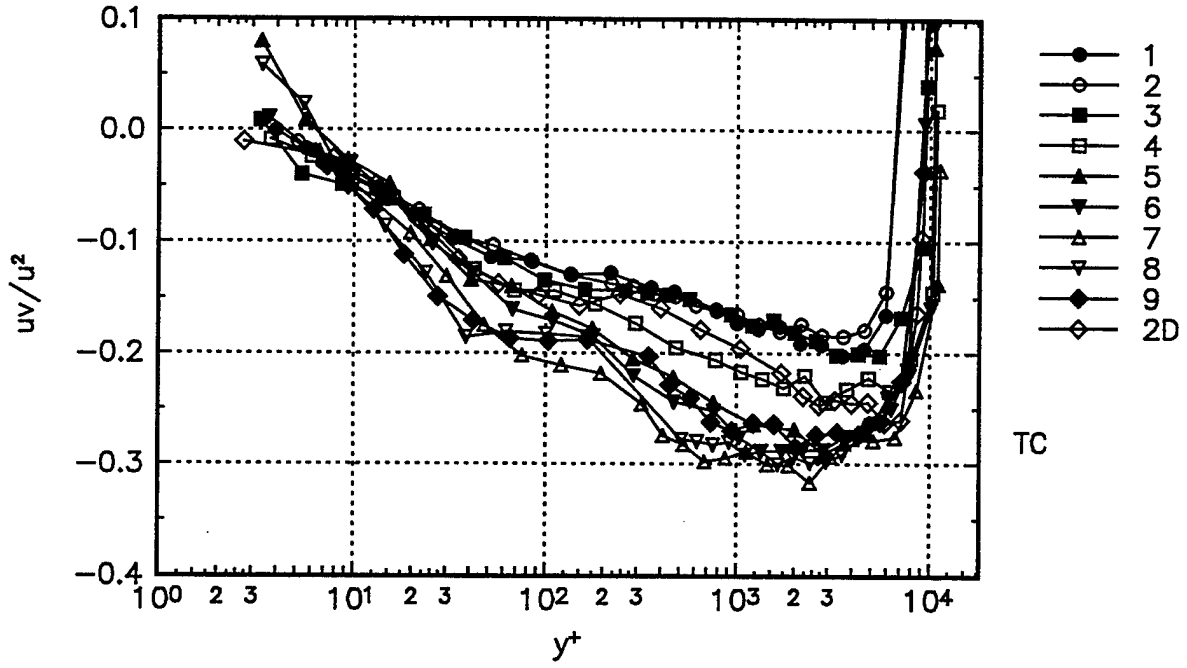

Figure 51. $\frac{\overline{uv}}{\overline{u^2}}$, shear stress to normal stress ratio.

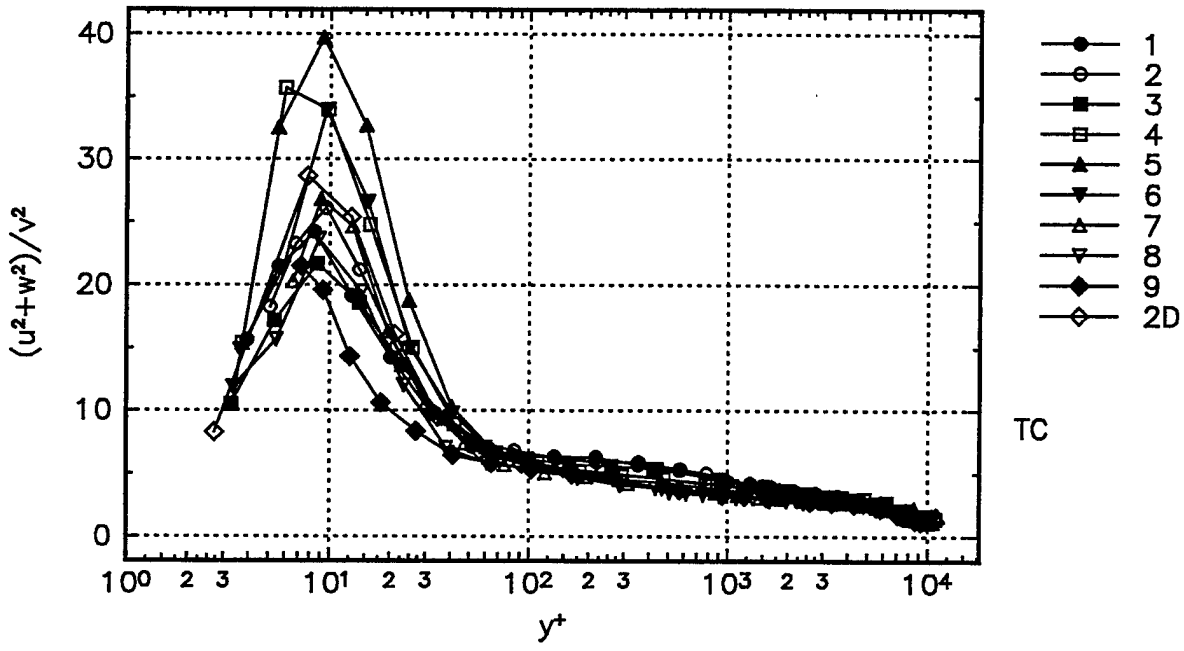

Figure 52a. $\frac{\overline{u^2}+\overline{w^2}}{\overline{v^2}}$, ratio of normal stresses.

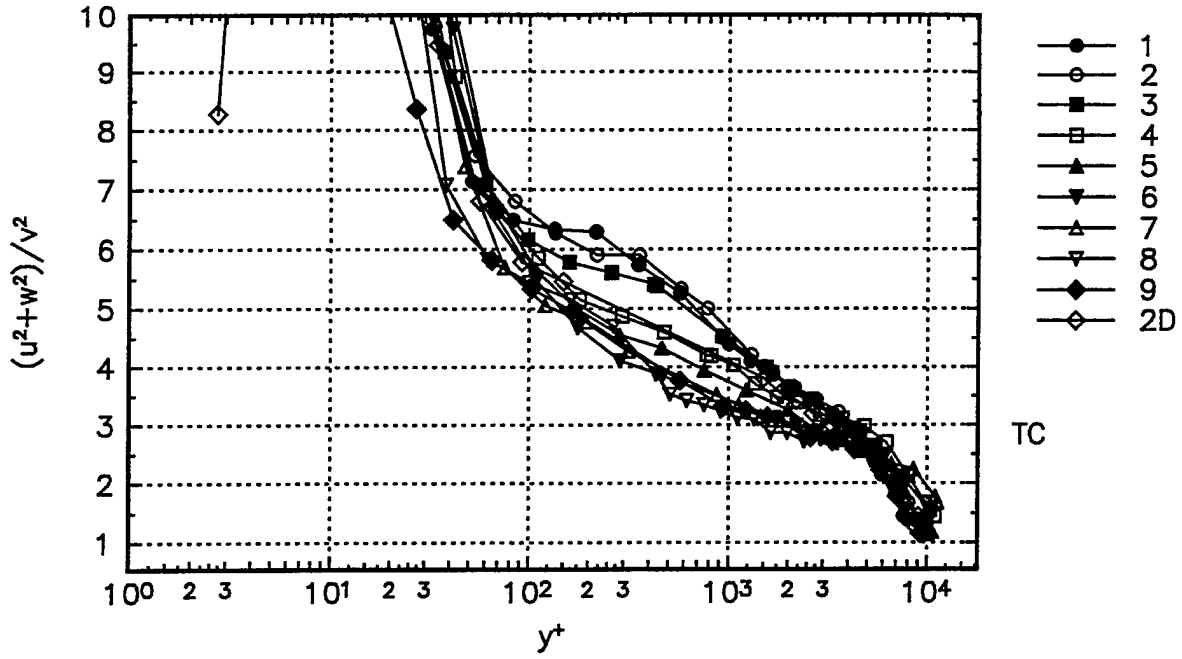

Figure 52b. $\frac{\overline{u^2}+\overline{w^2}}{\overline{v^2}}$, ratio of normal stresses.

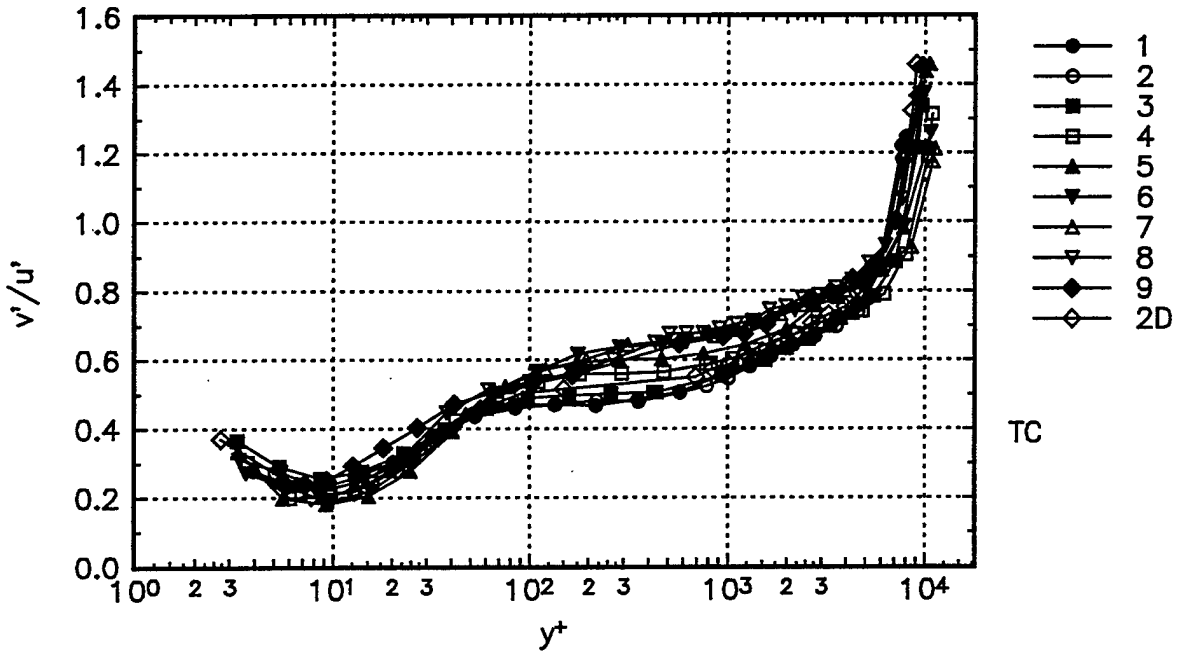

Figure 53. v'/u', ratio of the rms of the fluctuating velocities.

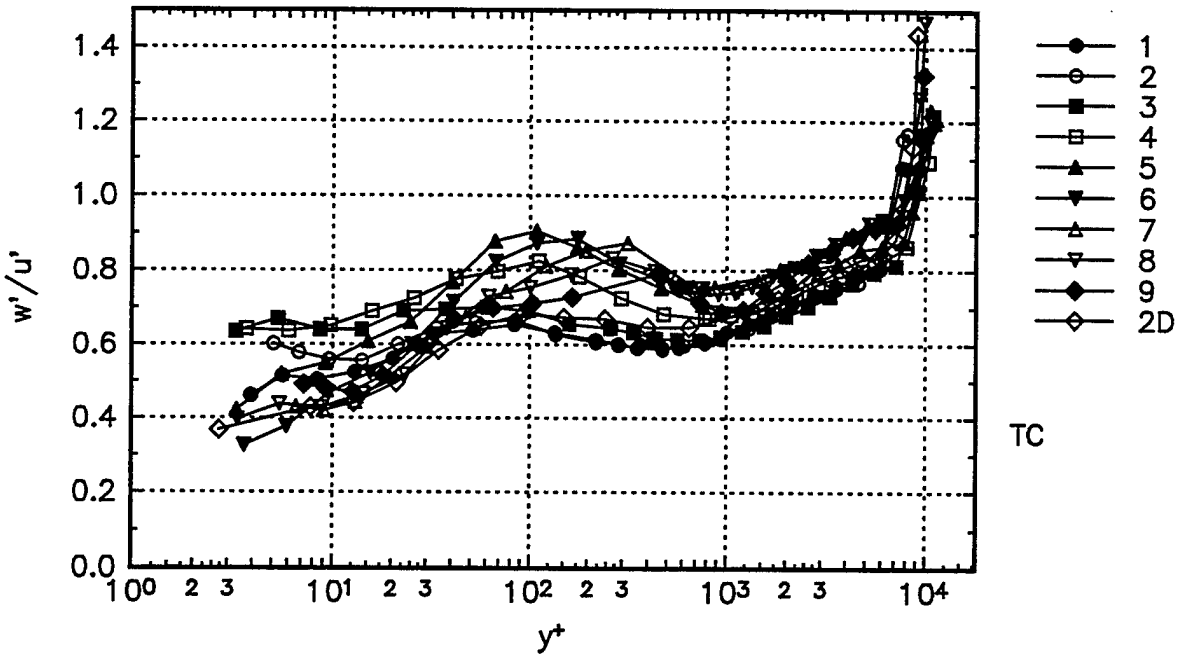

Figure 54. w'/u', ratio of the rms of the fluctuating velocities.

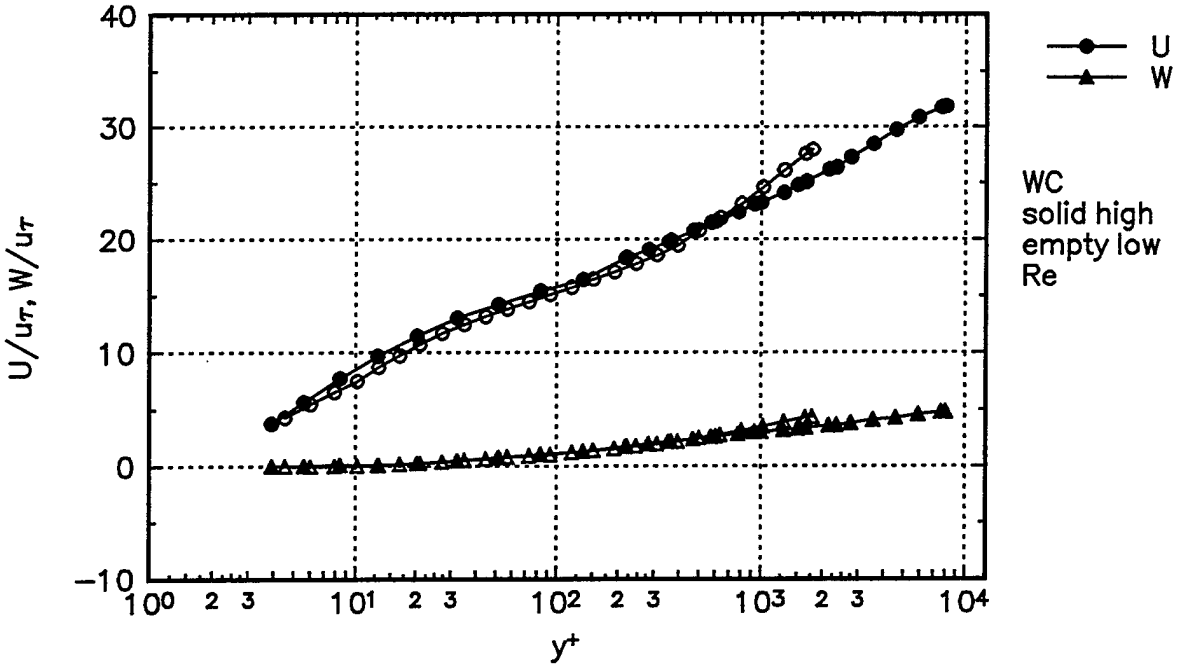

Figure 55a. U and W mean velocities presented in wall-coordinates at Station 1.

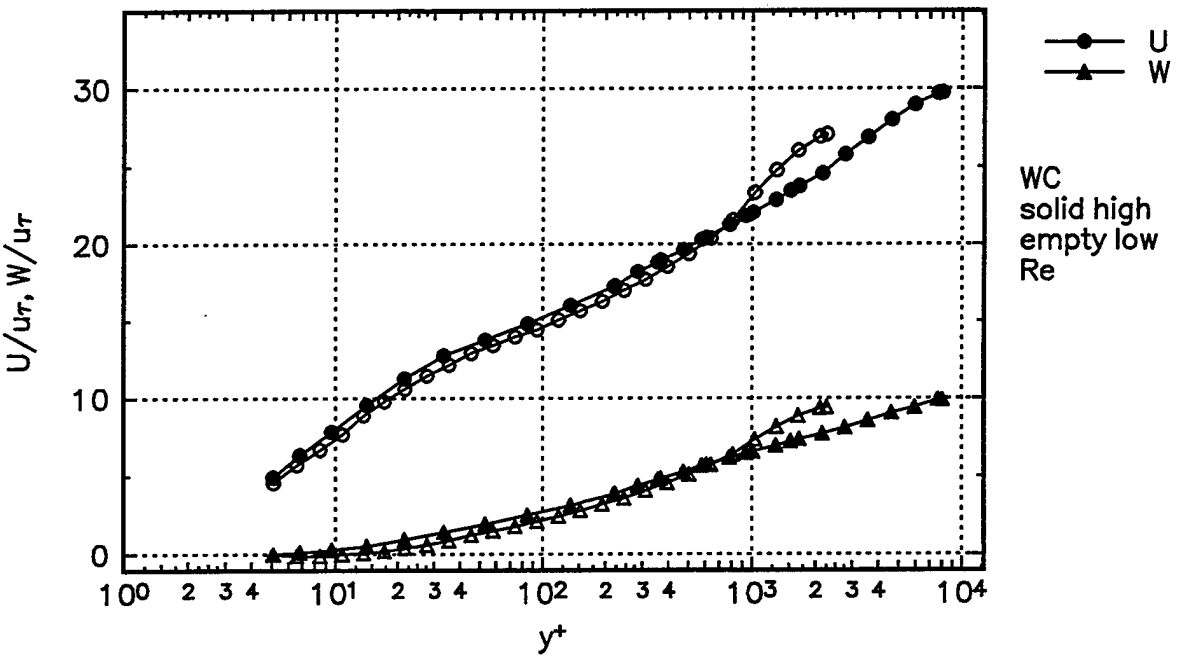

Figure 55b. U and W mean velocities presented in wall-coordinates at Station 2.

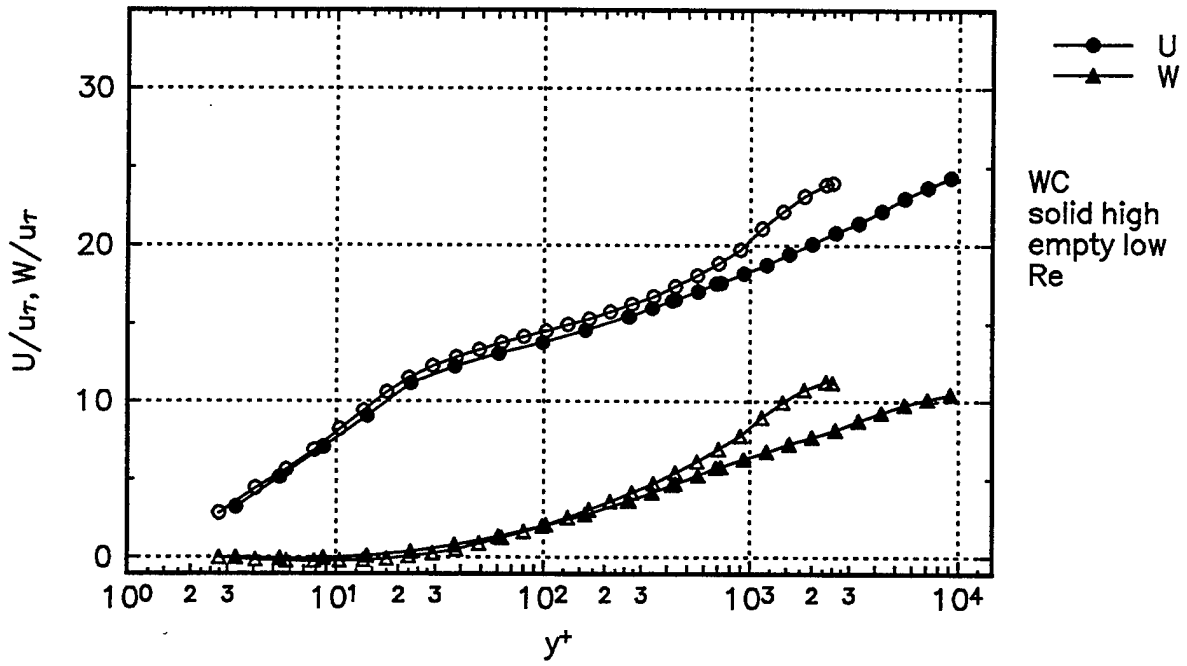

Figure 55c. U and W mean velocities presented in wall-coordinates at Station 3.

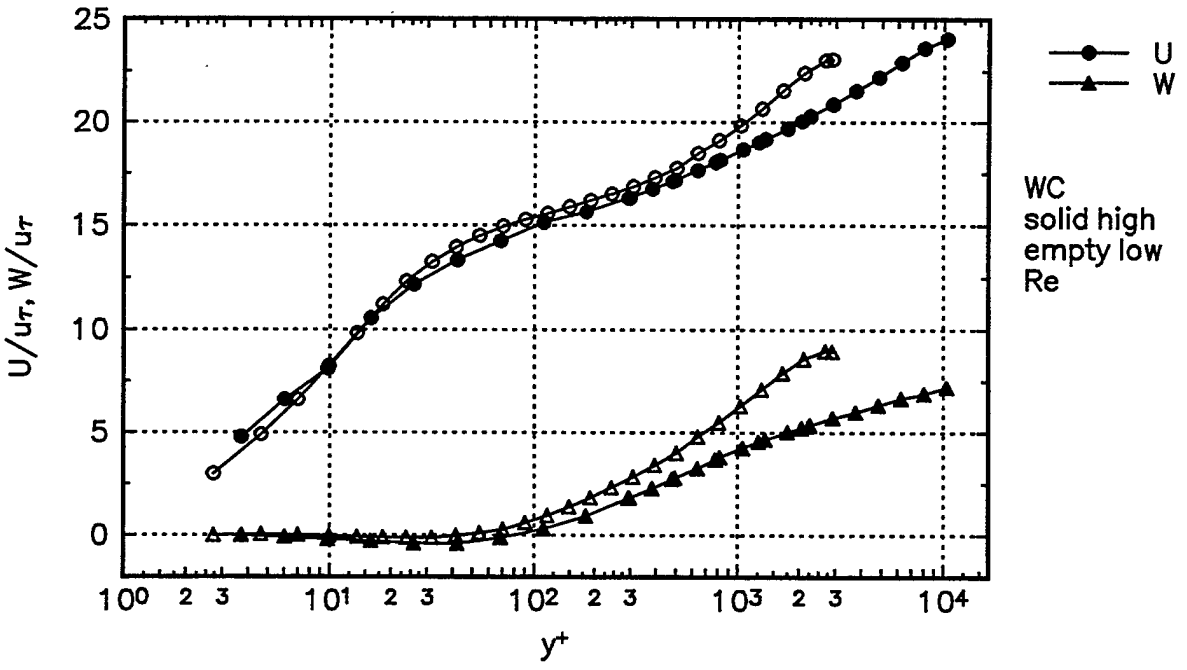

Figure 55d. U and W mean velocities presented in wall-coordinates at Station 4.

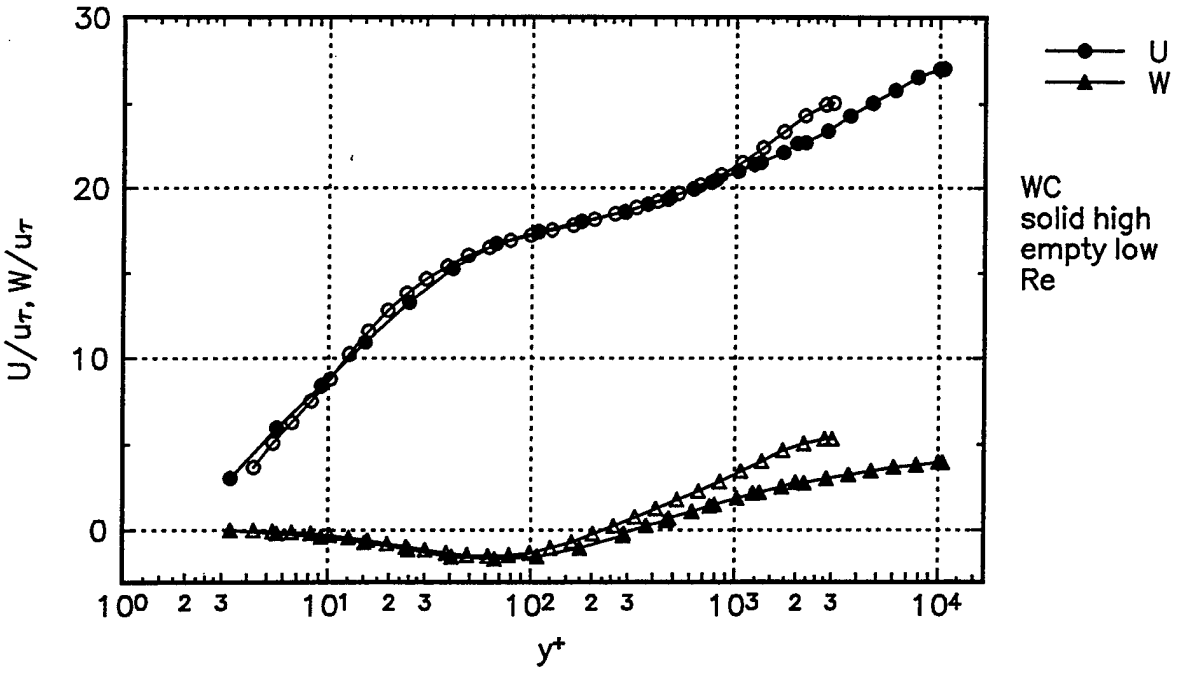

Figure 55e. U and W mean velocities presented in wall-coordinates at Station 5.

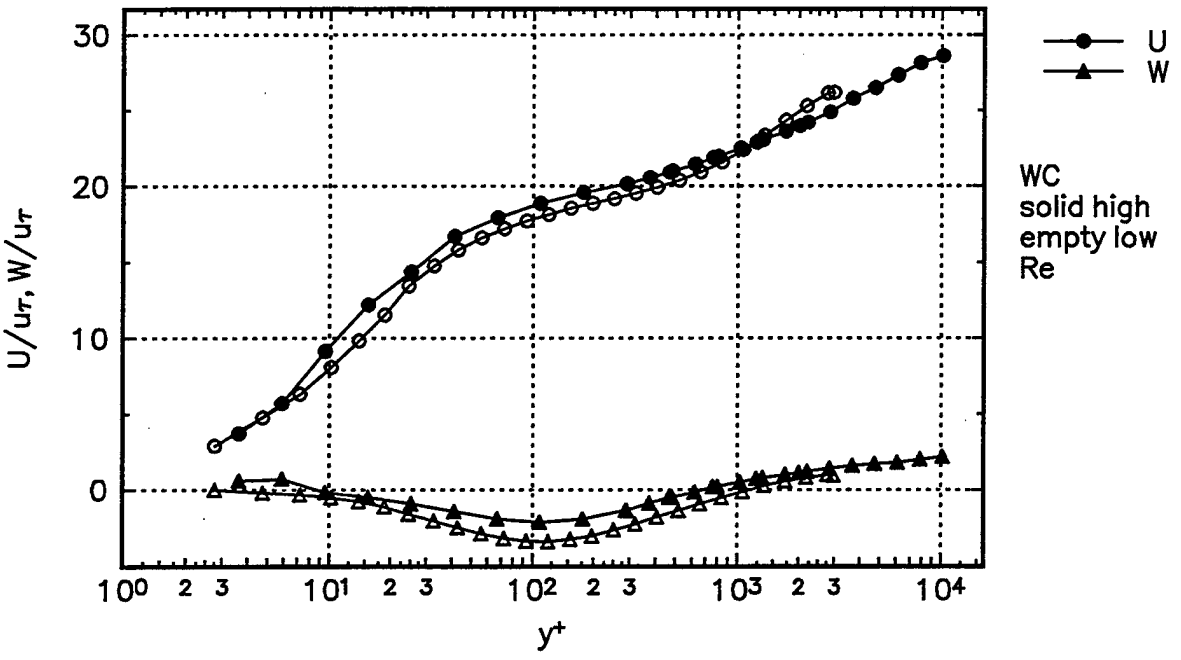

Figure 55f. U and W mean velocities presented in wall-coordinates at Station 6.

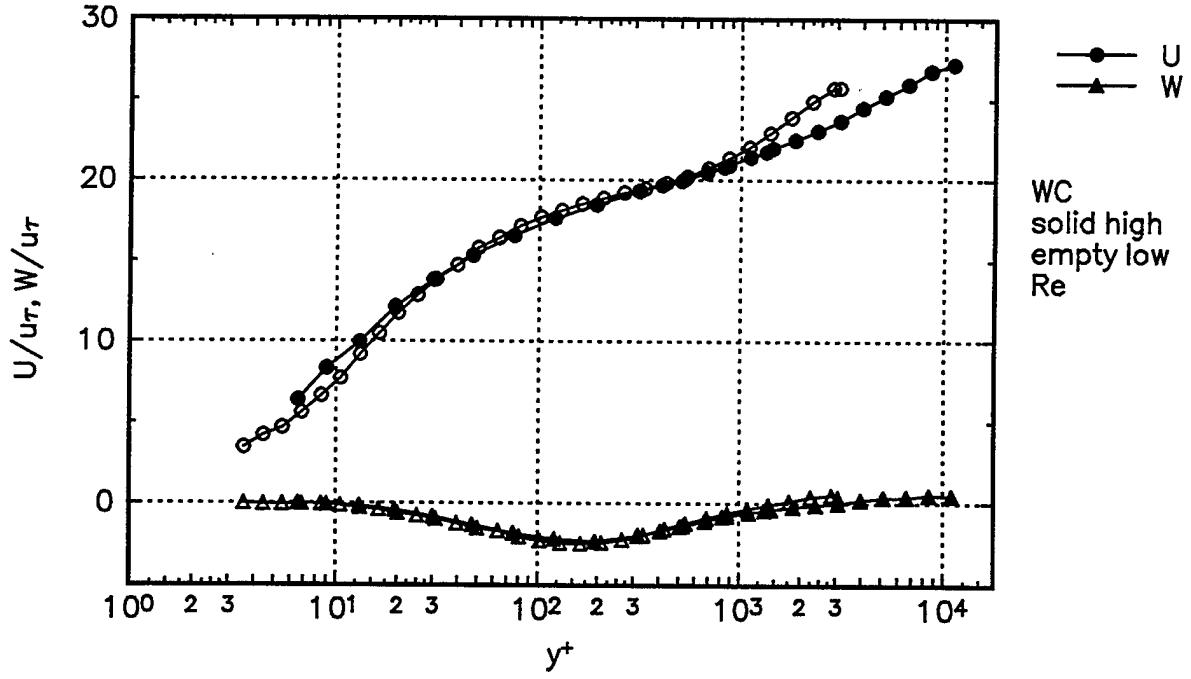

Figure 55g. U and W mean velocities presented in wall-coordinates at Station 7.

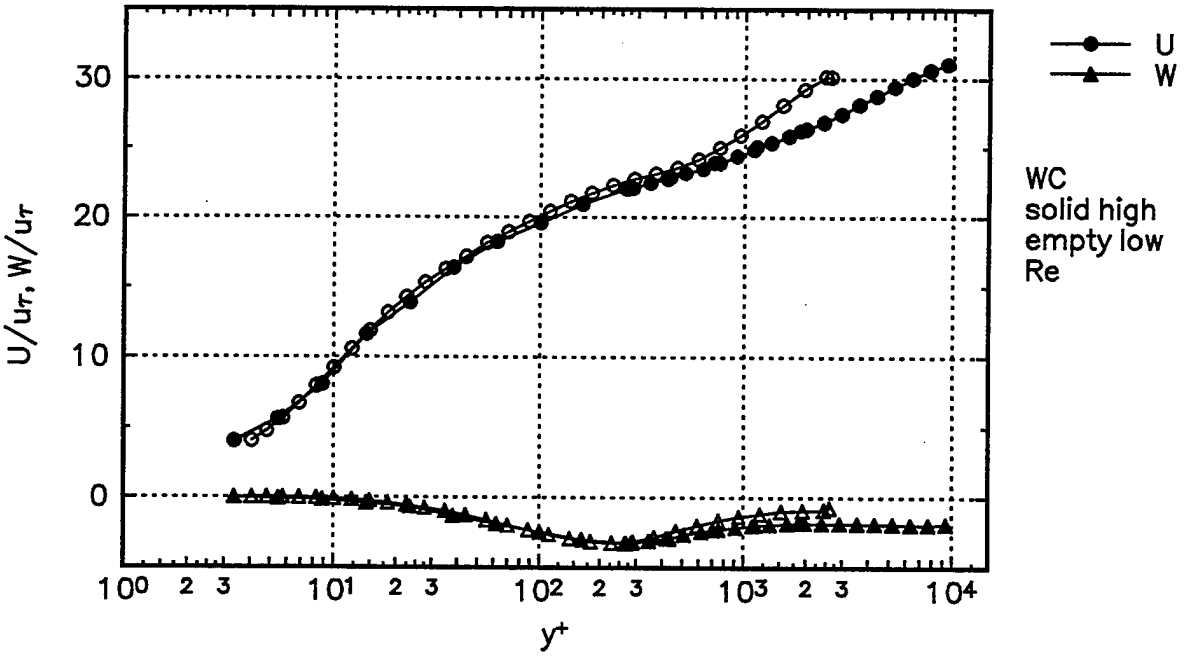

Figure 55h. U and W mean velocities presented in wall-coordinates at Station 8.

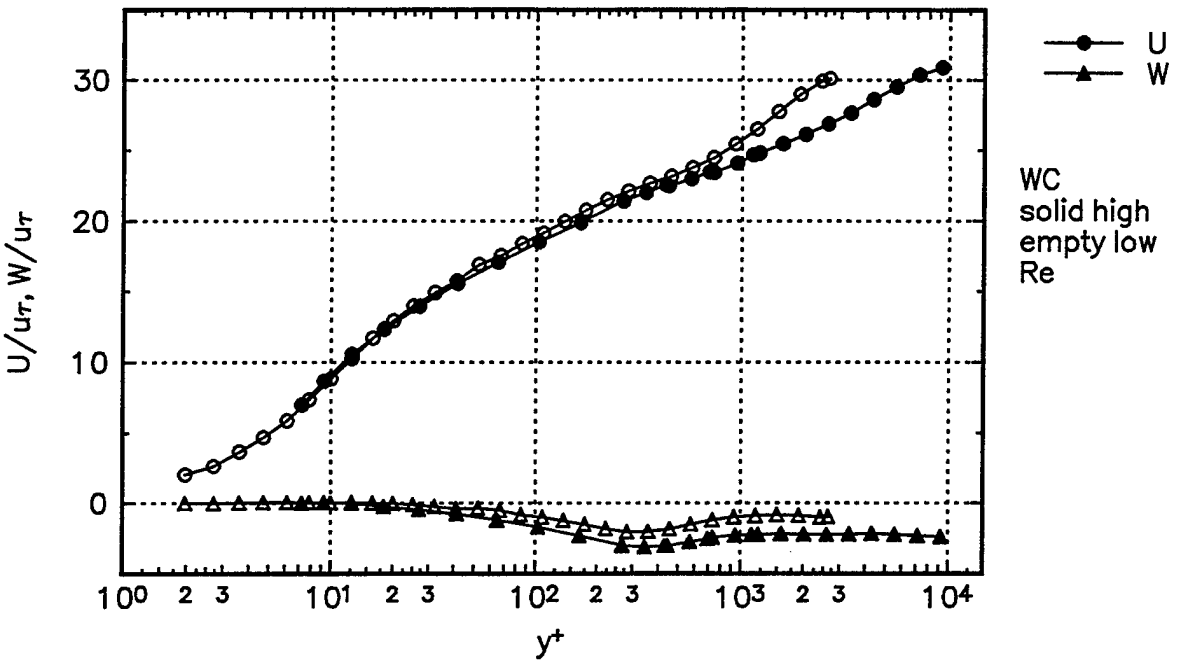

Figure 55i. U and W mean velocities presented in wall-coordinates at Station 9.

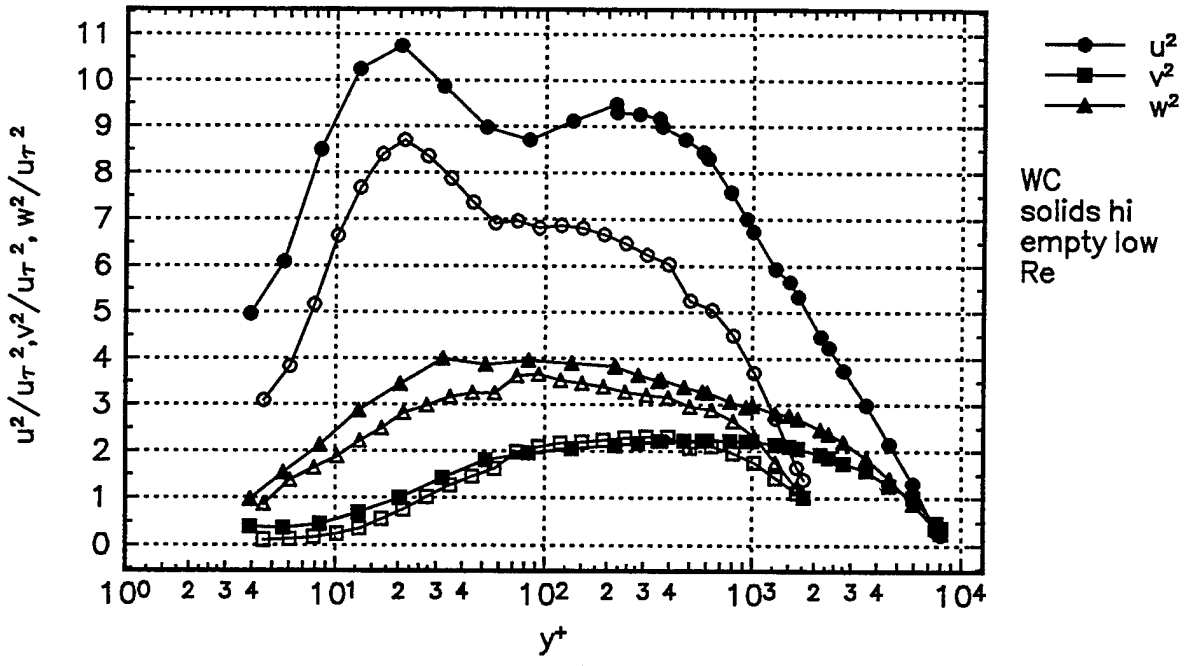

Figure 56a. Normal stresses presented in wall-coordinates at Station 1.

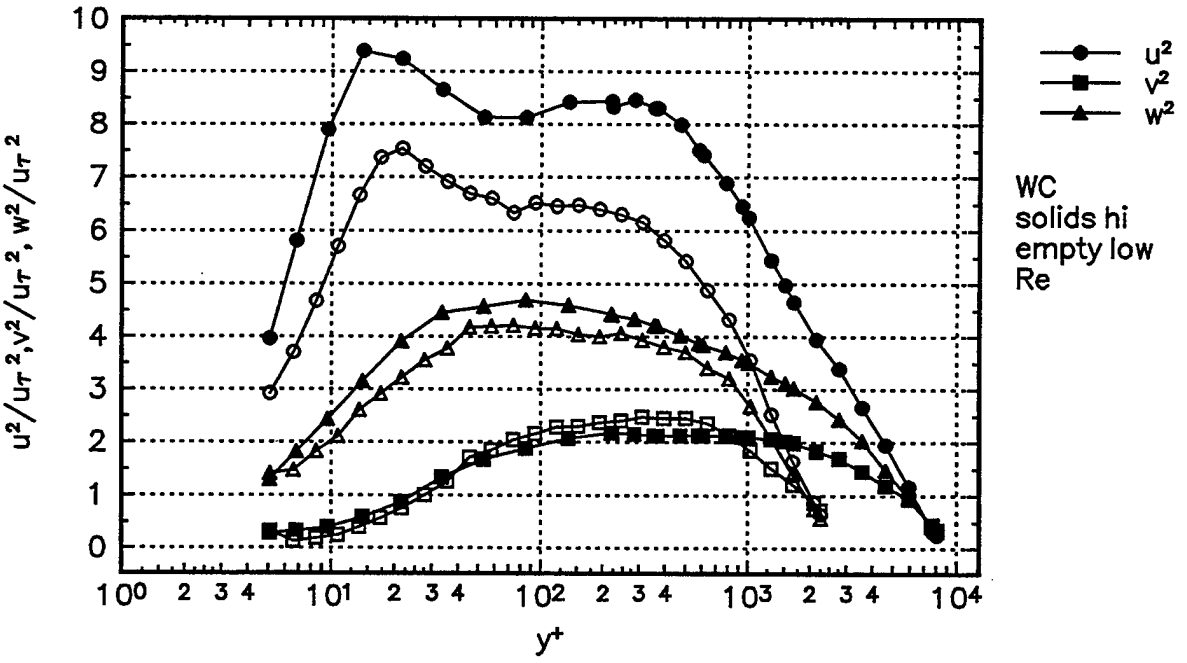

Figure 56b. Normal stresses presented in wall-coordinates at Station 2.

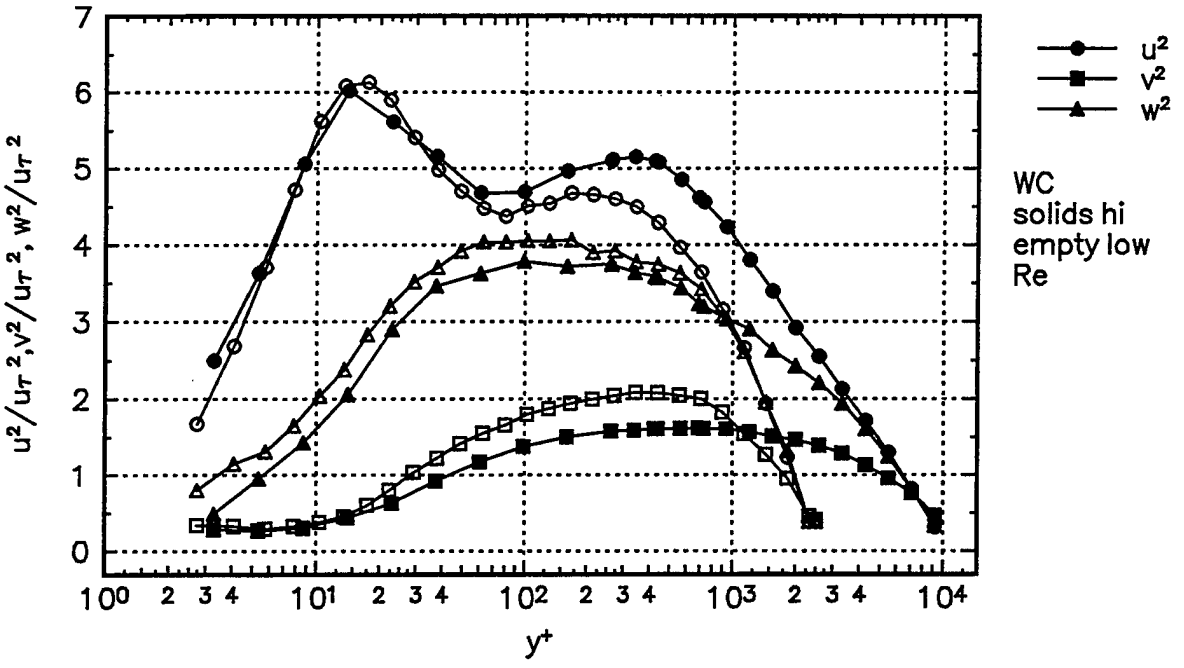

Figure 56c. Normal stresses presented in wall-coordinates at Station 3.

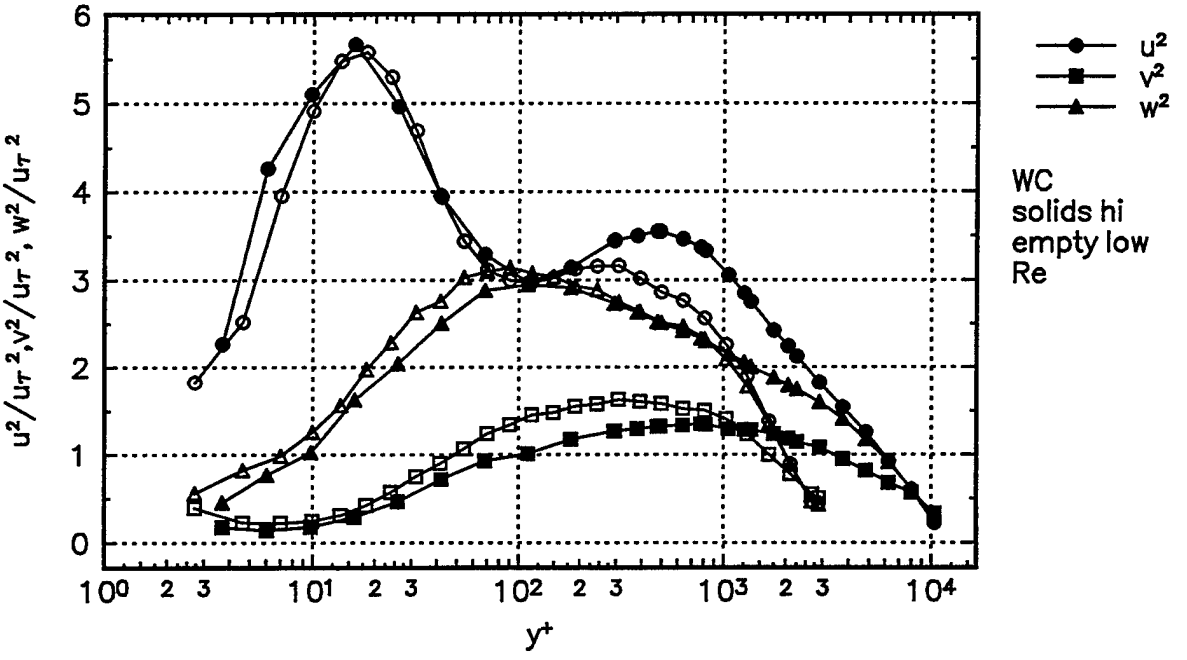

Figure 56d. Normal stresses presented in wall-coordinates at Station 4.

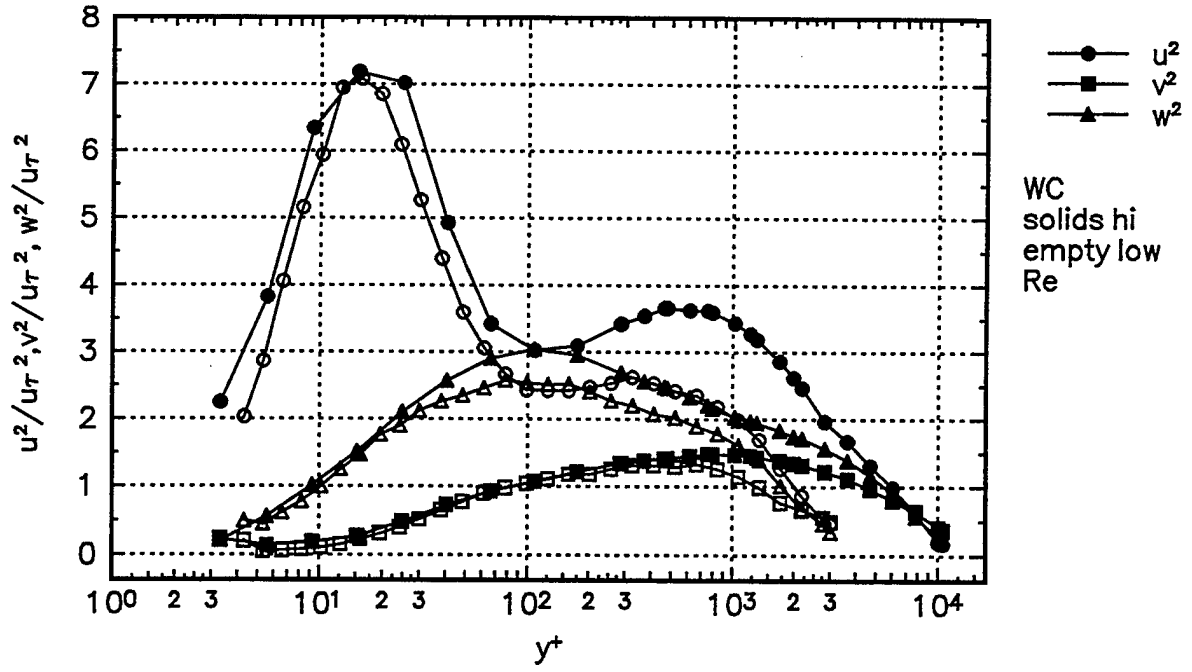

Figure 56e. Normal stresses presented in wall-coordinates at Station 5.

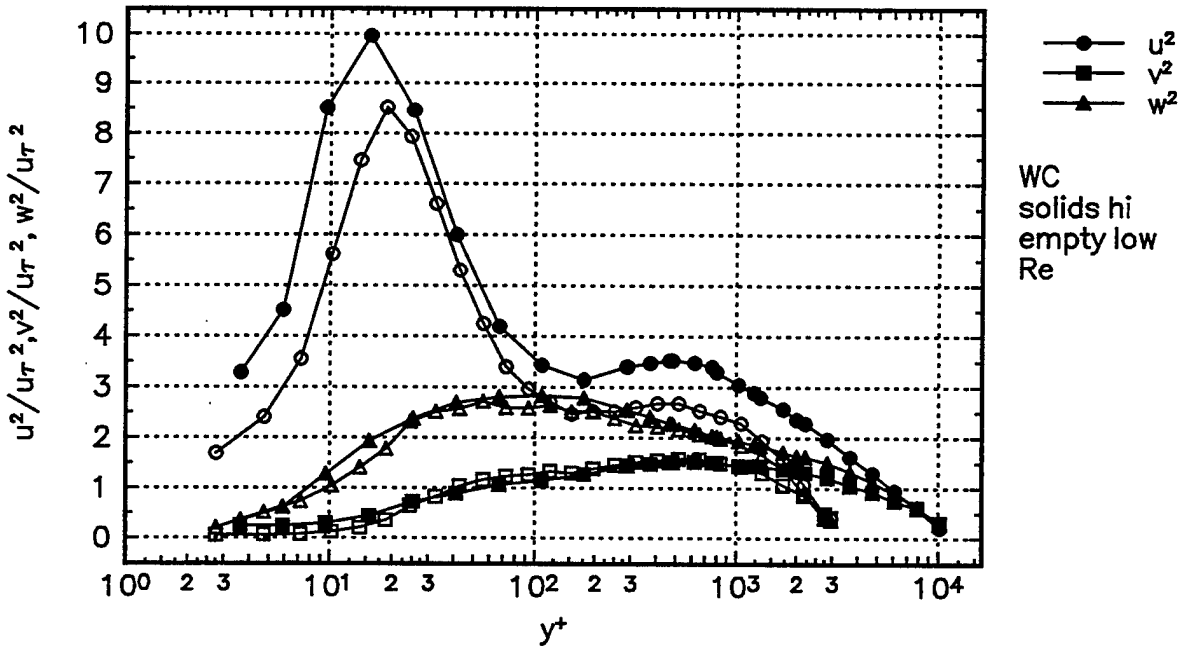

Figure 56f. Normal stresses presented in wall-coordinates at Station 6.

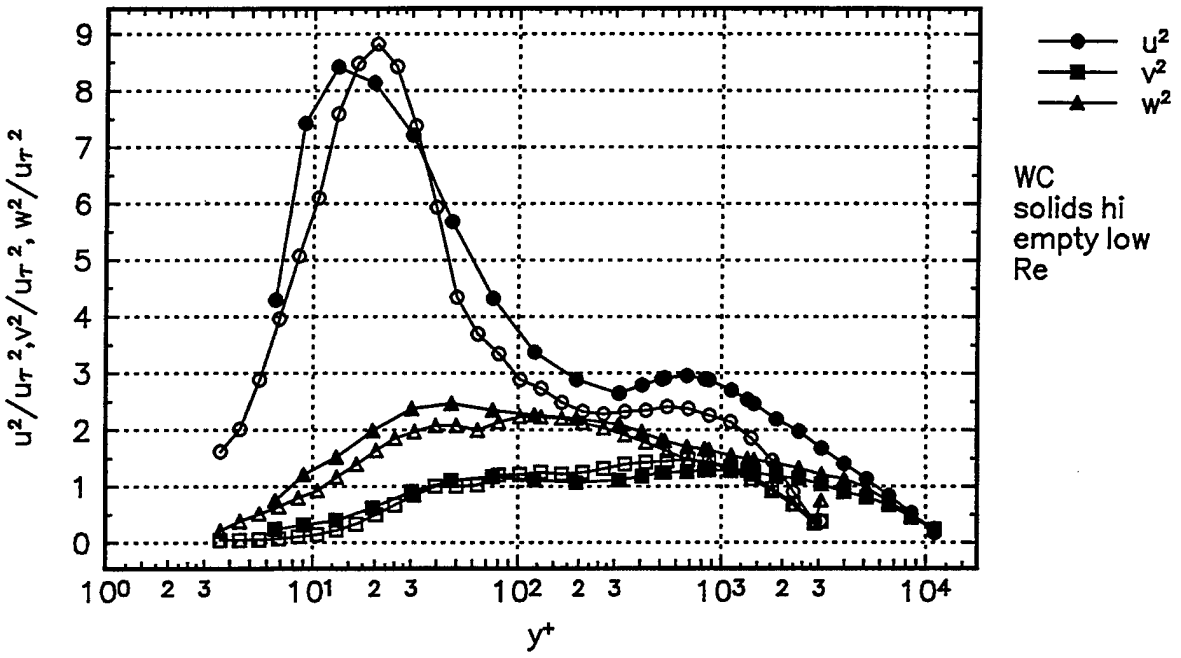

Figure 56g. Normal stresses presented in wall-coordinates at Station 7.

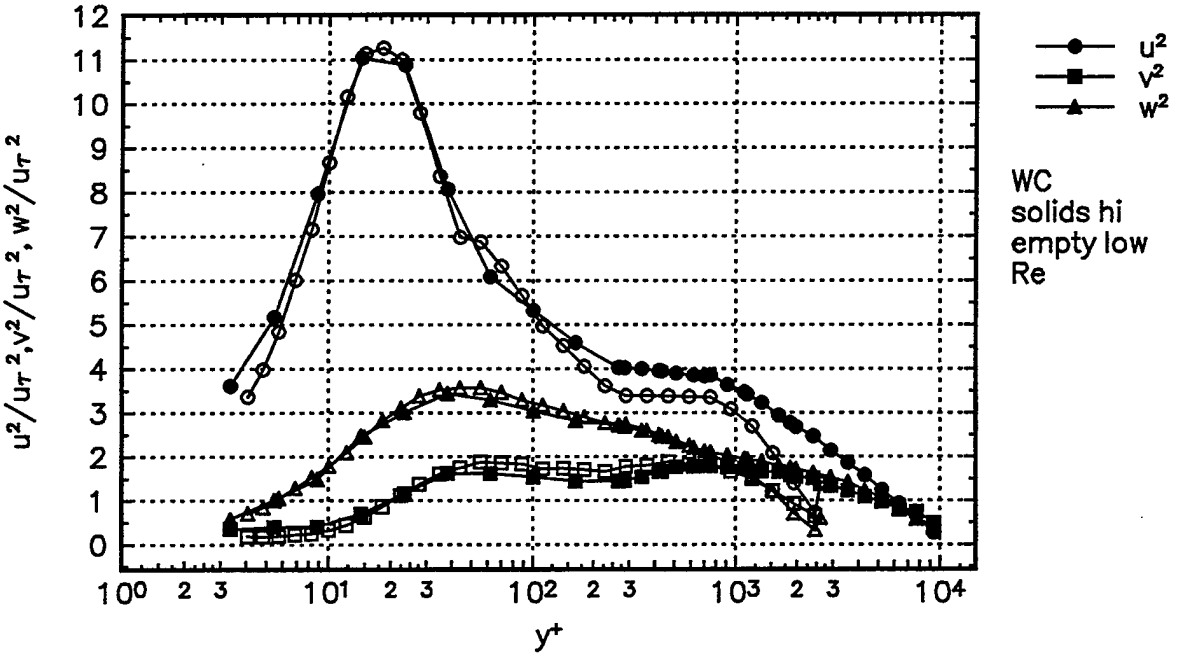

Figure 56h. Normal stresses presented in wall-coordinates at Station 8.

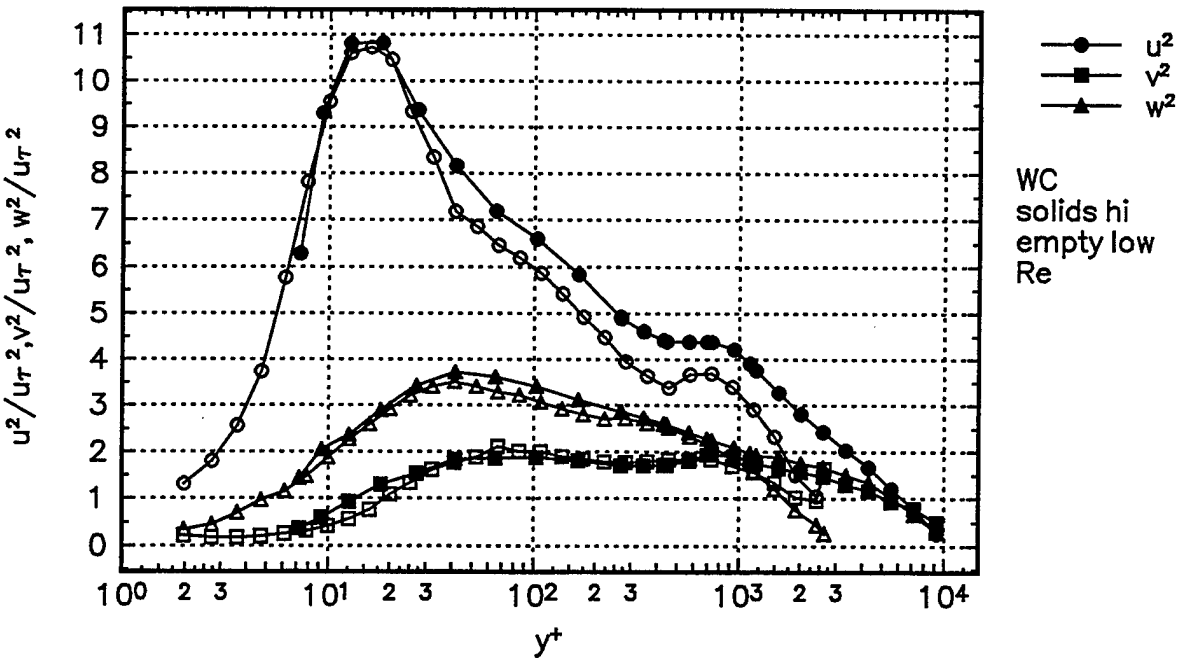

Figure 56i. Normal stresses presented in wall-coordinates at Station 9.

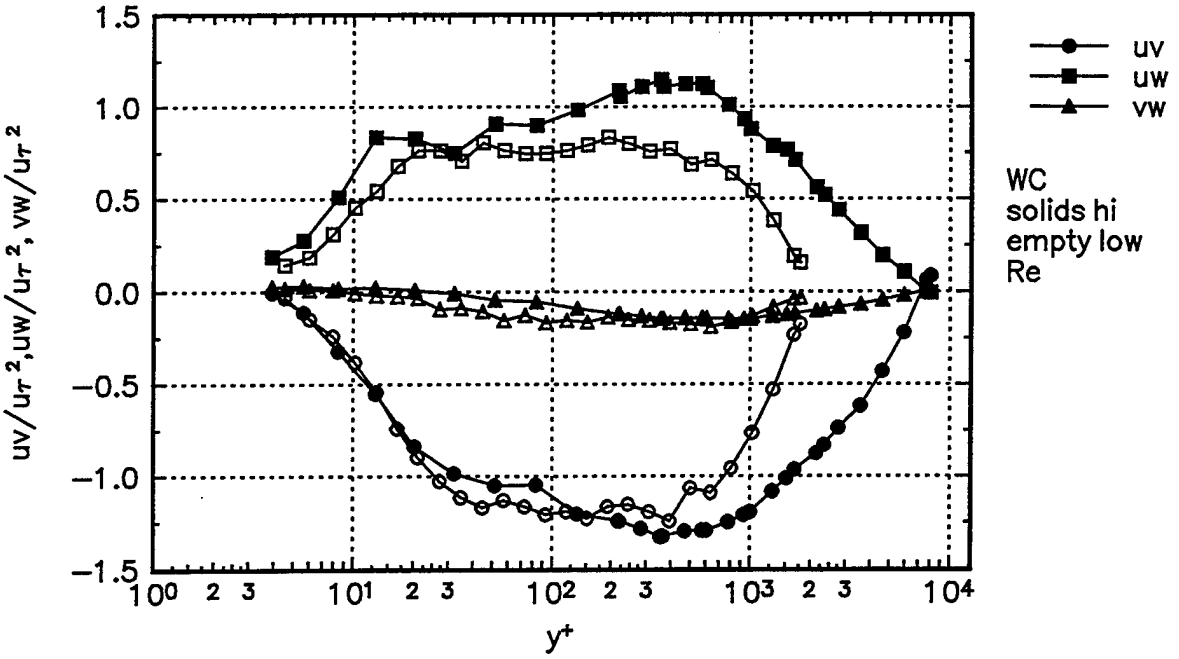

Figure 57a. Reynolds' stresses presented in wall-coordinates at Station 1.

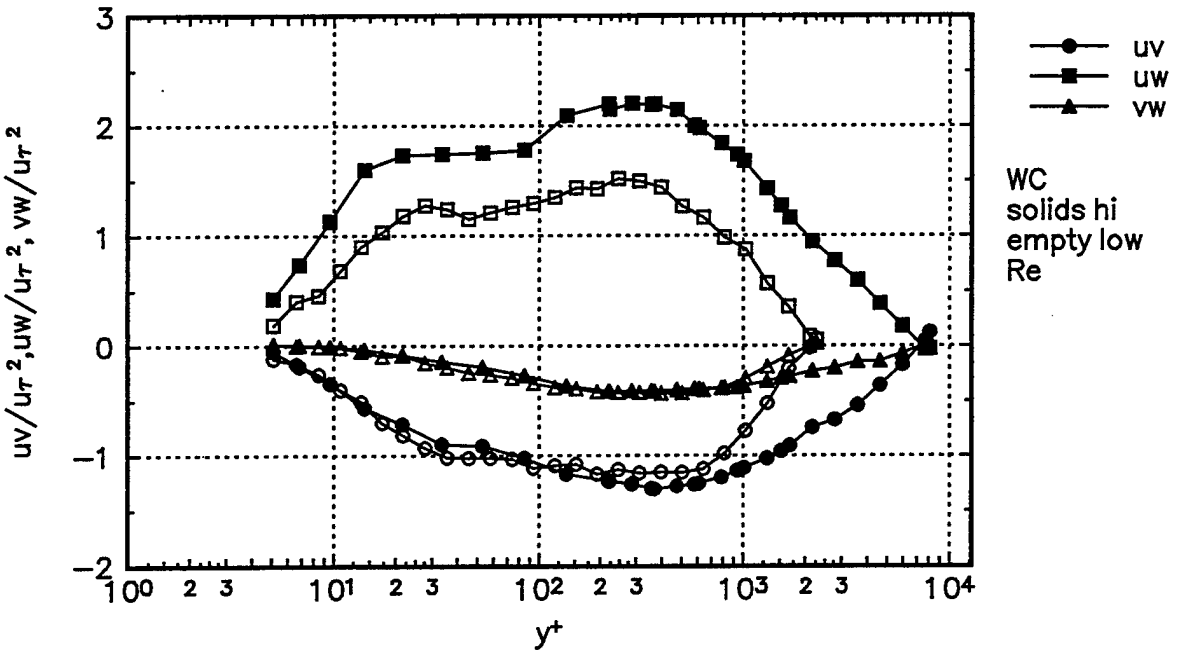

Figure 57b. Reynolds' stresses presented in wall-coordinates at Station 2.

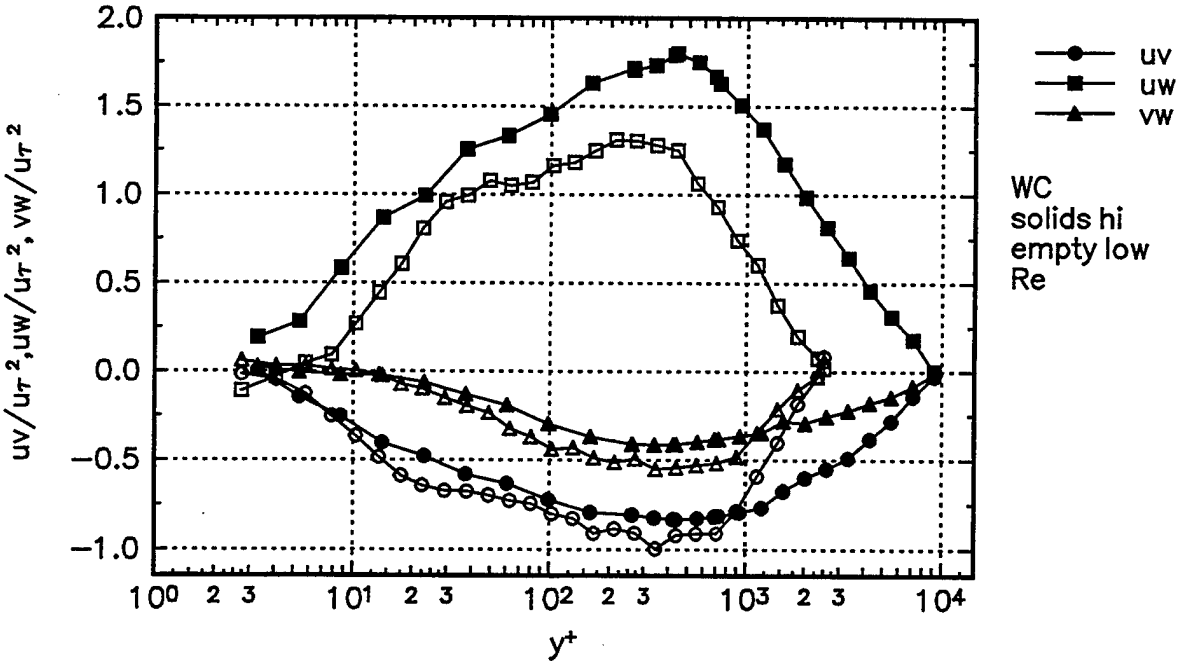

Figure 57c. Reynolds' stresses presented in wall-coordinates at Station 3.

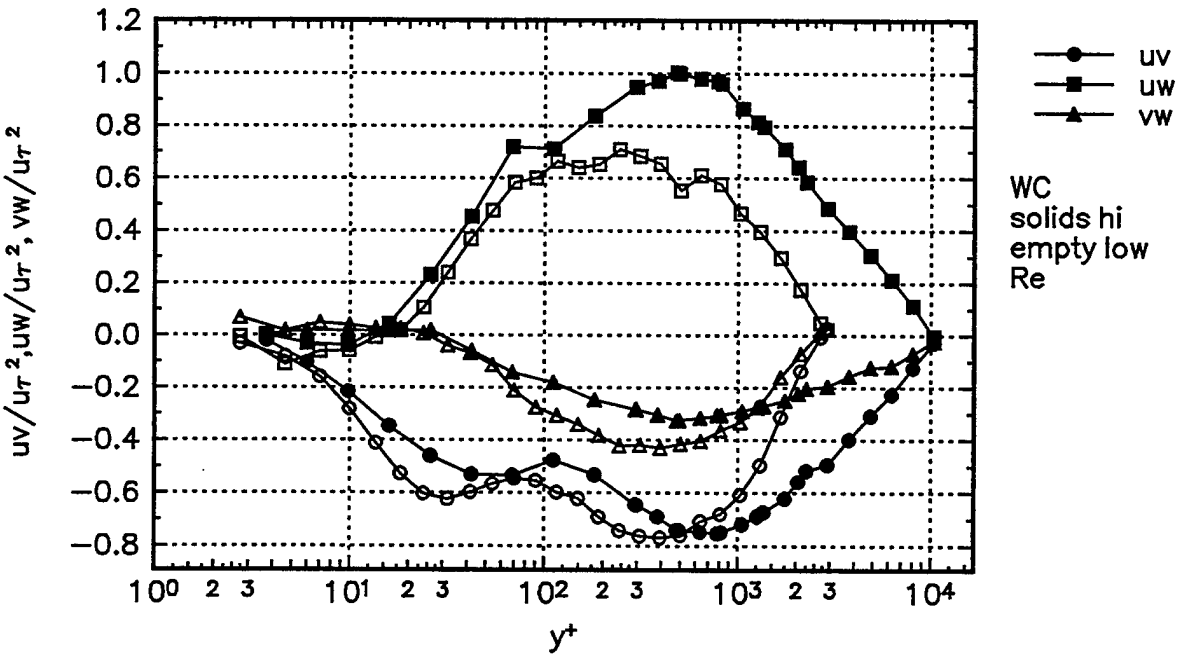

Figure 57d. Reynolds' stresses presented in wall-coordinates at Station 4.

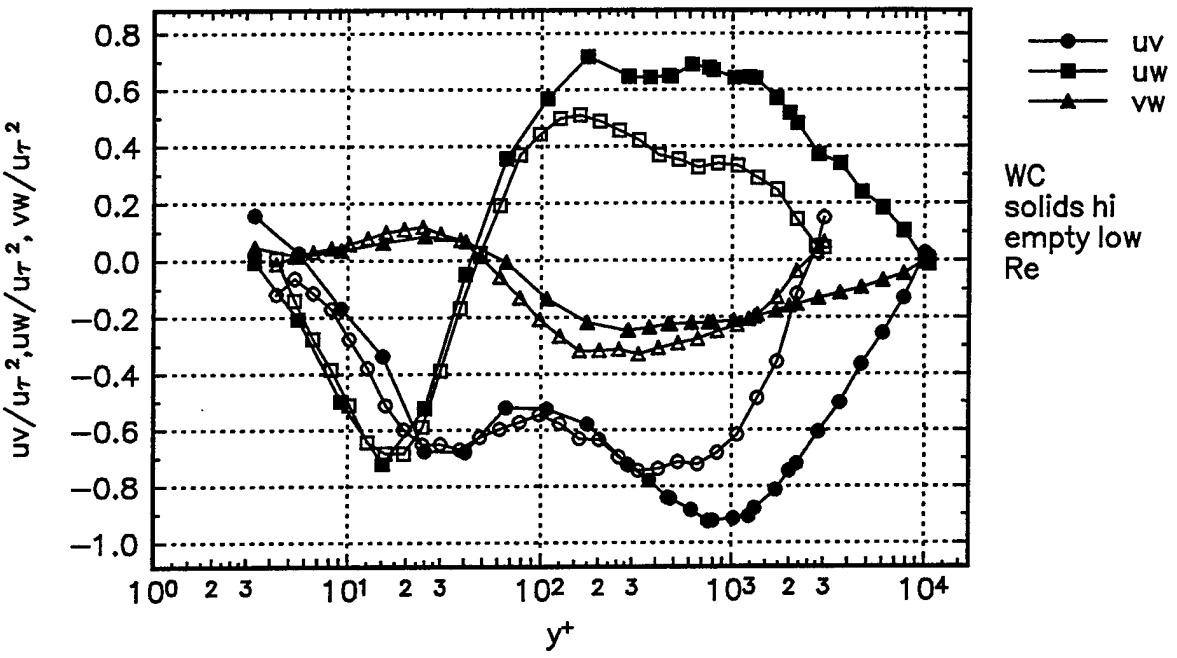

Figure 57e. Reynolds' stresses presented in wall-coordinates at Station 5.

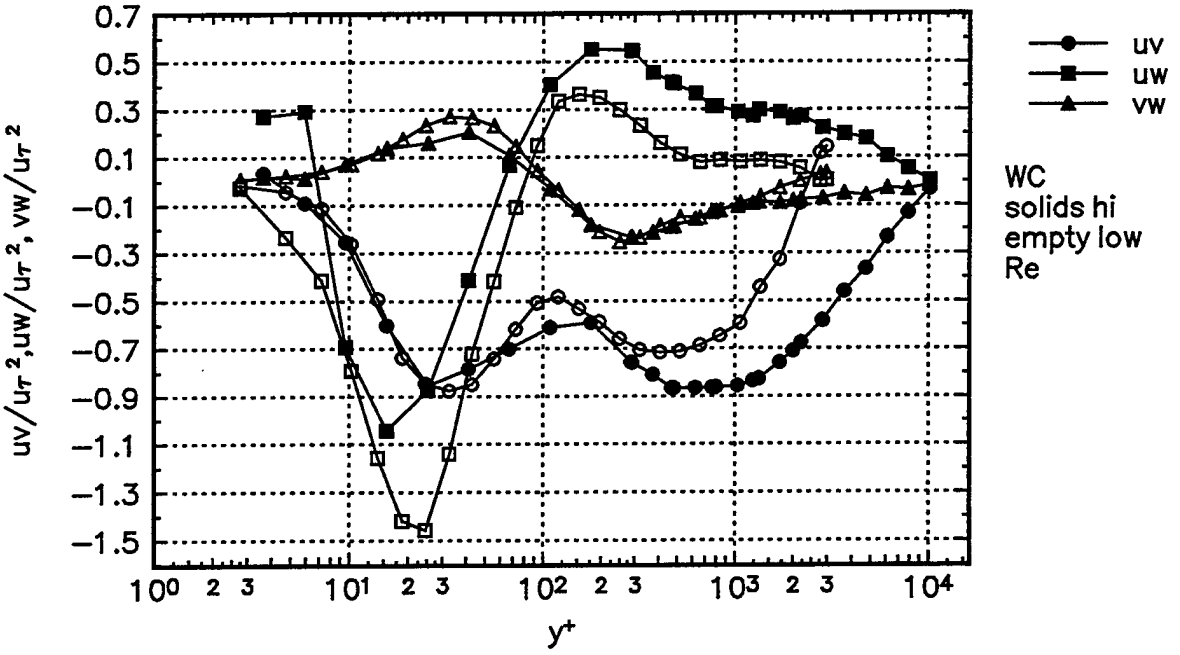

Figure 57f. Reynolds' stresses presented in wall-coordinates at Station 6.

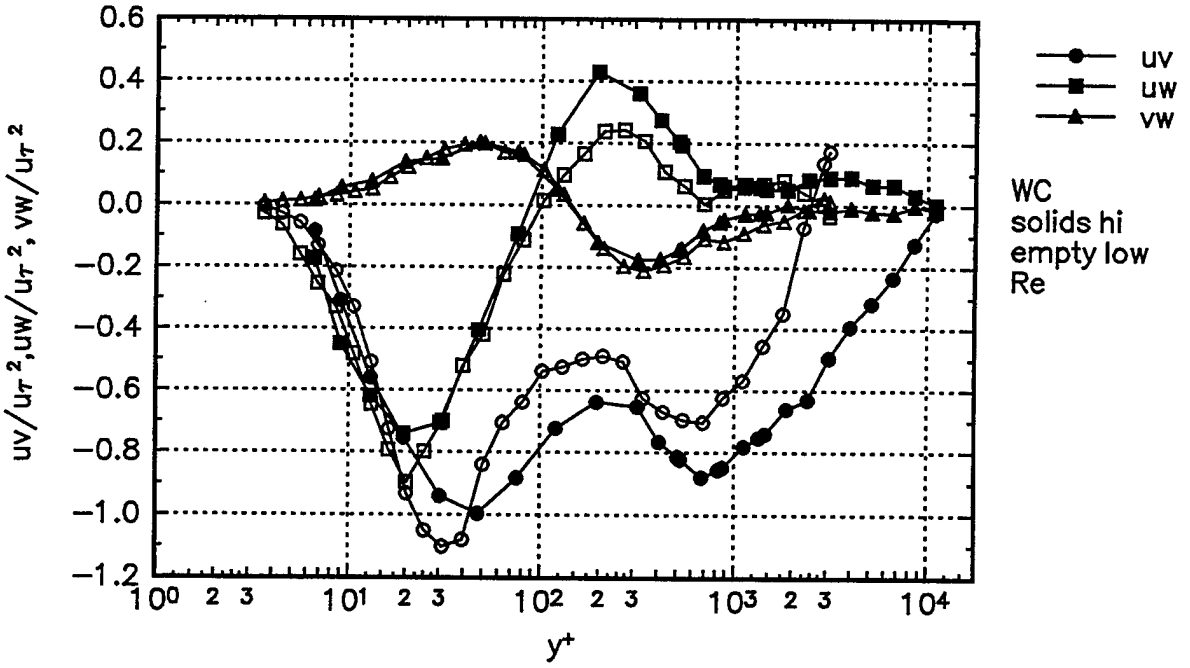

Figure 57g. Reynolds' stresses presented in wall-coordinates at Station 7.

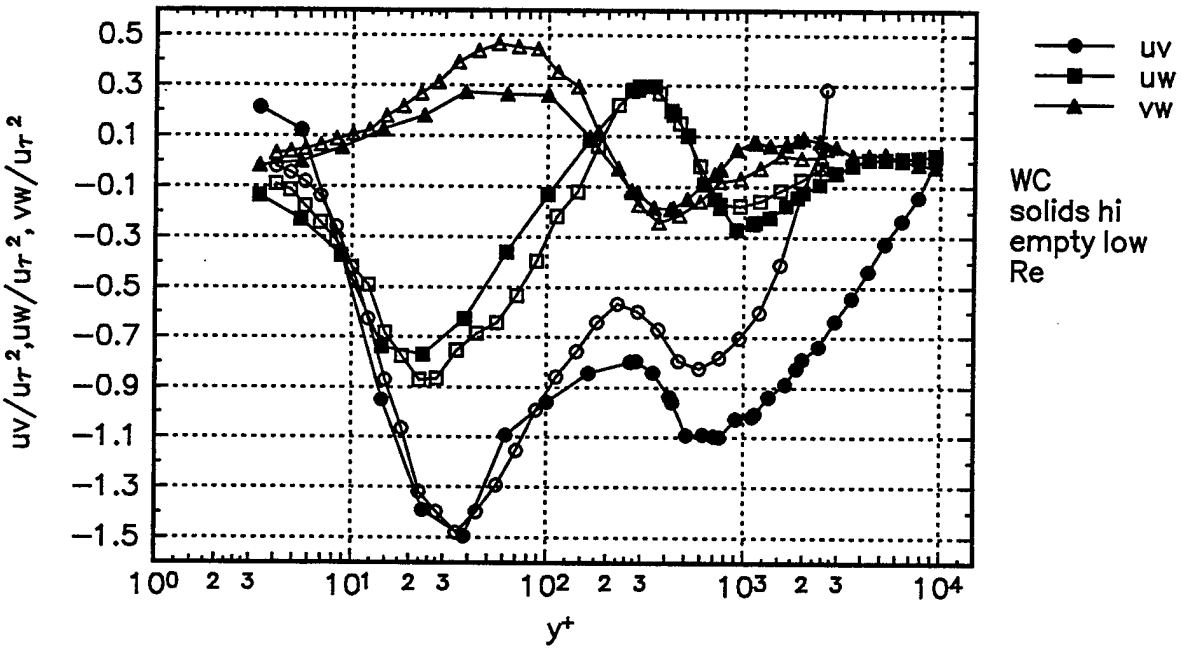

Figure 57h. Reynolds' stresses presented in wall-coordinates at Station 8.

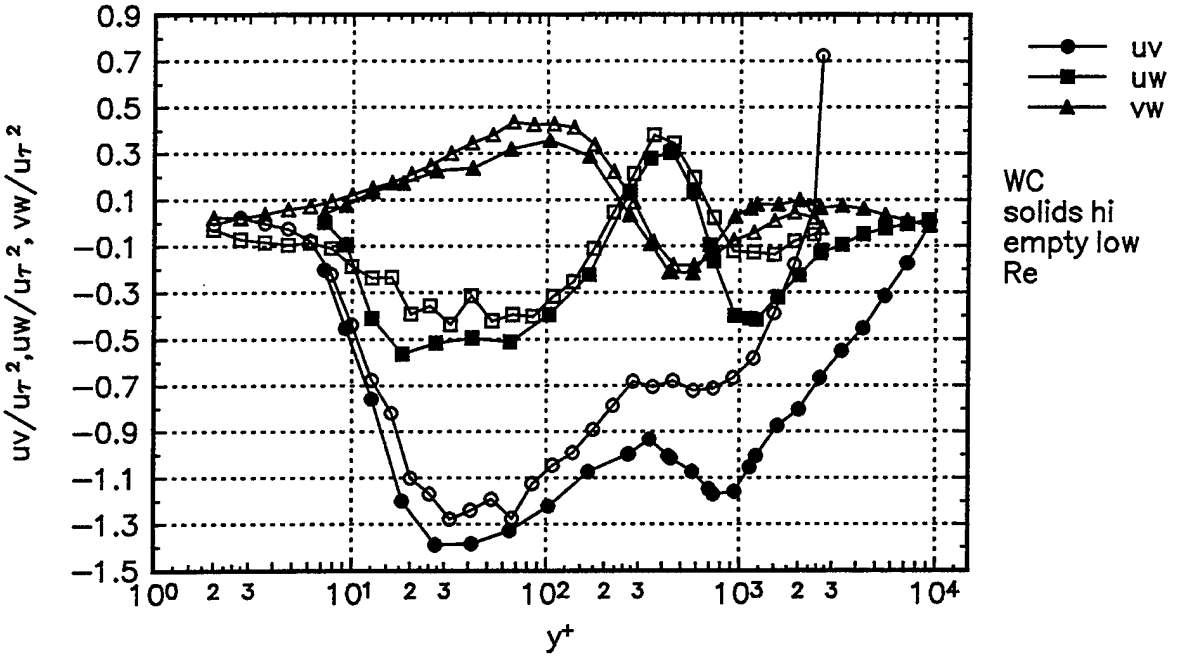

Figure 57i. Reynolds' stresses presented in wall-coordinates at Station 9.

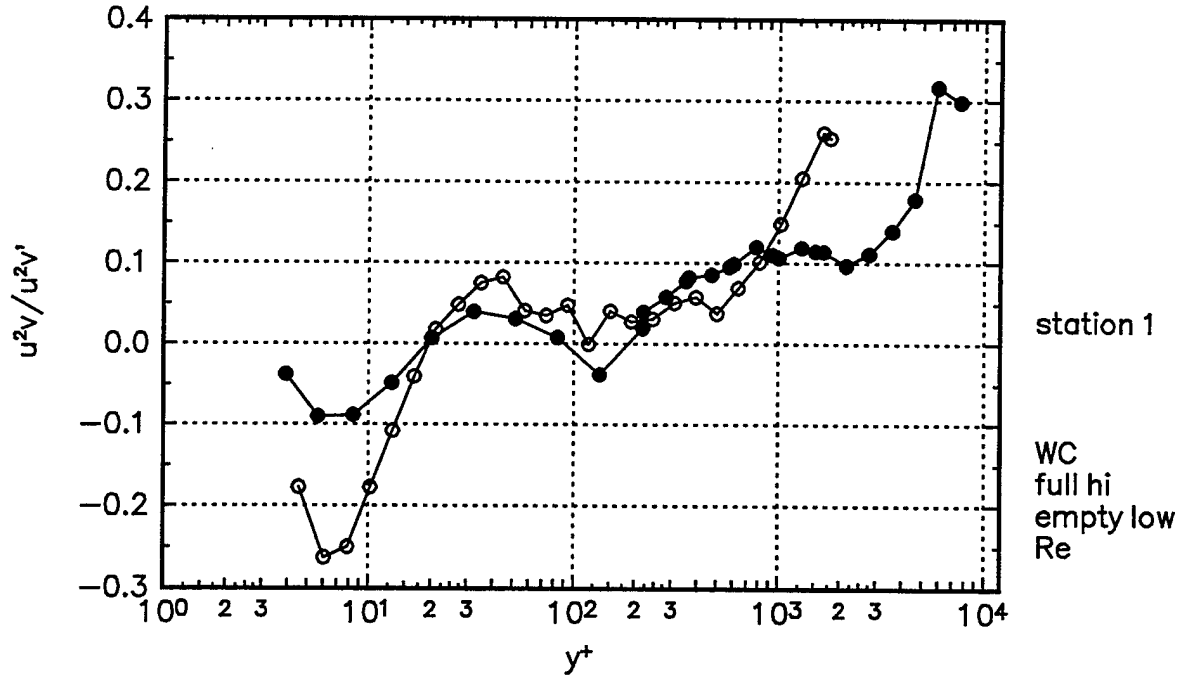

Figure 58a. $\overline{u^2v}$ triple products presented in wall-coordinates at Station 1.

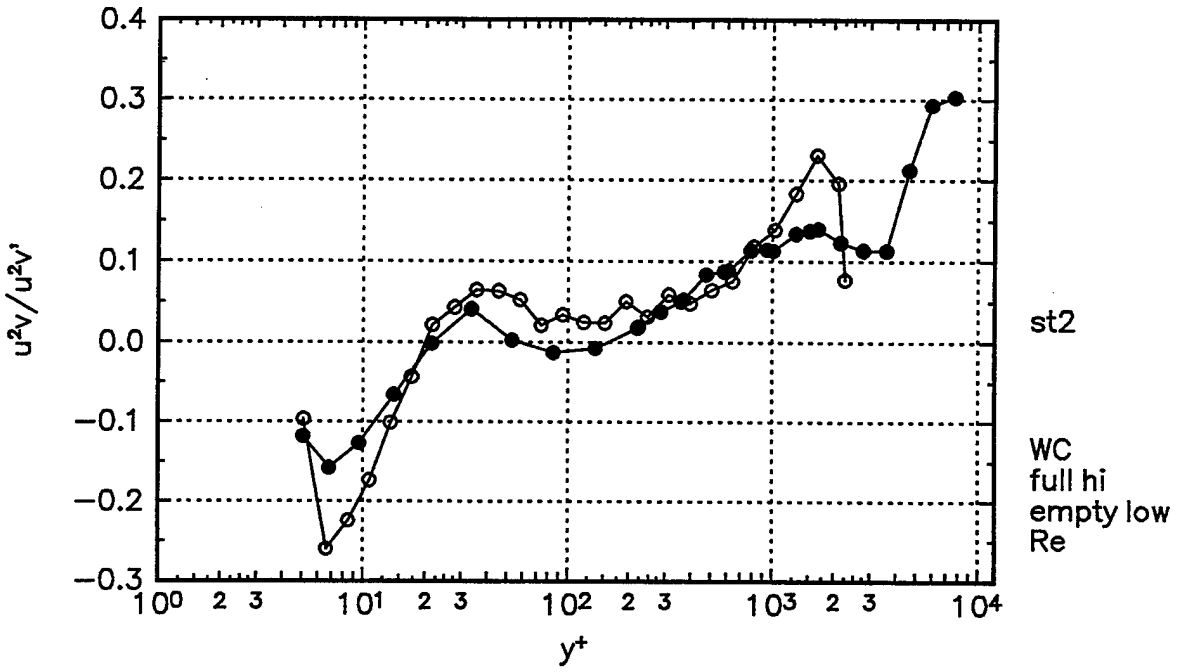

Figure 58b. $\overline{u^2v}$ triple products presented in wall-coordinates at Station 2.

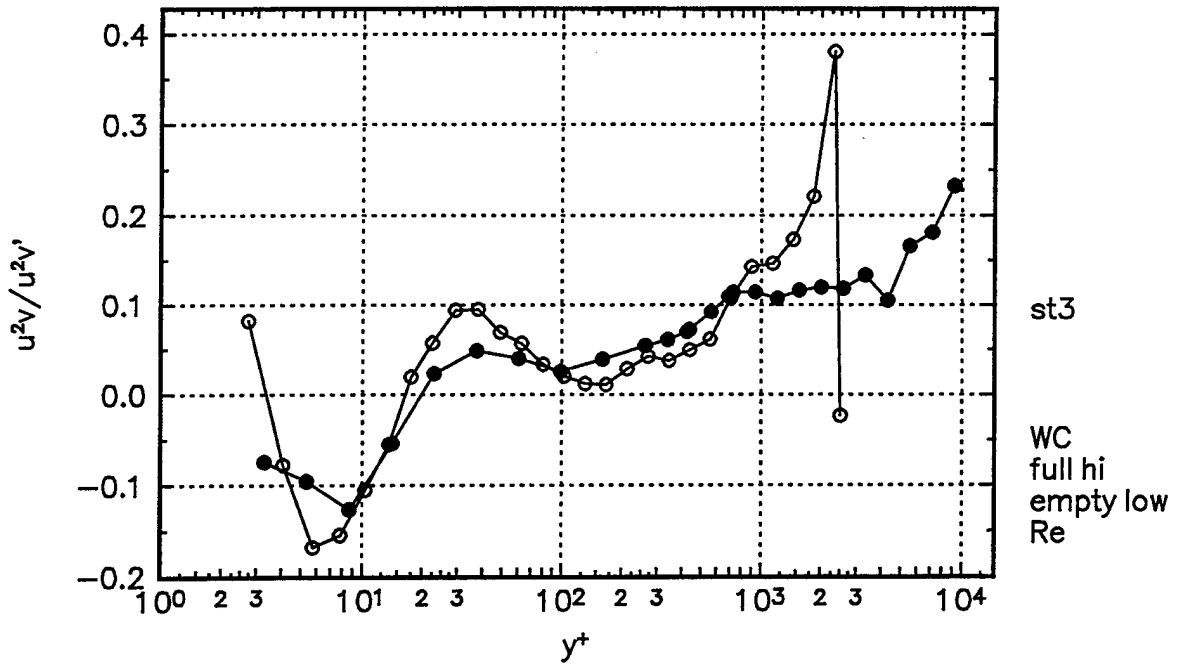

Figure 58c. $\overline{u^2v}$ triple products presented in wall-coordinates at Station 3.

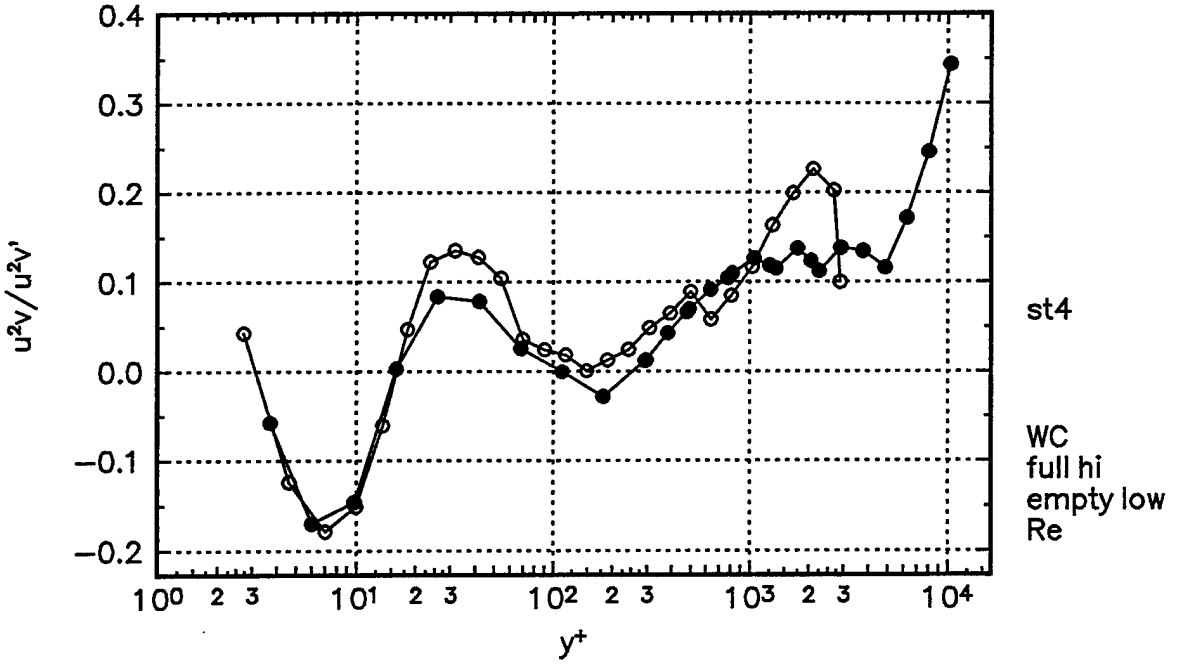

Figure 58d. $\overline{u^2v}$ triple products presented in wall-coordinates at Station 4.

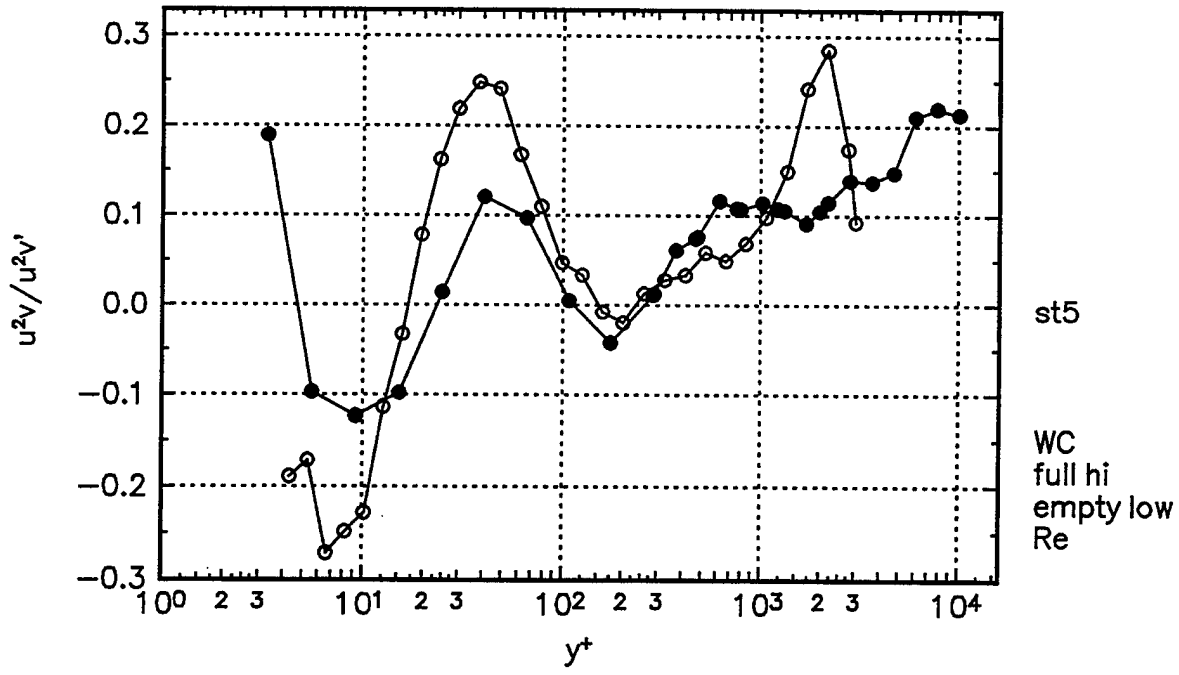

Figure 58e. $\overline{u^2v}$ triple products presented in wall-coordinates at Station 5.

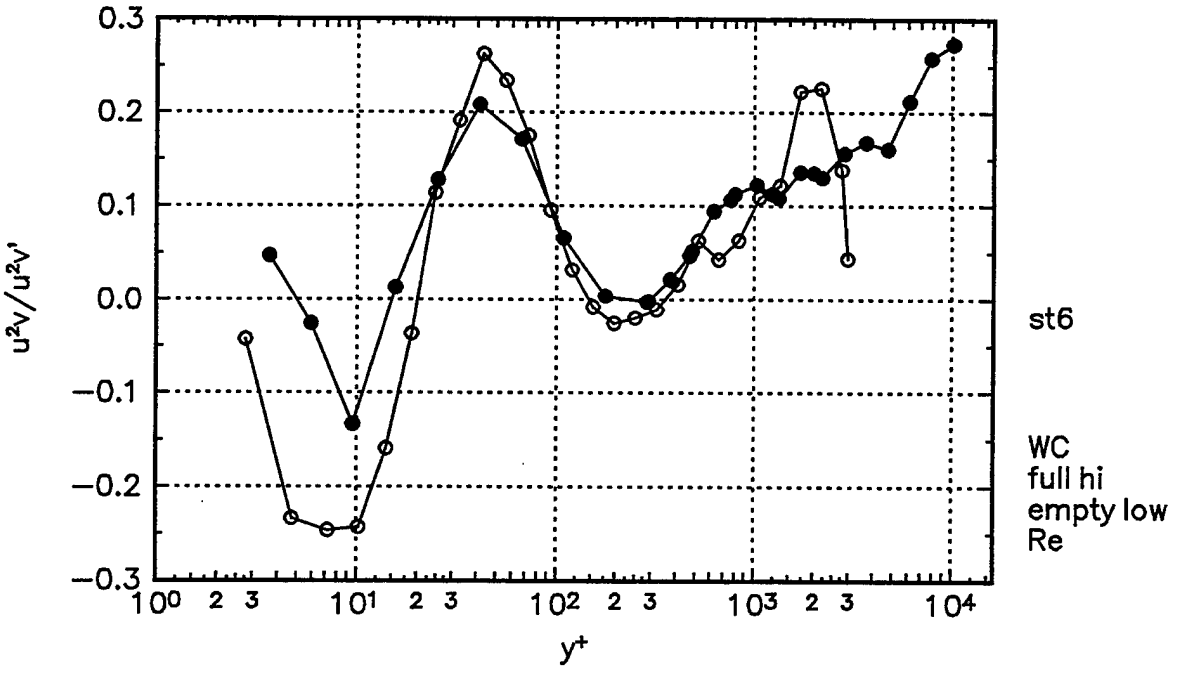

Figure 58f. $\overline{u^2v}$ triple products presented in wall-coordinates at Station 6.

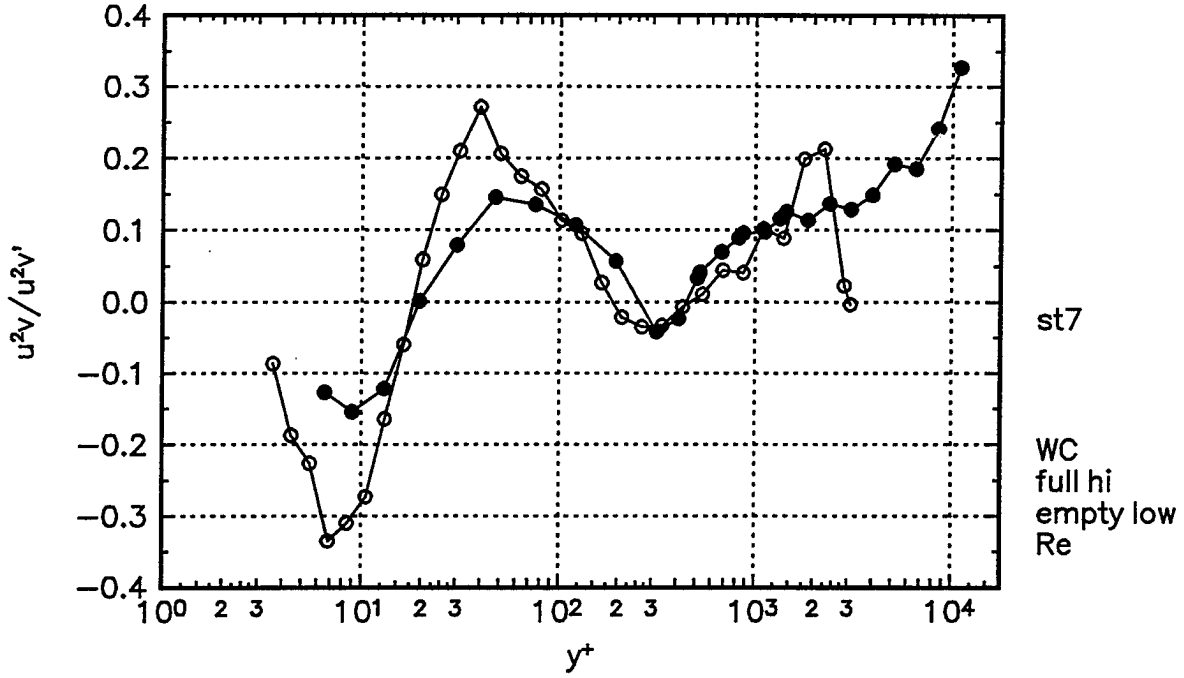

Figure 58g. $\overline{u^2v}$ triple products presented in wall-coordinates at Station 7.

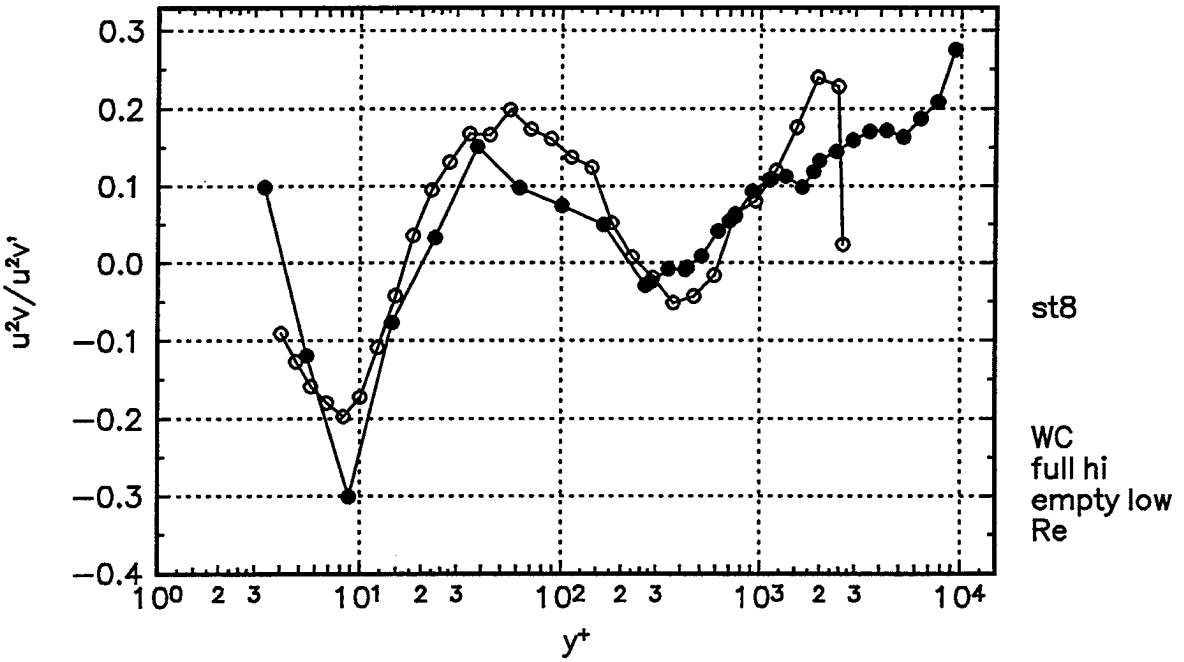

Figure 58h. $\overline{u^2v}$ triple products presented in wall-coordinates at Station 8.

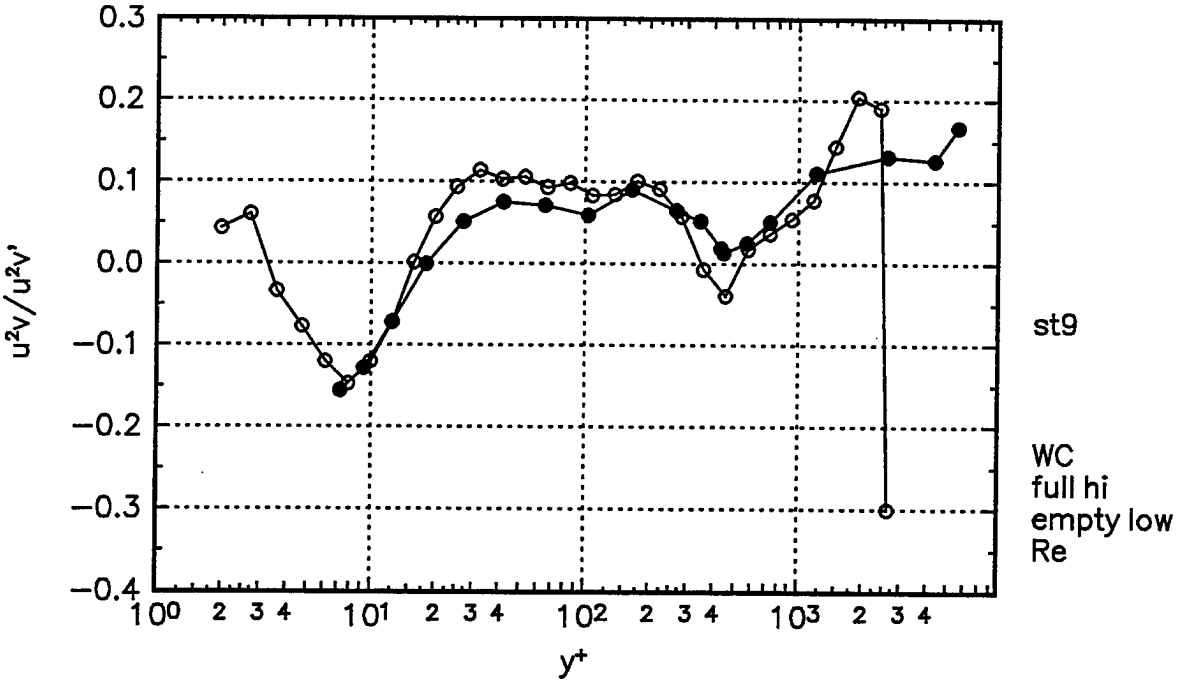

Figure 58i. $\overline{u^2v}$ triple products presented in wall-coordinates at Station 9.

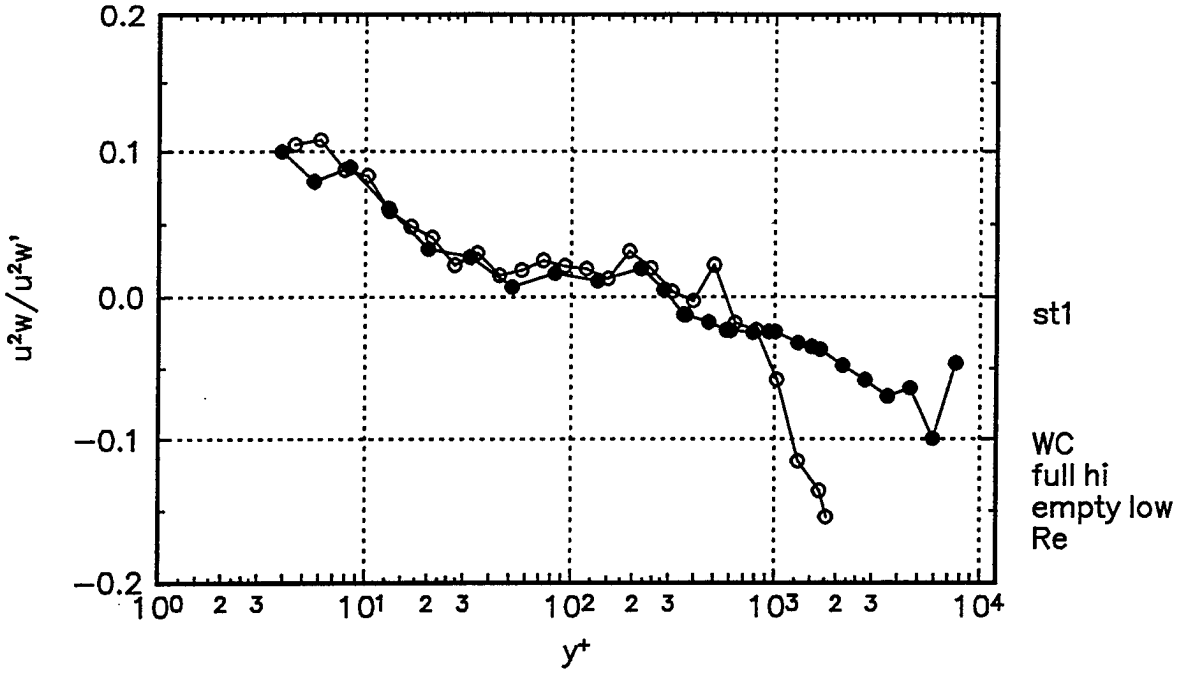

Figure 59a. $\overline{u^2w}$ triple products presented in wall-coordinates at Station 1.

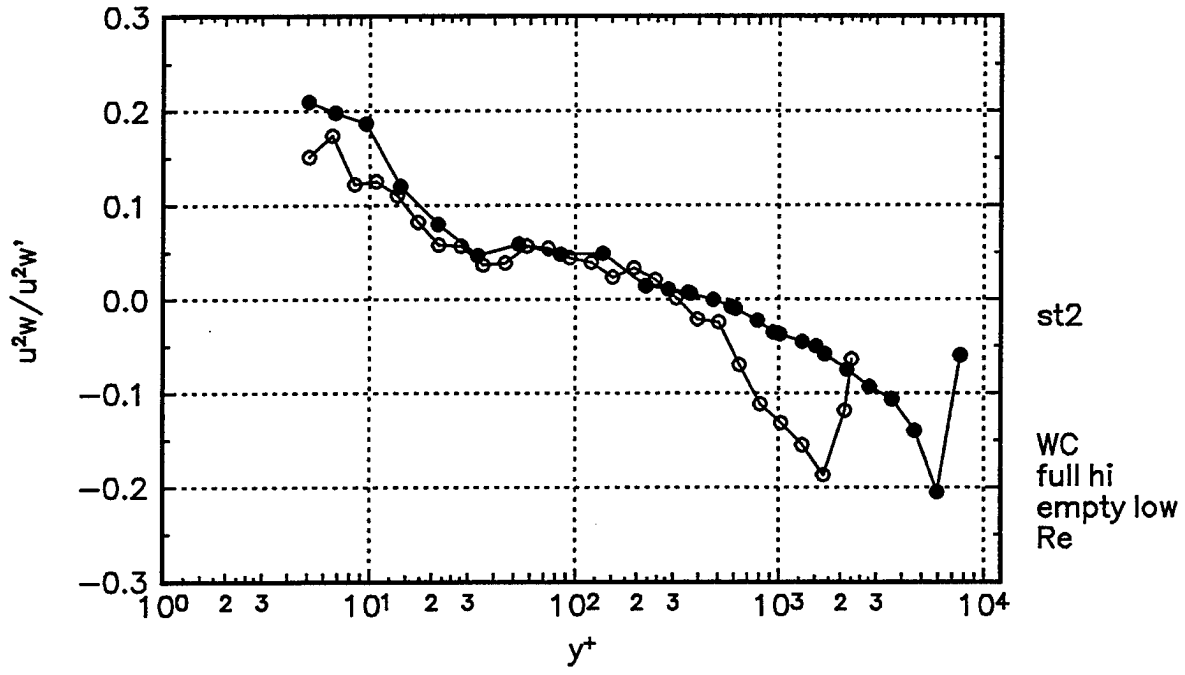

Figure 59b. $\overline{u^2w}$ triple products presented in wall-coordinates at Station 2.

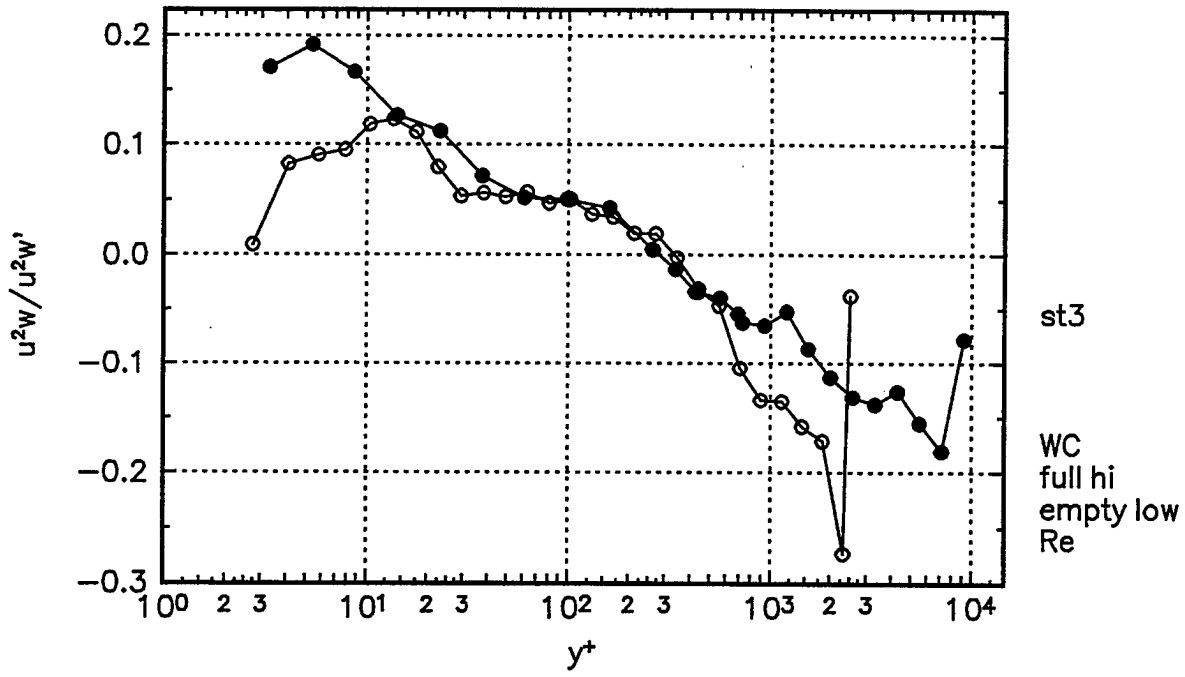

Figure 59c. $\overline{u^2w}$ triple products presented in wall-coordinates at Station 3.

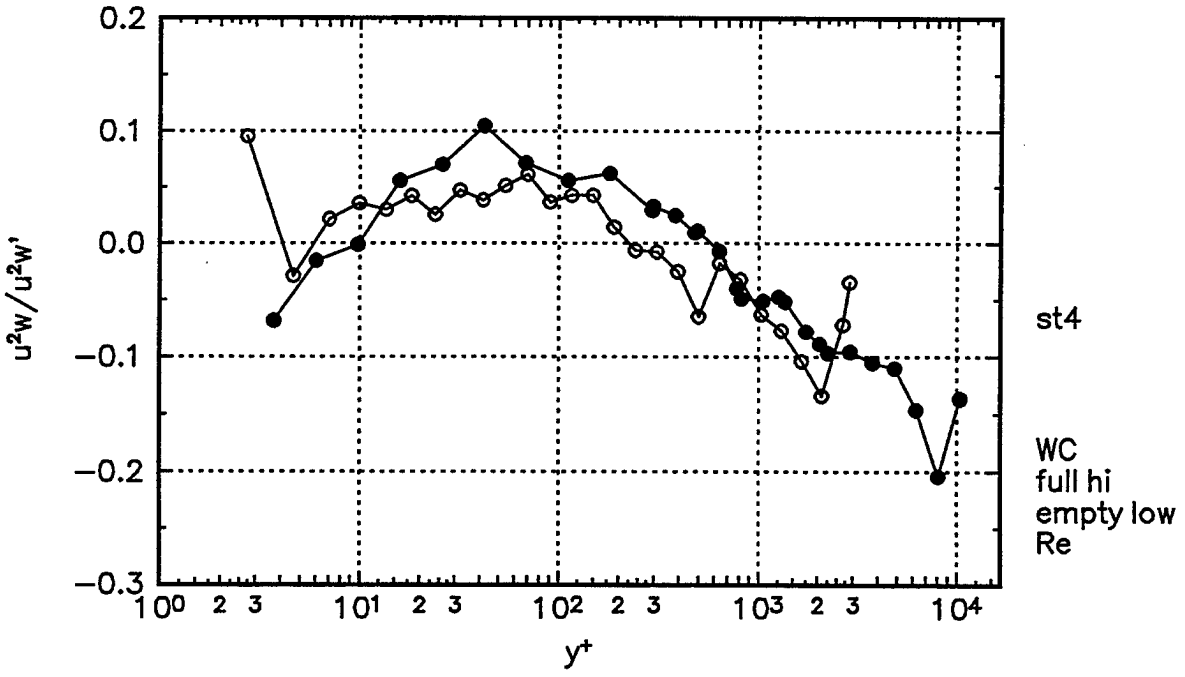

Figure 59d. $\overline{u^2w}$ triple products presented in wall-coordinates at Station 4.

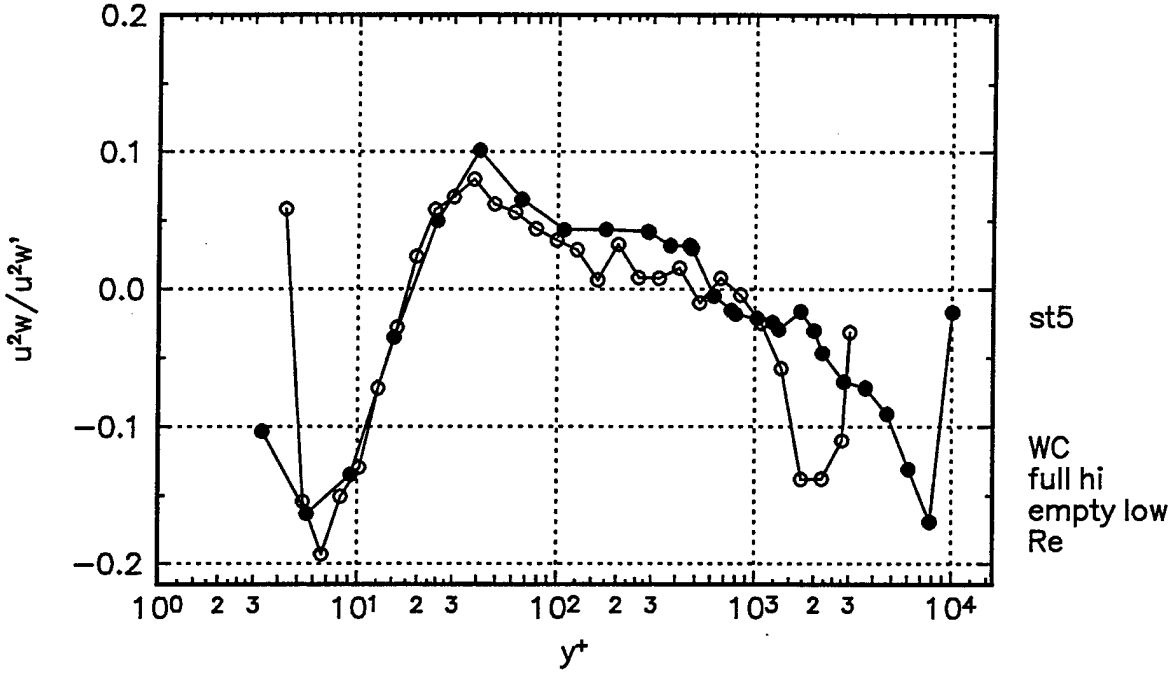

Figure 59e. $\overline{u^2w}$ triple products presented in wall-coordinates at Station 5.

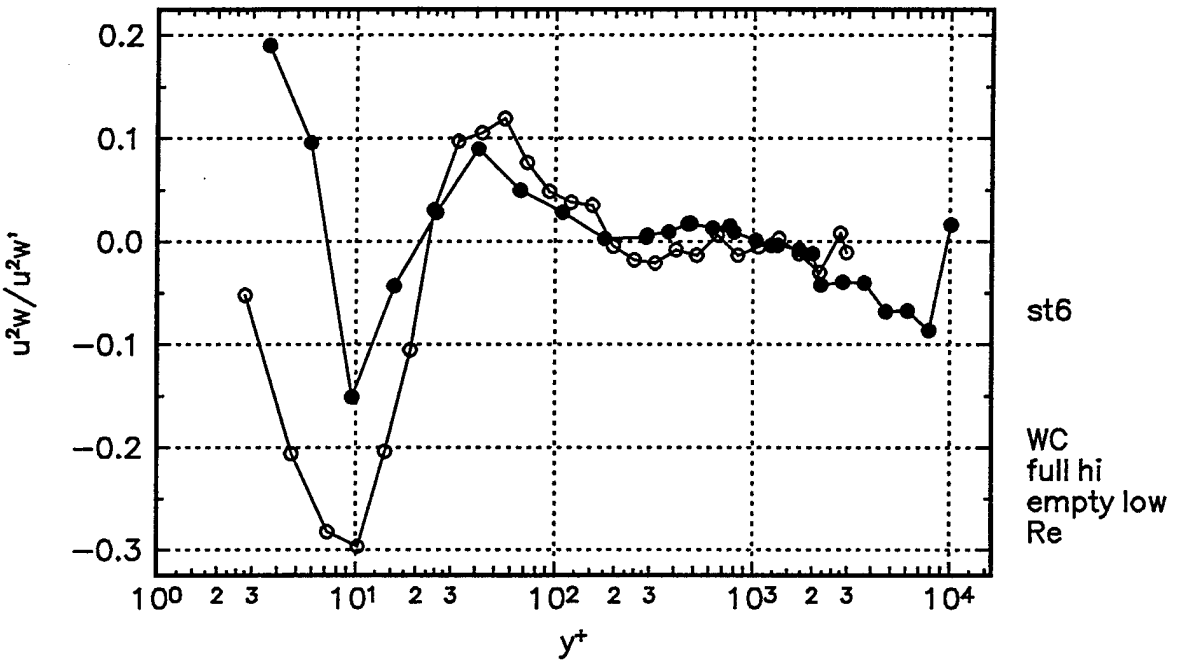

Figure 59f. $\overline{u^2w}$ triple products presented in wall-coordinates at Station 6.

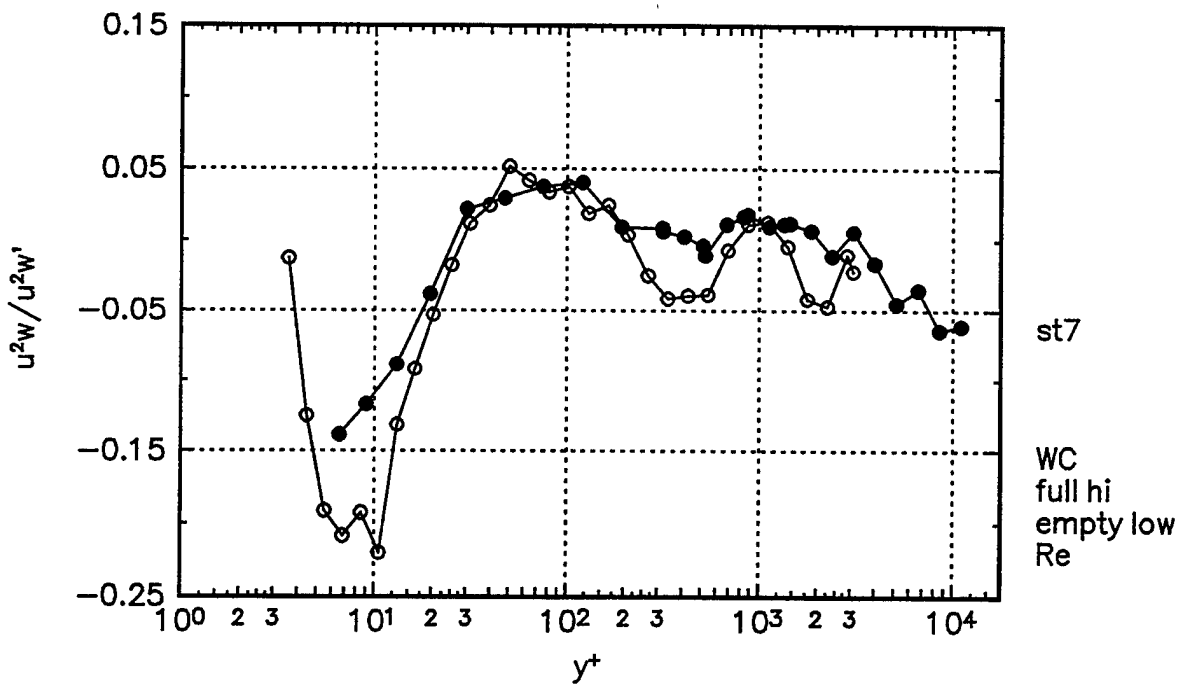

Figure 59g. $\overline{u^2w}$ triple products presented in wall-coordinates at Station 7.

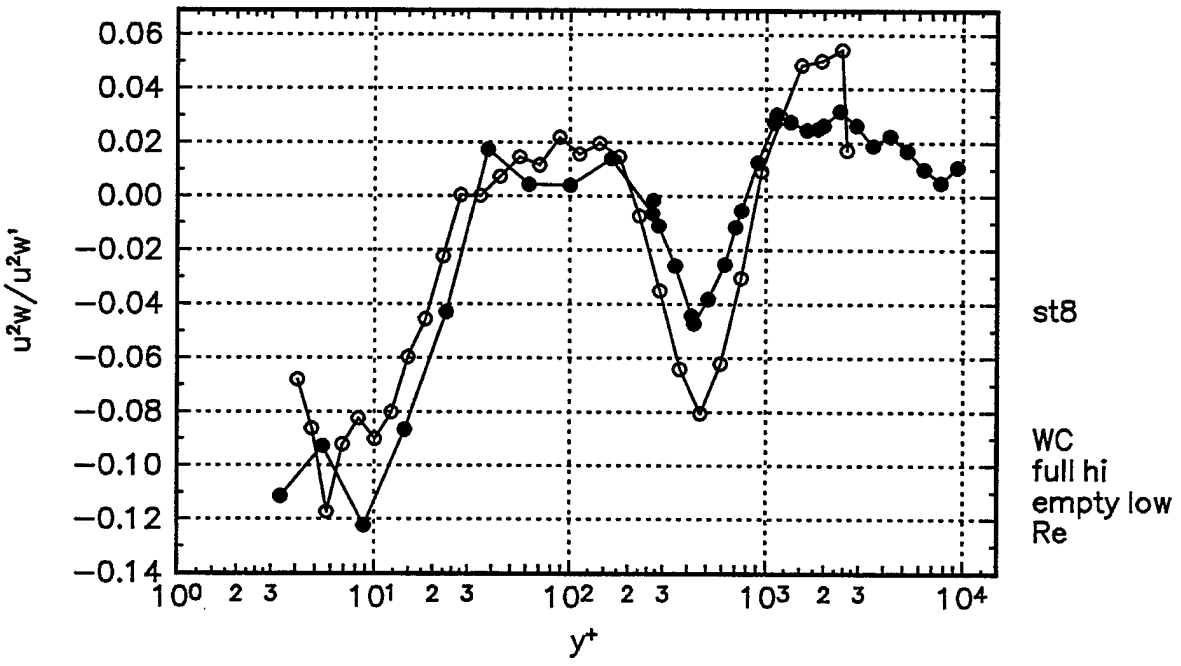

Figure 59h. $\overline{u^2w}$ triple products presented in wall-coordinates at Station 8.

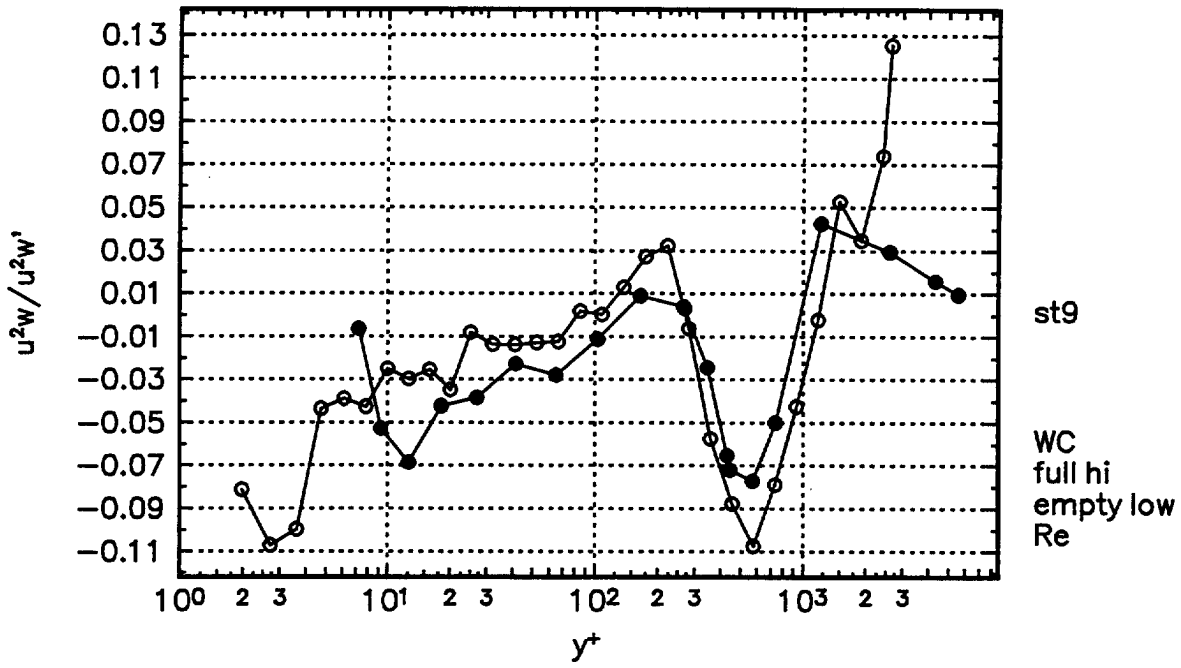

Figure 59i. $\overline{u^2w}$ triple products presented in wall-coordinates at Station 9.

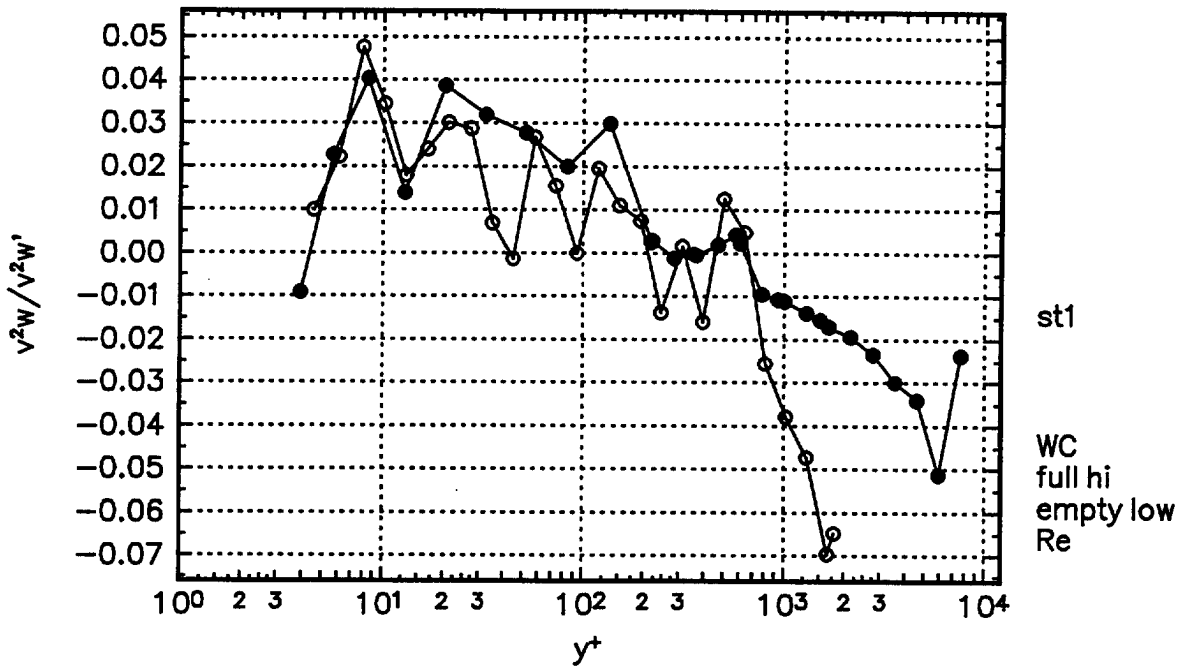

Figure 60a. $\overline{v^2w}$ triple products presented in wall-coordinates at Station 1.

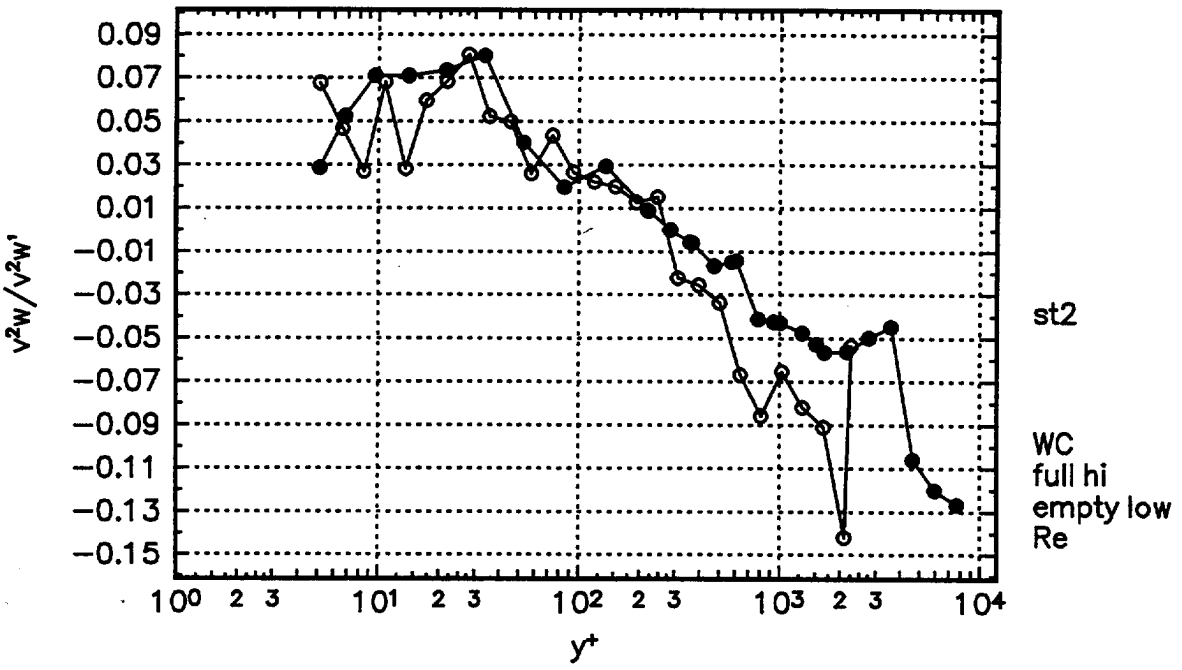

Figure 60b. $\overline{v^2w}$ triple products presented in wall-coordinates at Station 2.

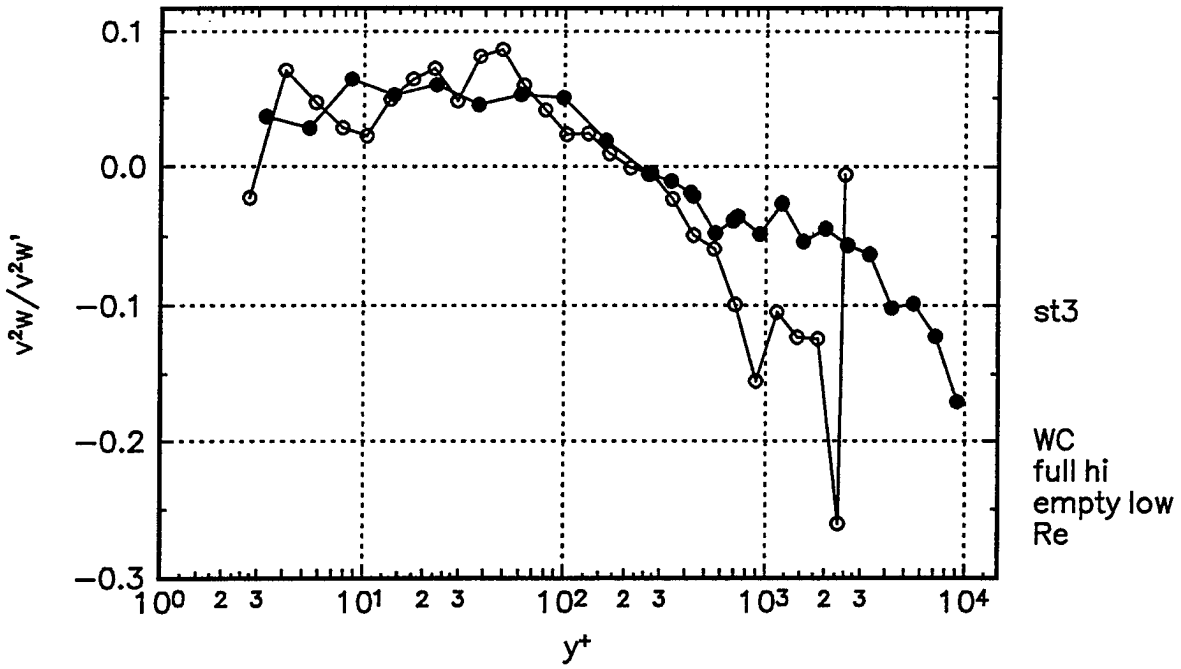

Figure 60c. $\overline{v^2w}$ triple products presented in wall-coordinates at Station 3.

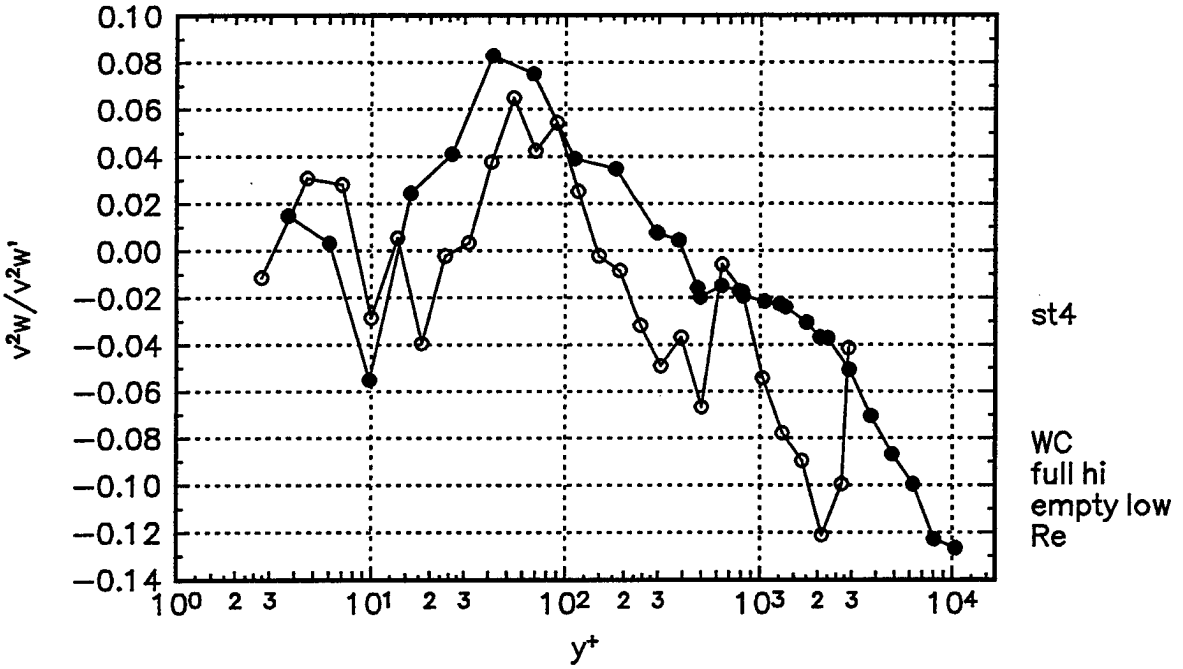

Figure 60d. $\overline{v^2w}$ triple products presented in wall-coordinates at Station 4.

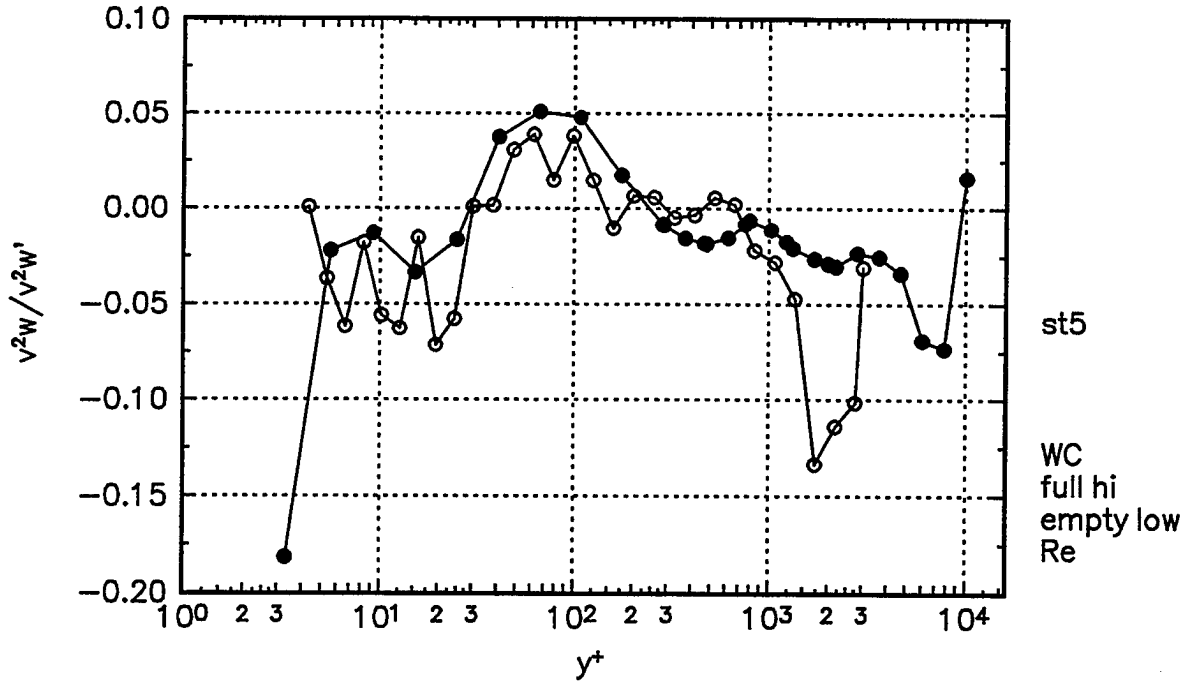

Figure 60e. $\overline{v^2w}$ triple products presented in wall-coordinates at Station 5.

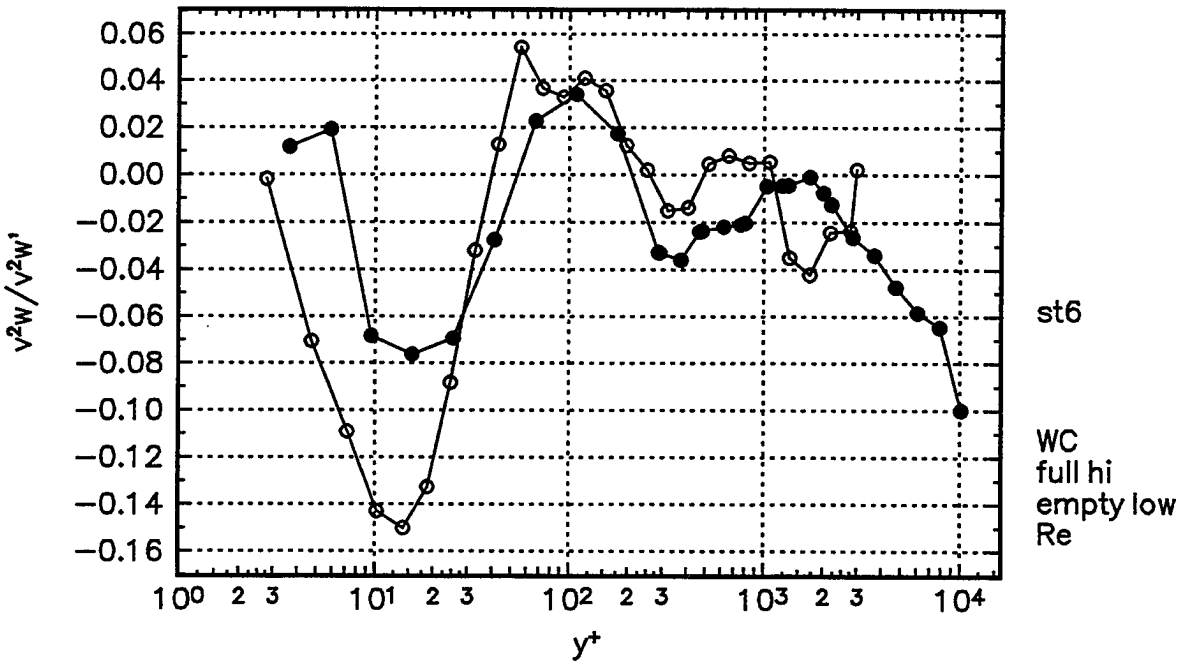

Figure 60f. $\overline{v^2w}$ triple products presented in wall-coordinates at Station 6.

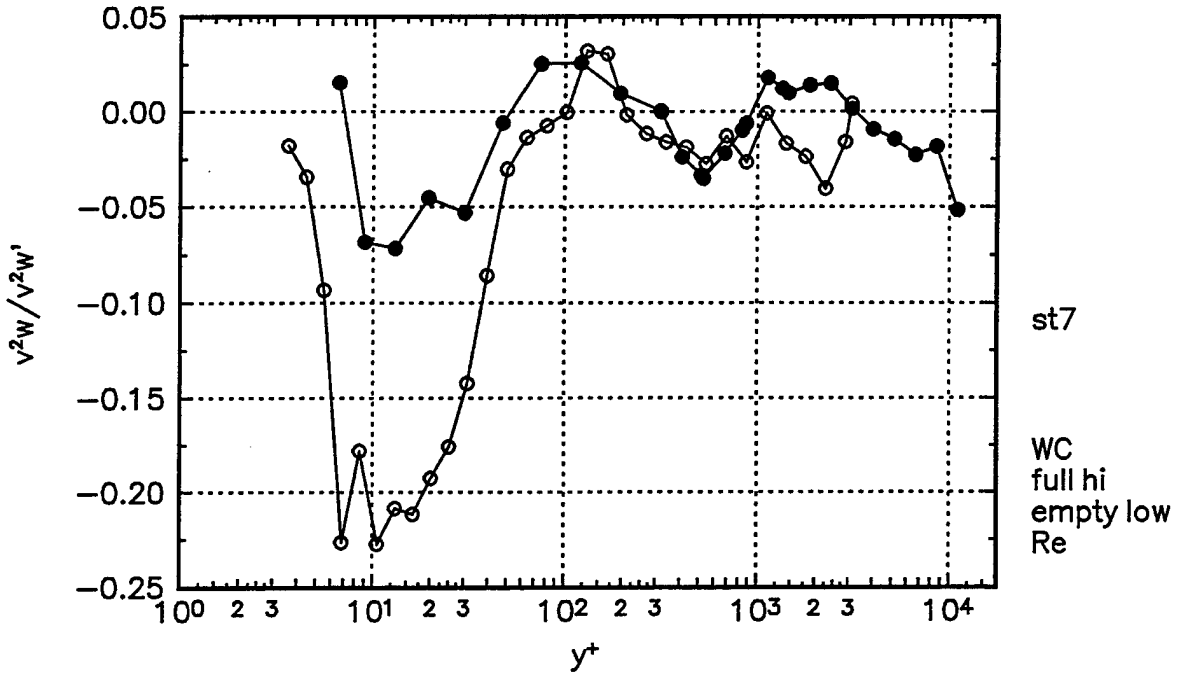

Figure 60g. $\overline{v^2w}$ triple products presented in wall-coordinates at Station 7.

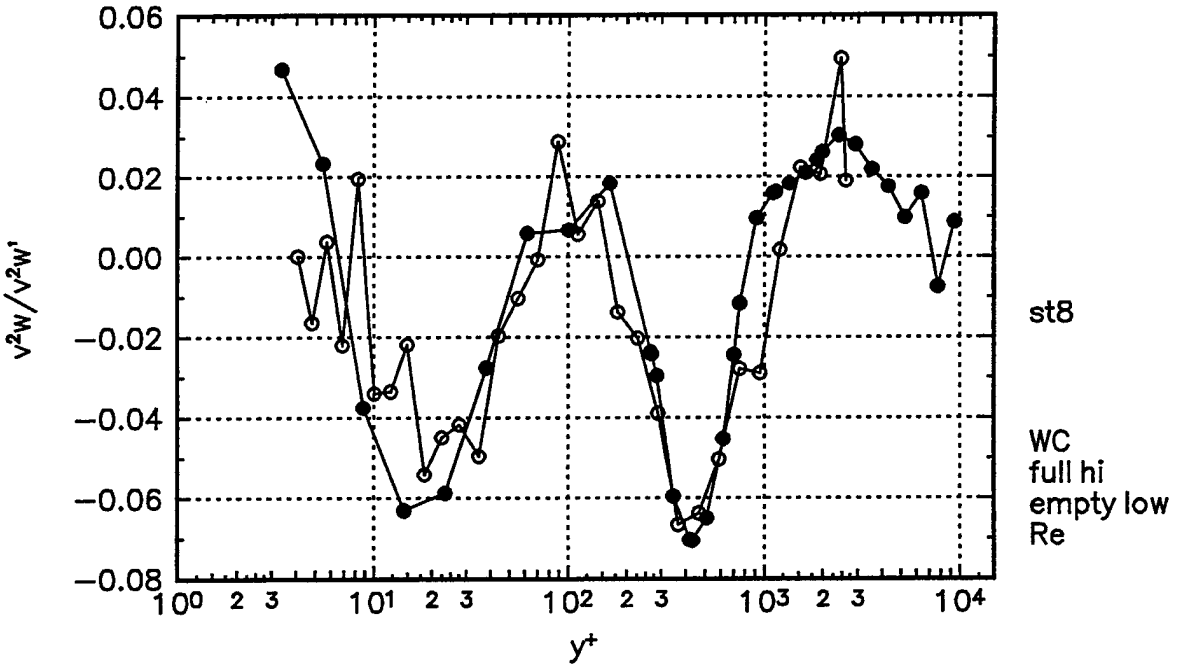

Figure 60h. $\overline{v^2w}$ triple products presented in wall-coordinates at Station 8.

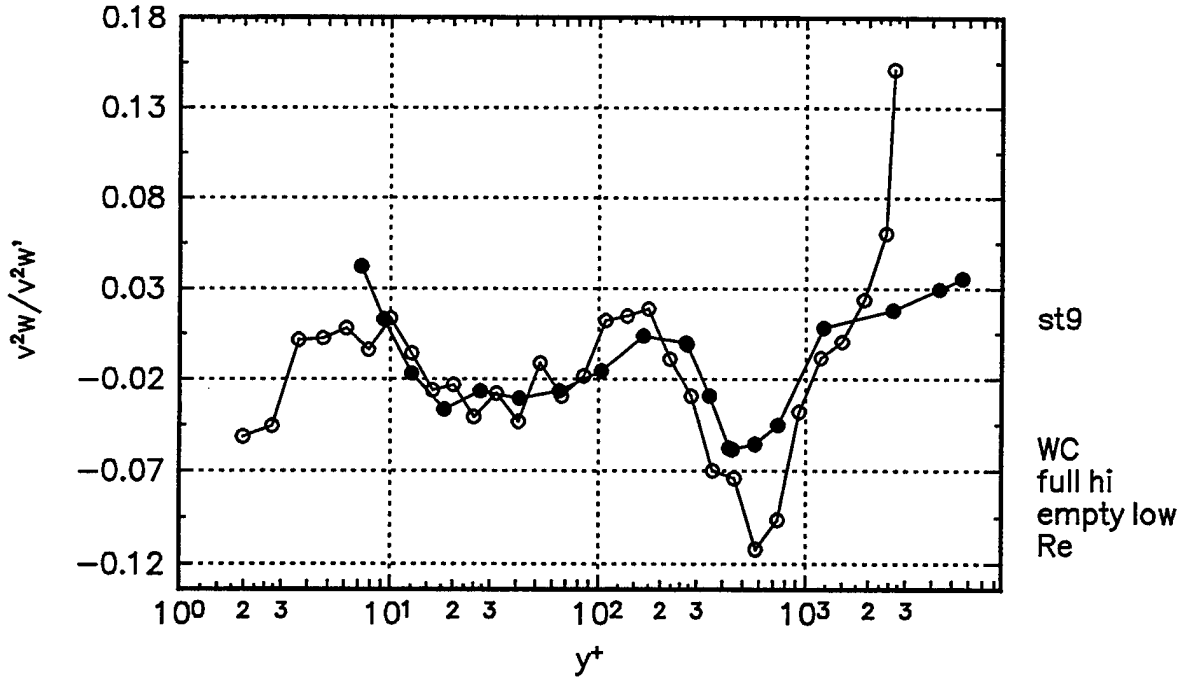

Figure 60i. $\overline{v^2w}$ triple products presented in wall-coordinates at Station 9.

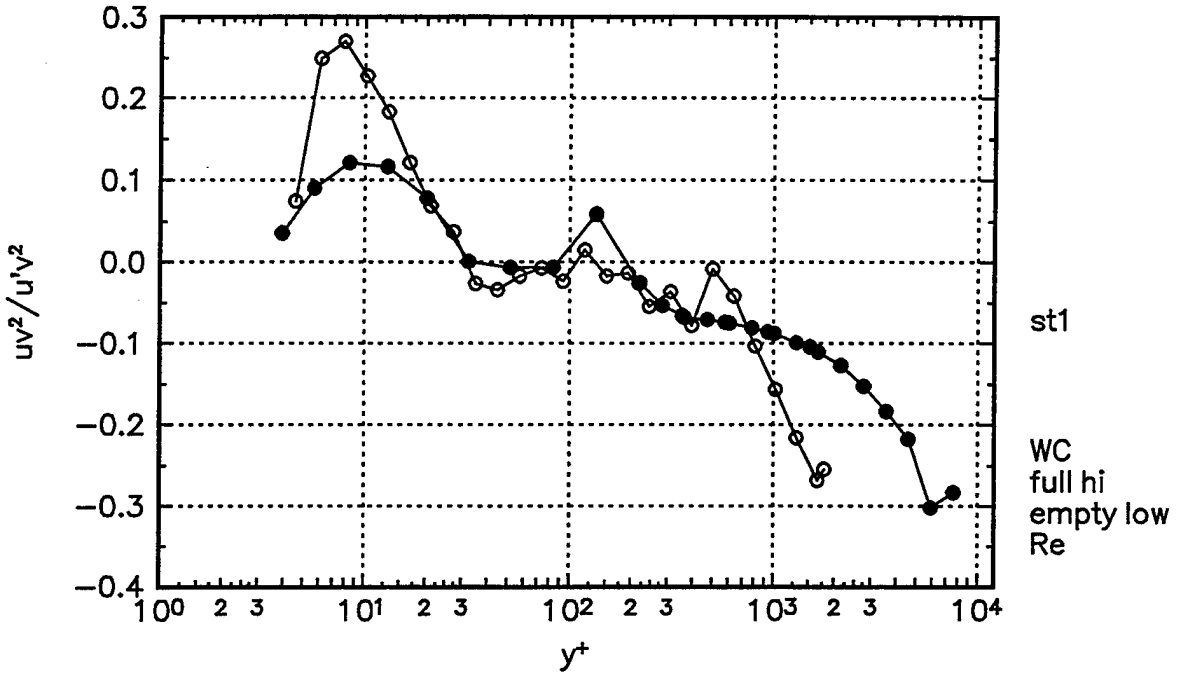

Figure 61a. $\overline{uv^2}$ triple products presented in wall-coordinates at Station 1.

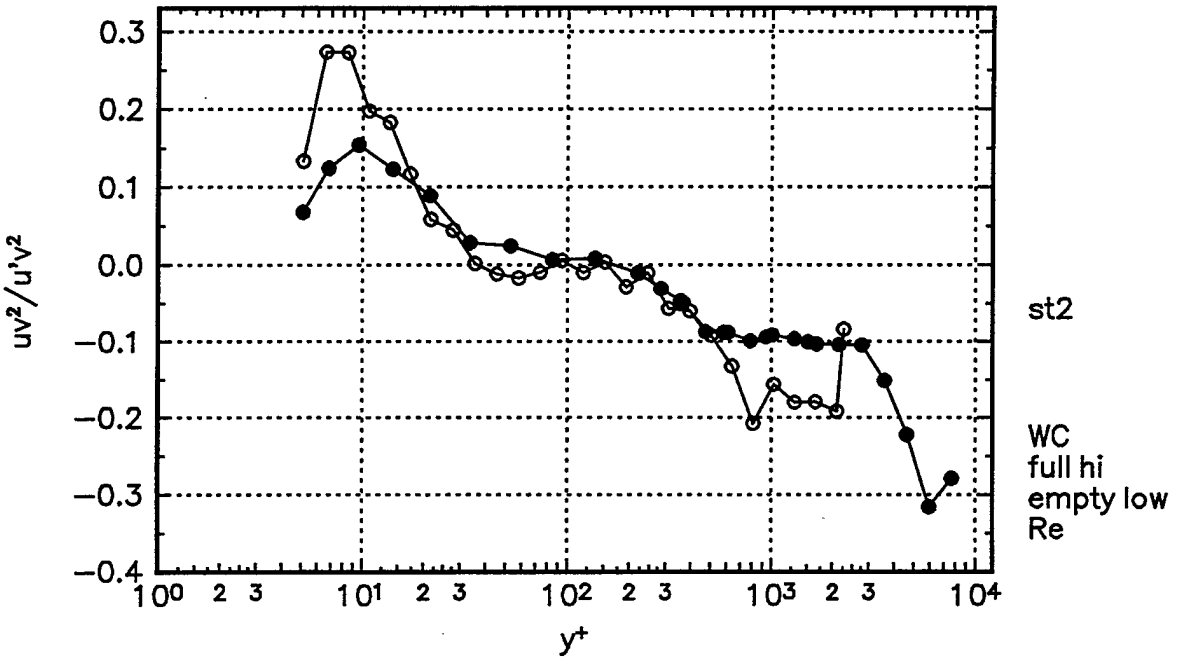

Figure 61b. $\overline{uv^2}$ triple products presented in wall-coordinates at Station 2.

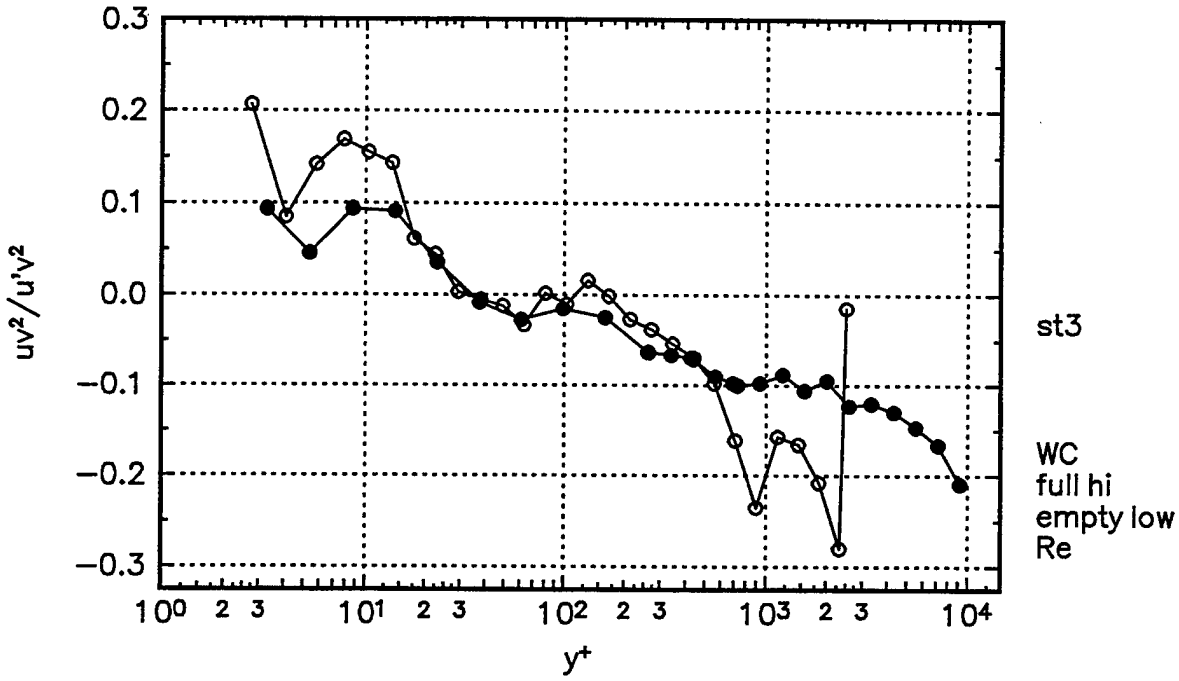

Figure 61c. $\overline{uv^2}$ triple products presented in wall-coordinates at Station 3.

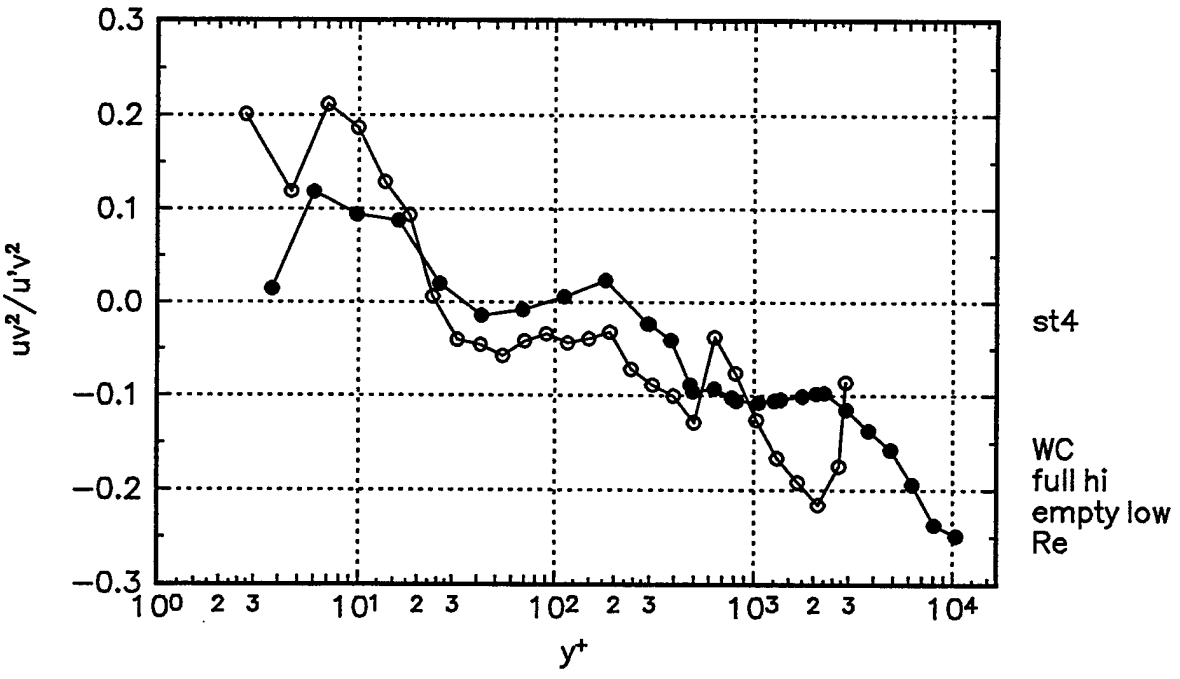

Figure 61d. $\overline{uv^2}$ triple products presented in wall-coordinates at Station 4.

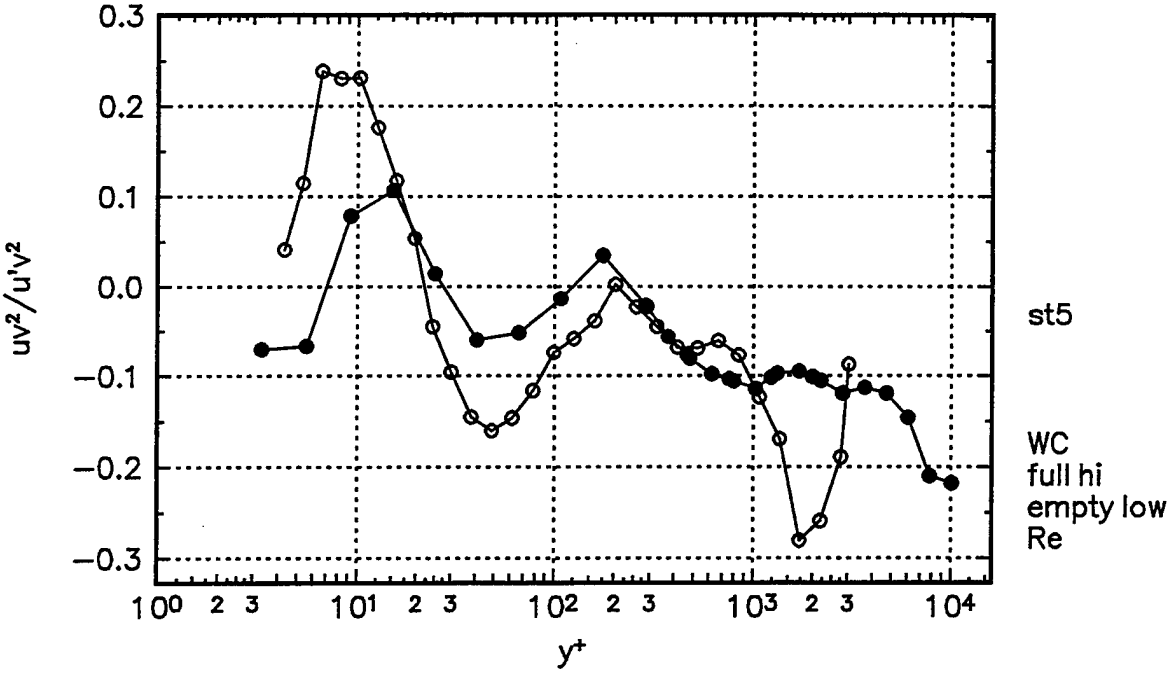

Figure 61e. $\overline{uv^2}$ triple products presented in wall-coordinates at Station 5.

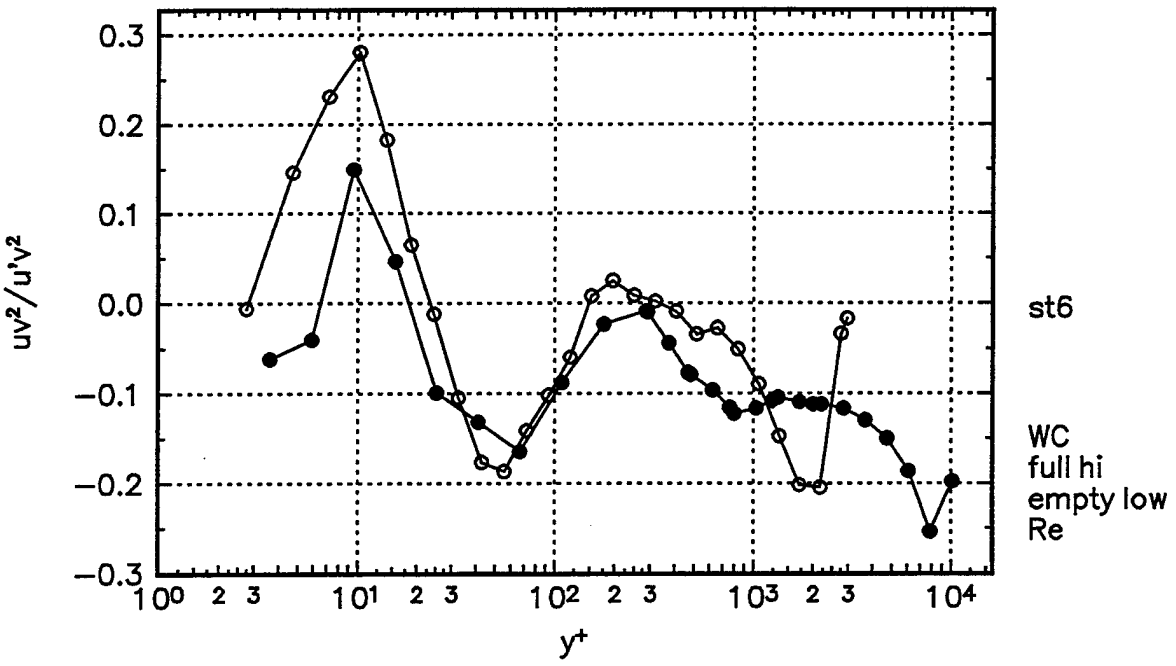

Figure 61f. $\overline{uv^2}$ triple products presented in wall-coordinates at Station 6.

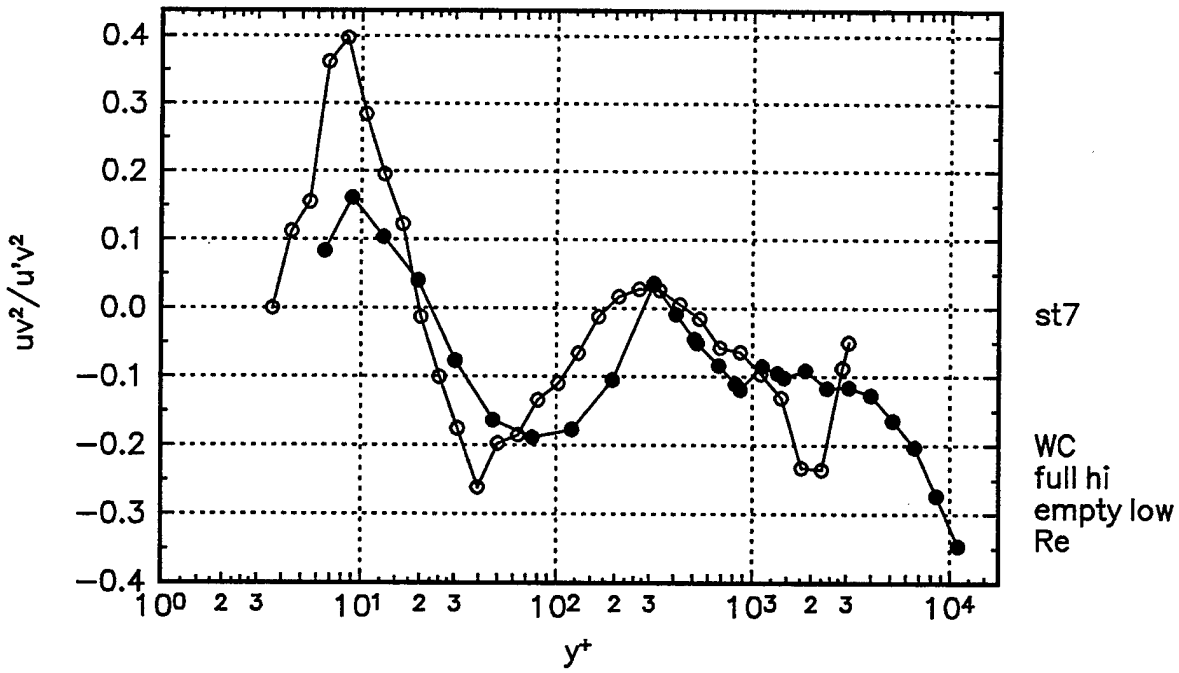

Figure 61g. $\overline{uv^2}$ triple products presented in wall-coordinates at Station 7.

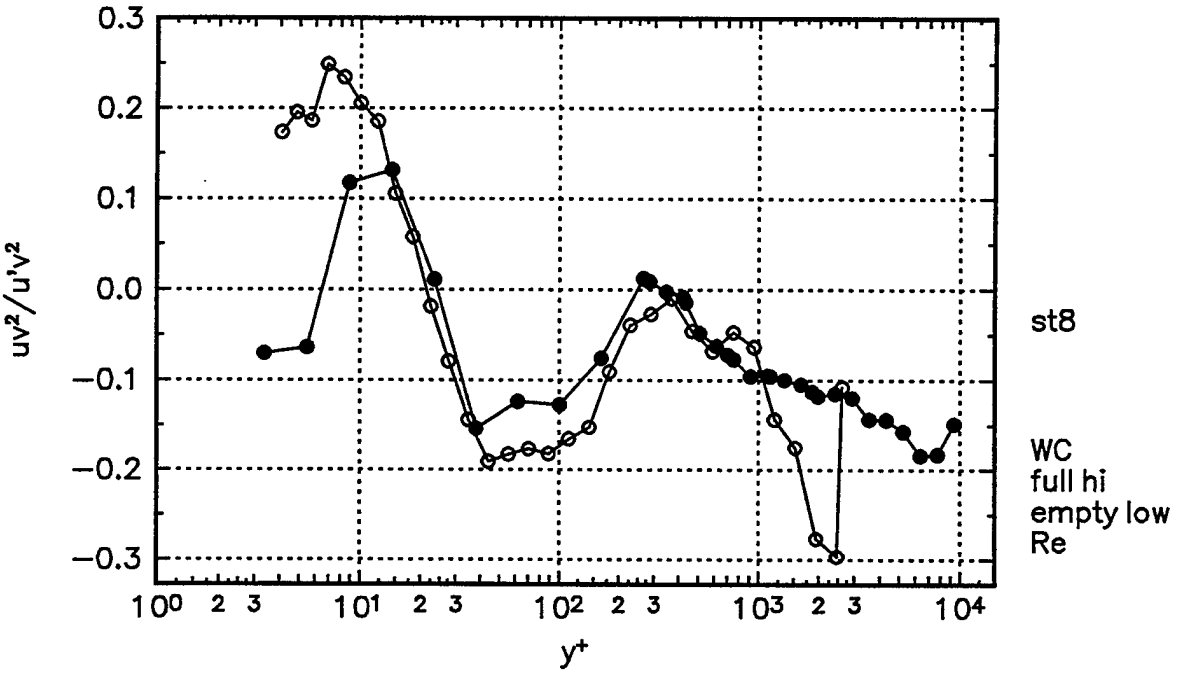

Figure 61h. $\overline{uv^2}$ triple products presented in wall-coordinates at Station 8.

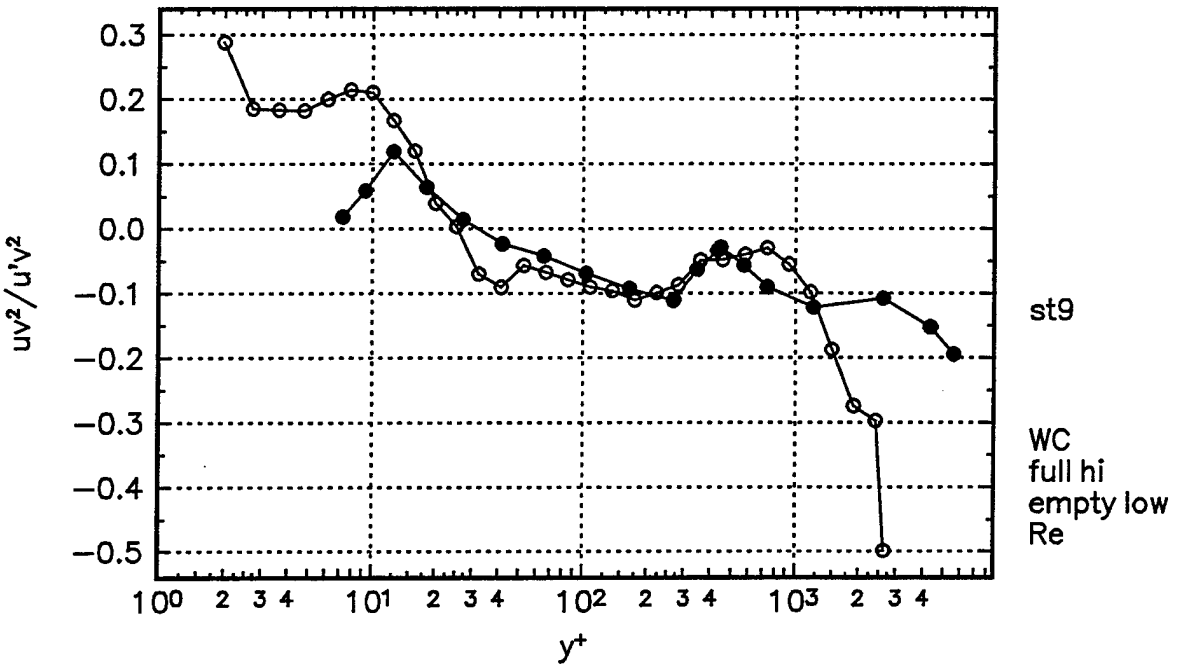

Figure 61i. $\overline{uv^2}$ triple products presented in wall-coordinates at Station 9.

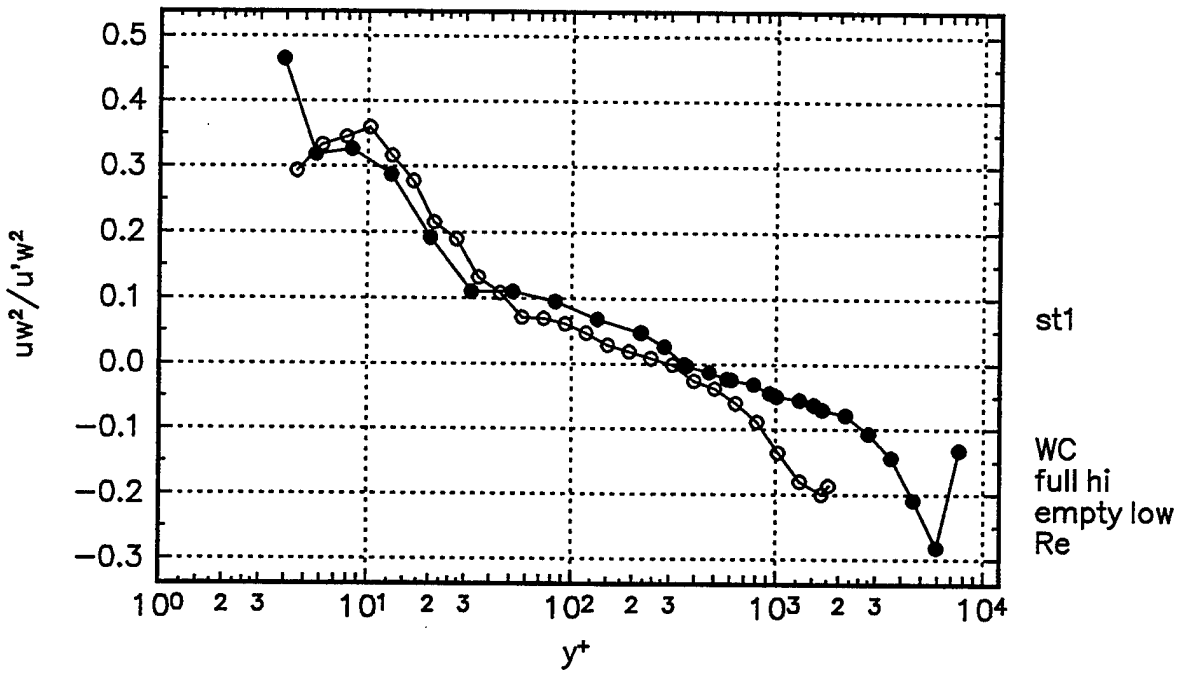

Figure 62a. $\overline{uw^2}$ triple products presented in wall-coordinates at Station 1.

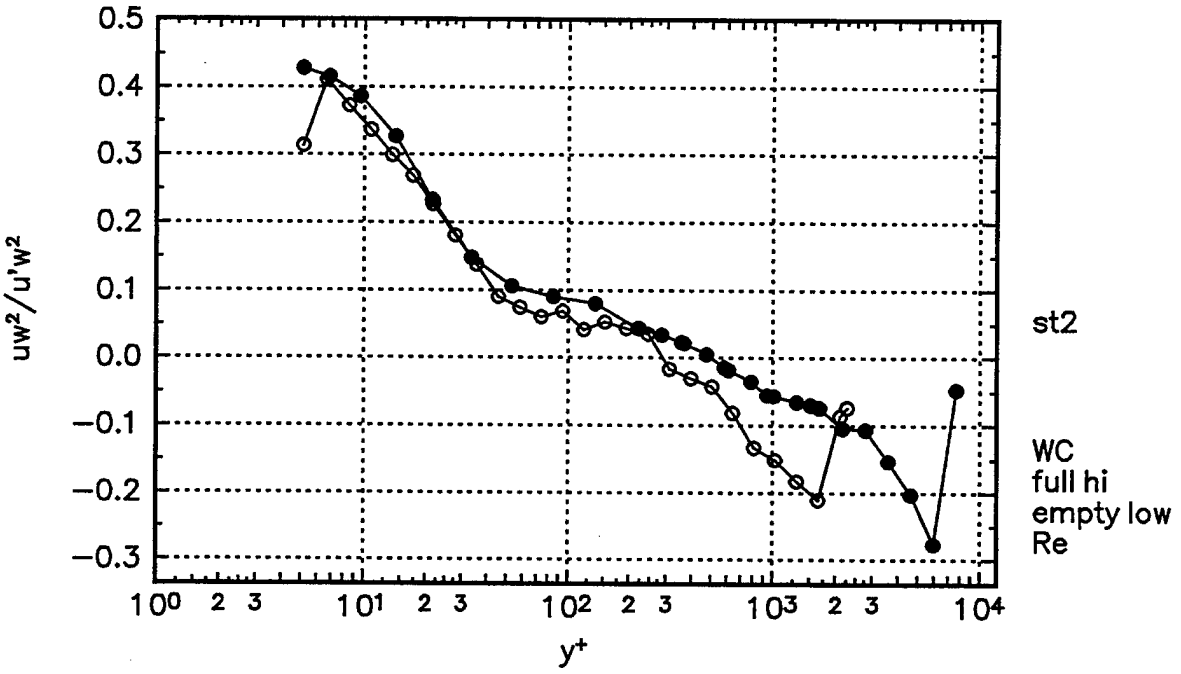

Figure 62b. $\overline{uw^2}$ triple products presented in wall-coordinates at Station 2.

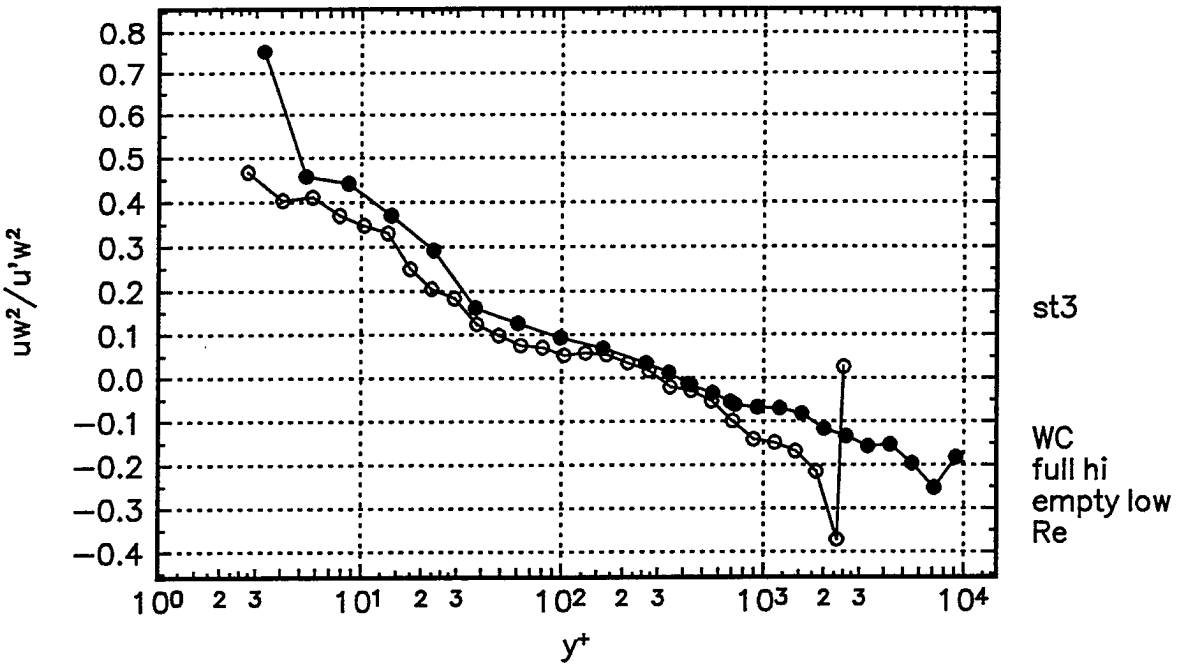

Figure 62c. $\overline{uw^2}$ triple products presented in wall-coordinates at Station 3.

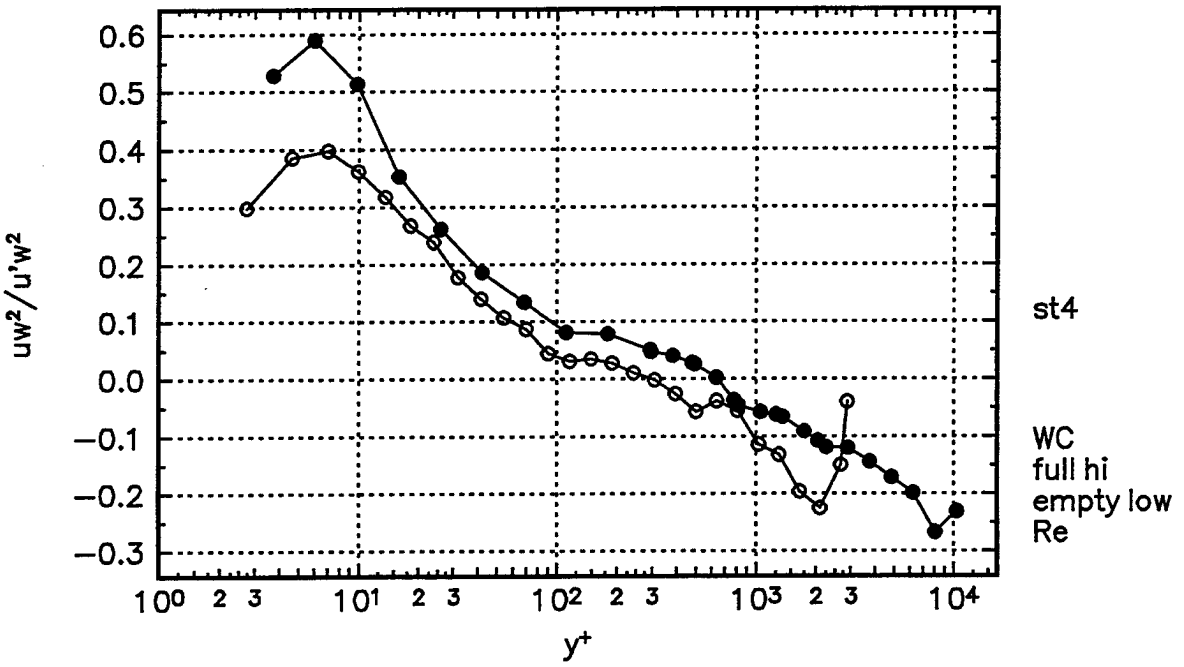

Figure 62d. $\overline{uw^2}$ triple products presented in wall-coordinates at Station 4.

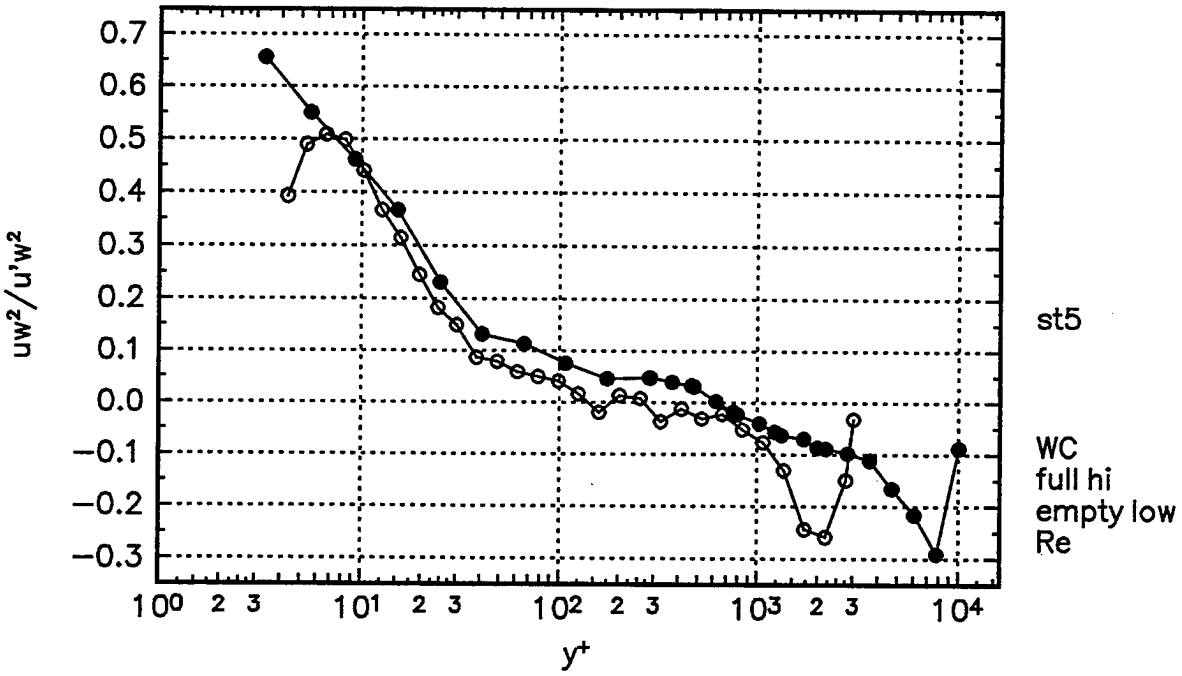

Figure 62e. $\overline{uw^2}$ triple products presented in wall-coordinates at Station 5.

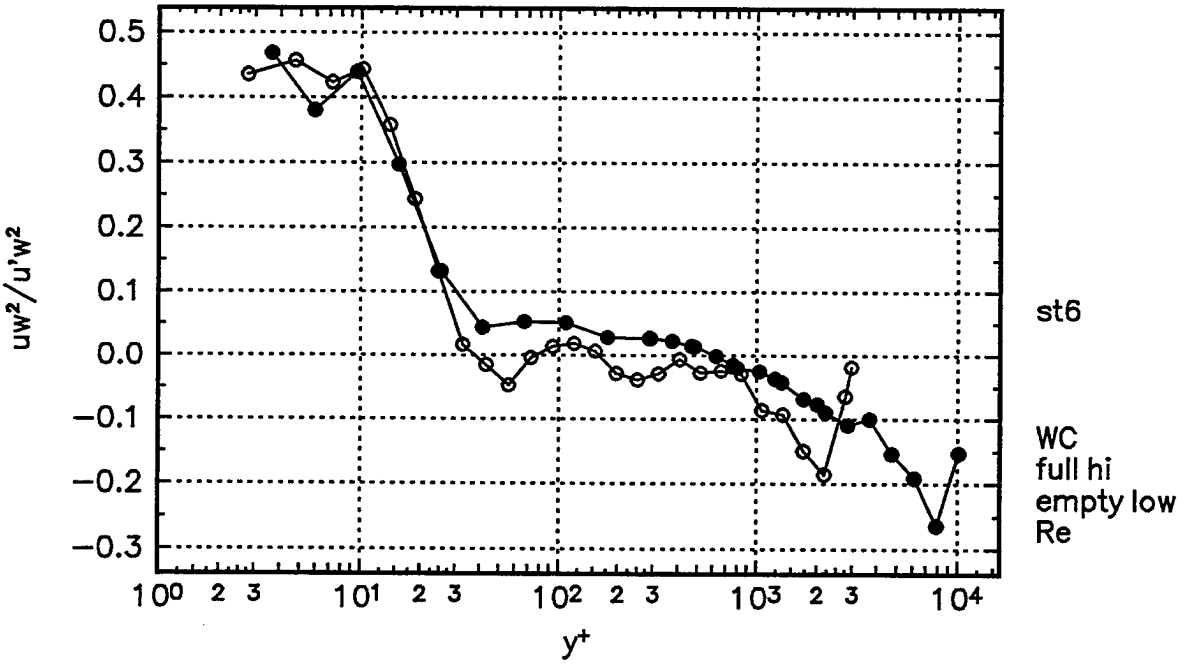

Figure 62f. $\overline{uw^2}$ triple products presented in wall-coordinates at Station 6.

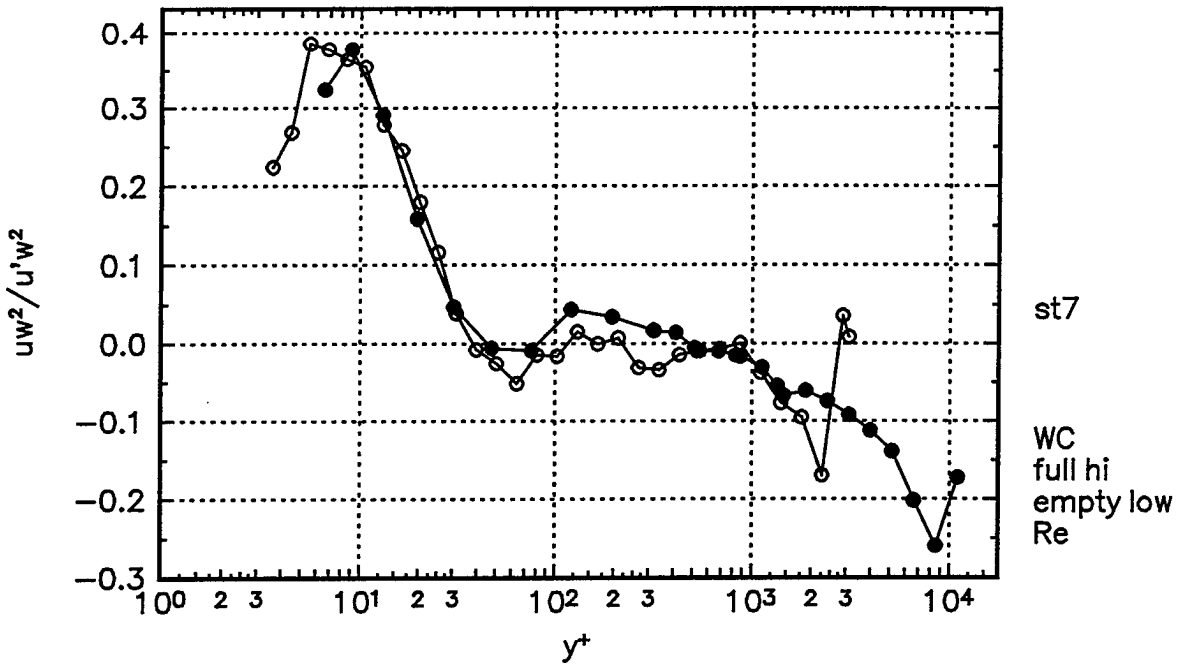

Figure 62g. $\overline{uw^2}$ triple products presented in wall-coordinates at Station 7.

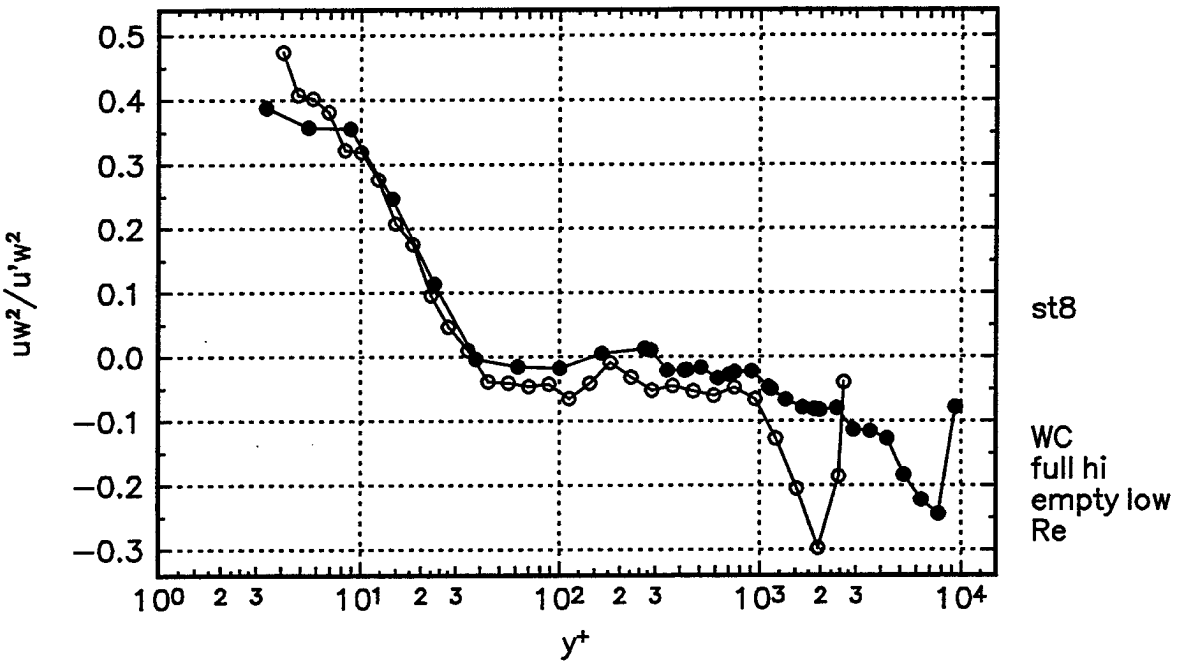

Figure 62h. $\overline{uw^2}$ triple products presented in wall-coordinates at Station 8.

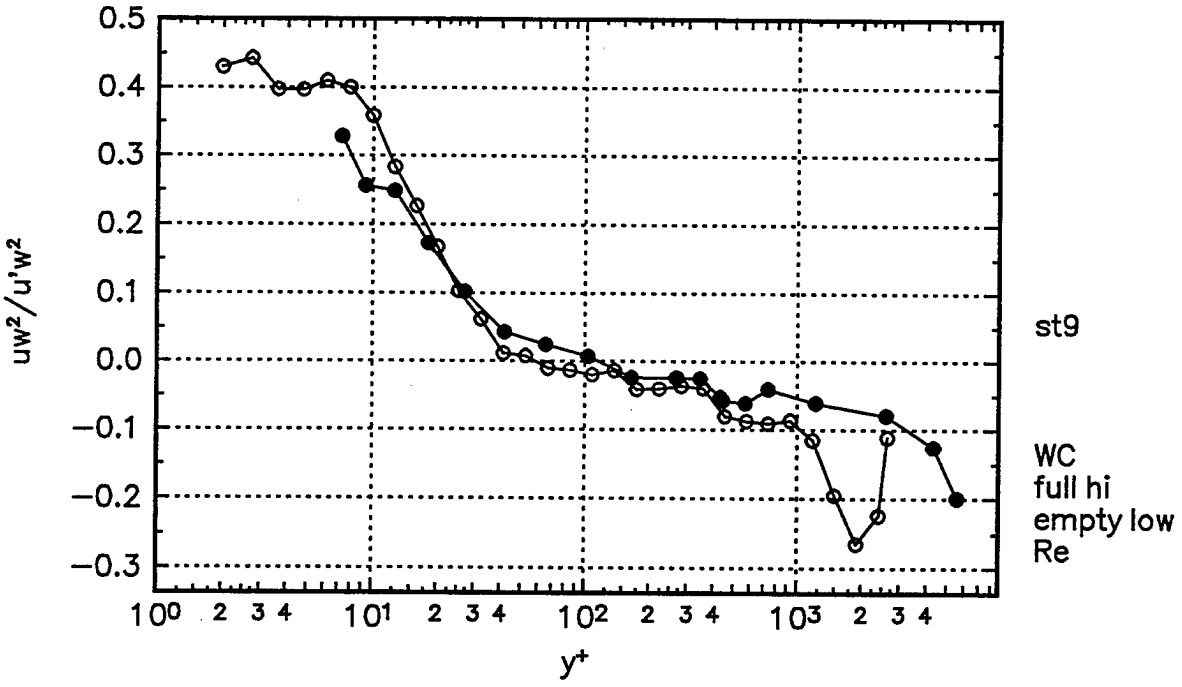

Figure 62i. $\overline{uw^2}$ triple products presented in wall-coordinates at Station 9.

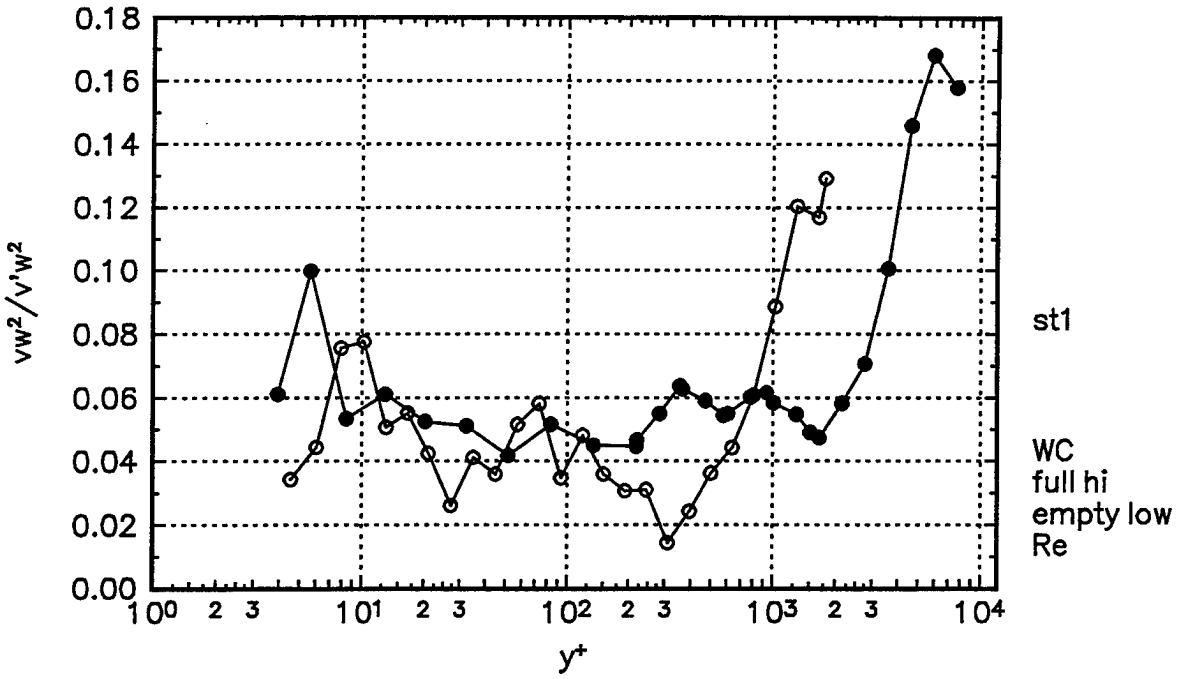

Figure 63a. $\overline{vw^2}$ triple products presented in wall-coordinates at Station 1.

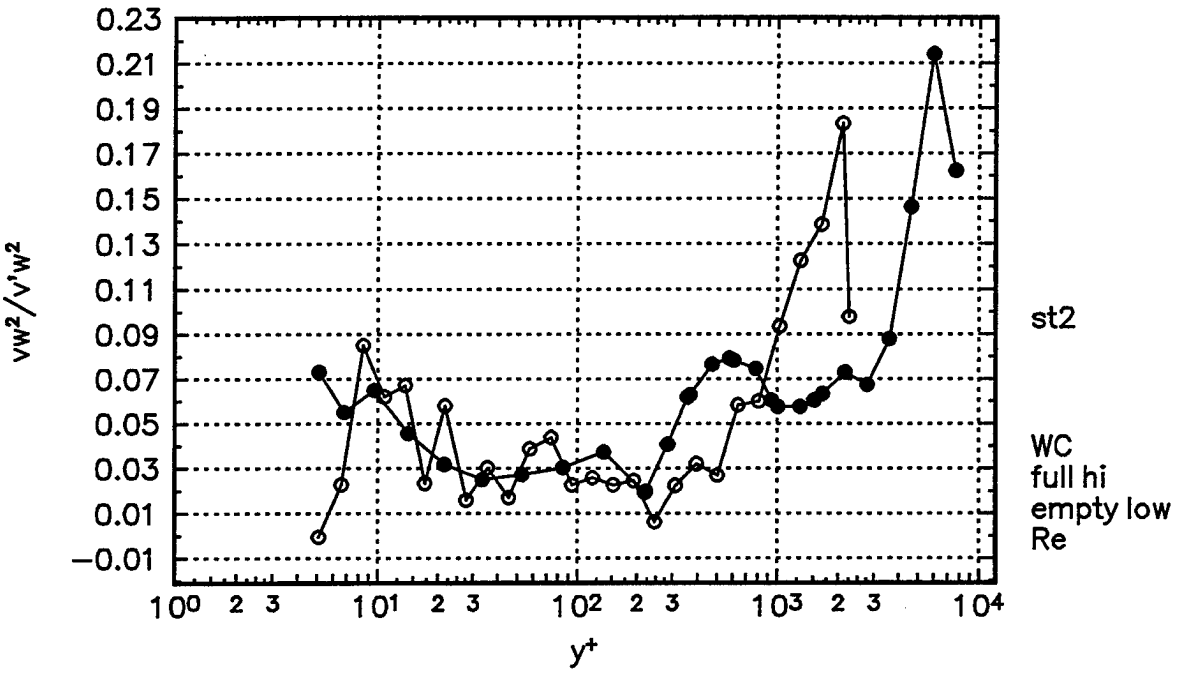

Figure 63b. $\overline{vw^2}$ triple products presented in wall-coordinates at Station 2.

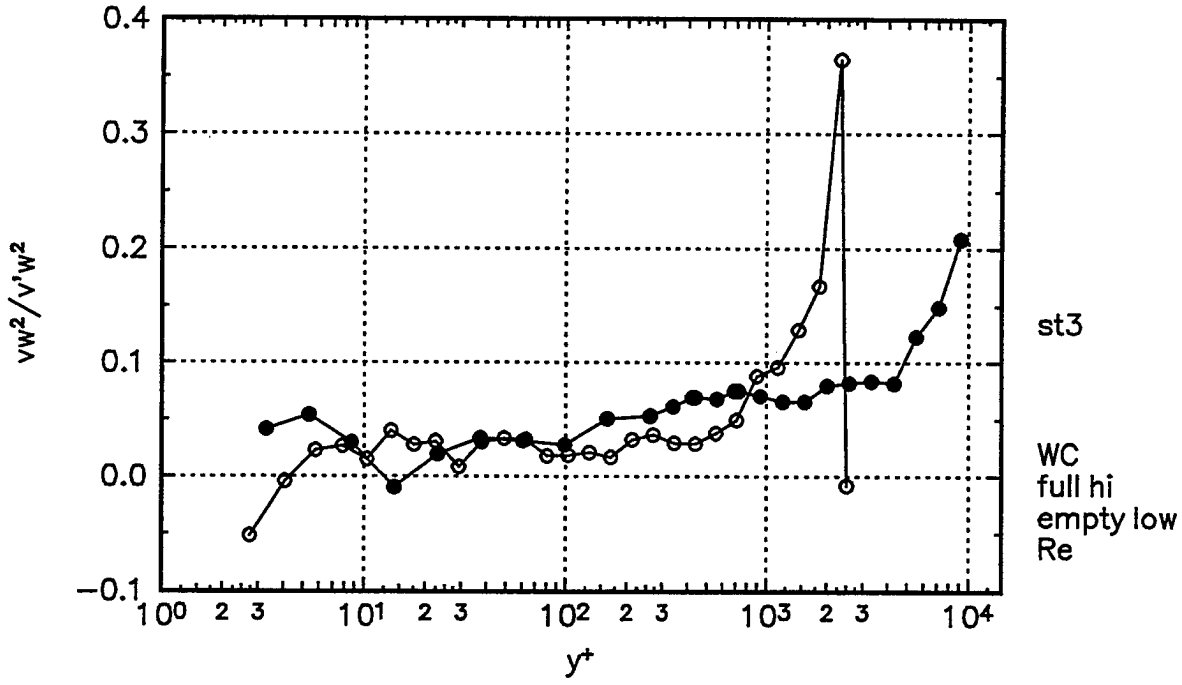

Figure 63c. $\overline{vw^2}$ triple products presented in wall-coordinates at Station 3.

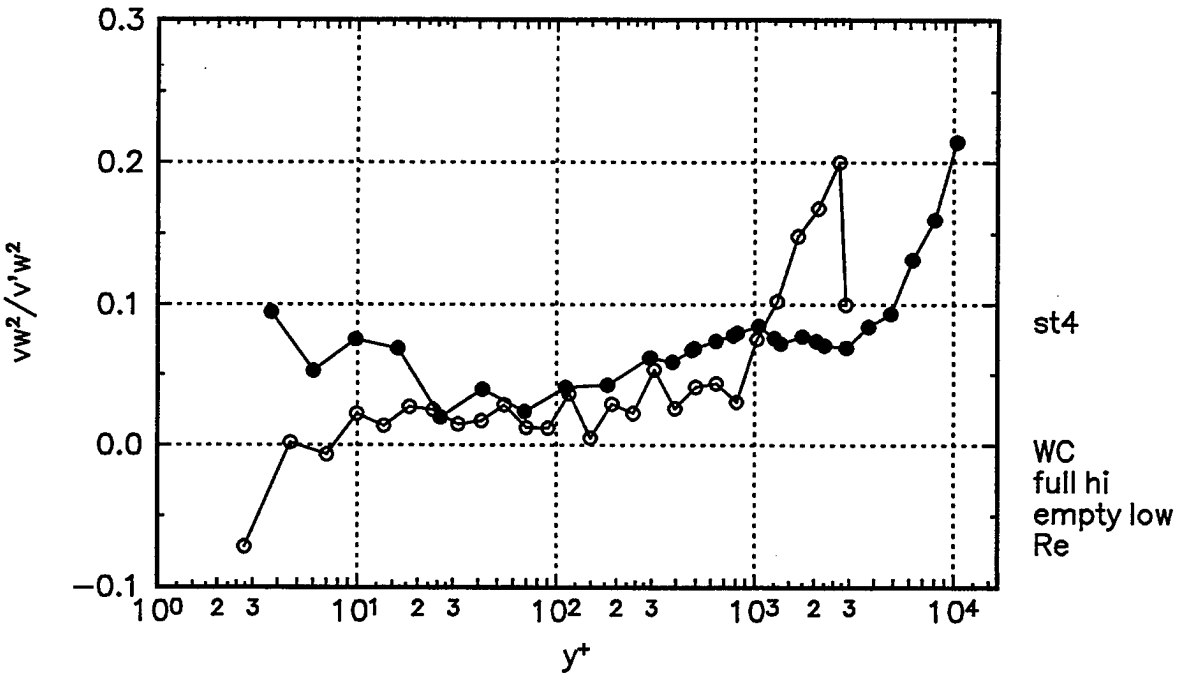

Figure 63d. $\overline{vw^2}$ triple products presented in wall-coordinates at Station 4.

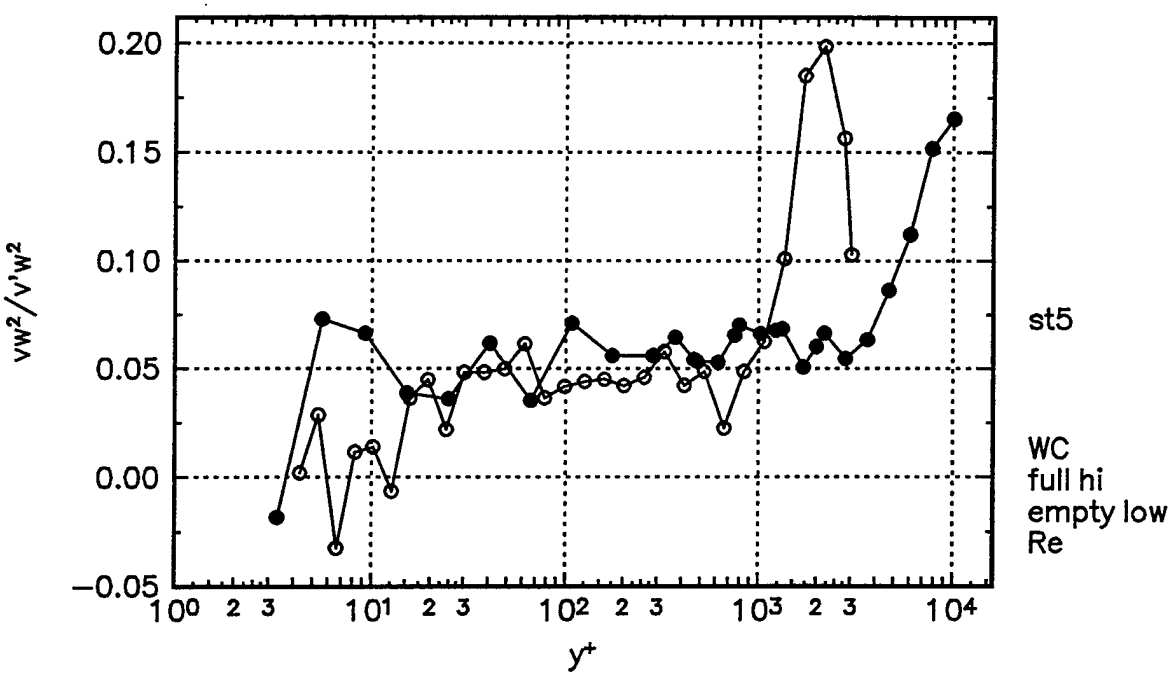

Figure 63e. $\overline{vw^2}$ triple products presented in wall-coordinates at Station 5.

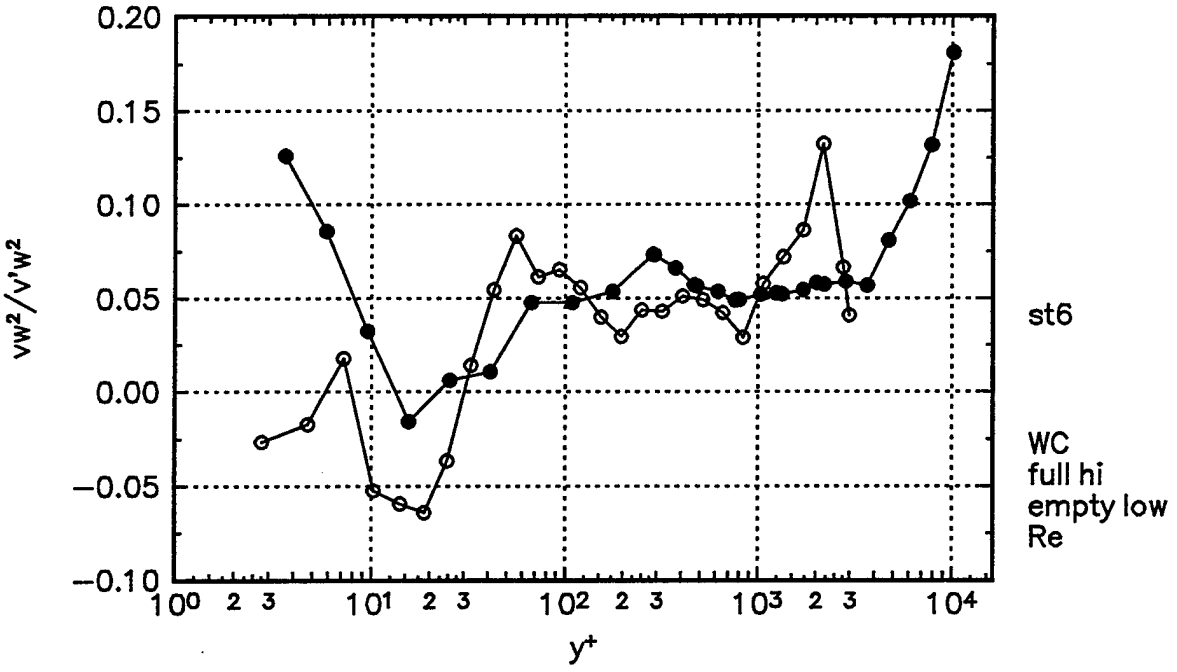

Figure 63f. $\overline{vw^2}$ triple products presented in wall-coordinates at Station 6.

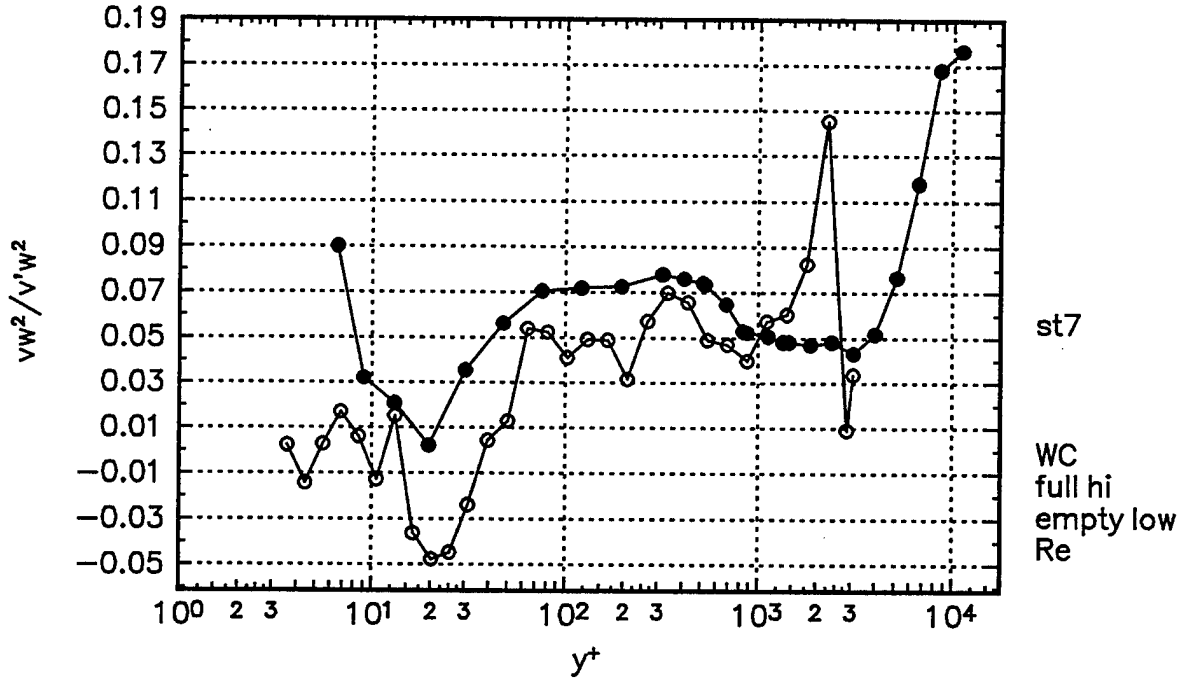

Figure 63g. $\overline{vw^2}$ triple products presented in wall-coordinates at Station 7.

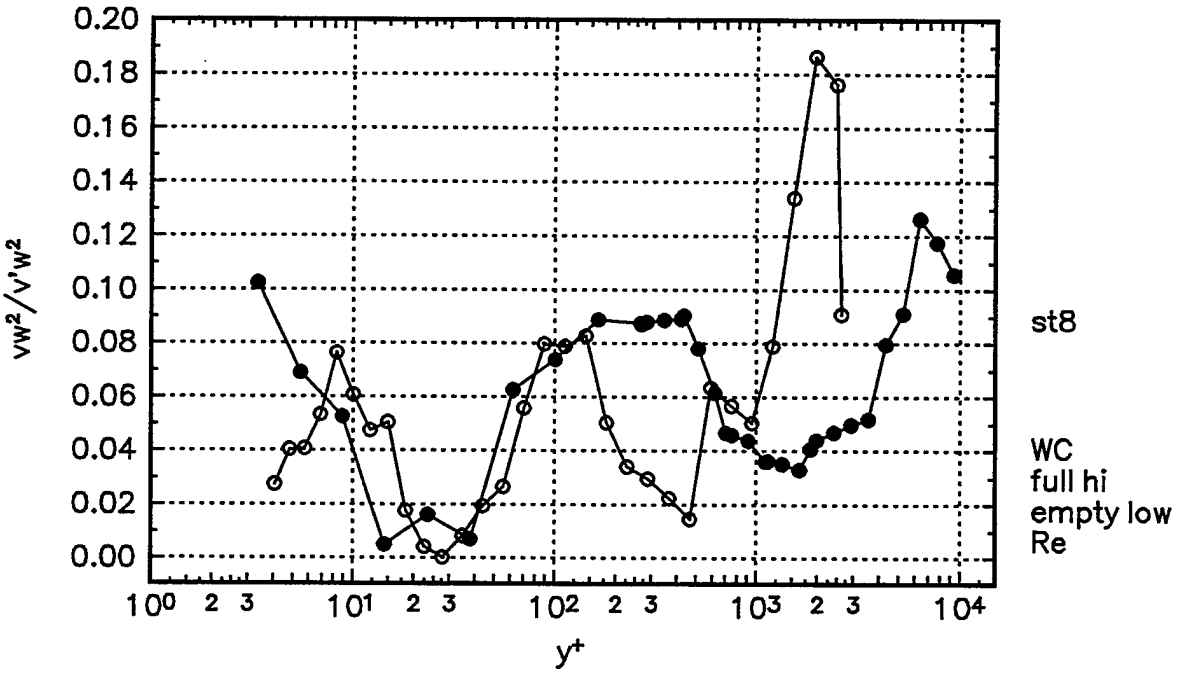

Figure 63h. $\overline{vw^2}$ triple products presented in wall-coordinates at Station 8.

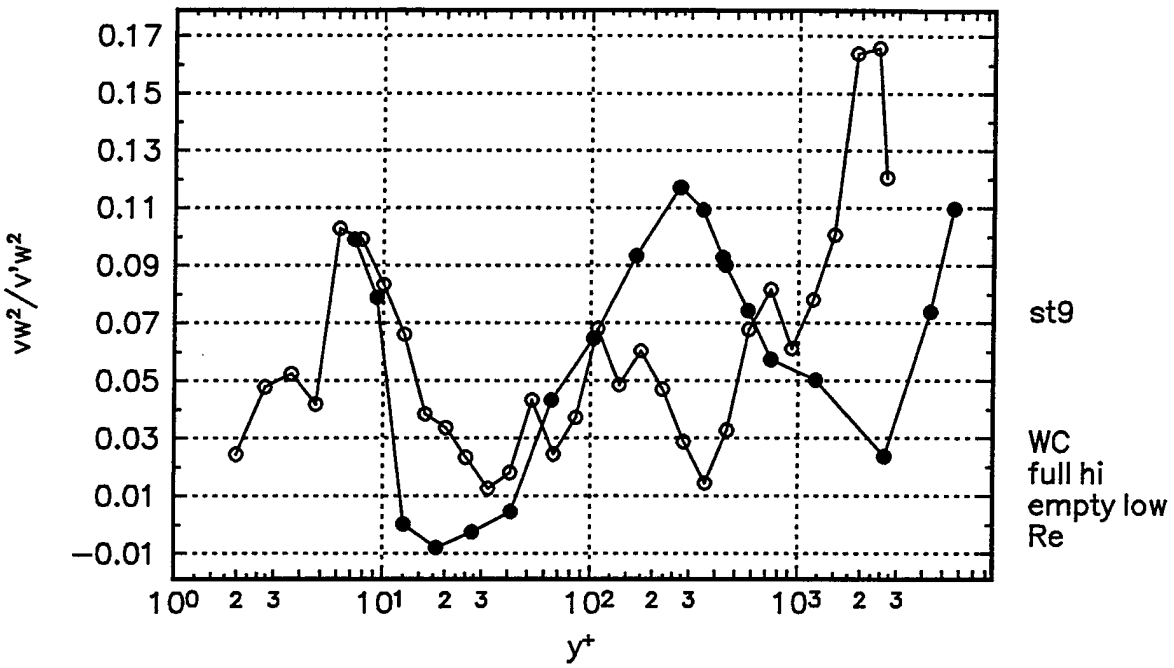

Figure 63i. $\overline{vw^2}$ triple products presented in wall-coordinates at Station 9.

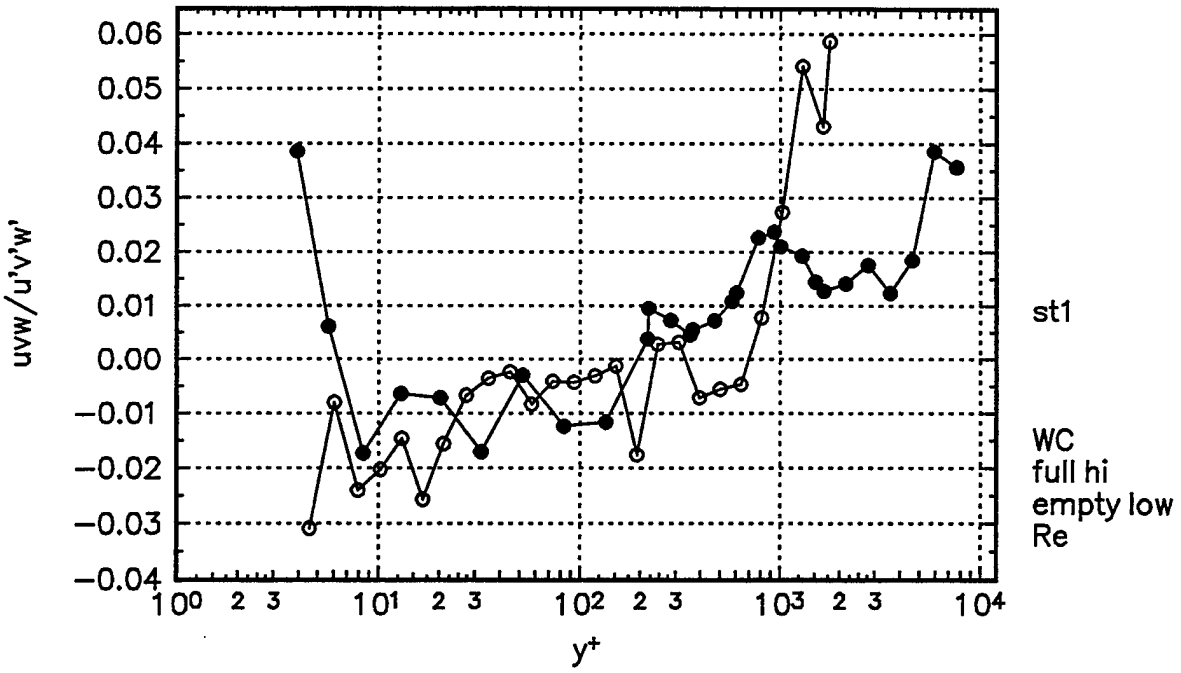

Figure 64a. $\overline{uvw}$ triple products presented in wall-coordinates at Station 1.

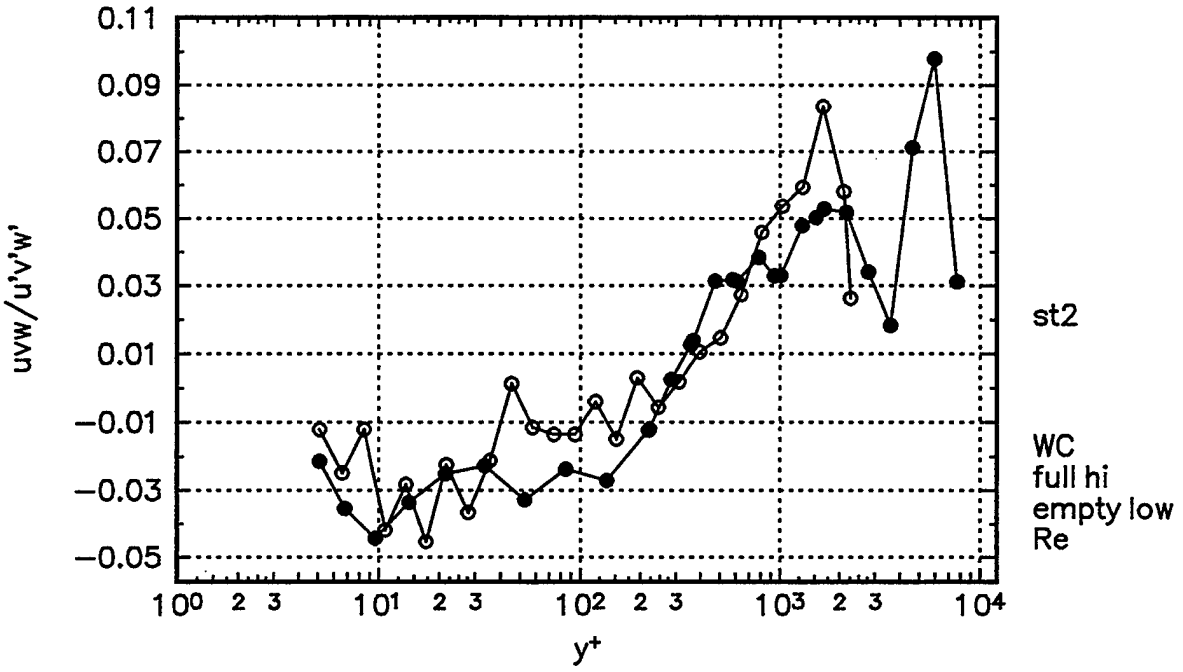

Figure 64b. $\overline{uvw}$ triple products presented in wall-coordinates at Station 2.

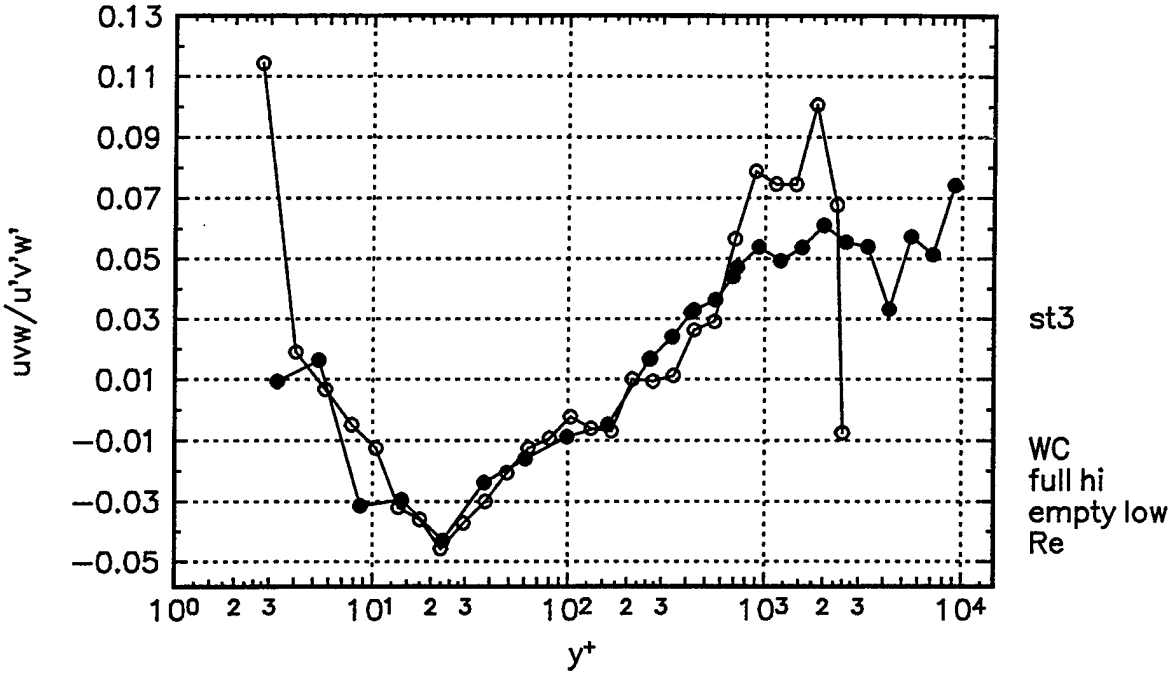

Figure 64c. $\overline{uvw}$ triple products presented in wall-coordinates at Station 3.

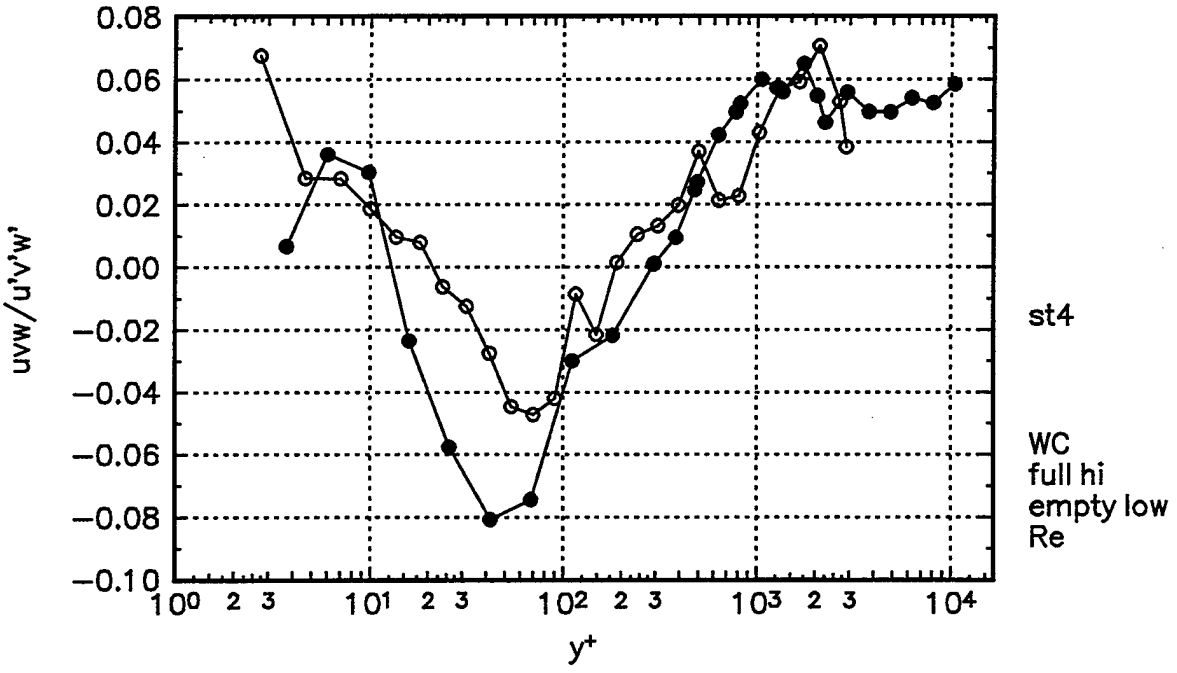

Figure 64d. $\overline{uvw}$ triple products presented in wall-coordinates at Station 4.

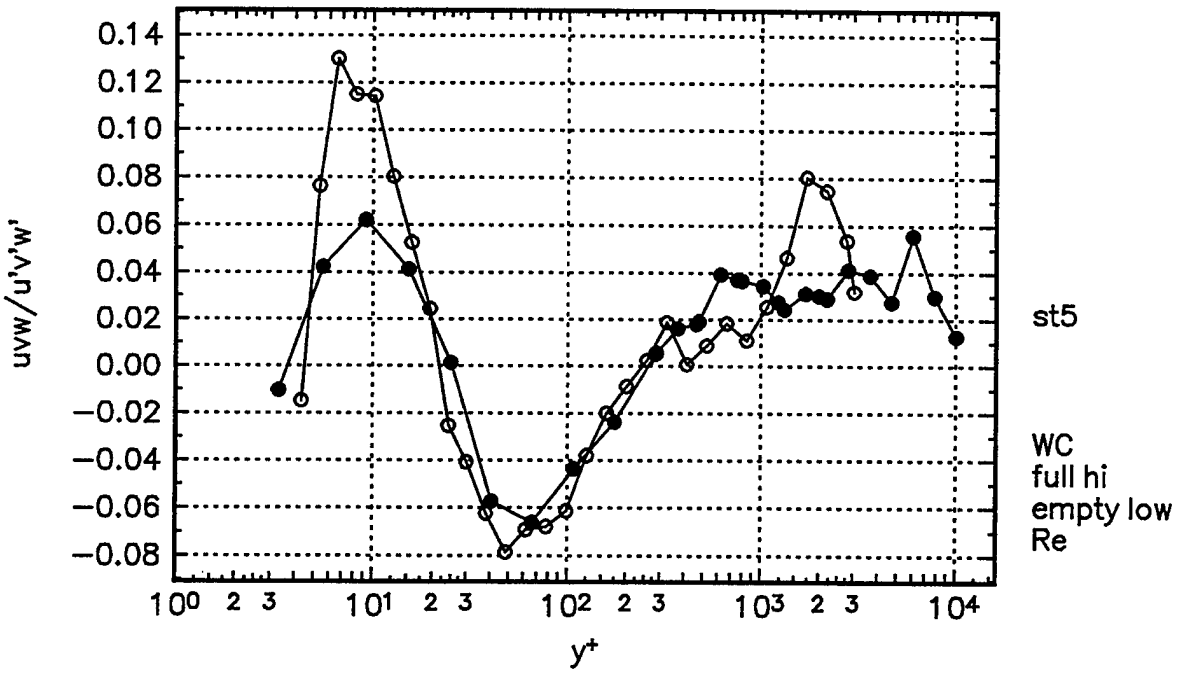

Figure 64e. $\overline{uvw}$ triple products presented in wall-coordinates at Station 5.

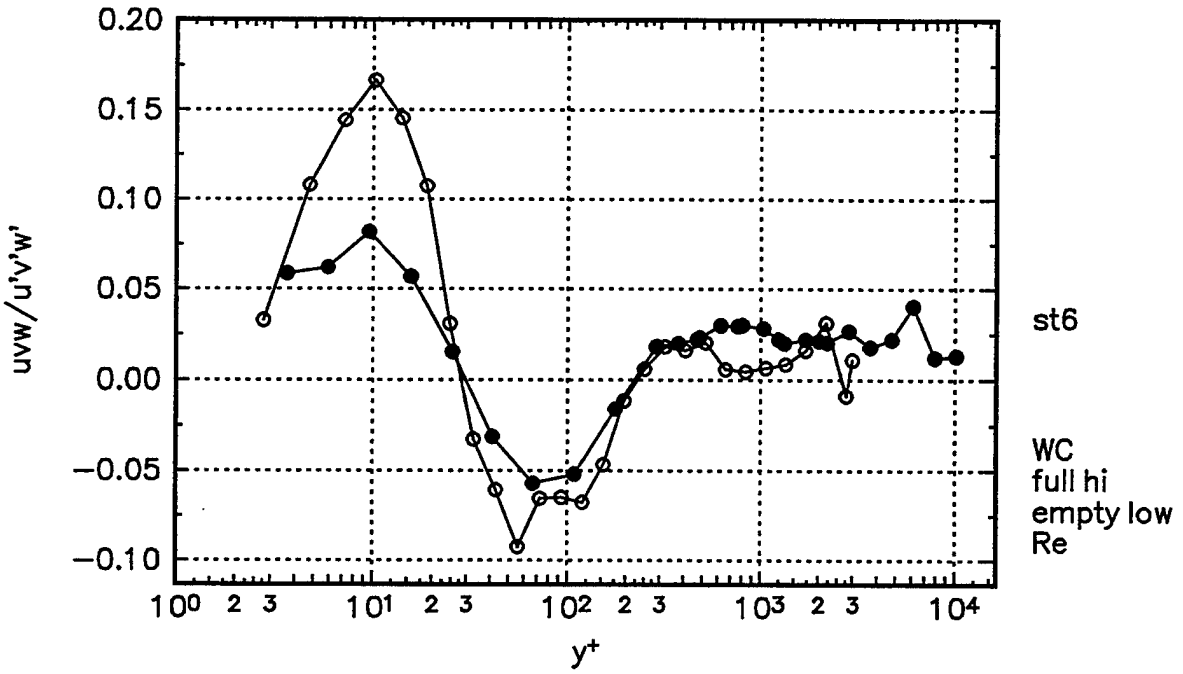

Figure 64f. $\overline{uvw}$ triple products presented in wall-coordinates at Station 6.

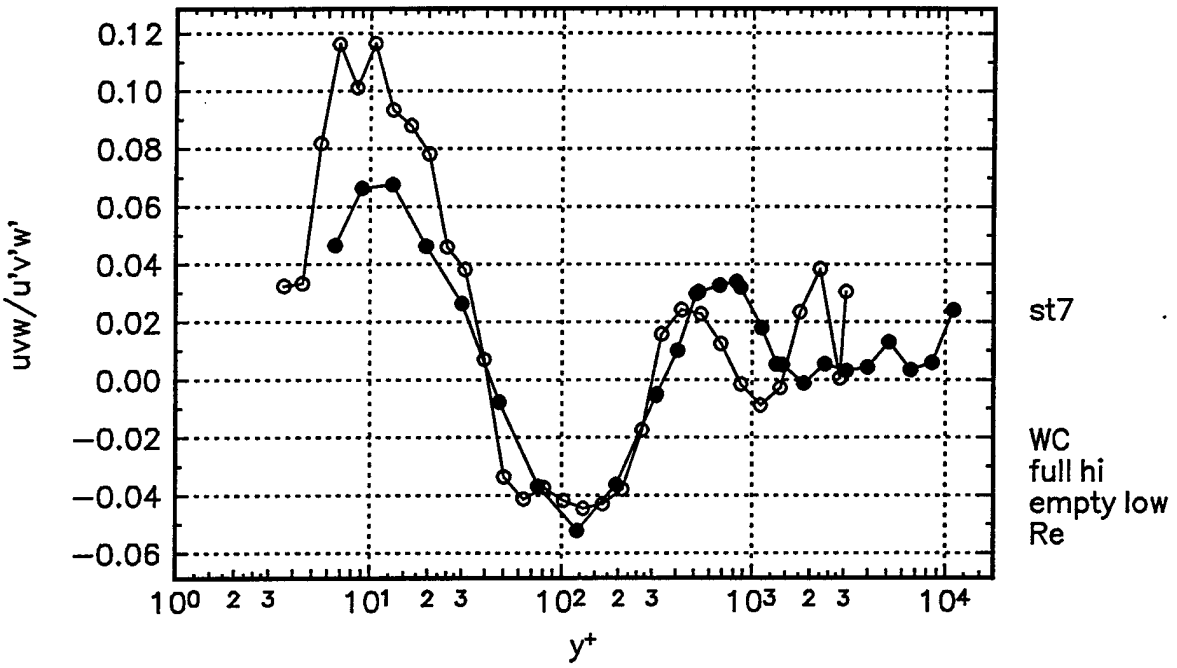

Figure 64g. $\overline{uvw}$ triple products presented in wall-coordinates at Station 7.

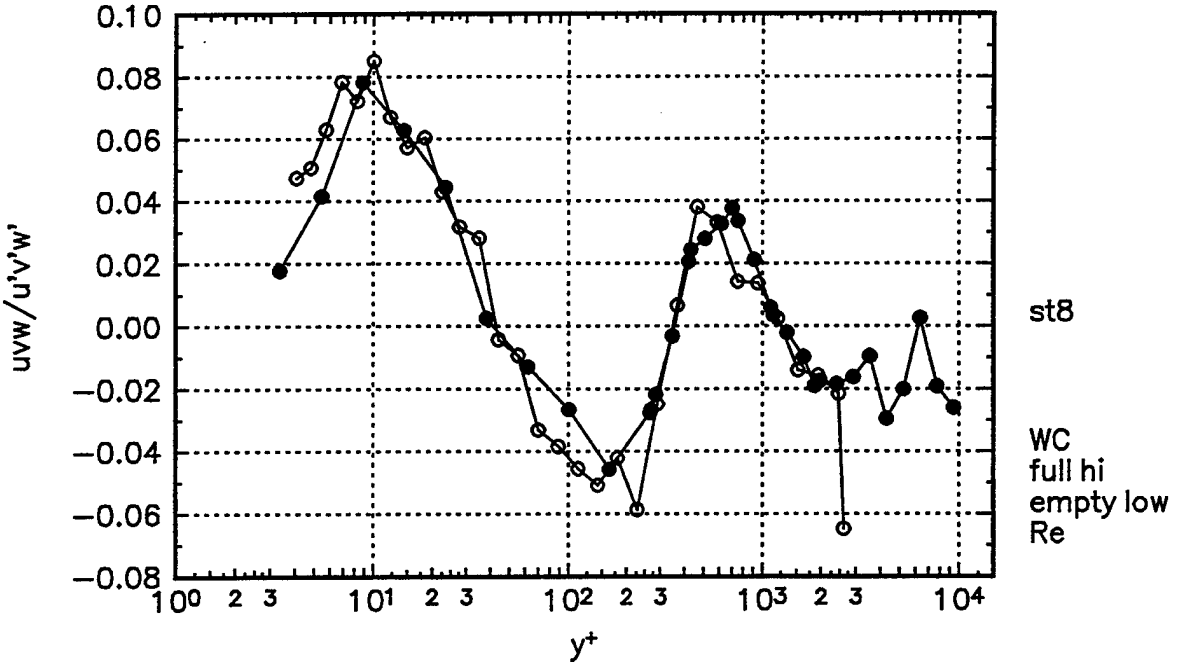

Figure 64h. $\overline{uvw}$ triple products presented in wall-coordinates at Station 8.

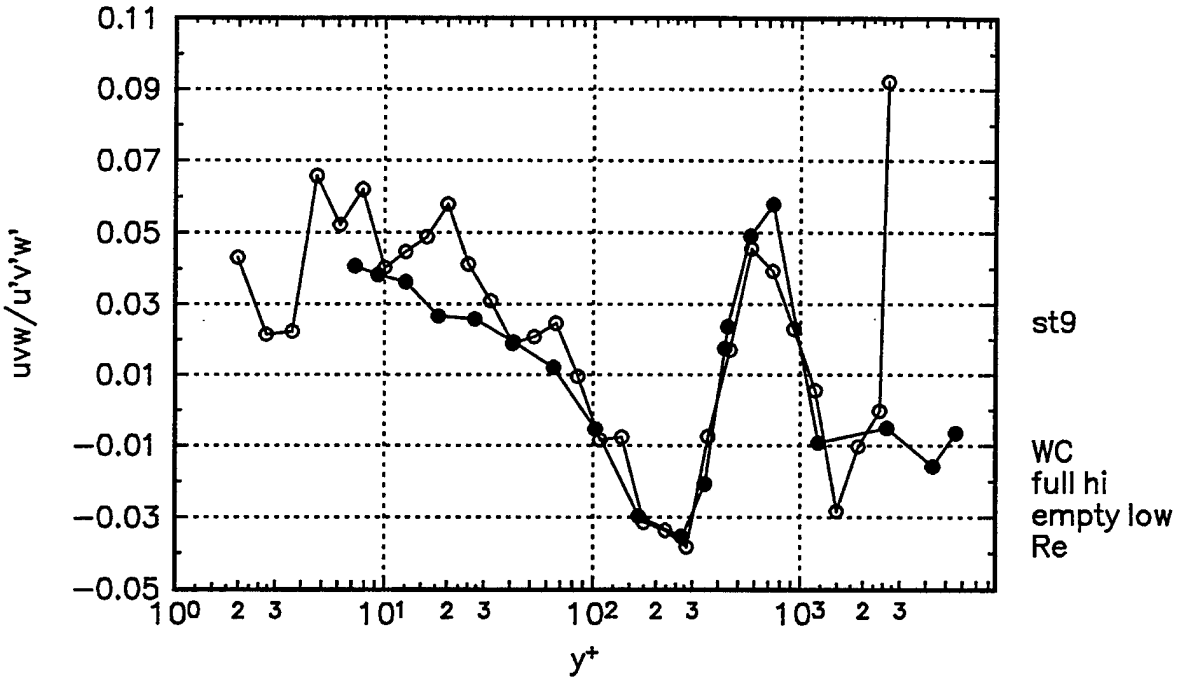

Figure 64i. $\overline{uvw}$ triple products presented in wall-coordinates at Station 9.

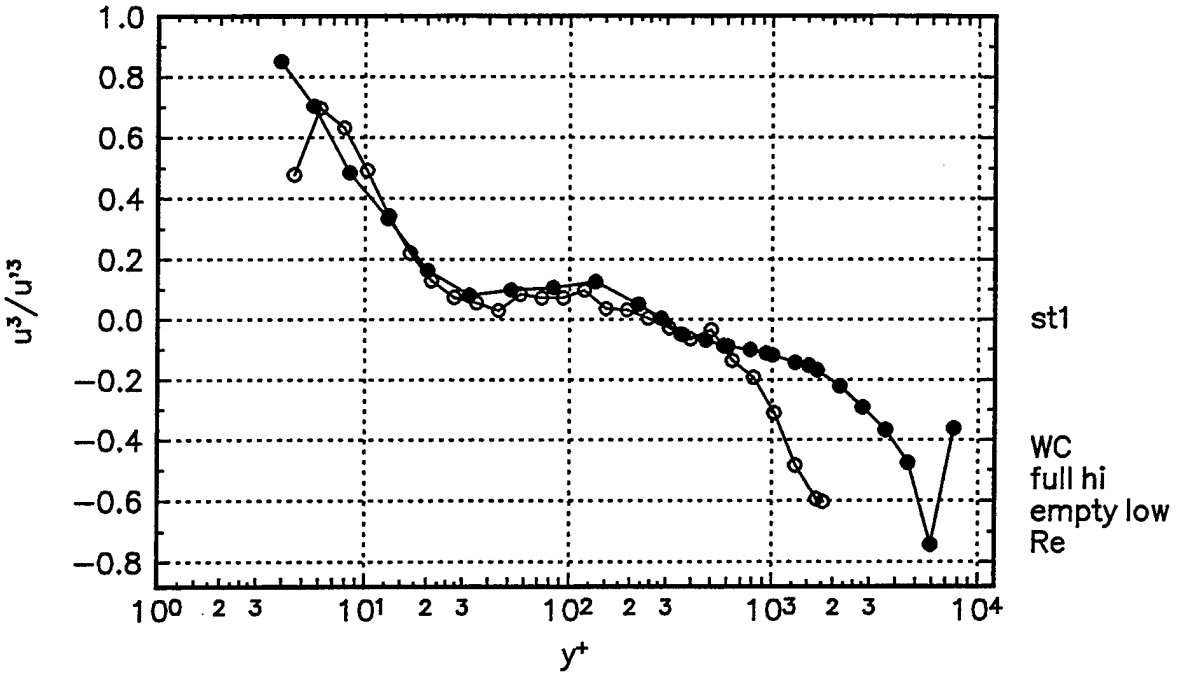

Figure 65a. $\overline{u^3}$ triple products presented in wall-coordinates at Station 1.

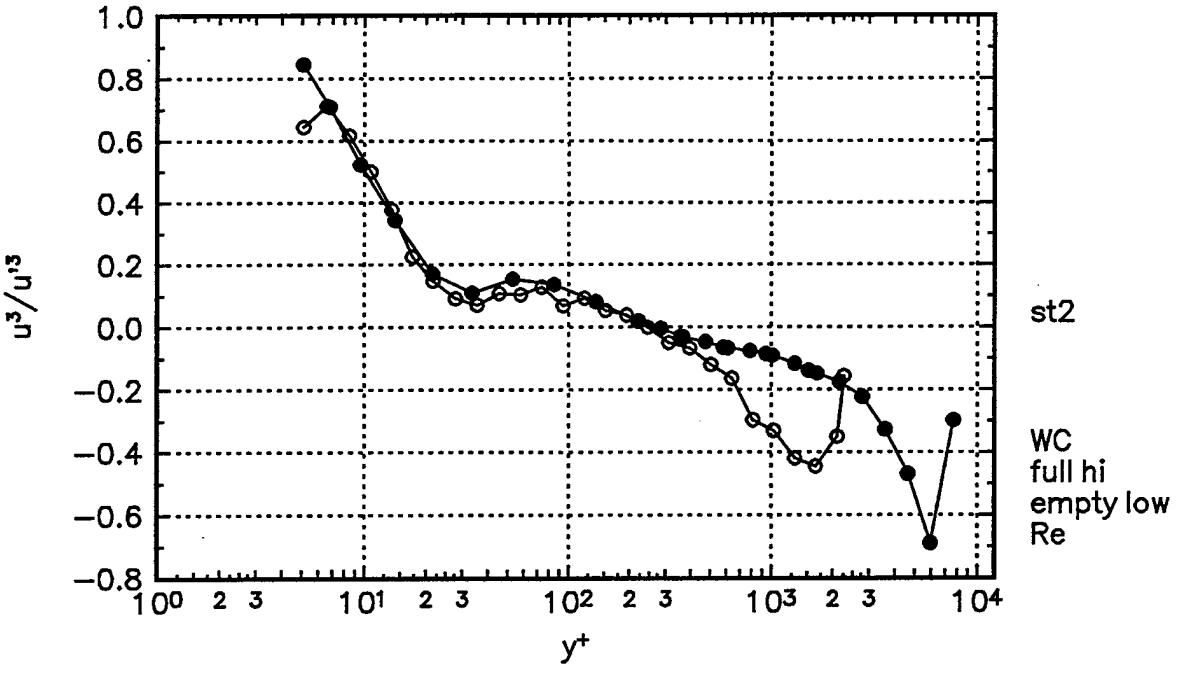

Figure 65b. $\overline{u^3}$ triple products presented in wall-coordinates at Station 2.

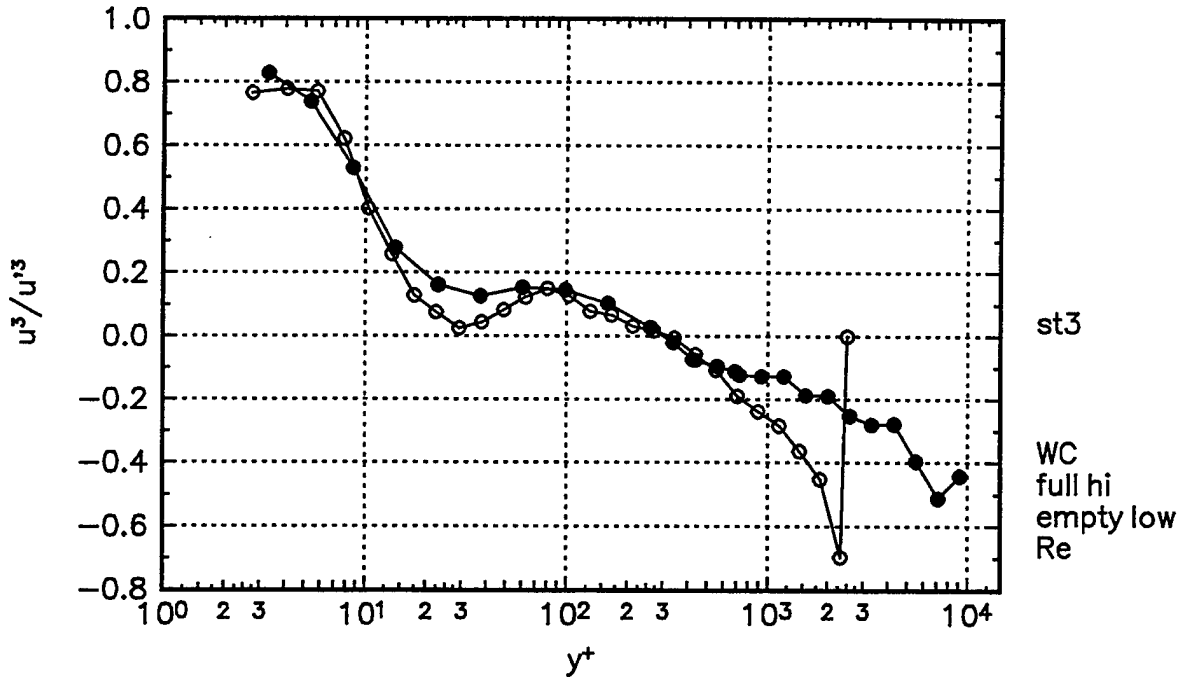

Figure 65c. $\overline{u^3}$ triple products presented in wall-coordinates at Station 3.

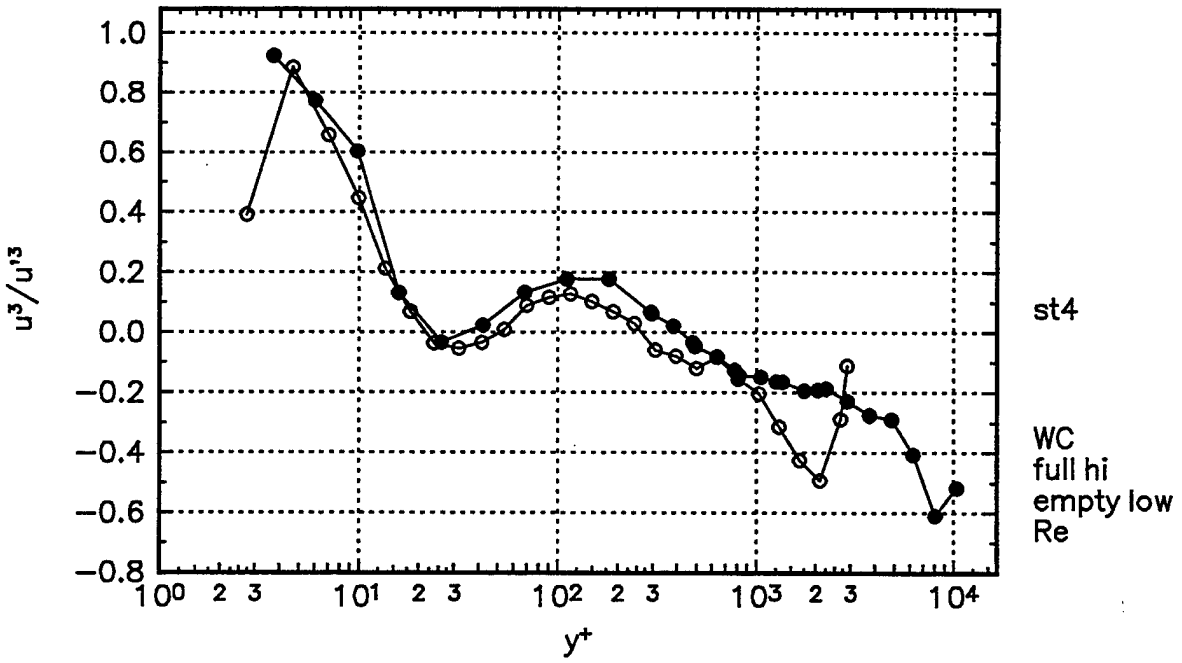

Figure 65d. $\overline{u^3}$ triple products presented in wall-coordinates at Station 4.

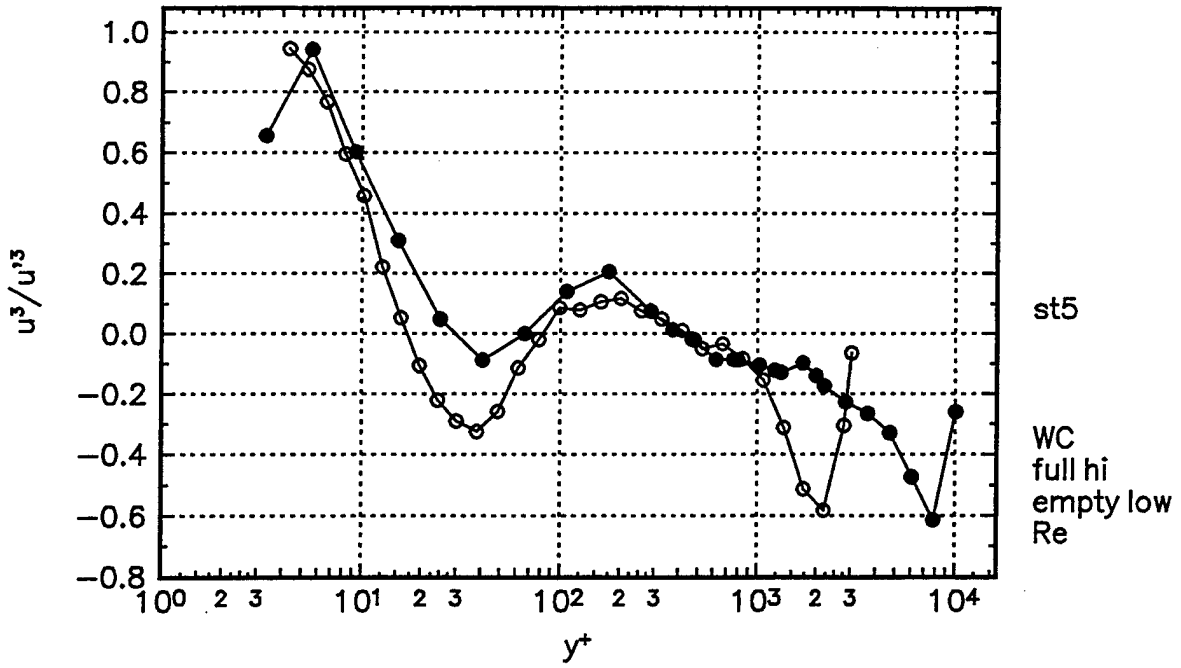

Figure 65e. $\overline{u^3}$ triple products presented in wall-coordinates at Station 5.

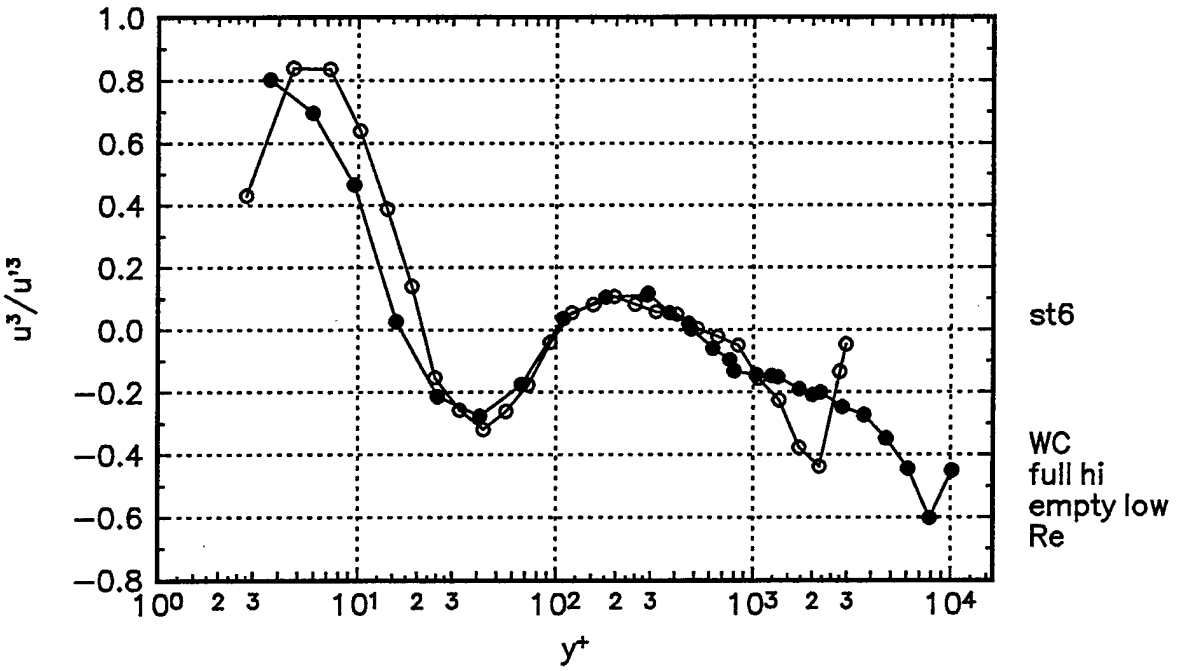

Figure 65f. $\overline{u^3}$ triple products presented in wall-coordinates at Station 6.

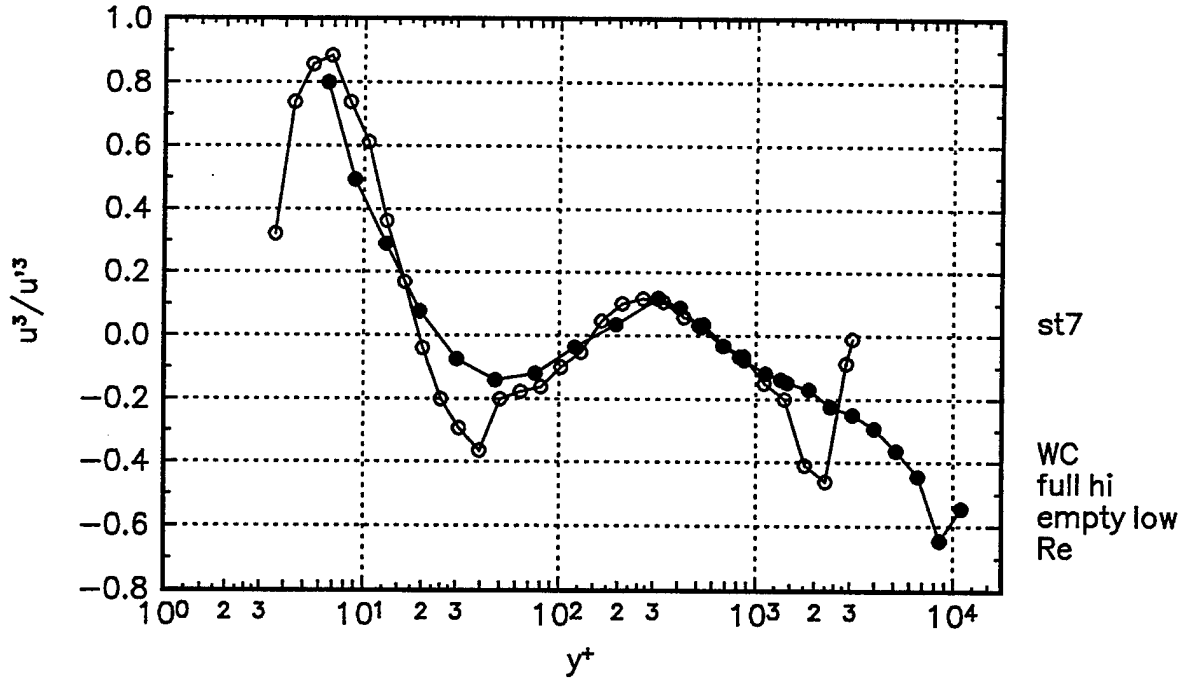

Figure 65g. $\overline{u^3}$ triple products presented in wall-coordinates at Station 7.

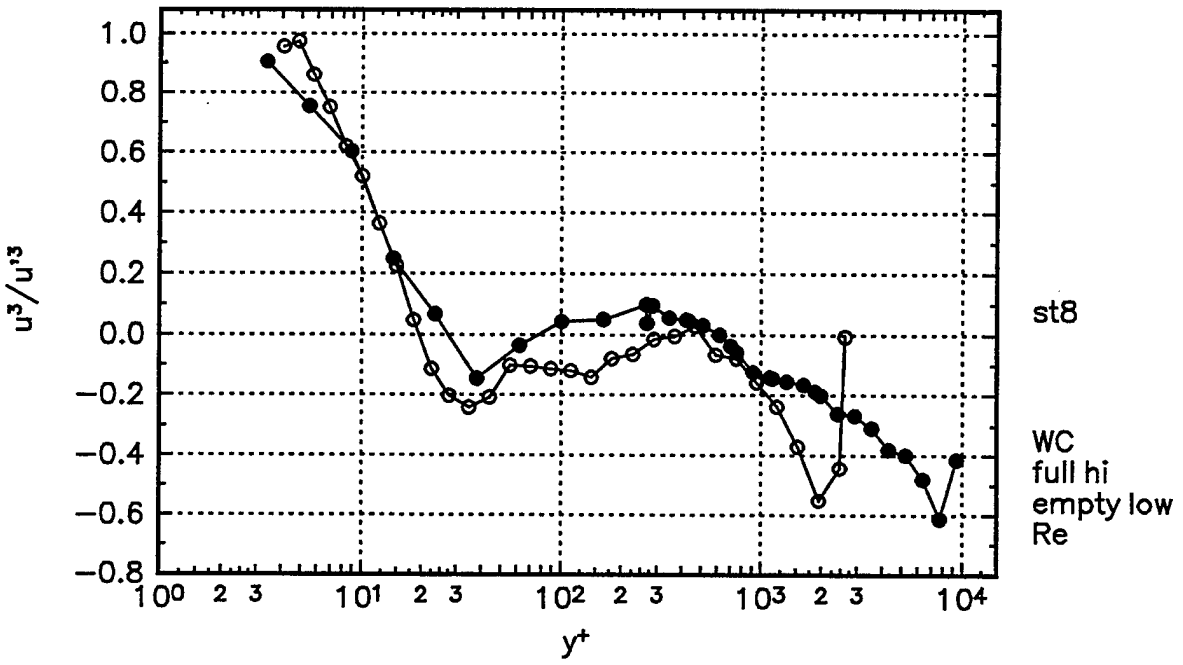

Figure 65h. $\overline{u^3}$ triple products presented in wall-coordinates at Station 8.

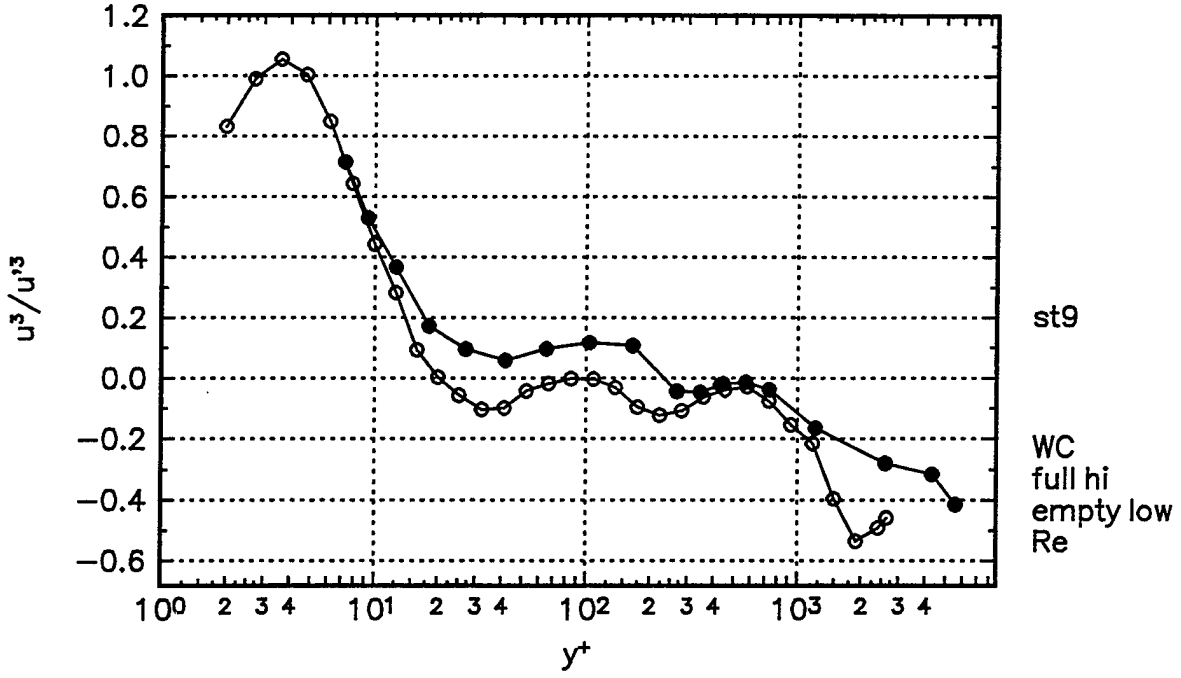

Figure 65i. $\overline{u^3}$ triple products presented in wall-coordinates at Station 9.

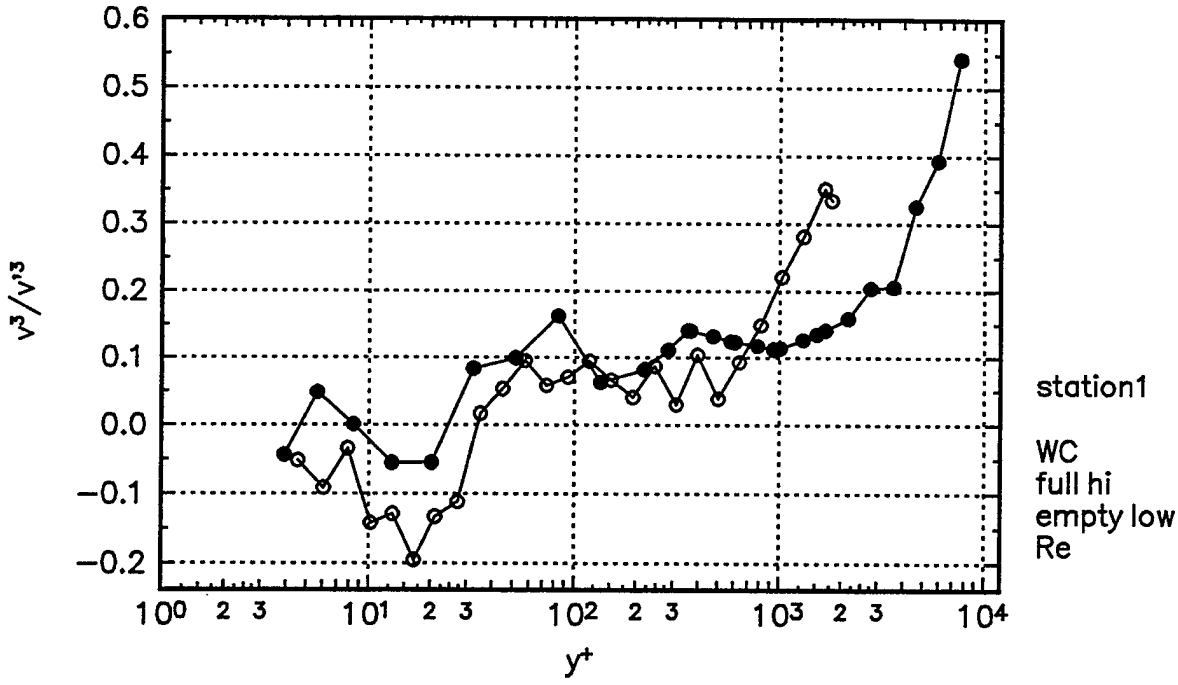

Figure 66a. $\overline{v^3}$ triple products presented in wall-coordinates at Station 1.

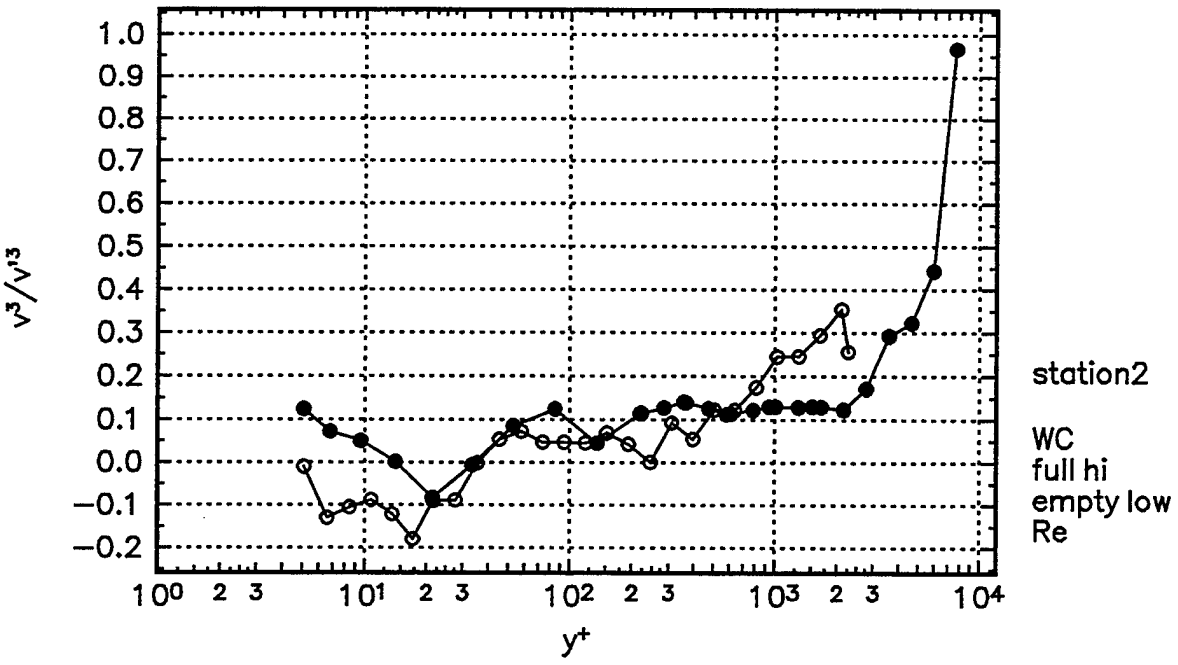

Figure 66b. $\overline{v^3}$ triple products presented in wall-coordinates at Station 2.

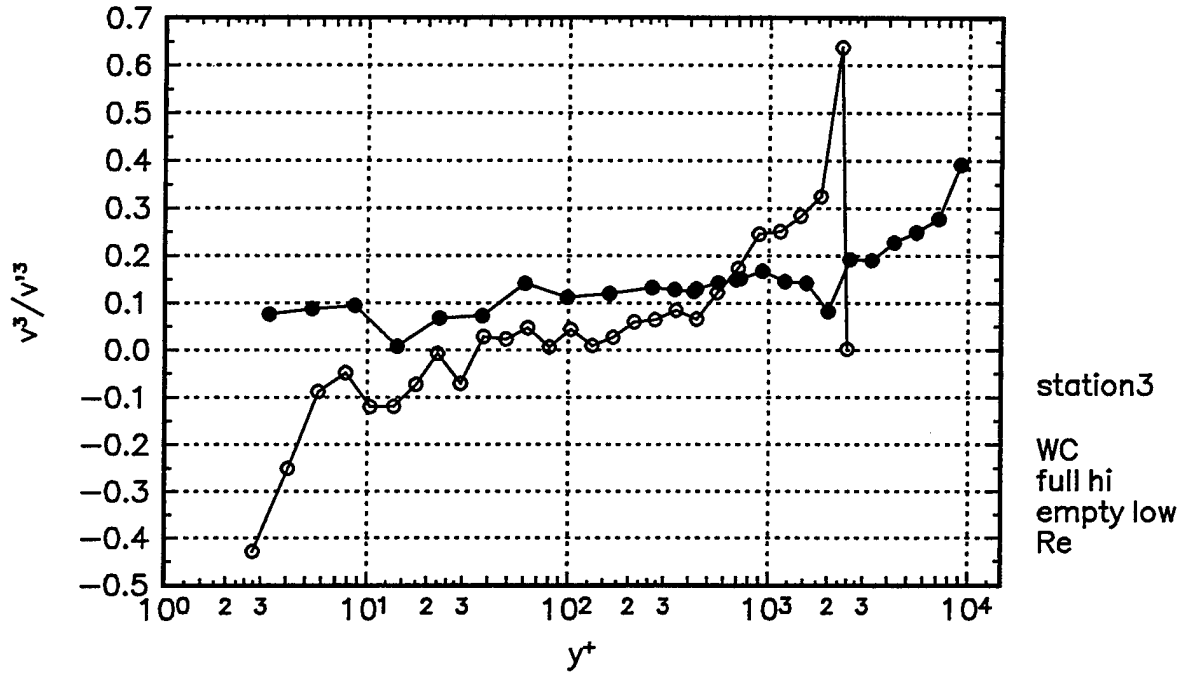

Figure 66c. $\overline{v^3}$ triple products presented in wall-coordinates at Station 3.

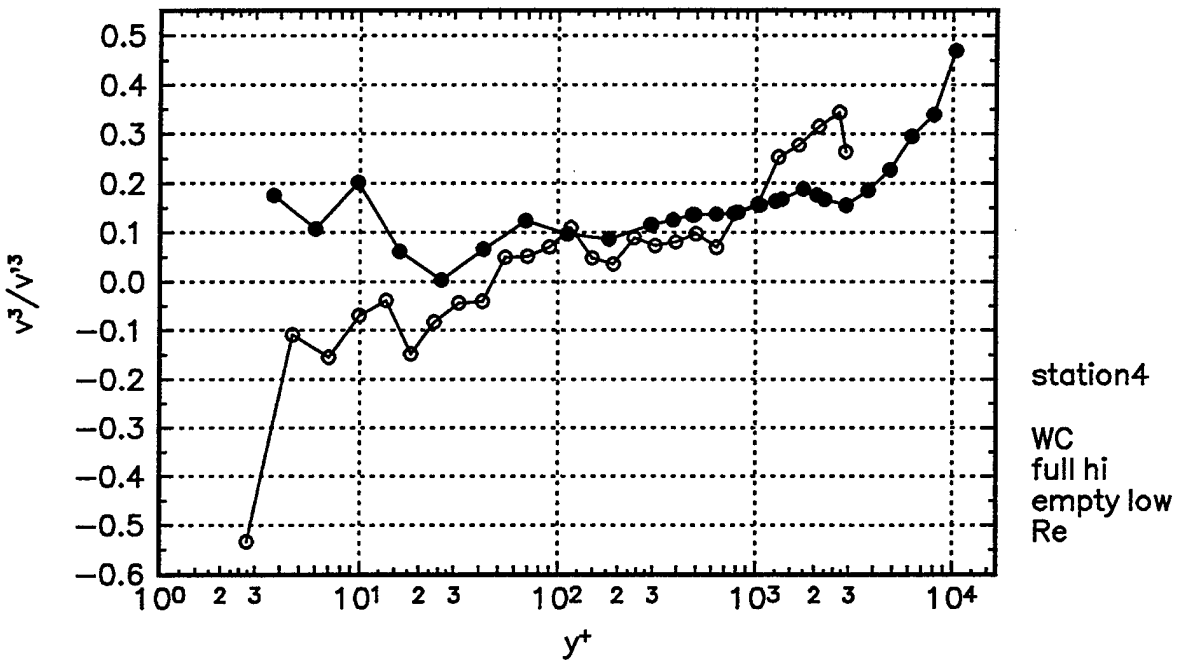

Figure 66d. $\overline{v^3}$ triple products presented in wall-coordinates at Station 4.

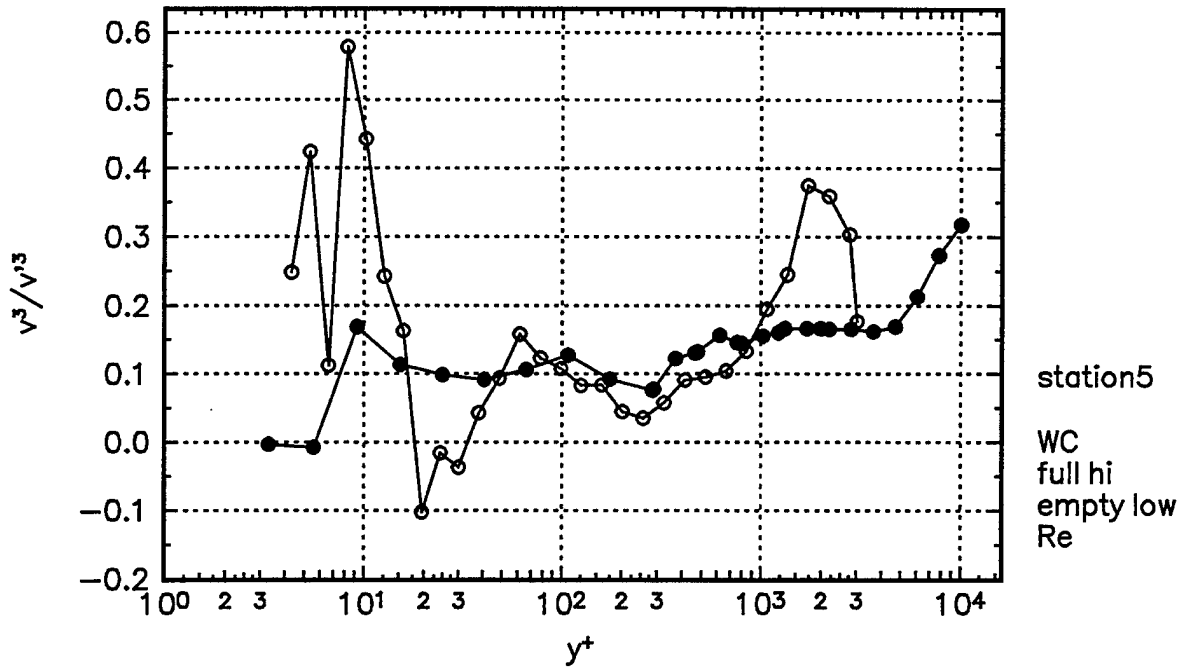

Figure 66e. $\overline{v^3}$ triple products presented in wall-coordinates at Station 5.

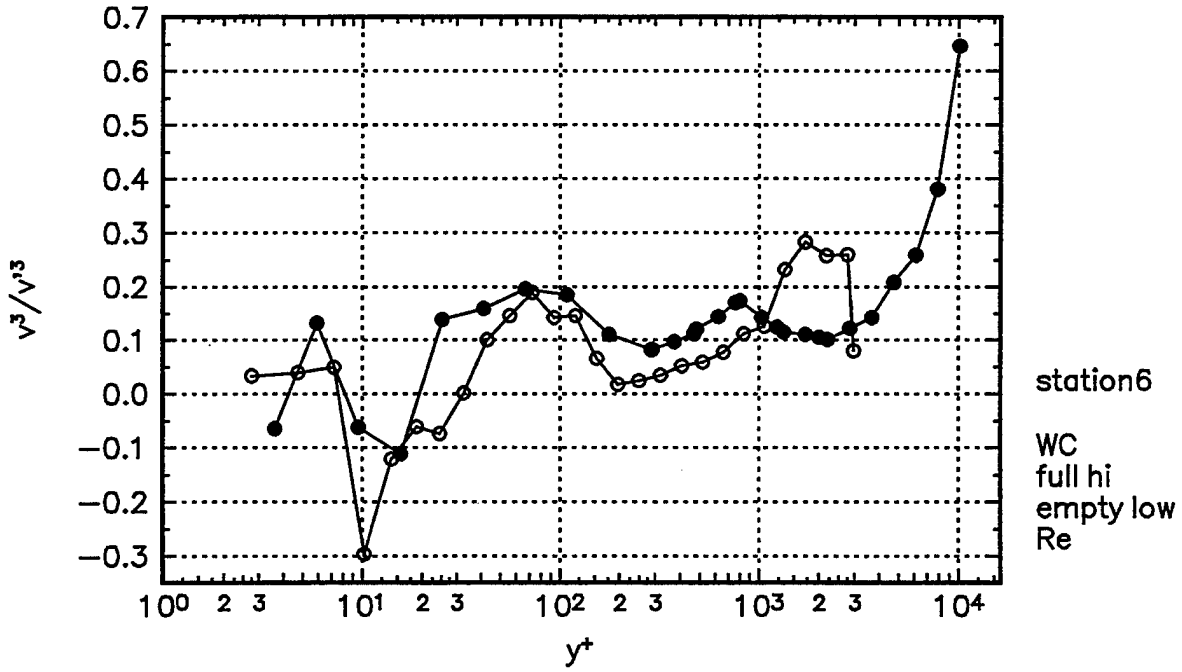

Figure 66f. $\overline{v^3}$ triple products presented in wall-coordinates at Station 6.

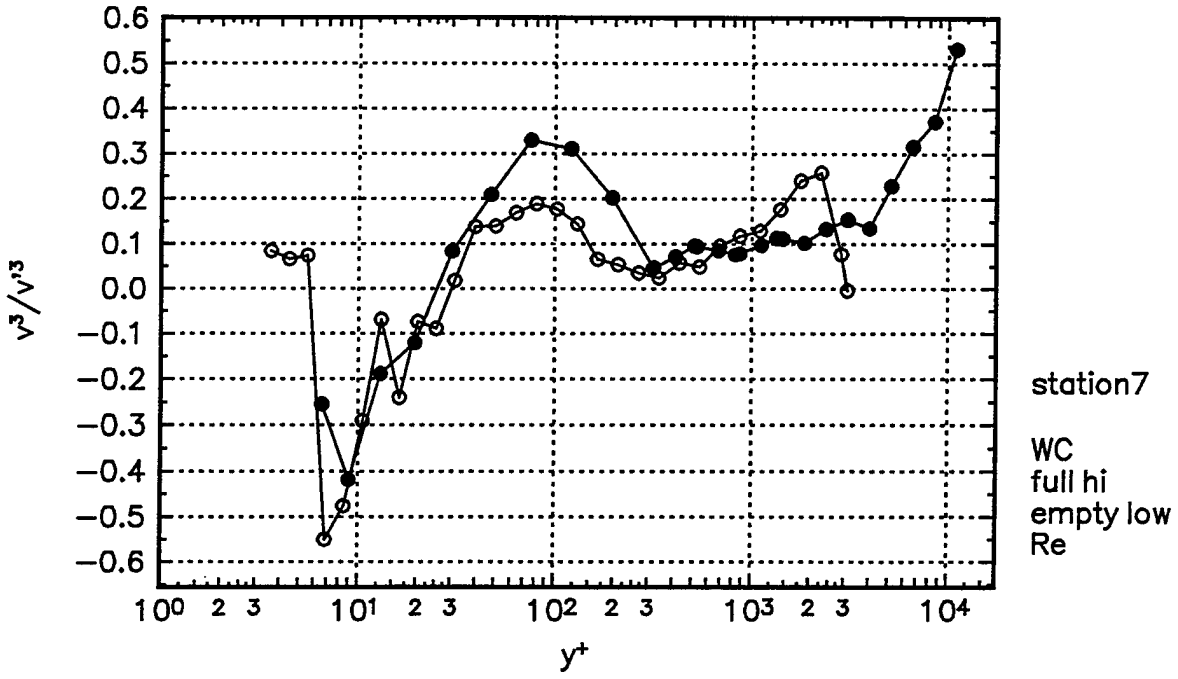

Figure 66g. $\overline{v^3}$ triple products presented in wall-coordinates at Station 7.

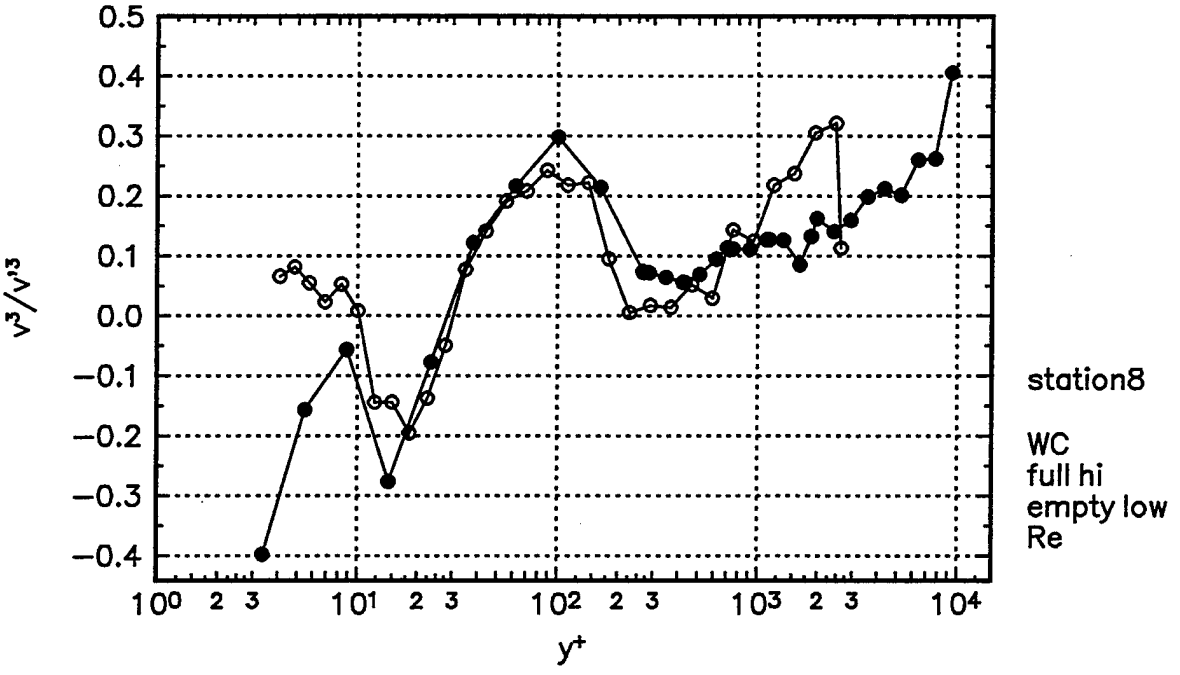

Figure 66h. $\overline{v^3}$ triple products presented in wall-coordinates at Station 8.

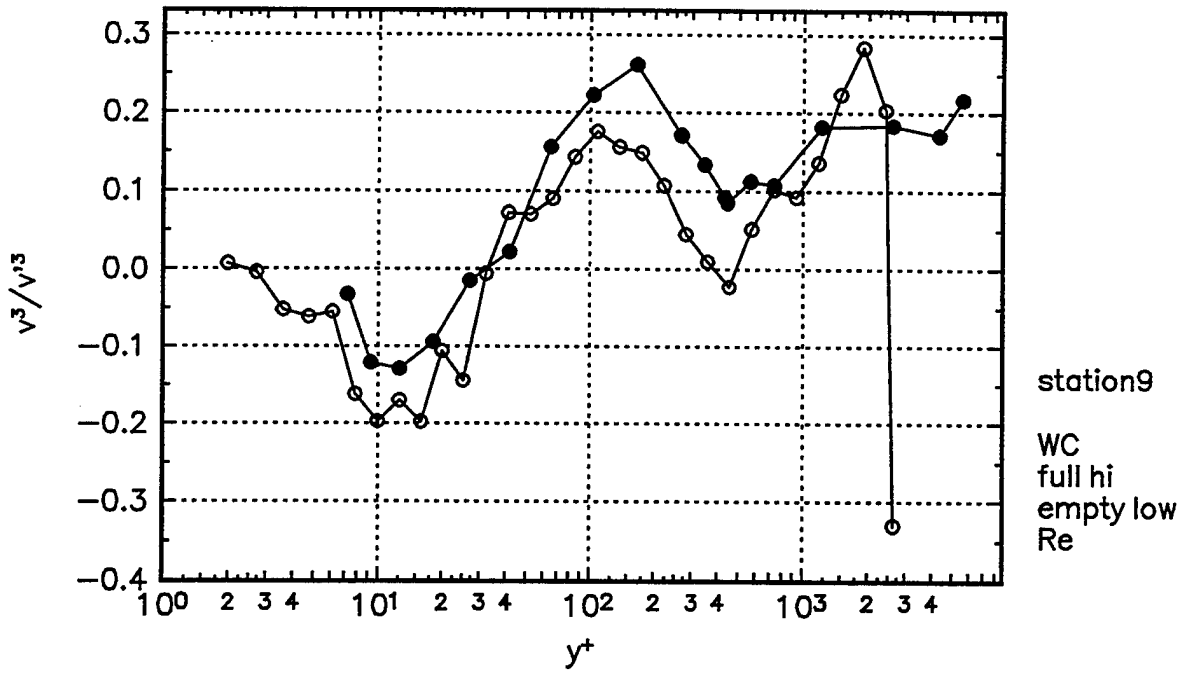

Figure 66i. $\overline{v^3}$ triple products presented in wall-coordinates at Station 9.

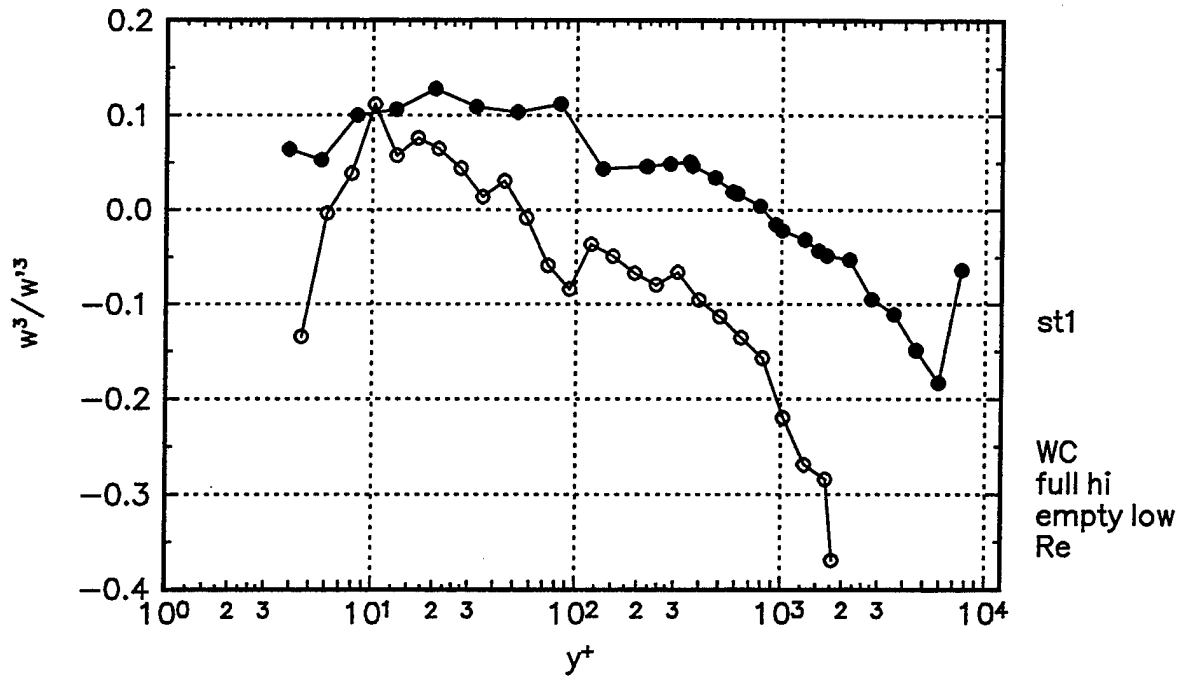

Figure 67a. $\overline{w^3}$ triple products presented in wall-coordinates at Station 1.

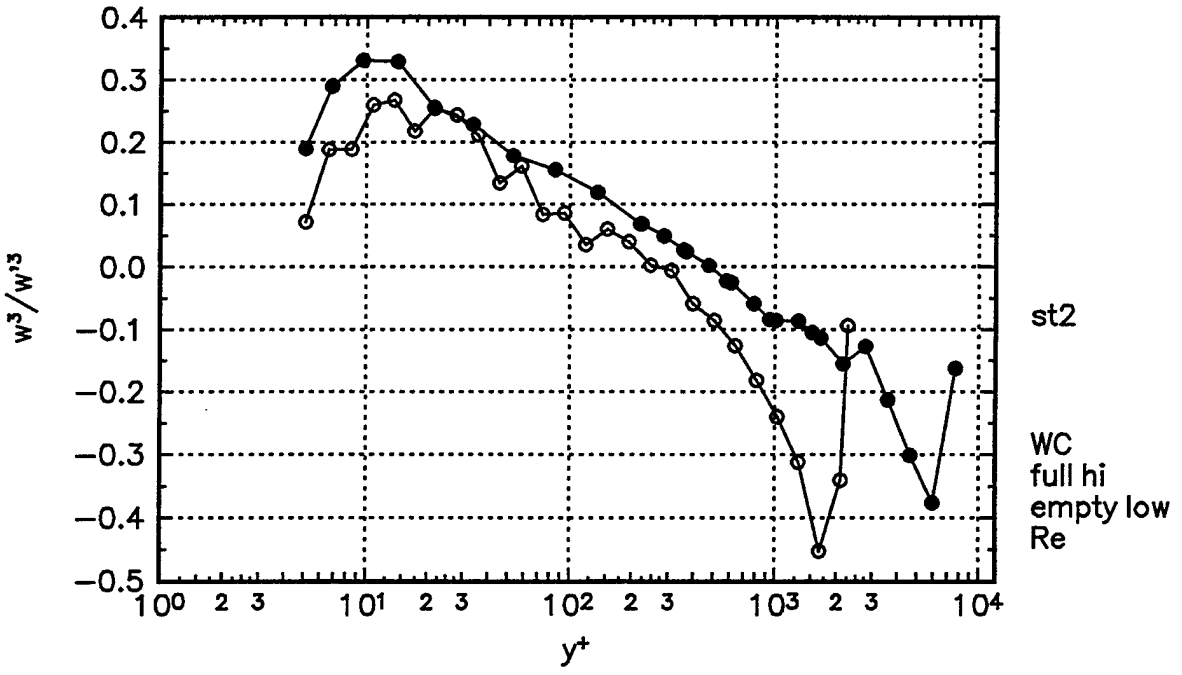

Figure 67b. $\overline{w^3}$ triple products presented in wall-coordinates at Station 2.

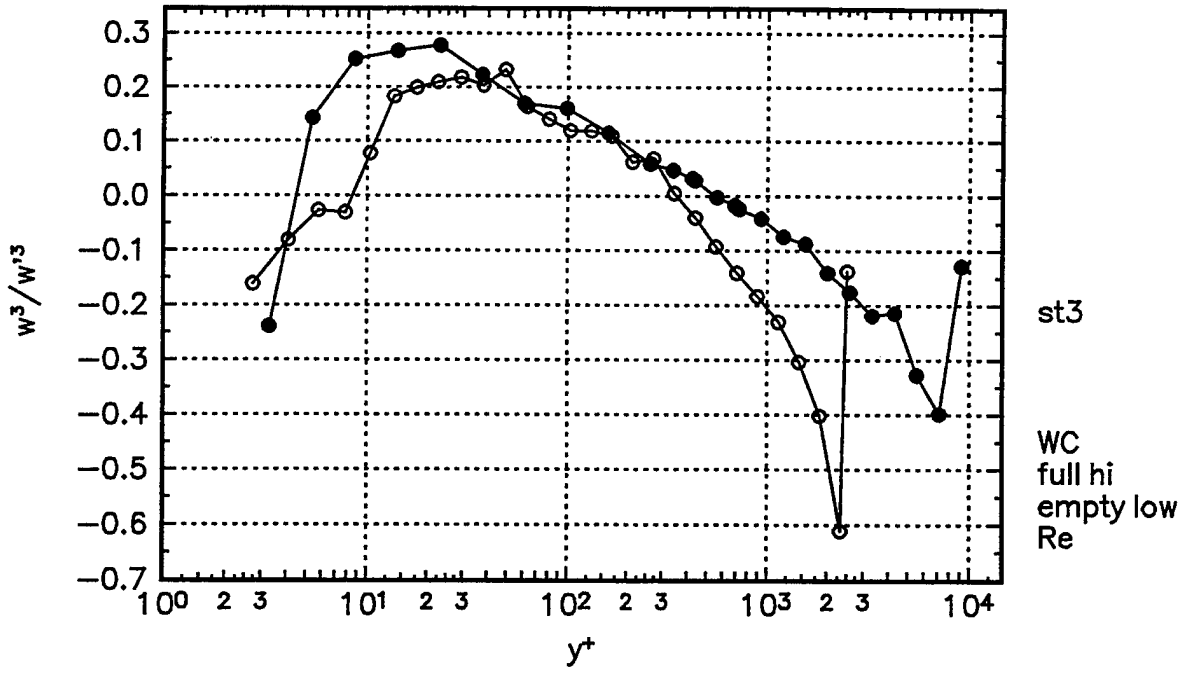

Figure 67c. $\overline{w^3}$ triple products presented in wall-coordinates at Station 3.

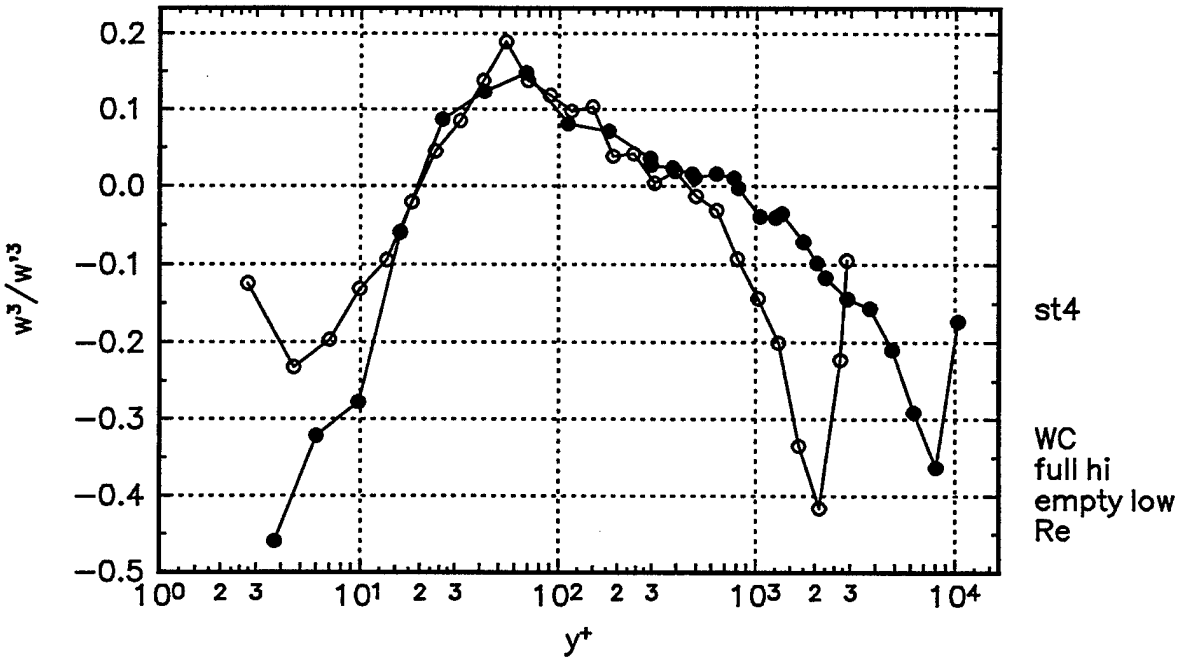

Figure 67d. $\overline{w^3}$ triple products presented in wall-coordinates at Station 4.

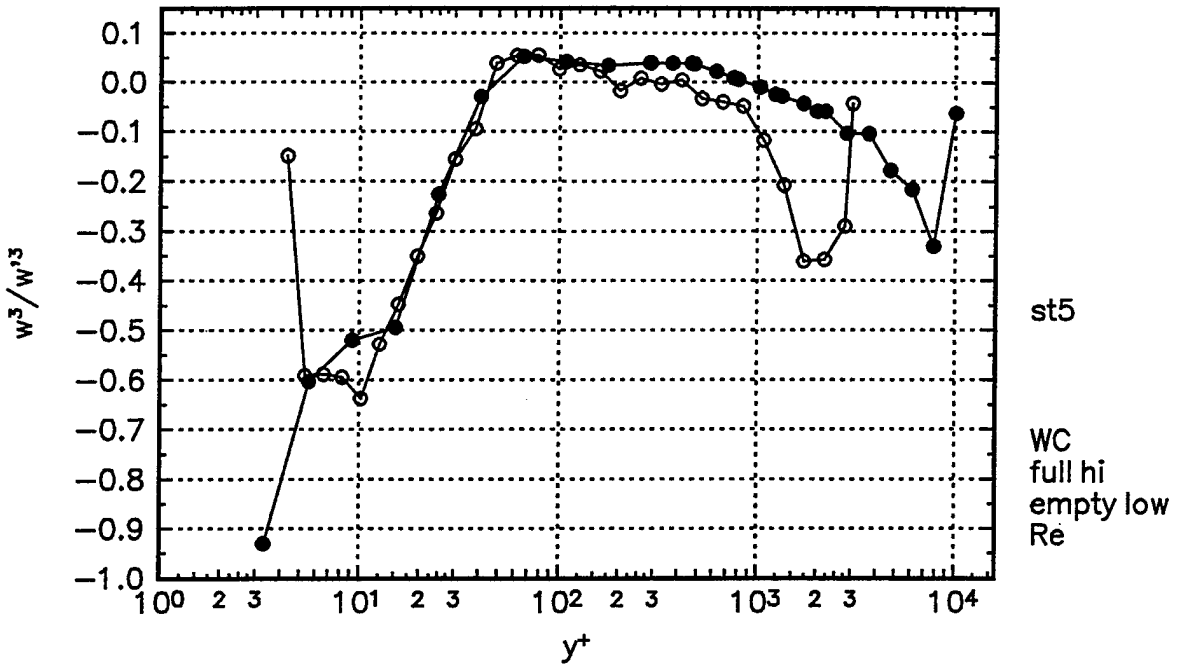

Figure 67e. $\overline{w^3}$ triple products presented in wall-coordinates at Station 5.

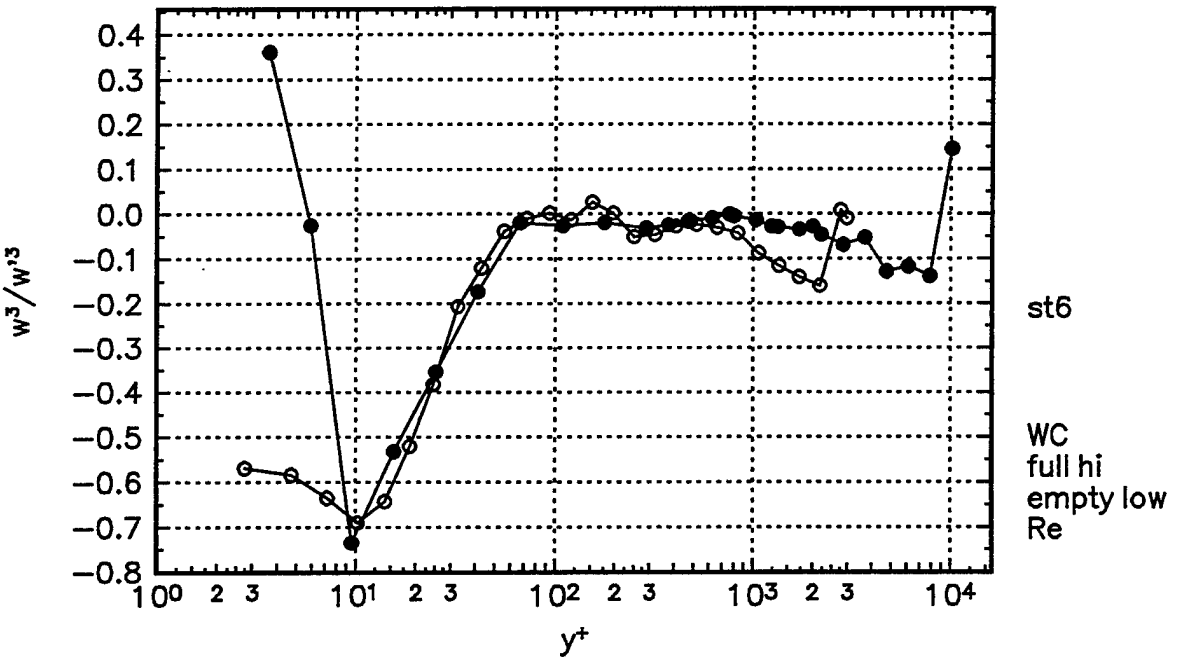

Figure 67f. $\overline{w^3}$ triple products presented in wall-coordinates at Station 6.

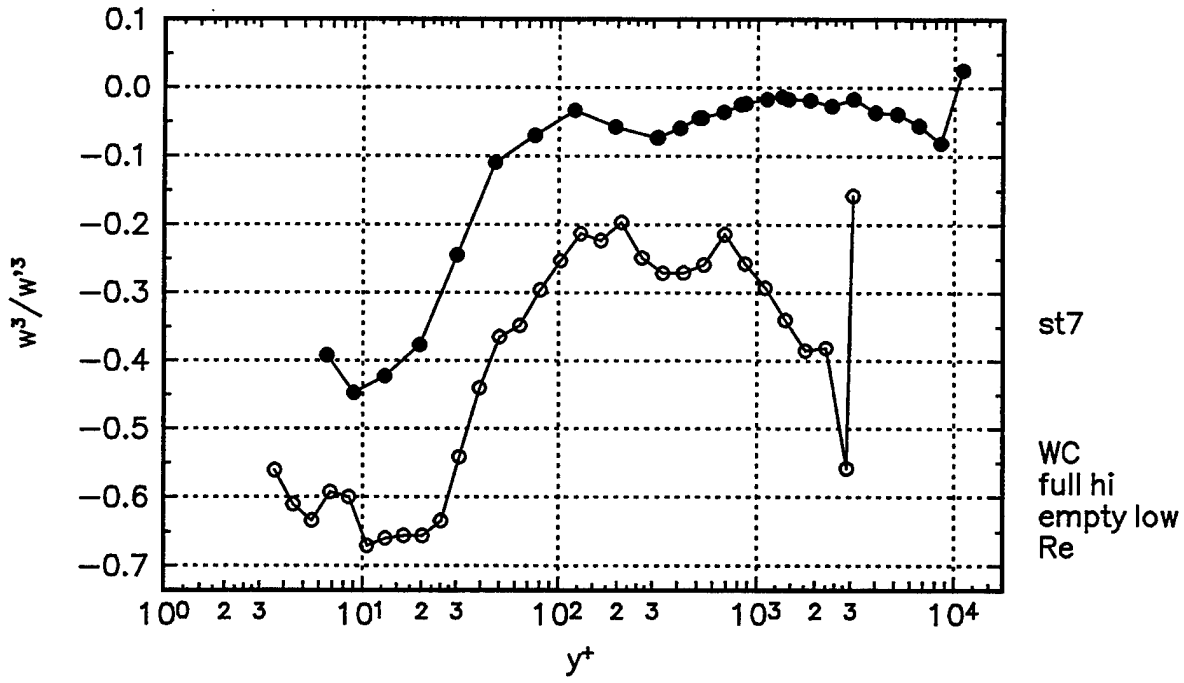

Figure 67g. $\overline{w^3}$ triple products presented in wall-coordinates at Station 7.

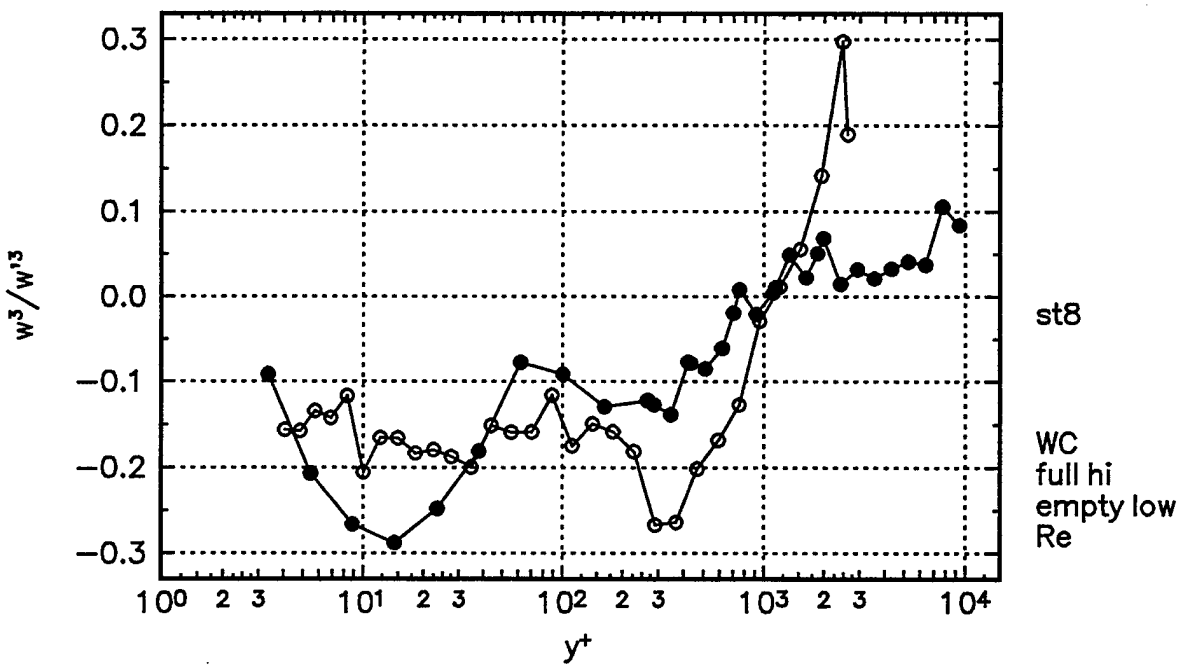

Figure 67h. $\overline{w^3}$ triple products presented in wall-coordinates at Station 8.

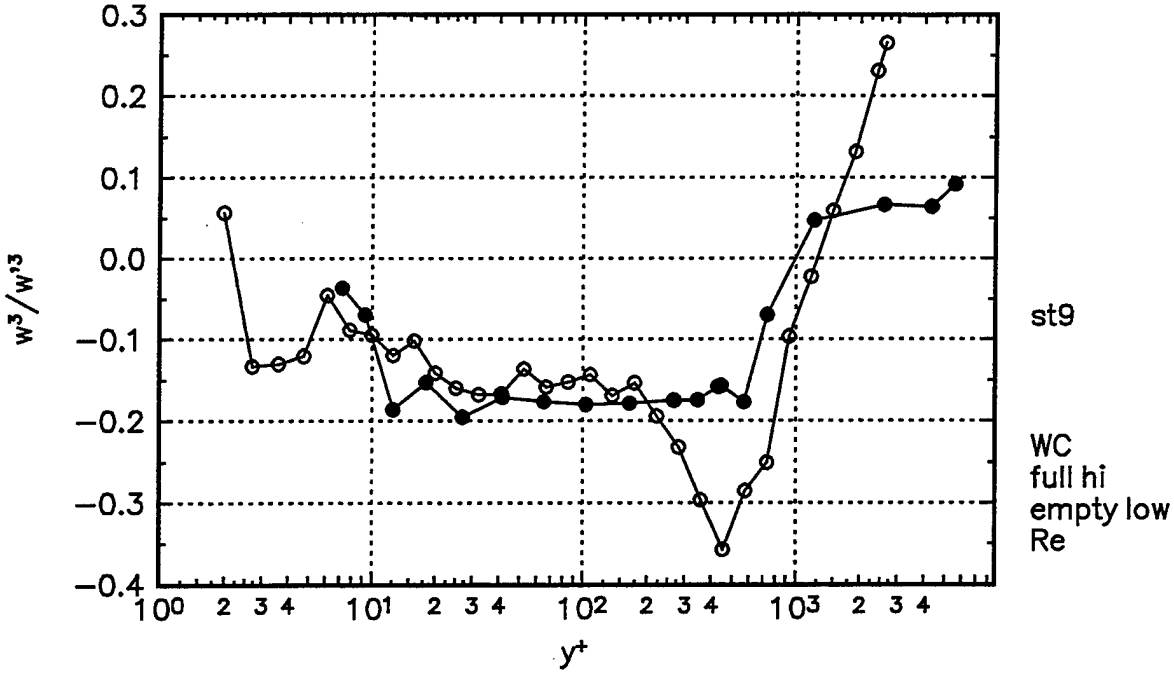

Figure 67i. $\overline{w^3}$ triple products presented in wall-coordinates at Station 9.

Appendix I

"Pitot Probe Boundary Layer Measurements"

by Cindy Whitfield

Introduction

Pressure measurements were made across a turbulent boundary layer using a pitot probe in the Virginia Tech Boundary Layer Wind Tunnel. Velocity profiles were calculated from the acquired pressure data for 11 spanwise locations in the tunnel test section. The momentum thickness (θ), and the corresponding Re_θ were calculated from the velocity profiles. These results verified that the installed roughness plate produced the desired turbulent boundary layer, and the flow was approximately symmetric about the centerline. The collected data were then used to calculate the correct placement of the upper tunnel wall to achieve a uniform freestream velocity throughout the test section.

Apparatus

The Virginia Tech Boundary Layer Wind Tunnel was utilized for the tests performed. The tunnel test section is 24 feet in length with a width of 3 feet and a variable height. The test section is divided into three eight-foot sections numbered from the contraction as sections one, two, and three. The first section has an accelerating flow up to five feet from the contraction and approximately a constant inviscid core velocity downstream. The second section has a constant height, but the third section has a linearly increasing height.

A custom made static pressure probe with a tip diameter of 0.035 inches and a Prandtl style Dwyer Pitot probe N28F with a diameter of 0.125 inches were used for the pressure measurements. The two probes were connected to an electronic manometer manufactured by Setra. The electronic manometer has a maximum pressure rating of 5 inches of water. It is calibrated for one volt per inch of water. Voltages were read directly from a Hewlett Packard 3478A multimeter with a displayed voltage resolution of five significant digits. The static probe was mounted in a threaded barrel and gear mechanism that was vertically traversed by a stepper motor that was powered by a Hewlett Packard 6200B power supply. One revolution of the threaded barrel was equivalent to a 0.025 inch vertical move.

Experiments

The first set of measurements that were taken was at 11 spanwise stations located 21.3 feet from the contraction of the tunnel. The tunnel height at this x location was 11.375 inches. A static probe was mounted so that the stagnation ports were at the same x location as the static port of the pitot probe but at a y location that was in the freestream. The wind tunnel was turned on and set to a velocity of approximately 32 m/s. The freestream pressure was obtained from the static probe. Once the freestream pressure was acquired, the pitot probe was connected to the electronic manometer. The pitot probe was then positioned at the lower wall of the tunnel and vertically traversed. Thirty-one points were logarithmically spaced throughout the boundary layer, and the dynamic pressure was recorded at each point. From these pressure readings, a velocity profile was calculated. A velocity profile was taken first at the centerline and then at ±6, ±9, ±12, and ±15 inches on either side of the centerline. The ±15 inch profiles were located 3 inches from the tunnel sidewall.

A single velocity profile was taken at the centerline in the second section of the wind tunnel at a x location of 9.5 feet from the contraction. The upper wall height was 10.375 inches in section 2. Again, dynamic pressure readings were taken at 31 points throughout the boundary layer.

The final tests were pitot measurements performed at 15 streamwise stations along the tunnel centerline. The stations were spaced at approximately 12 inches beginning from the second tunnel section to the test section exit. The freestream pressure was recorded and the velocity was calculated at each station.

Results

From the first set of experiments, the dynamic pressure was recorded at 31 points throughout a boundary layer for 11 spanwise locations. Utilizing a FORTRAN program, the pressure readings for each z location were nondimensionalized using the freestream pressure reading, and from these values, the nondimensional velocity values at each point were calculated. The velocity profile at the centerline was compared to a previous hot wire velocity profile performed in the same tunnel at approximately the same x location and under the same conditions. The graph in figure 1 shows the comparison between the two experiments.

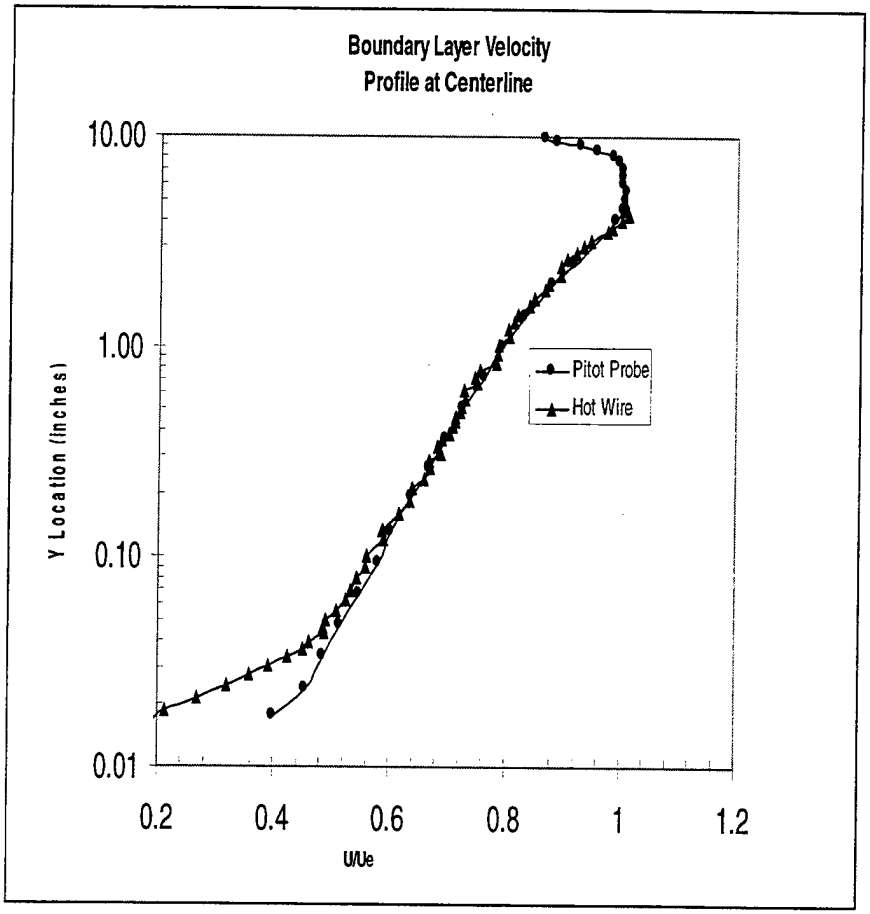

Figure 1: Comparison of Hot Wire and Pitot Probe Measurements

Figures 2 and 3 compare the velocity profiles for the positive z locations and the negative z locations respectively. The data indicates the flow is approximately symmetric about the centerline.

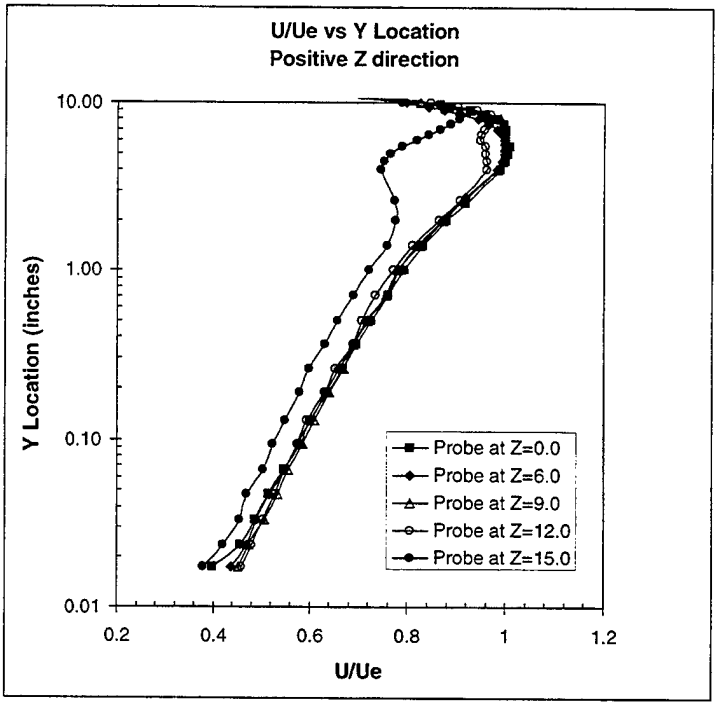

Figure 2: Boundary Layer Profiles for Positive Z Stations

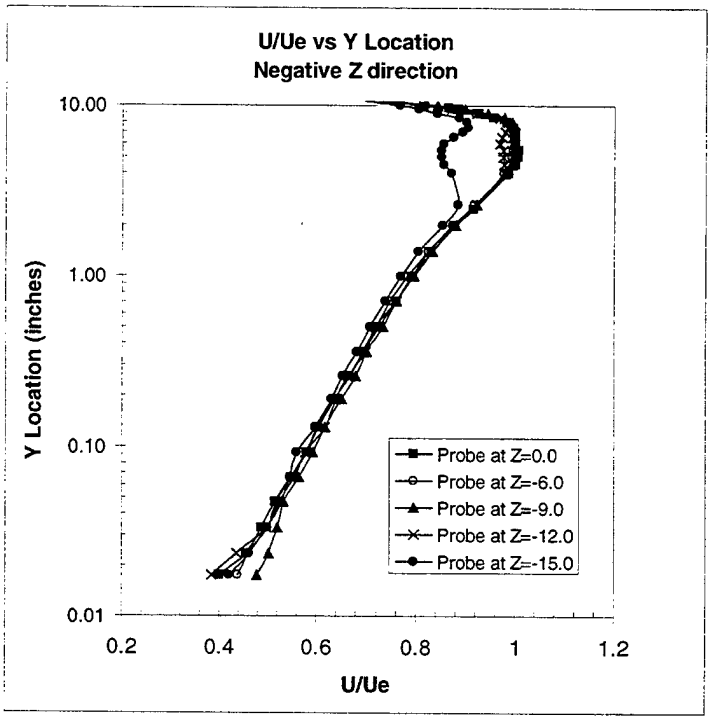

Figure 3: Boundary Layer Profiles for Negative Z Stations

For each of the z locations, the freestream velocity and viscosity were calculated using a Turbo BASIC program. The displacement thickness (δ^*) and the momentum thickness (θ) were calculated for the lower boundary layer using the following formulas.

$$\delta^* = \int_0^{\delta} \left(1 - \frac{U}{Ue}\right) dy \qquad \text{Equation 1}$$

$$\theta = \int_0^{\delta} \frac{U}{Ue}\left(1 - \frac{U}{Ue}\right) dy \qquad \text{Equation 2}$$

δ^* for the upper boundary layer was approximated using the following relationships.

$$\delta = y\Big|_{\frac{u}{ue}=.99} \qquad \text{Equation 3}$$

$$\frac{\delta_l^*}{\delta_l} = A \qquad \text{Equation 4}$$

$$\delta_u = .99\{h - [(1.01\delta_l) + h_f]\} \qquad \text{Equation 5}$$

$$\delta_u^* = A\delta_u \qquad \text{Equation 6}$$

Where the subscript *l* denotes the lower boundary layer, the subscript *u* denotes the upper boundary layer, *h* is the tunnel height, h_f is the height of the freestream, and *y* is the vertical coordinate measured zero from the lower wall.

The shape factor (*H*) and Re_θ for the lower boundary layer were calculated for each profile using the following equations.

$$H = \frac{\delta^*}{\theta} \qquad \text{Equation 7}$$

$$\mathrm{Re}_\theta = \frac{U\theta}{\nu} \qquad \text{Equation 8}$$

Table 1 compares all these calculated values for the 11 locations. Figure 4 is a graph of the lower boundary layer parameters.

Table 1: Boundary Layer Parameters

z (in)	U_e (m/s)	υ (m^2/s)	δ_l (in)	δ_l^* (in)	A (δ_l^*/δ_l)	θ (in)	δ_U (in)	δ_U^* (in)	Re_θ	H
-15.0	30.86	1.663E-05	7.425	0.563	0.0758	0.4674	3.837	0.291	23194.48	1.2041
-12.0	30.82	1.658E-05	3.960	0.582	0.1468	0.4513	5.817	0.854	22431.24	1.2885
-9.0	30.84	1.662E-05	4.455	0.569	0.1278	0.4397	3.342	0.427	21828.05	1.2947
-6.0	30.82	1.677E-05	5.940	0.631	0.1063	0.4843	3.837	0.408	23805.89	1.3033
0.0	30.61	1.660E-05	5.445	0.622	0.1143	0.4745	4.332	0.495	22149.86	1.3113
6.0	30.78	1.671E-05	4.950	0.633	0.1278	0.4828	5.322	0.680	22586.14	1.3103
9.0	30.86	1.673E-05	4.950	0.611	0.1235	0.403	3.837	0.474	23088.80	1.5171
12.0	30.79	1.672E-05	3.960	0.527	0.1331	0.4679	5.817	0.774	18850.07	1.1263
15.0	30.82	1.675E-05	8.415	1.159	0.1377	0.9307	2.847	0.392	43507.67	1.2453

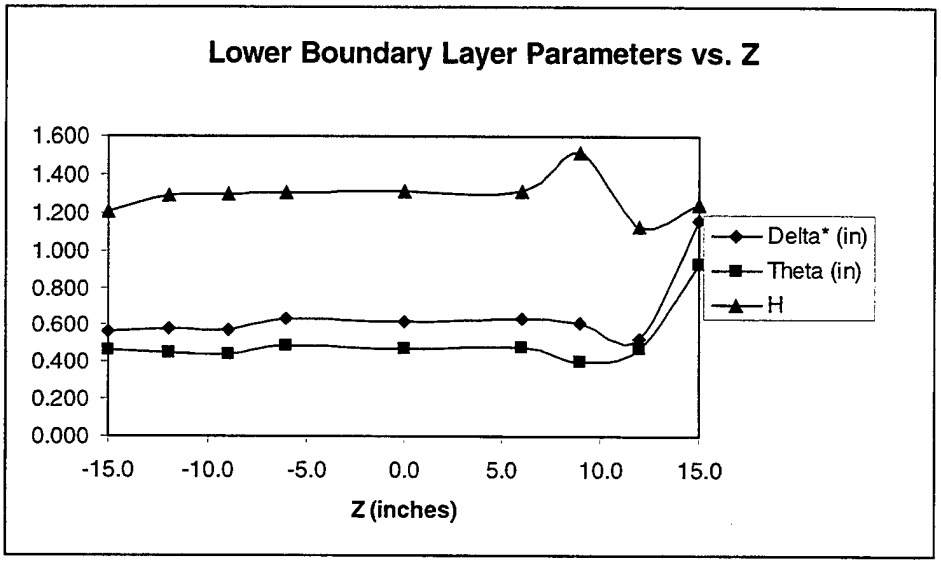

Figure 4: Lower Boundary Layer Parameters

The boundary layer in the second section of the wind tunnel was studied in the second experiment. Again, the freestream velocity and the viscosity were calculated using the Turbo BASIC program. The displacement thickness, momentum thickness, and the shape factor were calculated for this profile as well. From the momentum thickness, freestream velocity, and the viscosity, Re_θ was calculated to be approximately 19,000. Figure 5 is a graph of the data taken at the centerline in section 2 and 3 of the tunnel as well as the hot wire measurements and the data from the Danish-Netherlands Windtunnel (DNW)[1]. The DNW data is for a Reynolds number of approximately 20,000.

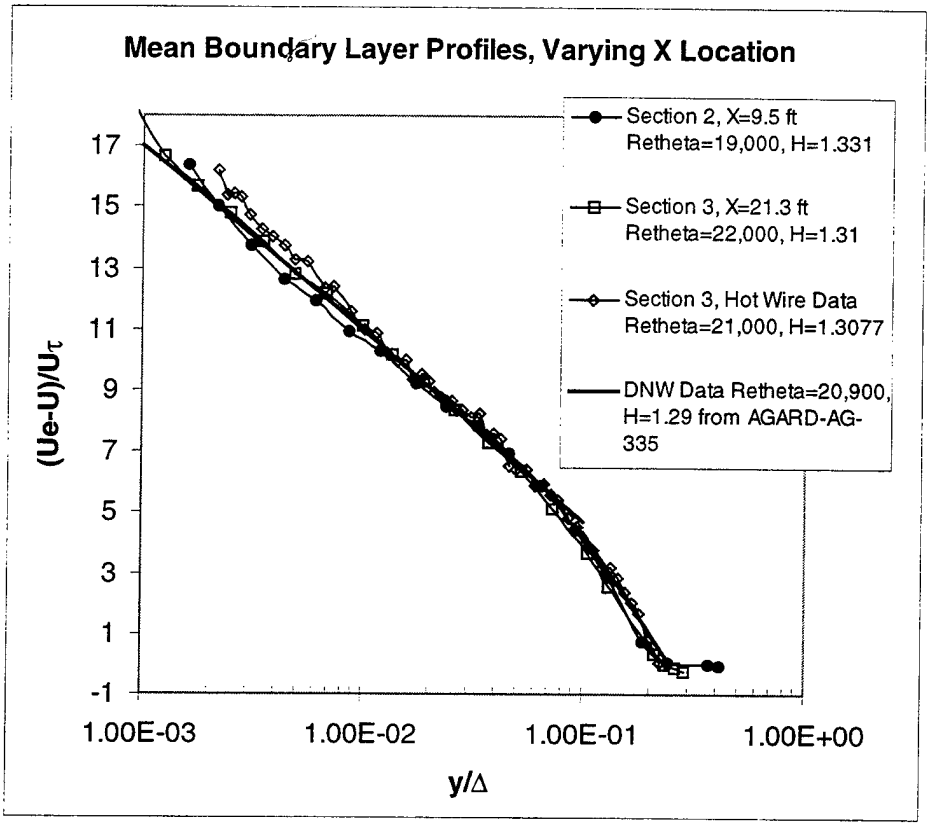

Figure 5: Comparison of mean boundary layer profiles for various X locations

The friction velocity (U_τ) was calculated using the following formula.

$$U_\tau = U_e\sqrt{\frac{c_f}{2}} \qquad \text{Equation 9}$$

Were c_f is the coefficient of friction calculated by the Ludwieg-Tillmann equation.

$$c_f = 0.246\times 10^{-0.678H}\left(U_e\theta/\nu\right)^{-0.268} \qquad \text{Equation 10}$$

Capital Delta (Δ) was calculated using

$$\Delta = \delta^*\sqrt{2/c_f} \qquad \text{Equation 11}$$

Table 2 lists the values for U_{ref}, c_f, Δ, and U_τ for the 11 spanwise locations. Table 3 lists the same values for the second section centerline location, the third section centerline location, the hot wire data, and the DNW data.

Table 2: Additional Boundary Layer Parameters

z (in)	Uref (m/s)	cf	Uτ (m/s)	Δ (in)
-15.0	31.93	0.002539	1.100	15.796
-12.0	31.97	0.002245	1.033	17.355
-9.0	31.92	0.00224	1.032	17.011
-6.0	31.90	0.002159	1.013	19.209
0.0	31.86	0.002143	1.002	19.010
6.0	31.87	0.002137	1.006	19.355
9.0	31.87	0.001623	0.879	21.462
12.0	31.88	0.002872	1.167	13.908
15.0	31.91	0.001984	0.971	36.801

Table 3: Comparison of Data Sets

Data Set (in)	Uref (m/s)	cf	Uτ (m/s)	Δ (in)
Section 2	31.96	0.002415	1.0857	10.72
Section 3	31.86	0.002143	1.002	19.01
Hot Wire	32.00	0.002217	0.995	18.09
DNW	20	0.002333	0.6819	22.89

The third set of experiments gave the freestream pressure readings for 15 locations on the centerline of the tunnel. From each value, the velocity of the flow was calculated at that x location. Figure 6 shows the streamwise velocity variation down the tunnel centerline.

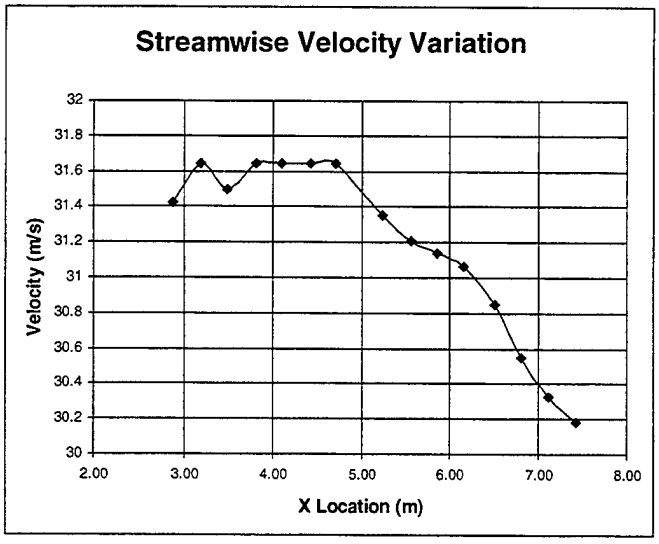

Figure 6:Streamwise Velocity Variation

This experiment was used to check the uniformity of the velocity throughout the tunnel test section. It was desired to have the same velocity in the third section as the velocity in the second section. Using the results from the first two experiments, a new tunnel height for the third section was calculated using the following formula.

$$h_{new} = \frac{h_i U_i - (\delta_u^* + \delta_l^*)(U_i - U_{new})}{U_{new}} \qquad \text{Equation 12}$$

Where h_i is the initial height, U_i is the initial velocity, U_{new} is the desired velocity, and δ_u^* and δ_l^* are the upper and lower displacement thicknesses respectively. The new tunnel height was calculated to be approximately 0.26 inches lower then the original height.

Conclusions

After comparing the velocity profiles for the 11 spanwise locations in the third section of the wind tunnel, the flow appears to be symmetric about the centerline. Also, the roughness plate placed in the first section of the tunnel produces the high Reynolds numbers needed at the end of the tunnel. Lowering the upper wall in the third section of the tunnel will increase the velocity to the desired uniformed value.

Reference

1 AGARD-AG-335, "Turbulent Boundary Layers in Subsonic and Supersonic Flow." Edited by Professor William S. Saric, p.16.

Appendix-II

Pressure Distribution on Flat Plate near Appendage

Abstract

Measurements were taken to document the mean surface pressure distribution in a wing/body junction flow at $\mathrm{Re}_\theta = U_e\theta/\nu$ (Reynolds number based on the momentum thickness, θ) of 23,200. These measurements yielded the time mean static pressure distribution on the flat test wall and the surface of the wing, and the data set complemented the mean velocity and turbulence measurements acquired by the Laser Doppler Velocimetry technique. These measurements were also used to check the flow symmetry around the wing.

Description of Apparatus

The tests were performed in the Virginia Tech Boundary Layer Wind Tunnel. The tunnel test section is about 29 feet in length with a width of 3 feet and a variable height. The test section is divided into two eight-foot sections numbered from the contraction as sections one and two, and a section numbered three which is about 13 feet long. The first section has an accelerating flow up to five feet from the contraction and approximately a constant inviscid core velocity downstream. The second section has a constant height, but the third section has a varying height that has been suitably adjusted to get a zero pressure gradient 2-D boundary layer. The tests were performed in this section.

The wing model used in the present measurements is a NACA 0020 tail with a 3:2 elliptical nose. The model has the dimensions of 9 inches in height, a chord length of 12 inches, and a maximum thickness of 2.824 inches. The wing model was aligned to the flow by considering the pressure taps at the maximum thickness point (t), on either side of the wing ($x/t \approx 0.770$, $y/t \approx 1.7263$, $z/t \approx 0.5$). Equalizing the pressure at these locations was sufficient for the model to be aligned with the flow (details are in the results section). To reduce the blockage effect generated by the presence of the wing, 0.25 inch thick plates upstream of the wing, $x \leq 11.875$ inches, are placed on the side walls. The 36.25 inch spanwise distance of the tunnel side walls at the wing changes to 35.8125 upstream and downstream with the insert plates.

To measure the wall static pressure, a plexiglass plate with 230 pressure taps around the contour of the wing and a small metal plate with 139 pressure taps at the nose region are placed on the tunnel floor. A drawing of the pressure plate is shown in figure 1.

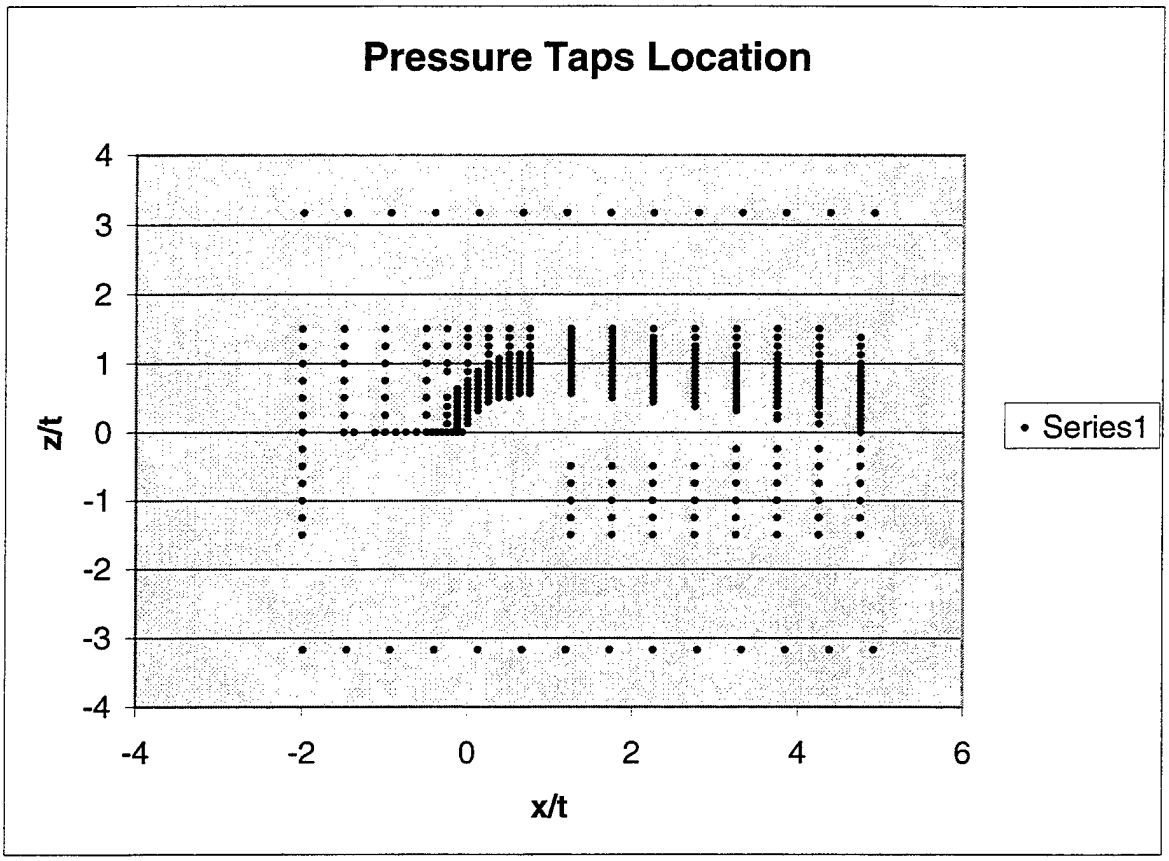

Fig.1 Pressure plate

The wing model with 24 pressure taps on its surface was mounted on the plexiglass plate, and a Scanivalve system, CTLR2P/S2-S6 Scanivlave Corp., was connected to all taps on the tunnel floor and on the nose of the model using Scanivalve diaphragms and Tygon tubing. The diaphragms were connected sequentially to the system. The Scanivalve system has 48 to 1 multiplexing, and the sampling frequency is 1000/sec. The data was sampled for 2 seconds with a settling time of 30 seconds. A Setra 239 pressure transducer with a calibrated range of 0-15 inches of water was used to measure the reference dynamic pressure. Another Setra 239 pressure transducer with a calibration range of -2.5 to 2.5 inches of water was used to measure the static pressure at the pressure taps. An inclined manometer with a resolution of 0.01 inches was used to verify the calibration of the two pressure transducers. A data acquisition board (DT2801) in conjunction with a PC-AT286 was used to acquire the data from the pressure transducers.

Procedure

A Prandtl type Pitot-static probe mounted about 58 inches from the end of the upstream contraction at the test section entrance is connected to the reference pressure transducer. The static port of the pitot probe is also connected to the low end of the measurement pressure transducer. The output of the two pressure transducers is read by the data acquisition board. The pressure readings are reduced by the data acquisition computer, and the pressure coefficients are calculated using.

$$C_p = \frac{P - P_{ref}}{P_{o\,ref} - P_{ref}}$$

The subscript *ref* denotes values at the reference station. P_{ref} is the static pressure, $P_{o\,ref}$ is the stagnation pressure, and P is the pressure read at each location.
The data set (shown in Table 1) obtained was made when the tunnel was run at a 32 m/s nominal reference velocity. This run took approximately 200 minutes, and this included the time required for the diaphragms to be changed. The uncertainty in the measurement of C_p is over the domain is $C_p \pm 0.018$ (20 to 1 odds).

Results

Figure 2 shows a contour plot of the C_p values. Also plotted on the graph is the data taken by Ölçmen and Simpson (1995) for the same wing/body configuration at a $\mathrm{Re}_\theta \approx 6000$. The contours are similar to each other.

Figure 3 shows the comparison of the measured values with the potential flow values calculated in Ölçmen and Simpson (1995). The graphs in figures 4a and 4b are plots of the data taken on the surface of the wing at two Y/T locations. The data collected from the pressure taps on the wing and from the pressure plate are listed in Table 1.

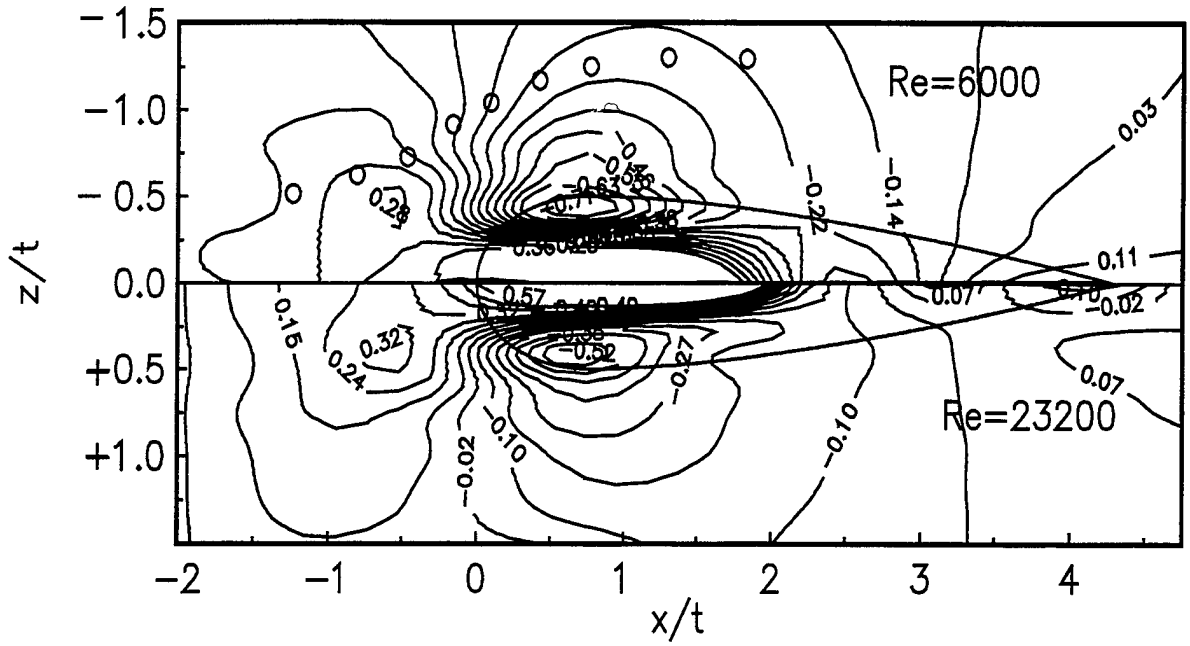

Fig 2. C_p contours. (Contours inside wing shape are meaningless but show contour values)

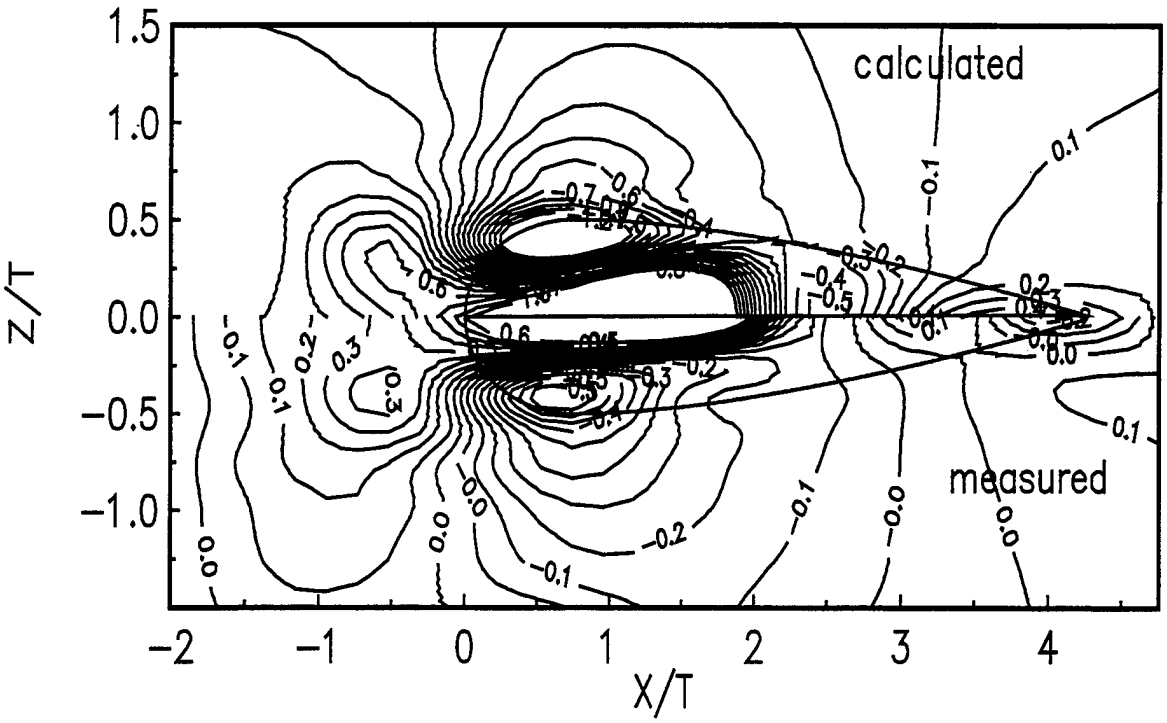

Fig 3. Measured and calculated C_p contours. (Contours inside wing shape are meaningless but show contour values)

Ölçmen and Simpson (1995) carried out LDV measurements at eight locations in the wing/body junction flow at $Re_\theta \approx 6000$ (see Fig. 5). For the present case of $Re_\theta \approx 23{,}200$ flow, the pressure gradient vectors for these eight locations are calculated from the pressure

measurements. These values are in Table 2. The values indicate that the at the same stations, the magnitudes of the pressure gradients in both x and z are lower in the high Reynolds

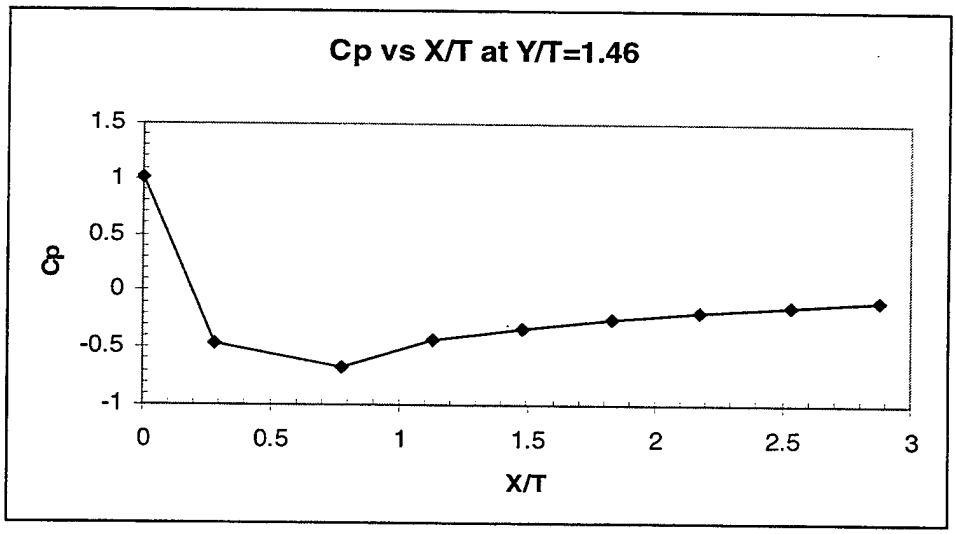

Fig 4a: Cp values on wing at Y/T=1.46

number case as compared to the lower Reynolds number case, indicating that the higher Reynolds number flow subjects these stations to a milder pressure gradient as compared to the lower Reynolds number. As mentioned earlier, the wing model was aligned to the flow by considering the pressure taps at the maximum thickness point (t), on either side of the wing ($x/t \approx 0.770$, $y/t \approx 1.7263$, $z/t \approx 0.5$). Equalizing the pressure at these locations was sufficient for the model to be aligned with the flow. This is seen in Fig. 6 where the C_p values are plotted versus z/t values at either sides of the wing at constant x/t values.

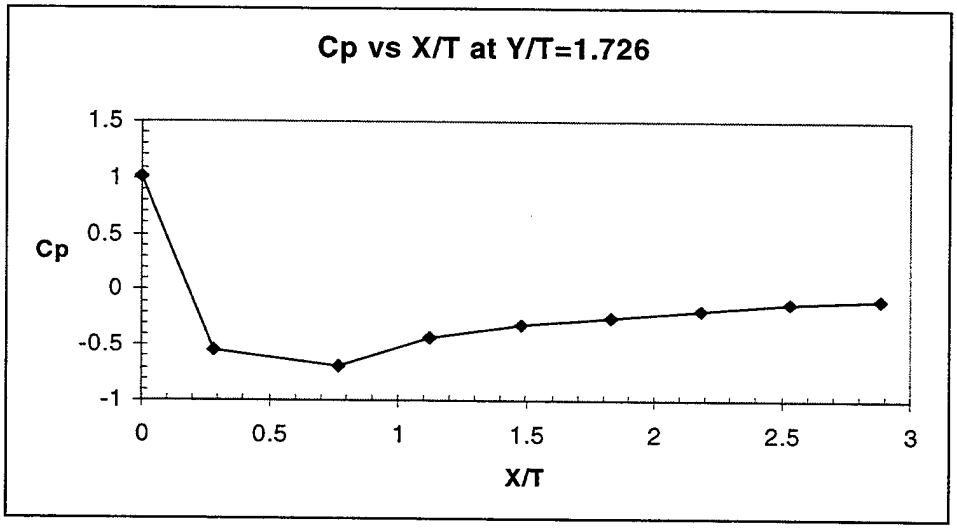

Fig 4b: Cp values on wing at Y/T=1.726

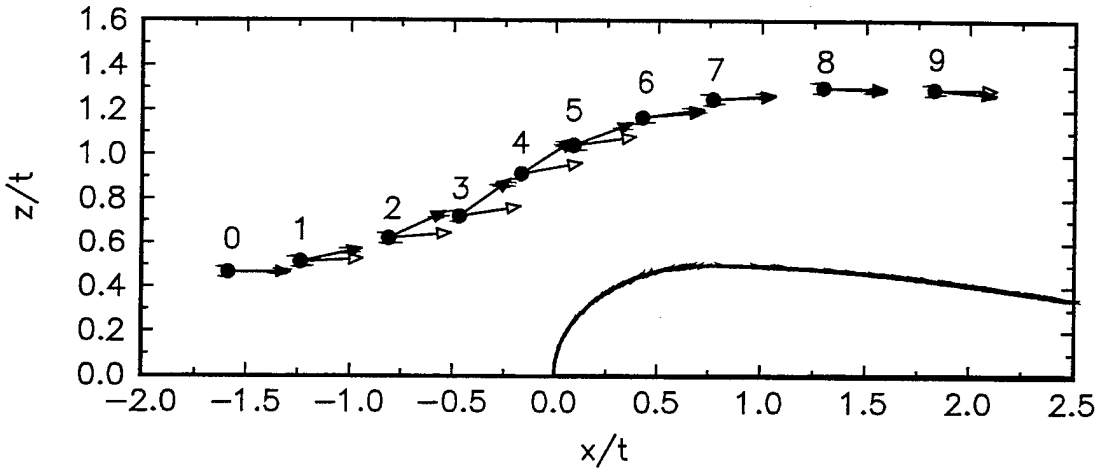

Figure 5. Wing shape and measurement locations. Full arrows wall-stress direction. Empty arrows free-stream direction.

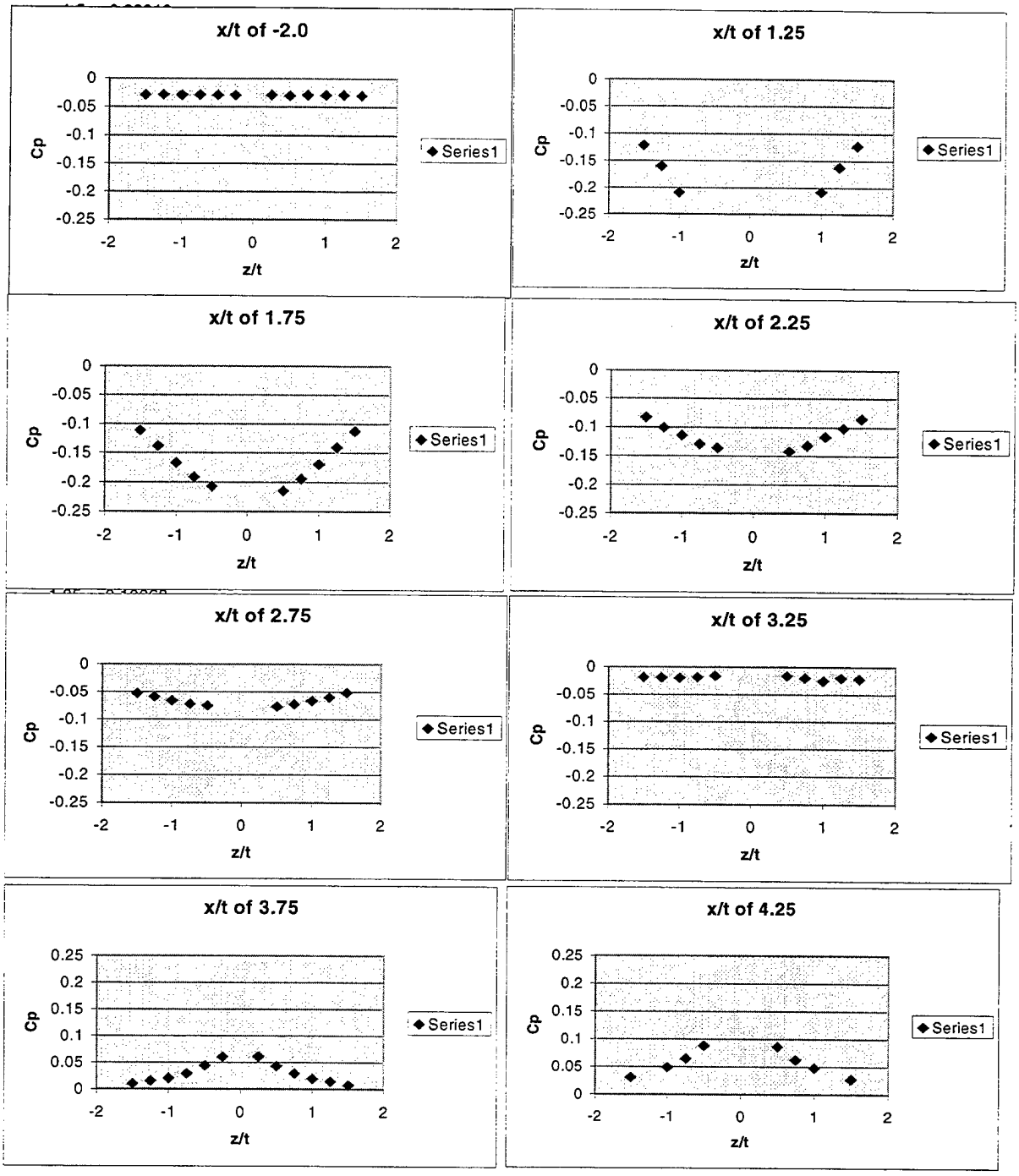

Fig 6. Variation of C_p versus z/t at various x/t

Conclusions

Pressure measurements were mapped in a wing/body junction at a Reynolds number of 23,200. The measurements also yielded the pressure gradients at the eight locations where LDV measurements have already been carried out. The values indicate that at the higher Reynolds number flow these stations are subjected to a milder pressure gradient as compared to the lower Reynolds number flow. The data obtained indicated that the flow is symmetric around the wing, and this is shown in figure 6. It should be noted that taps on the wing at ($x/t \approx 0.770$, $y/t \approx 1.7263$, $z/t \approx 0.5$) were used for the alignment of the wing, and this proved sufficient for the flow to be symmetric elsewhere.

Reference

Ölçmen, S. M. and Simpson, R. L. "An experimental study of a three-dimensional pressure-driven turbulent boundary layer." *J. Fluid Mech.* 1995, vol. 290, pp.225-262.

Whitfield, C. C. "Pitot Probe Boundary Layer Measurements." Appendix-I of this Report.

Uncertainty Analysis

The uncertainty in the measurement of C_p is calculated by the method outlined by Kline and McClintock (1953). As mentioned earlier, C_p is defined as

$$C_p = \frac{P - P_{ref}}{P_{oref} - P_{ref}}$$

The measurement of C_p with the two transducers (called the measurement transducer and the reference transducer) were calculated using the reduced expression for C_p which is

$$C_p = \frac{P - P_{ref}}{P_{oref} - P_{ref}} = \frac{(\Delta P)_{meas}}{(\Delta P)_{ref}}$$

It may be noted that $(\Delta P)_{meas}$ is measured using the measurement transducer (range of -2.5 to 2.5 inches of water) and $(\Delta P)_{ref}$ is measured using the reference transducer (range of 0 to 15 inches of water). The uncertainty in the measurement of C_p would be due to the uncertainty in the measurement of these two quantities. For the purpose of calculation the range of pressure sensed is taken to be 2.5 inches of water.

Let $\delta[(\Delta P)_{meas}]$ be the uncertainty in $(\Delta P)_{meas}$ and $\delta[(\Delta P)_{ref}]$ be the uncertainty in $(\Delta P)_{ref}$, then the uncertainty in C_p, which is δC_p, is given by

$$\frac{\delta C_p}{C_p} = \sqrt{\left(\frac{\delta (\Delta P)_{meas}}{(\Delta P)_{meas}}\right)^2 + \left(\frac{\delta (\Delta P)_{ref}}{(\Delta P)_{ref}}\right)^2}$$

Uncertainties in the individual transducers

(i) Measurement transducer (-2.5 to 2.5 inches of water)

Non-linearity : ± 0.1 % FS (full scale)
Zero error : ± 0.4 % FS
FS error : ± 0.4 % FS

Therefore, $\delta[(\Delta P)_{meas}]$ is equal to $\pm\sqrt{0.001^2 + 0.004^2 + 0.004^2} \approx \pm$ 0.0058 FS

That is, $\frac{\delta (\Delta P)_{meas}}{(\Delta P)_{meas}}$ is $\approx \pm$ 0.0058

(ii) Reference transducer (0 to 15 inches of water)

Non-linearity : ± 0.1 % FS
Zero error : ± 0.4 % FS
FS error : ± 0.4 % FS

Therefore, $\delta[(\Delta P)_{meas}]$ is equal to $\pm\sqrt{0.001^2 + 0.004^2 + 0.004^2} \approx \pm$ 0.0058 FS

For our range of pressures, $\frac{\delta (\Delta P)_{ref}}{(\Delta P)_{ref}}$ works out to be $\pm$ 0.0058×15/5 ≈ ±0.0174

Hence, the net uncertainty in C_p is $\pm\sqrt{0.0058^2 + 0.0174^2} \approx \pm$ 0.018 which is ± 0.018

Table 1. Data Set

Flow Conditions

Flow temperature (°C) = 24.2
density (Kg/m^3) = 1.093452
viscosity (m^2/s) = 1.676351E-05
Atmospheric pressure (Pa) = 93300
Velocity of undisturbed free stream (U_{ref} in m/s) = 31.90351
Reynolds number based on U_{ref} and chord of wing (c) = 580080.8

Table 1 (Continued) : Data collected from the wing

ON THE WING			
X/T	Y/T	Z/T	Cp
0	1.4607	0	1.007089
0.28463	1.4607	-0.3921	-0.547441
0.76991	1.4607	-0.50011	-0.68712
1.8357	1.4607	-0.4319	-0.247373
0.28526	1.4607	0.39244	-0.465812
0.77881	1.4607	0.50008	-0.672856
1.1327	1.4607	0.49014	-0.429646
1.4818	1.4607	0.4666	-0.327168
1.83	1.4607	0.43253	-0.252858
2.1769	1.4607	0.39014	-0.193071
2.5331	1.4607	0.33938	-0.136104
2.8771	1.4607	0.28434	-0.084942
0	1.7263	0	1.007089
0.28213	1.7263	-0.39078	-0.542879
0.76991	1.7263	-0.50011	-0.696738
1.1229	1.7263	-0.49063	-0.42889
1.4805	1.7263	-0.46671	-0.326211
1.8307	1.7263	-0.43245	-0.249586
2.1822	1.7263	-0.38944	-0.190772
2.5373	1.7263	-0.33874	-0.122926
2.889	1.7263	-0.28234	-0.086234
0.27589	1.7263	0.38742	-0.499354
0.77102	1.7263	0.50011	-0.694919
1.8441	1.7263	0.43096	-0.252828

x/t	z/t	Cp	x/t	z/t	Cp	x/t	z/t	Cp
-1.5	0	0.15663	0	0.62571	-0.00177	0.625	0.81303	-0.30033
-1.5	0.25	0.15337	0	0.68839	-0.00986	0.625	0.87571	-0.26918
-1.5	0.50035	0.14314	0	0.75035	-0.01304	0.625	0.93839	-0.24084
-1.5	0.75035	0.12842	0	0.87571	-0.01956	0.625	1.0004	-0.21631
-1.5	1.0004	0.11323	0	1.0004	-0.01983	0.625	1.0637	-0.19137
-1.5	1.2504	0.097045	0	1.2504	-0.02103	0.625	1.1264	-0.17538
-1.5	1.5004	0.075	0	1.3754	-0.01997	0.75	0.56303	-0.39648
-1.375	0	0.16495	0	1.5004	-0.01808	0.75	0.62571	-0.3691
-1.125	0	0.19257	0.125	0.31232	0.032893	0.75	0.68839	-0.34031
-1	0	0.20919	0.125	0.375	-0.04445	0.75	0.75035	-0.3136
-1	0.25	0.20001	0.125	0.43768	-0.08312	0.75	0.81303	-0.28966
-1	0.50035	0.17723	0.125	0.50035	-0.10345	0.75	0.87571	-0.26726
-1	0.75035	0.14807	0.125	0.56303	-0.12028	0.75	0.93839	-0.24487
-1	1.0004	0.11889	0.125	0.62571	-0.11689	0.75	1.0004	-0.22135
-1	1.2504	0.095316	0.125	0.68839	-0.10372	0.75	1.0637	-0.20226
-1	1.5004	0.076993	0.125	0.75035	-0.09514	0.75	1.1264	-0.18432
-0.875	0	0.22748	0.125	0.81268	-0.08478	0.75	1.2504	-0.15722
-0.75	0	0.25027	0.125	0.87571	-0.07418	0.75	1.3754	-0.12367
-0.625	0	0.27921	0.25	0.43768	-0.26564	0.75	1.5004	-0.11476
-0.5	0	0.30829	0.25	0.50035	-0.25678	-1.9919	-3.1707	-0.02982
-0.5	0.25	0.27659	0.25	0.56303	-0.23945	-1.4607	-3.1707	-0.02991
-0.5	0.50035	0.20569	0.25	0.62571	-0.22784	-0.92953	-3.1707	-0.02907
-0.5	0.75035	0.13902	0.25	0.68839	-0.20652	-0.39837	-3.1707	-0.03016
-0.5	1.0004	0.092003	0.25	0.75035	-0.18126	0.13279	-3.1707	-0.0284
-0.5	1.2504	0.063268	0.25	0.81303	-0.1593	0.66395	-3.1707	-0.02866
-0.5	1.5004	0.046497	0.25	0.87571	-0.13924	1.1951	-3.1707	-0.02986
-0.43732	0	0.32804	0.25	0.93839	-0.12437	1.7263	-3.1707	-0.02962
-0.375	0	0.34654	0.25	1.0004	-0.11194	2.2574	-3.1707	-0.02964
-0.31232	0	0.3615	0.25	1.1264	-0.09095	2.7886	-3.1707	-0.02971
-0.25	0	0.36648	0.25	1.2504	-0.07742	3.3198	-3.1707	-0.0297
-0.25	0.125	0.35429	0.25	1.375	-0.06497	3.8509	-3.1707	-0.02985
-0.25	0.25	0.29912	0.25	1.5004	-0.05621	4.3821	-3.1707	-0.02855
-0.25	0.375	0.23054	0.375	0.50035	-0.40416	4.9132	-3.1707	-0.02893
-0.25	0.50035	0.17382	0.375	0.56303	-0.35066	-1.9919	3.1707	-0.02901
-0.25	0.87571	0.068005	0.375	0.62571	-0.31899	-1.4607	3.1707	-0.02897
-0.25	1.0004	0.051062	0.375	0.68839	-0.28656	-0.92953	3.1707	-0.02907
-0.25	1.2504	0.027616	0.375	0.75035	-0.25871	-0.39837	3.1707	-0.02869
-0.25	1.5004	0.016864	0.375	0.81303	-0.24086	0.13279	3.1707	-0.03004
-0.18732	0	0.37928	0.375	0.87571	-0.19872	0.66395	3.1707	-0.02935
-0.125	0	0.45136	0.375	0.93839	-0.17367	1.1951	3.1707	-0.0293
-0.125	0.062677	0.42881	0.375	1.0004	-0.15469	1.7263	3.1707	-0.02921
-0.125	0.125	0.37924	0.375	1.0637	-0.1373	2.2574	3.1707	-0.02976
-0.125	0.18732	0.31585	0.5	0.50035	-0.60175	2.7886	3.1707	-0.02936
-0.125	0.25	0.25518	0.5	0.56303	-0.4533	3.3198	3.1707	-0.02925
-0.125	0.31232	0.20877	0.5	0.62571	-0.38619	3.8509	3.1707	-0.02958
-0.125	0.375	0.17175	0.5	0.68839	-0.34156	4.3821	3.1707	-0.02951
-0.125	0.43732	0.14368	0.5	0.75035	-0.30983	4.9132	3.1707	-0.02927
-0.125	0.50035	0.11407	0.5	0.81303	-0.27482	-2	-1.5	-0.02919
-0.125	0.56303	0.09317	0.5	0.87571	-0.24446	-2	-1.25	-0.02838
-0.125	0.62571	0.073581	0.5	0.93839	-0.21529	-2	-1	-0.02921
-0.06267	0	0.57041	0.5	1.0004	-0.19008	-2	-0.75	-0.0289
0	0.125	0.52595	0.5	1.0637	-0.16968	-2	-0.5	-0.02942
0	0.18732	0.37816	0.5	1.1264	-0.15386	-2	-0.25	-0.02942
0	0.25	0.26008	0.5	1.2504	-0.1284	-2	0	-0.0294
0	0.31232	0.16081	0.5	1.3754	-0.10696	-2	0.25	-0.0292
0	0.375	0.083339	0.5	1.5004	-0.02974	-2	0.5	-0.03025
0	0.43732	0.035148	0.625	0.56303	-0.45856	-2	0.75	-0.02921
0	0.50035	0.016238	0.625	0.62571	-0.41028	-2	1	-0.02957
0	0.56303	0.00173	0.625	0.68839	-0.3629	-2	1.25	-0.02904
			0.625	0.75035	-0.33103	-2	1.5	-0.03001

x/t	z/t	Cp	x/t	z/t	Cp	x/t	z/t	Cp
1.25	-1.5	-0.12206	2.25	1.1875	-0.10502	3.75	0.5	0.043313
1.25	-1.25	-0.16011	2.25	1.25	-0.10127	3.75	0.5625	0.039426
1.25	-1	-0.20921	2.25	1.3125	-0.09658	3.75	0.625	0.034571
1.25	-0.75	-0.24965	2.25	1.375	-0.09286	3.75	0.6875	0.033231
1.25	-0.5	-0.28888	2.25	1.5	-0.0851	3.75	0.75	0.02972
1.25	0.5625	-0.27738	2.75	-1.5	-0.05264	3.75	0.8125	0.026113
1.25	0.625	-0.27817	2.75	-1.25	-0.05934	3.75	0.875	0.023938
1.25	0.6875	-0.27025	2.75	-1	-0.06599	3.75	0.9375	0.021941
1.25	0.75	-0.25769	2.75	-0.75	-0.07191	3.75	1	0.020016
1.25	0.8125	-0.24747	2.75	-0.5	-0.075	3.75	1.0625	0.017928
1.25	0.875	-0.23356	2.75	0.375	-0.07866	3.75	1.125	0.017221
1.25	0.9375	-0.22289	2.75	0.4375	-0.07656	3.75	1.25	0.014592
1.25	1	-0.20832	2.75	0.5	-0.07682	3.75	1.375	0.01044
1.25	1.0625	-0.19911	2.75	0.5625	-0.07587	3.75	1.5	0.007722
1.25	1.125	-0.18597	2.75	0.625	-0.07483	4.25	-1.5	0.030732
1.25	1.1875	-0.17539	2.75	0.6875	-0.07384	4.25	-1	0.049071
1.25	1.25	-0.16247	2.75	0.75	-0.07238	4.25	-0.75	0.064658
1.25	1.3125	-0.1522	2.75	0.8125	-0.07277	4.25	-0.5	0.088425
1.25	1.375	-0.14078	2.75	0.875	-0.07265	4.25	-0.25	0.12997
1.25	1.4375	-0.13053	2.75	0.9375	-0.07072	4.25	0.125	0.096321
1.25	1.5	-0.12272	2.75	1	-0.06621	4.25	0.25	0.127184
1.75	-1.5	-0.11127	2.75	1.0625	-0.06506	4.25	0.375	0.10316
1.75	-1.25	-0.13762	2.75	1.125	-0.06354	4.25	0.4375	0.09409
1.75	-1	-0.16659	2.75	1.1875	-0.06136	4.25	0.5	0.086519
1.75	-0.75	-0.19098	2.75	1.25	-0.06006	4.25	0.5625	0.077691
1.75	-0.5	-0.20648	2.75	1.375	-0.05535	4.25	0.625	0.0727
1.75	0.5	-0.2142	2.75	1.5	-0.05132	4.25	0.6875	0.067238
1.75	0.5625	-0.20512	3.25	-1.5	-0.01867	4.25	0.75	0.062729
1.75	0.625	-0.20372	3.25	-1.25	-0.01928	4.25	0.8125	0.058188
1.75	0.6875	-0.20164	3.25	-1	-0.01994	4.25	0.875	0.054647
1.75	0.75	-0.19417	3.25	-0.75	-0.01856	4.25	0.9375	0.051649
1.75	0.8125	-0.18713	3.25	-0.5	-0.01597	4.25	1	0.048353
1.75	0.875	-0.18208	3.25	-0.25	-0.01148	4.25	1.125	0.042654
1.75	0.9375	-0.17576	3.25	0.3125	-0.013063	4.25	1.25	0.038225
1.75	1	-0.1693	3.25	0.375	-0.01467	4.25	1.375	0.033227
1.75	1.0625	-0.16122	3.25	0.4375	-0.01542	4.25	1.5	0.027942
1.75	1.125	-0.15378	3.25	0.5	-0.0161	4.75	-1.5	0.042156
1.75	1.1875	-0.14707	3.25	0.5625	-0.0175	4.75	-1.25	0.050248
1.75	1.25	-0.14015	3.25	0.625	-0.01802	4.75	-1	0.059845
1.75	1.3125	-0.13292	3.25	0.6875	-0.0187	4.75	-0.75	0.072892
1.75	1.375	-0.1248	3.25	0.75	-0.01974	4.75	-0.5	0.091237
1.75	1.4375	-0.11877	3.25	0.8125	-0.01949	4.75	-0.25	0.098001
1.75	1.5	-0.11251	3.25	0.875	-0.02013	4.75	0	0.032915
2.25	-1.5	-0.08251	3.25	0.9375	-0.02019	4.75	0.0625	0.1301
2.25	-1.25	-0.10068	3.25	1	-0.02502	4.75	0.125	0.12694
2.25	-1	-0.11428	3.25	1.0625	-0.01979	4.75	0.1875	0.120432
2.25	-0.75	-0.12928	3.25	1.125	-0.02021	4.75	0.25	0.11694
2.25	-0.5	-0.13581	3.25	1.25	-0.01988	4.75	0.3125	0.10804
2.25	0.4375	-0.14144	3.25	1.375	-0.01933	4.75	0.375	0.10137
2.25	0.5	-0.14236	3.25	1.5	-0.02141	4.75	0.4375	0.095734
2.25	0.5625	-0.13936	3.75	-1.5	0.010105	4.75	0.5	0.089078
2.25	0.625	-0.13404	3.75	-1.25	0.015711	4.75	0.5625	0.084128
2.25	0.6875	-0.13484	3.75	-1	0.021158	4.75	0.625	0.080407
2.25	0.75	-0.13203	3.75	-0.75	0.029472	4.75	0.6875	0.075632
2.25	0.8125	-0.12793	3.75	-0.5	0.044745	4.75	0.75	0.071401
2.25	0.875	-0.12366	3.75	-0.25	0.061	4.75	0.8125	0.068224
2.25	0.9375	-0.11788	3.75	0.1875	0.015511	4.75	0.875	0.061083
2.25	1	-0.11662	3.75	0.25	0.061224	4.75	0.9375	0.058949
2.25	1.0625	-0.11282	3.75	0.375	0.051749	4.75	1	0.053618
2.25	1.125	-0.10921	3.75	0.4375	0.045926	4.75	1.125	0.049775
						4.75	1.25	0.045525
						4.75	1.375	0.041774

Table 2. Pressure gradient vectors at the measurement locations

Station	Re_θ =23200		Re_θ =6000	
	$\left.\frac{\partial C_p}{\partial (x/T)}\right\|_{TC}$	$\left.\frac{\partial C_p}{\partial (z/T)}\right\|_{TC}$	$\left.\frac{\partial C_p}{\partial (x/T)}\right\|_{TC}$	$\left.\frac{\partial C_p}{\partial (z/T)}\right\|_{TC}$
1	0.0667	0.0890	0.0899	0.0960
2	0.0211	0.1734	0.0354	0.2118
3	-0.2060	0.2771	-0.2328	0.3312
4	-0.3438	0.1875	-0.4360	0.1454
5	-0.3670	-0.0587	-0.4649	-0.0649
6	-0.3208	-0.2643	-0.3346	-0.3609
7	-0.0103	-0.2544	0.0122	-0.4818
8	0.0395	-0.1599	0.0991	-0.3161
9	0.0740	-0.1094	0.0926	-0.1516